Effects of Heat Treatments and Compositional Modification on Carbide Network and

Matrix Microstructure in Ultrahigh Carbon Steels

A dissertation submitted in partial satisfaction of the requirements for

the degree of

Doctor of Philosophy

in

Materials Science and Engineering

by

Matthew David Hecht

B.S., Chemistry and Materials Science, University of California, Los Angeles

Carnegie Mellon University

Pittsburgh, PA

August, 2017

`

`

Abstract

This dissertation investigates microstructure/property relations in ultrahigh carbon steel (UHCS) with the aim of improving toughness while retaining high hardness. Due to high C contents (ranging from 1 to 2 wt%), UHCS exhibit high strength, hardness, and wear resistance. Despite this, applications for UHCS are currently limited because they typically contain a continuous network of proeutectoid cementite that greatly reduces ductility and toughness. In previous research, thermomechanic processing had seen considerable success in breaking up the network. However, the processing is difficult and has thus far seen very limited industrial application. Chemical modification of the steel composition has also seen some success in network break-up, but is still not well understood. There have been relatively few fundamental studies of microstructure evolution in UHCS; studies in the literature typically focused on lower C steels (up to 1 wt% C) or on cast irons (>2.1 wt% C). Thus, this work was undertaken to gain a better understanding of microstructural changes that occur during heat treatment and/or chemical modification of UHCS with a focus on the distribution of proeutectoid cementite within the microstructure.

This dissertation is composed of eight chapters. The first chapter presents an introduction to phases found in UHCS, descriptions of research materials used in each chapter, and the hypotheses and objectives guiding the work. The second chapter describes a study of the microstructure found in a 2C-4Cr UHCS before and after an industrial-scale austenitizing heat treatment that increased hardness and toughness and also produced discrete carbide particles in the matrix. The third chapter establishes and demonstrates a metric for measuring connectivity in carbide networks. The fourth chapter describes a series of heat treatments designed to investigate kinetics of spheroidization and coarsening of carbide particles and denuded zones near cementite

`

network branches in 2C-4Cr UHCS. The fifth chapter describes an additional series of heat treatments comparing coarsening kinetics in 2C-1Cr and 2C-4Cr UHCS. Lowering the Cr content caused clustering of cementite particles near grain boundaries, in contrast to the denuded zones observed in the higher Cr UHCS. The fifth chapter details four *in situ* confocal laser scanning microscopy heat treatments of 2C-4Cr UHCS. The seventh chapter investigates the effects of a 2wt% Nb addition on 2C-4Cr UHCS. The eighth and final chapter summarizes the findings of all the experiments of the previous chapters and revisits the objectives and conclusions.

`

Acknowledgements

Advised by

Yoosuf N. Picard

Bryan A. Webler

Thesis Committee:

David A. Laughlin

Chris P. Pistorius

Ian Sadler

I must also thank my family. Without their support this dissertation would not exist.

`

Contents

`

`

`

`

`

List of Figures

`

`

`

Figure 4.6 Log particle size distributions of each (a-o) time and temperature combination ranging from 800-970°C and 5 minutes to 24 hours. Multiple peaks within the distributions were

`

`

`

`

`

`

List of Tables

`

Chapter 1. Technical Background and Introduction

1.1 Abstract

The five sections in this chapter provide an overview of the phases found in typical Fe-C steels, some of the effects of Cr alloying on steels, an introduction to ultrahigh carbon steels (UHCS), a description of the UHCS materials that were studied, and the hypotheses and objectives guiding our research in this area. The first section of the chapter describes the morphology and mechanical properties for the single-phase regions in the Fe-C phase diagram (liquid, austenite, cementite, and ferrite), high temperature two-phase regions (eutectic and proeutectoid), and the products of the eutectoid reaction (eutectoid pearlite/spheroidite, bainite, and martensite). The second section of this chapter describes the effects of Cr on the stability of phases in steel, the compositions of the phases in the steel, and the diffusivity of chemical species (specifically Fe, C, and Cr). The third section of this chapter describes the potential benefits and processing challenges of UHCS. Additionally, potential methods for mitigating low toughness in UHCS are discussed (thermomechanical processing, rare earth and Niobium alloying, austenitizing heat treatments). The fourth section of this chapter describes all UHCS samples that were either received from an industrial supplier or produced at Carnegie Mellon University, as well as briefly detailing the chapters in which those steels are discussed. The fifth section of this chapter establishes hypotheses and objectives guiding the dissertation.

1.2 Plain Fe-C Alloy Phases & Microstructural Constituents

The simplest steels are alloys of iron and carbon. The binary phase diagram relevant to steels is the Fe-Fe$_3$C system shown in **Figure 1.1**. Fe$_3$C, also known as cementite, is a carbide phase commonly found in steels. Although graphite (essentially pure carbon) is thermodynamically more stable than cementite, it is extremely difficult to nucleate during

cooling (*1*) and thus is not typically included in iron-carbon phase diagrams. The following subsections give brief descriptions of each of the stable phases and microstructural constituents relevant to this dissertation.
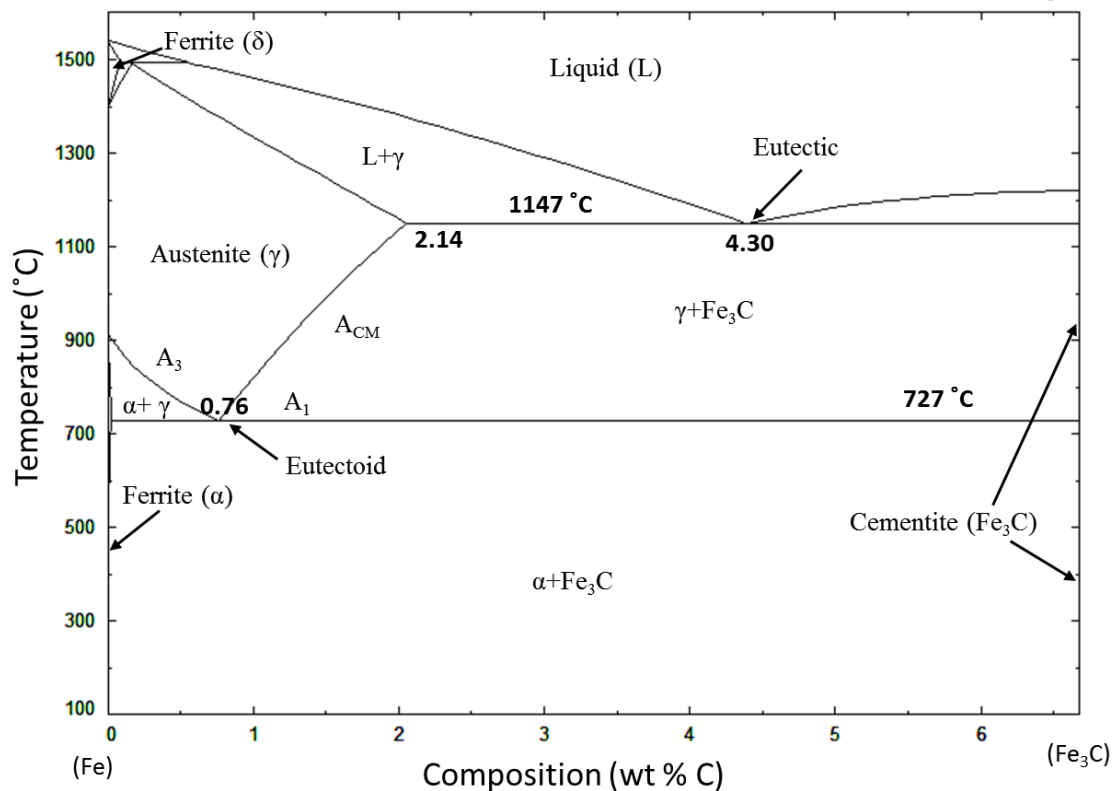
Figure 1.1 Fe-C phase diagram indicating temperature/composition regions of interest in UHCS. (This phase diagram was generated using the Factsage® version 6.4 thermochemical software (*2*), using the FSstel database.)

1.2.1 Single Phase Regions in the Fe-Fe₃C Phase Diagram

Liquid (L)

At high temperatures, steel exists as a liquid phase. The melting temperature of a steel alloy may vary considerably (on the order of hundreds of degrees Celsius) based on its composition. Pure iron has a melting point of about 1538°C, while iron alloyed with 4.3 wt% C (the eutectic composition) melts at 1147°C. Steels with carbon contents less than the eutectic

composition are termed "hypoeutectic", while steels with carbon contents greater than the eutectic composition are termed "hypereutectic".

Austenite (γ)

Austenite is a ductile paramagnetic face-centered cubic (FCC) allotrope of iron, which is stable above the eutectoid temperature of 727°C (*3*).   Solubility of carbon in austenite increases with temperature. The maximum carbon solubility in austenite of 2.14 wt% C occurs in a plain iron carbon steel at the eutectic temperature of 1147°C.

Cementite (Fe₃C/M₃C/θ)

Cementite (θ) is a hard and brittle orthorhombic iron carbide phase which is nominally 25 atom percent C, or 6.67 wt% C. Hardness of cementite decreases with temperature, as shown in **Figure 1.2** (*4*). Room temperature hardness is around 1000-1200 (HV), equivalent to about 69-72 on the Rockwell C scale (HRC). Cementite ductility at room temperature is negligible, but significant ductility in compression is observed above 500°C (*5*). Cementite formed during the eutectic reaction is classified as "eutectic cementite" (more specifically ledeburite or plate-like cementite depending on the morphology). Cementite formed above the eutectoid temperature but not during the eutectic reaction is termed "proeutectoid cementite" (encompasses various morphologies). Cementite formed below the eutectoid temperature is referred to simply as "eutectoid cementtie". Cementite above the eutectoid temperature may be significantly off stoichiometry (skewed towards iron rich $Fe_{(3+x)}C_{(1-x)}$) which may result in precipitation of ferrite adjacent to cementite in order achieve the correct stoichiometric ratio during cooling (*6*).
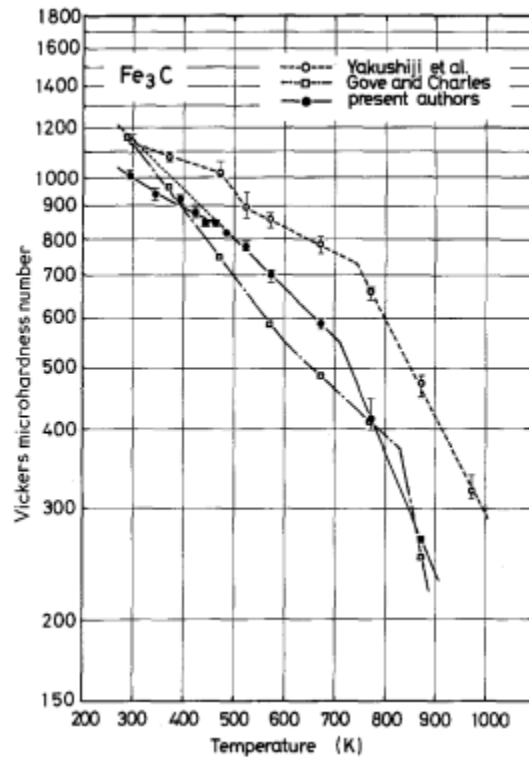
Figure 1.2 Cementite hardness at various temperatures (reproduced from Kagawa *et al.* (*4*) with permission from Springer).

Ferrite (α)

Ferrite is a body-centered cubic (BCC) phase with very low carbon solubility. Below 770°C (*3*), it is ferromagnetic. Although the BCC structure of ferrite is less closely packed than the FCC austenite, the sizes of the octrahedral interstitial sites are significantly smaller than in austenite. Interstitial carbon atoms in the ferrite consequently cause considerably more lattice distortion than in austenite, which is the cause of the relatively low C solubility in ferrite. On the other hand, the more open BCC structure does allow for faster diffusion of both interstitial and substitutional alloying elements.

1.2.2 High Temperature Two Phase Regions in Hypereutectoid Steels

Liquid + Austenite (L + γ)

During solidification of hypereutectoid steels, austenite is the first phase to solidify. In steels below 2.14 wt% C, solidification is completed above the eutectic temperature and thus no

eutectic reaction occurs. When carbon content is in excess of 2.14 mass percent, some liquid remains stable until the eutectic temperature and thus undergoes the eutectic (L->γ+θ) reaction. Assuming that there is dendritic solidification, the spacing of austenite dendrites and eventually the size of the austenite grains depends on the solidification rate and composition. For instance, Won and Thomas (7) developed an empirical model to predict secondary dendrite arm spacing in plain carbon steels based on carbon content and solidification rate in steels above 0.15 wt% C:

$$\lambda_{SDAS} = 143.9 \cdot C_R^{-0.3616} \cdot C_C^{0.5501-1.996 \cdot C_C}$$

C_R is the cooling rate in ˚C/sec, C_C is the carbon concentration in wt%. The model was only derived by the authors for carbon contents up to 1 wt% due to a lack of data for steels of higher C contents, but the trends should remain the same at higher carbon contents. As shown in **Figure 1.3**, austenite secondary dendrite arm spacing and thus grain size decreases with cooling rate and carbon content.
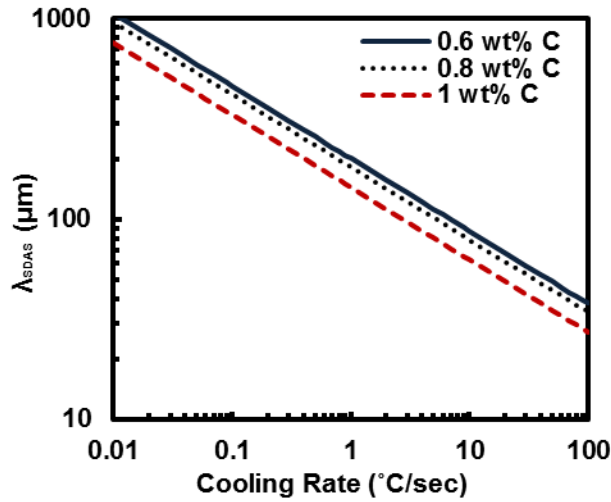
Figure 1.3 Effect of cooling rate on secondary dendrite arm spacing at three different carbon contents calculated using the equation of Won and Thomas (7).

Eutectic (γ + θ)

The eutectic reaction occurs during solidification of plain Fe-C alloys with carbon contents in excess of 2.14 wt% C. Eutectic cementite and austenite form from the remaining

`

carbon-enriched liquid surrounding newly solidified austenite dendrites (*8*). Eutectic cementite/austenite morphology is either ledeburitic, as shown in **Figure 1.4(a)**, or plate-like, as in **Figure 1.4(b)** (*9*). Ledeburitic cementite is interspersed with globes or rods of austenite and forms in preference to the plate-like morphology when there is less undercooling (*9*).

(a)   **(b)**
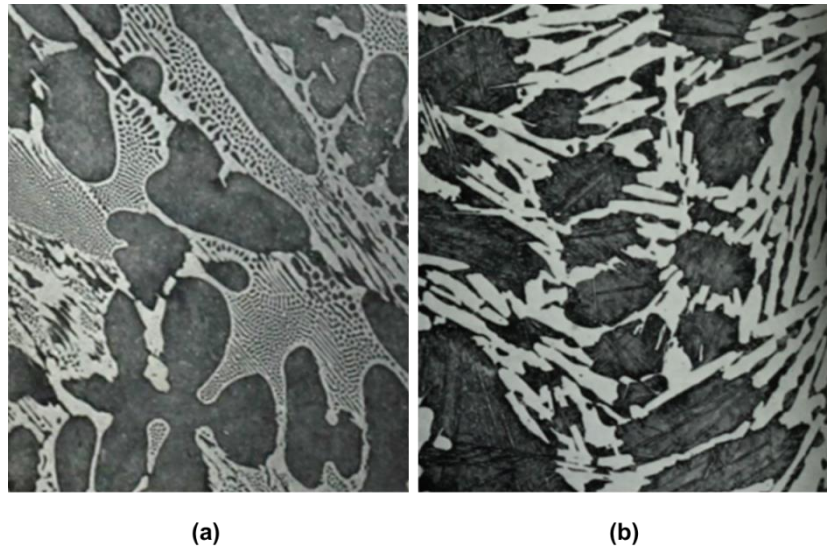
Figure 1.4 (a) Ledeburitic and (b) plate-like morphologies of eutectic cementite (adapted from Rickard and Hughes (*9*)).

Proeutectoid (γ + θ)

"Proeutectoid" refers to phases formed between the eutectic and eutectoid temperatures. In plain Fe-C steels, proeutectoid cementite is formed from supersaturated austenite during cooling or heating. Proeutectoid cementite generally forms on austenite grain boundaries but may also form within austenite grains or on previously existing cementite. Proeutectoid cementite forms in various morphologies (*10*) as shown in **Figure 1.5** (Dubé-Aaronson classification scheme). This work on UHCS will be primarily concerned with allotriomorphic grain boundary cementite, shown in **Figure 1.5 (a)**, and inter- and intra-granular idiomorphic cementite shown in **Figure 1.5 (f)** and **(g)**.
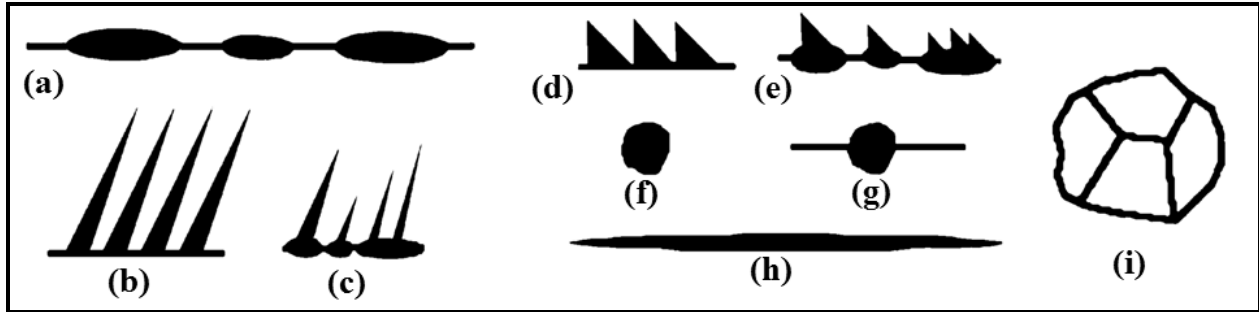
Figure 1.5 Dubé-Aaronson classification of proeutectoid cementite morphologies:(a) grain boundary allotriomorphs, (b) primary and (c) secondary Widmanstätten plates, (d) primary and (e) secondary Widmanstätten sawteeth, (f) intragranular and (g) intergranular idiomorphs, (h) intragranular Widmanstätten sideplates and (i) massive structures (adapted from Spanos and Kral (*10*)).

1.2.3 Products of the Eutectoid Transformation

Austenite becomes unstable below the eutectoid temperature, and decomposes into one or more new phases in the eutectoid transformation. Typical transformation products are pearlite bainite, and/or martensite. The products of austenite decomposition may vary depending on the cooling rate; this variety of possible eutectoid microstructures (and therefore mechanical properties) is one of the reasons steel is such a widely used engineering material. The possible transformation products may be illustrated by a time-temperature-transformation (TTT) diagram, such as that shown in **Figure 1.6** for steel close to the eutectoid composition.

Pearlite (α+θ)

Pearlite is a structure of alternating lamellae of cementite and ferrite. Typical pearlite morphology found in one of the UHCS analyzed in this dissertation is shown in **Figure 1.7**.
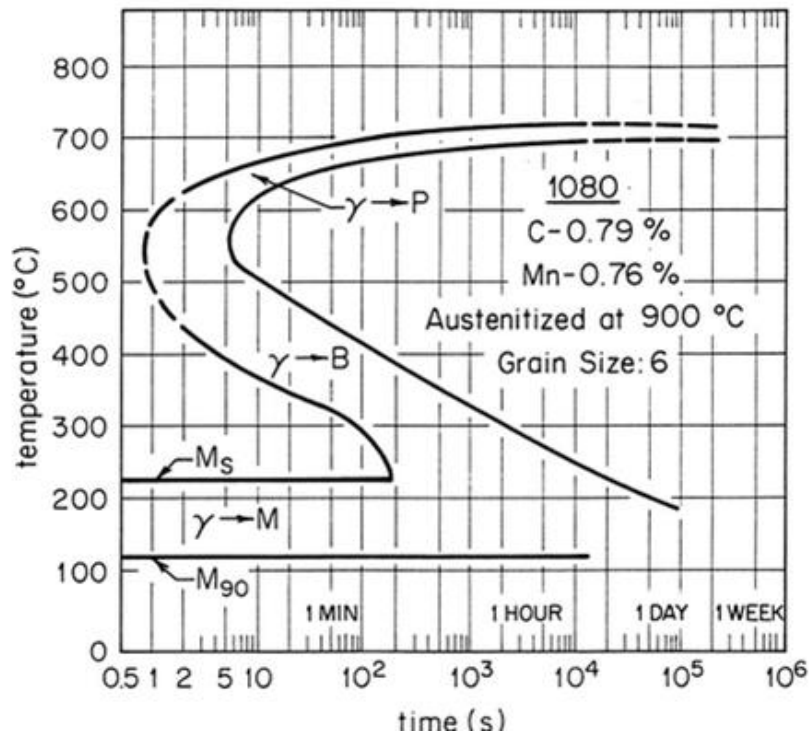
Figure 1.6 Example of a TTT diagram from Jones and Smith (*11*). This diagram shows the constituents that develop when a steel is first austenitized at 900°C, quenched to various temperatures, and held isothermally at those temperatures. In this diagram γ = austenite, P = pearlite, B = bainite, and M = martensite.
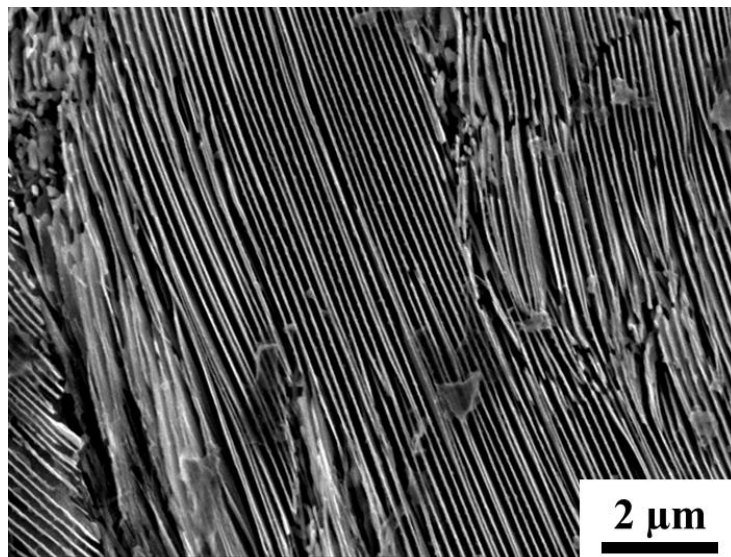
Figure 1.7 SEM micrograph of lamellar pearlite etched with 5% nital (nitric acid+alcohol).

The growth rate of pearlite depends on ΔT, the degree of undercooling below the eutectoid temperature and on Q, the activation energy of carbon diffusion in austenite (*12*).

8

$$Growth\ rate = K(\Delta T)^n exp(-\frac{Q}{RT})$$

Lamellar spacing (λ) in pearlite depends on the growth rate and hence the undercooling; faster growth/greater undercooling leads to smaller interlamellar spacing (*13*). There is some uncertainty about the exact relationship between λ and undercooling, but criteria are generally of the following form (*14*):

$$\lambda = \frac{A\sigma^{\alpha c}T_\varepsilon}{\Delta H_V \Delta T}.$$

In this equation, A is either 4 or 6, $\sigma^{\alpha c}$ is the α/θ interface energy, T_ε is the eutectoid temperature, ΔH_v is the change in enthalpy of pearlite formation, and ΔT is the undercooling below the eutectoid temperature. The equation indicates that lamellar spacing and undercooling are inversely proportional, which is the relation seen in experimental results (*14*).

Hardness of steels with predominantly pearlite microstructures can vary considerably depending on the interlamellar spacing of pearlite laths. Hall and Petch showed that yield strength was related to confinement of dislocations by grain boundaries or by cementite lamellae (*15, 16*):

$$\sigma_y = \sigma_o + k_y/\sqrt{\lambda}$$

In this equation, σ_y is the yield strength, γ is the interlamellar spacing of pearlite laths, and σ_o and k_y are constants which depend on pearlite colony size and composition. Since hardness is generally proportional to yield strength (*17*), this equation should also express the relationship between pearlite hardness and interlamellar spacing.

Spheroidization of pearlite is desirable in certain steels. This can be achieved through subcritical (below the eutectoid temperature), intercritical (between eutectoid and eutectic temperature) and cyclic (switching between sub- and inter-critical) heat treatments (*18*). A spheroidized structure can also form directly from austenite decomposition by the divorced

eutectoid transformation (DET). Divorced pearlite occurs when the austenite contains a large number of closely spaced nucleation sites for cementite, e.g. 'seeds' of cementite, grain boundaries, or dislocations (*19*). A few studies have examined intercritical heat treatments in steels around 2 wt% C (*20–23*), but none specifically examined pearlite spheroidization.

Coarsening

Given sufficient times and temperatures, spheroidized pearlite particles will coarsen. Coarsening is a process by which larger particles grow at the expense of smaller particles. The driving force for coarsening is twofold: first, at constant volume larger particle sizes reduce the over-all interface area, reducing the energy of the system. Second, the greater curvature of smaller particle results in an increase in solute concentration at the particle/matrix interface resulting in a concentration gradient from small particles large. Kinetics of the coarsening process is explained in detail in chapter 4, section 4.2.2.

Bainite (γ to B)

Bainite is a hard mixture of irregular ferrite laths and cementite which forms if cooling is fast enough to avoid complete transformation of austenite to pearlite**.** Bainite forms directly from the austenite via a mechanism that is still in debate (*24*) but may involve short range carbon diffusion and a displacive transformation. Bainite is classified as "upper bainite" or "lower bainite" depending on the transformation temperature. Upper bainite (**Figure 1.8(a)**) forms at temperatures between 400-550˚C. Lower bainite (**Figure 1.8(b)**) forms at temperatures between 250-550˚C. Bhadeshia proposed that carbon-rich bainite plates formed by a displacive mechanism, followed by carbon diffusion to form cementite (*25*). Cementite formation mechanisms in upper and lower bainite are shown in **Figure 1.9**.
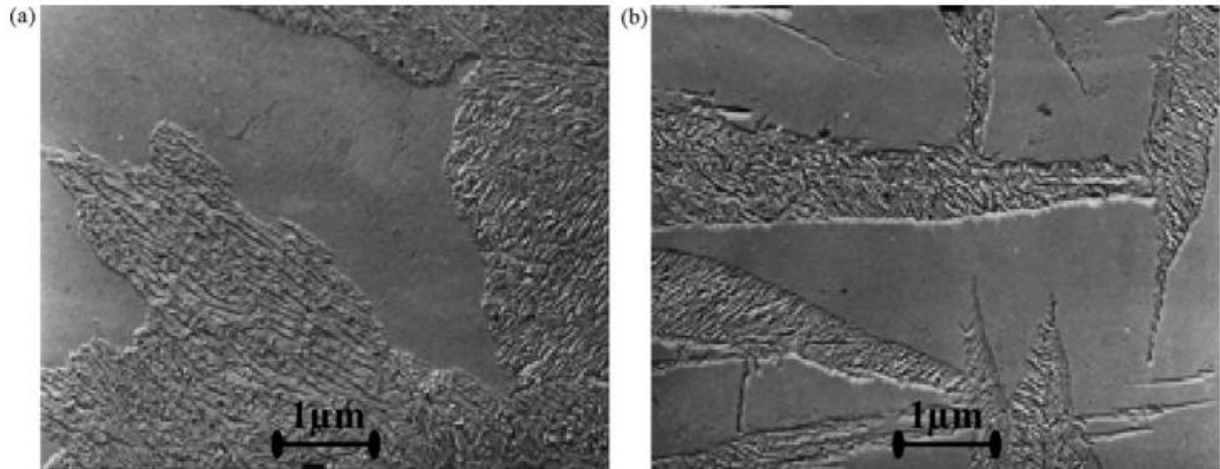
Figure 1.8 SEM micrographs of (a) upper bainite formed at 450°C and (b) lower bainite formed at 250°C (reproduced from Sajjadi (*26*) with permission from Elsevier).
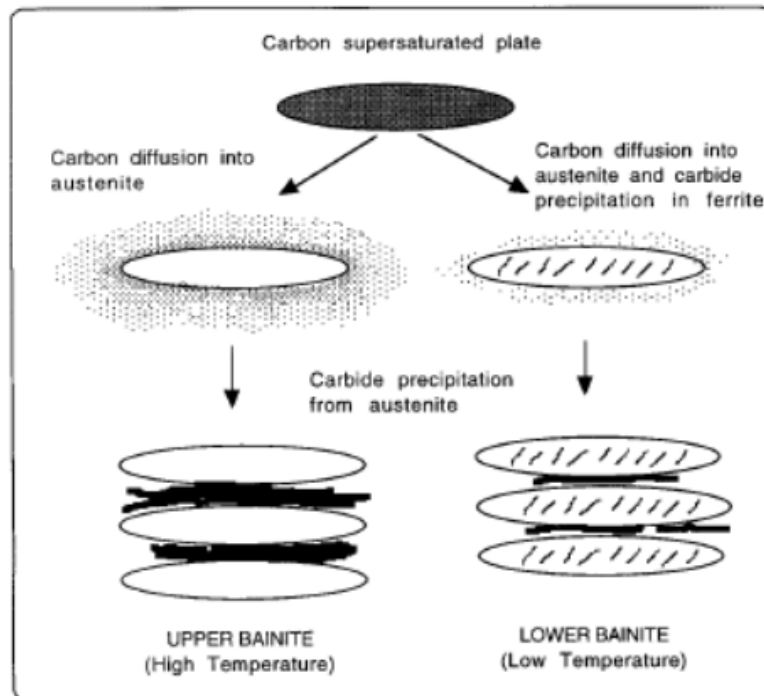
Figure 1.9 Schematic of formation of carbides in upper and lower bainite (reproduced from Bhadeshia (*25*).)

The hardness of bainite depends on the carbon content and transformation temperature (*25*). Hardness increases as the carbon content increases and the transformation temperature decreases. For instance, the bainite hardness in the 0.69 wt% C steel shown in **Figure 1.10** steadily decreased with transformation temperature.

11
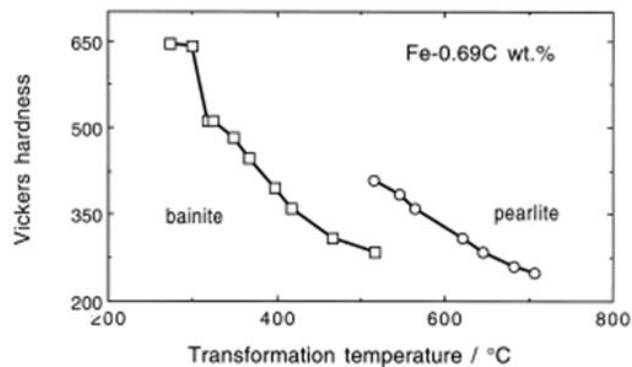
Figure 1.10 Bainite hardness as a function of transformation temperature in a 0.69 wt% C steel [reproduced from Bhadheshia (*25*)].

Martensite (γ to M)

Martensite is an extremely hard carbon-rich iron phase with a tetragonal crystal structure formed by a displacive transformation during rapid cooling of austenite. The M_s temperature refers to the onset of the martensitic transformation. Martensite can have four different morphologies: lath, butterfly, lenticular, and thin-plate (*27*). An example of the thin plate martensite microstructure is shown in **Figure 1.11**.

The high hardness of martensite is due to high dislocation densities and lattice strains caused by trapped carbon atoms. Thus, increased carbon content in steel causes increased martensite hardness as shown in **Figure 1.12** (*28*)). Martensite hardness can be as high as 70 HRC in the as-quenched state with high carbon contents. Reheating (tempering) the martensitic microstructure above the M_s temperature allows carbon diffusion to occur which relieves some from the tetragonal lattice, softening the martensite and reducing its brittleness.
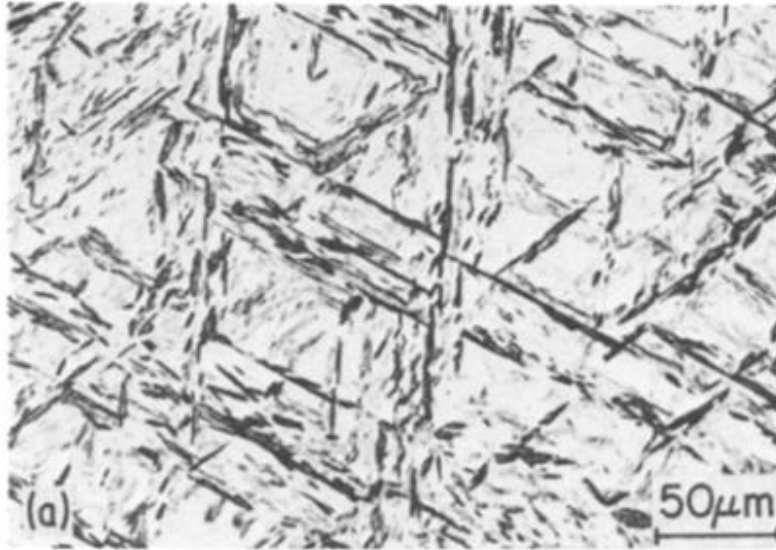
Figure 1.11 Optical micrograph showing thin plate Martensite (reproduced from Umemoto (*27*) with permission).
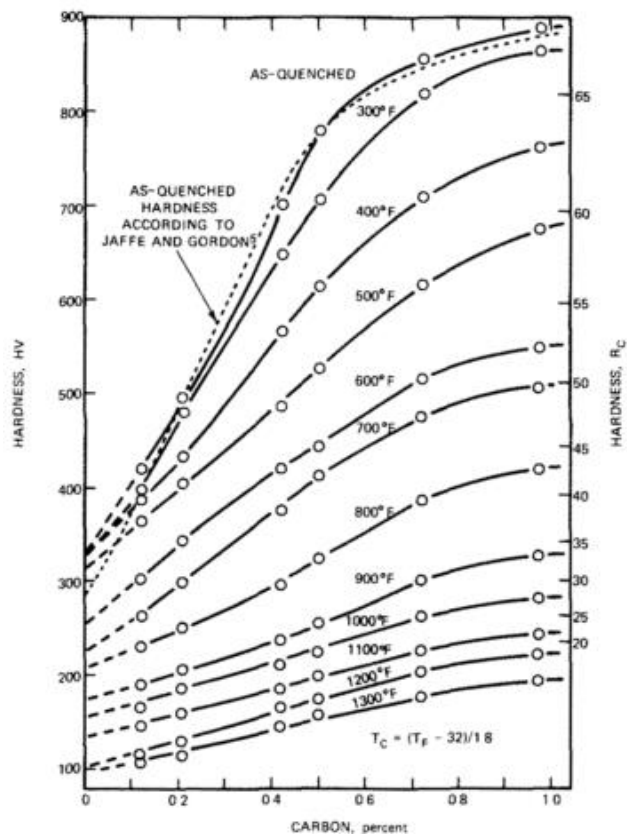
Figure 1.12 Hardness of martensite as a function of tempering temperature and carbon content (reproduced from Grange (*28*) with permission from Springer).

`

1.3 Ultrahigh Carbon Steel

Distinctions in the nomenclature of steels may be made based on carbon content. Alloys of iron with carbon contents up to 2.14 wt% are termed "steels", and alloys with higher carbon contents are termed "cast irons". Within the category of steels, "low carbon steels" or "mild steels" refer to alloys with less than 0.3 wt% C; "medium carbon steels" refer to alloys of 0.3 to 0.6 wt% C; "high carbon steels" refer to alloys of 0.6 to 1 wt% C; and "ultrahigh carbon steels (UHCS)" refer to alloys of 1 to 2.14 wt% C. This thesis is concerned with understanding the effects of heat treatments and/or chemistry modifications on UHCS.

Ultrahigh carbon steels (UHCS) have been used for many years in various applications demanding high strength and excellent wear resistance. UHCS are hypereutectoid steels with carbon contents from 1.0-2.1 wt%. As a result of this high C content, there is precipitation of proeutectoid cementite (Fe_3C) during cooling from casting and/or during heat treatment processes. The hard and brittle cementite contributes to the high hardness and wear resistance of UHCS, which is desirable for applications involving the cutting or shaping of other metals. UHCS have a long history of usage in ancient weaponry, such as Wootz/Damascus steel (*29–31*) and have been used in rolling mills as far back as 1913 (*32*); UHCS are also commonly used in tool steels. There has been interest over the last few decades in using UHCS for other applications where traditionally lower carbon content steels have been utilized, such as sheet and automotive steels(*33, 34*).

1.3.1 Brittleness in UHCS

A downside to high carbon steels and UHCS is extremely low ductility as carbon content increases. The relationship between carbon content and ductility was first demonstrated by Howe in the 1890s (*35*), who created the plot shown in **Figure 1.13** from the data available at the time.

14

`

Howe's plot represents a longstanding trend where few, if any, processes could effectively mitigate the extreme brittleness associated with UHCS. This trend held until the mid-1970s (*36, 37*), when advances in understanding of the origins of the brittleness in high carbon steels and UHCS resulted in processing methods that could reliably produce high and ultrahigh carbon steels with good ductility (*38*).
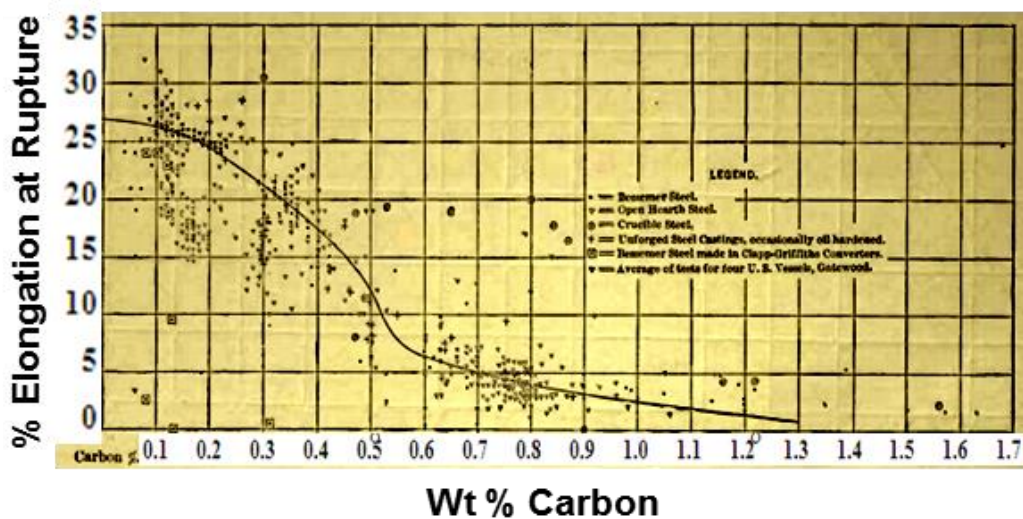
Figure 1.13 Adaptation of Howe's 1890 chart (*35*) showing decrease in steel ductility with carbon content. Axes were relabeled to improve readability from the original figure.

Carbide Networks in UHCS

Brittleness in UHCS is primarily caused by a carbide network that runs through the microstructure. The network forms from allotriomorphic proeutectoid carbides that form on austenite grain boundaries during cooling. Heckel and Paxton (*39*) investigated proeutectoid cementite precipitation in hypereutectoid steels and concluded that grain boundary (allotriomorphic) cementite formed very quickly during cooling prior to other types of cementite such as Widmanstätten laths (**Figure 1.14**). The grain boundary allotriomorphs coalesced to form a connected film along the grain boundaries. *In situ* scanning electron microscope (SEM) images of fracture tests demonstrated that cracks initiate at the carbide/matrix interface and propagate within the carbides (*40, 41*). An example of a cementite network in an UHCS utilized in this

dissertation is shown in **Figure 1.15(a)**; **Figure 1.15(b)** shows a crack propagating along the network. Breaking up or eliminating this network is a major processing goal for UHCS, and effects of processing on the network will be considered in this thesis. Details of methods that have been successfully employed for network breakup will be discussed in the following sections.
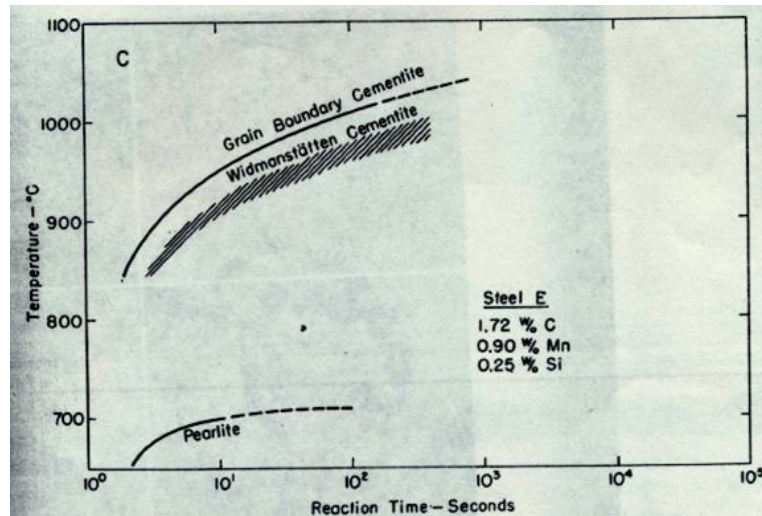
Figure 1.14 Time and temperature ranges for forming grain boundary (allotriomorphic) and widmanstatten cementite (adapted from Heckel and Paxton (*39*)).
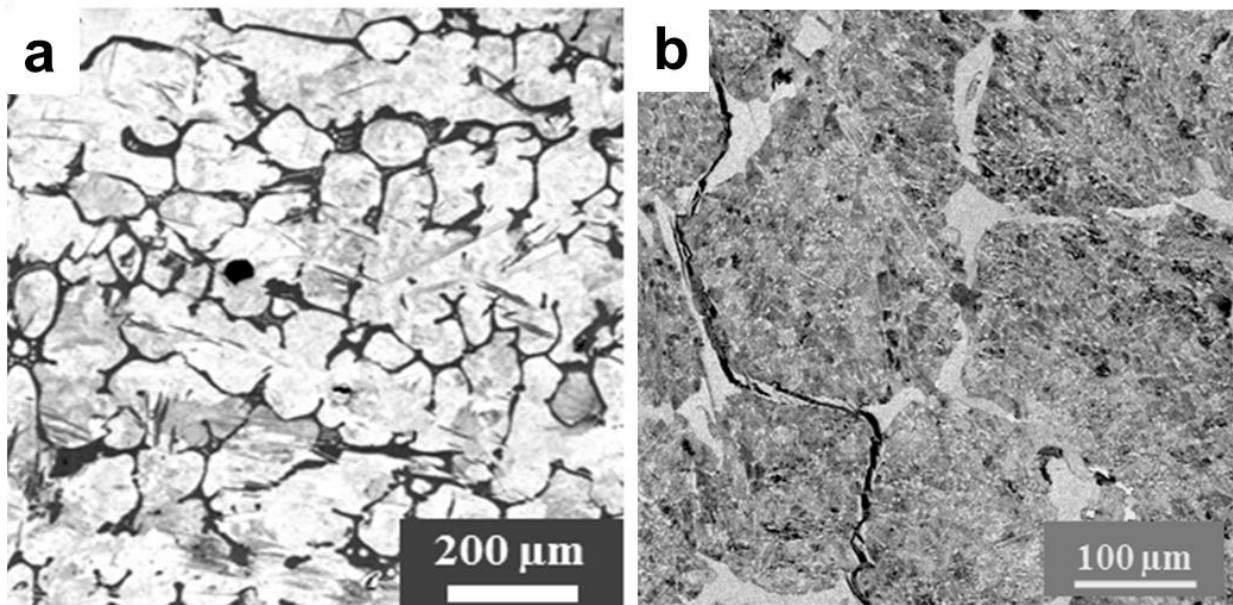
Figure 1.15 SEM micrographs of showing (a) a carbide network (dark phase) in an UHCS and (b) a different UHCS with a crack running along a carbide network (bright phase).

1.3.2 Network Break-Up Methods

Thermomechanical Processing

Thermomechanical processing of UHCS was pioneered by Sherby *et al* in the mid 1970's (*37*) and involves hot working the steel within the single phase austenite field, followed by warm working in the $Fe_3C+\gamma$ phase field. The thermomechanical processing refines the austenite grains and introduces intragranular sites with high dislocation densities, resulting in far more intra- and inter-granular nucleation sites for cementite (*42*). The result is a matrix made up of completely spheroidized cementite particles in a ferrite matrix. Precipitation of cementite on the refined austenite grain boundaries pins the boundaries and prevents additional grain growth, keeping the grains very fine even at high temperatures and allowing superplastic behavior above the eutectoid temperature (*36*, *37*, *43*, *44*).

Thermomechanical processing may also take advantage of the divorced eutectoid transformation (DET) for further spheroidization of the microstructure, with or without additional deformation during the DET. DET processing involves a short isothermal austenitizing hold just above the eutectoid temperature followed by an air cool without deformation to take advantage of the divorced eutectoid transformation as shown in **Figure 1.16(a)**. DETWAD (DET with associated deformation) processing induces a divorce eutectoid microstructure by continuing deformation during cooling below the eutectoid temperature without an isothermal hold as shown in **Figure 1.16(b)** (*42*). **Figure 1.17** shows an example of the microstructure refinement possible through hot and warm working and DETWAD/DET.
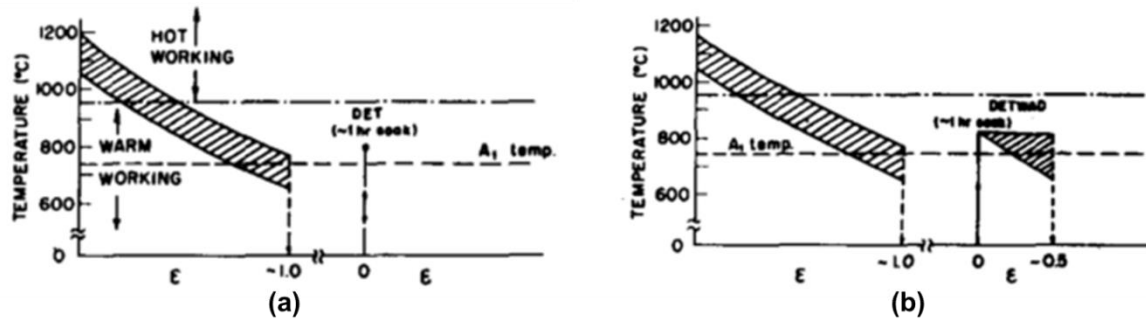
Figure 1.16 Thermomechanical processing routes for UHCS involving the divorced eutectoid transformation (a) without (b) with (b) additional working during the divorced eutectoid transformation (adapted from Oyama (*42*)).
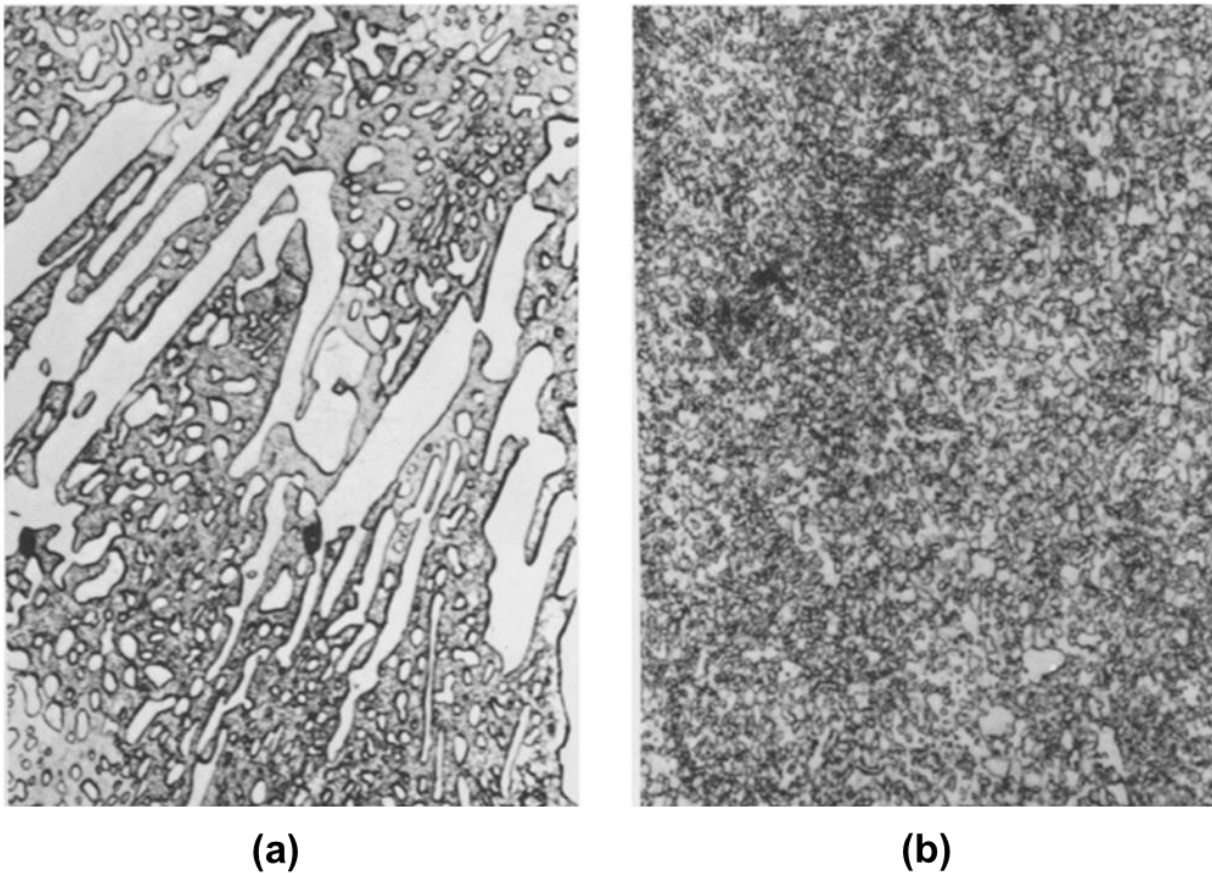
Figure 1.17 Optical micrographs of (a) as-Cast 1.9 wt% C UHCS and (b) the same steel after hot and warm working with DETWAD (from (*36*).

Mechanical properties of the thermomechanically processed UHCS are vastly improved

over the as-cast properties. Sherby *et al* revisited Howe's 1890 chart of steel elongations/ductility

versus carbon content (**Figure 1.18**), and showed that thermomechanically processed UHCS

`

could reach the same levels of ductility as very low carbon steels (*43*). Furthermore, the yield strength/ductility combination of the UHCS was comparable to or better than conventional or dual phase steels (**Figure 1.19**). Funds were set aside in the late 1990s by the DOE for UHCS research and development for industry-scale adoption (*45*). However it is unclear whether the processing is yet or will ever be economically feasible for widespread adoption.
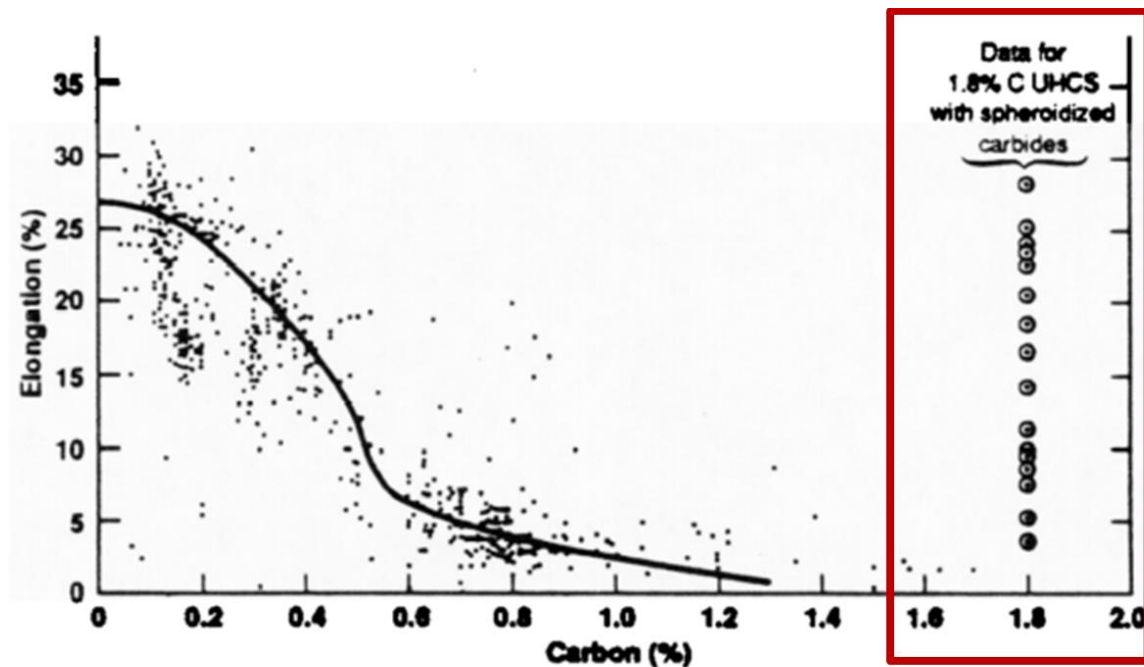
Figure 1.18 Howe's chart revisited by Sherby – red box added here to emphasize range of UHCS elongations, or ductility (adapted from Sherby (*43*)).
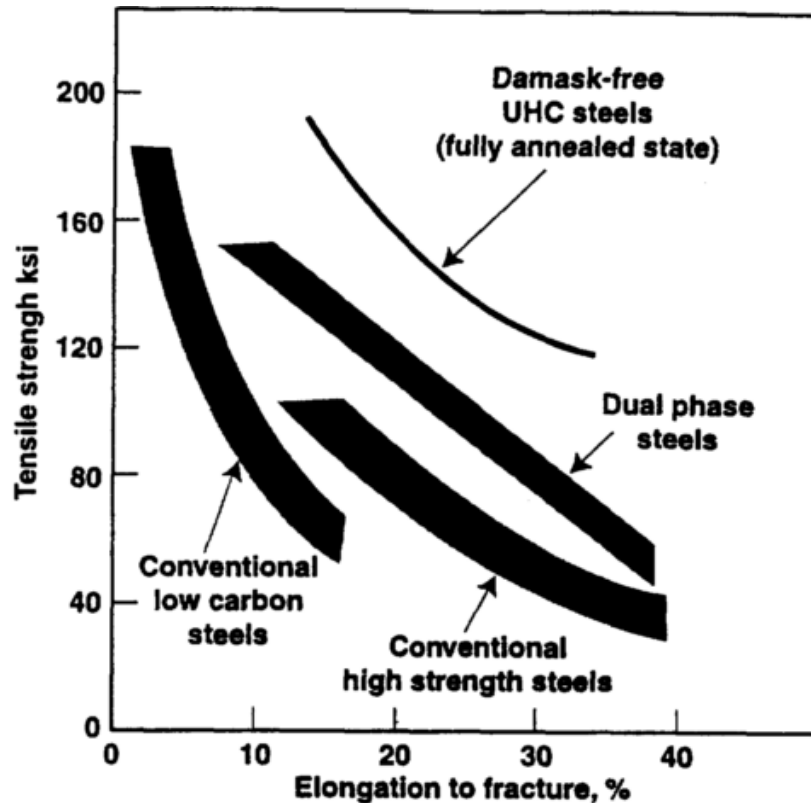
Figure 1.19 Fully spheroidized thermomechanically processed UHCS properties on a chart of strength versus ductility (reproduced from Sherby (*43*)).

Chemical Modification

A different method of network break-up in UHCS is alloying with rare earths (RE) or niobium. The advantage of chemistry modification over thermomechanical processing is the greater simplicity in processing, and the ability to adapt existing processing methods to the new chemistry. Liu *et al* (*46*) observed close to 100% toughness enhancement (from 6.5 to 12.6 J/cm^2) in a 1.9C-1.4Cr UHCS modified by a mixture of rare earths and Al-B-Sb + Ca-Si of about 0.08 wt%. Wang *et al* (*47*) observed that additions of rare earths in high speed steel (1.5-2 wt% C) broke up the connectivity of eutectic carbides (**Figure 1.20**) and improved mechanical properties (**Figure 1.21**) based on the amount of RE added. Hamidzadeh *et al* showed a 75-100% improvement in toughness due to network break-up of a 1.4C-11.5Cr alloyed with either 1-1.5% niobium (*48*) (**Figure 1.22(b)**) or 0.03 wt% RE(Ce+La) (*49*) (**Figure 1.22(c)**).
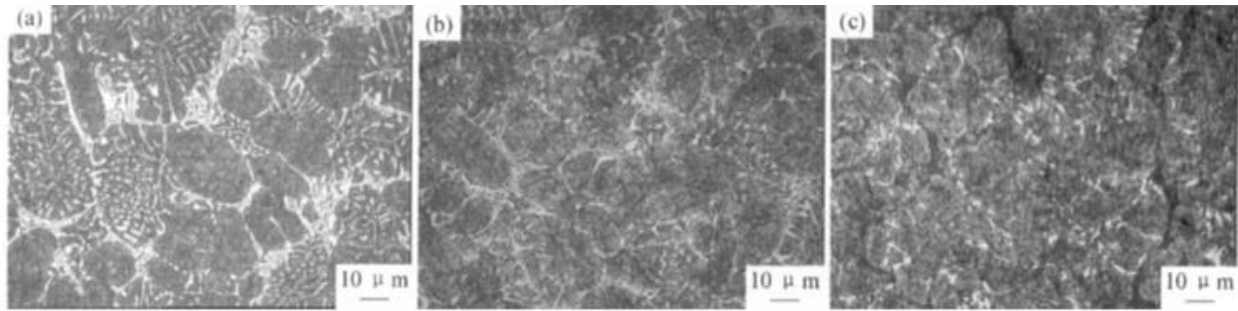
Figure 1.20 SEM micrographs of a high speed steel modified by (a) 0 wt% RE, (b) 0.04 wt% RE, and (c) 0.08 wt% RE (reproduced from Wang *et al* (*47*) with permission).
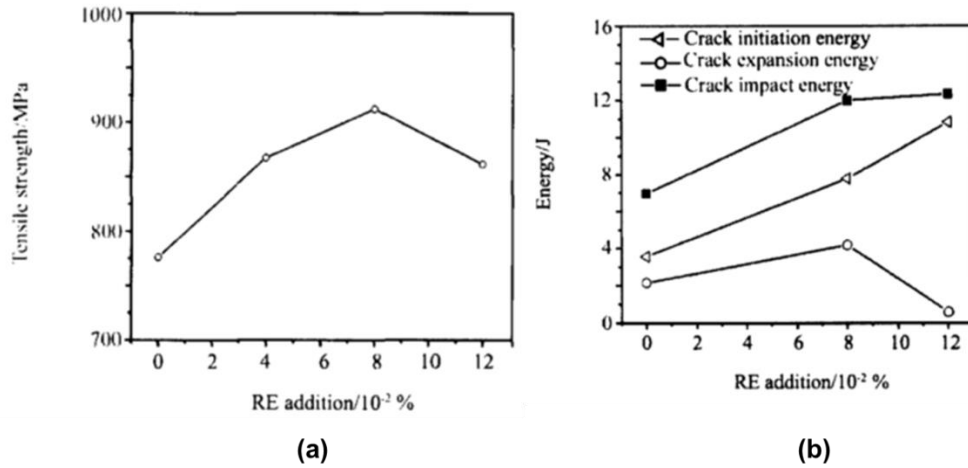
Figure 1.21 Mechanical properties of a high speed steel as a function of amount of RE modifiers (adapted from Wang *et al* (*47*) with permission).
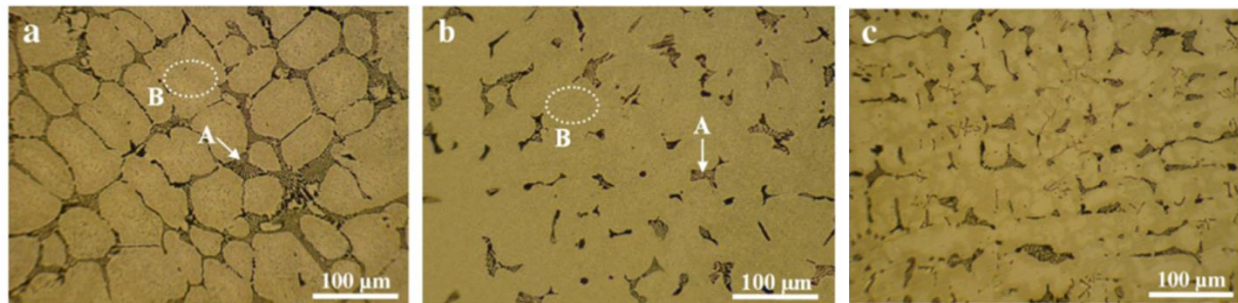
Figure 1.22 Chemical modification of (a) as-cast 1.5-C 11Cr steel alloyed with (b) 0.03 wt% La+Ce and (c) 1 wt% Nb (adapted from Hamidzadeh *et al.* (*48, 49*) with permission).

Heat Treatments

Intercritical anneals (heat treatments within the γ+Fe₃C two-phase region) without thermomechanical processing or chemical additions have the advantage of simplicity, but have seen limited success in network modification. Qian and Liu observed some network breakup in

2.5C-1.7Cr white cast iron held at 980°C for 2 hours (*50*) (**Figure 1.22**). The network carbides appeared to neck in regions with local curvature, and intragranular carbides were observed in the matrix. Pacyna and Rozniata studied the effects of 10 hour holds and 48°C/min cooling at 50°C intervals from 850°C to 1050°C in a 1.9C-1.1Cr UHCS (*51*). They noted that some cementite had moved from the network into the matrix. However, toughness was not improved over the as-cast condition, possibly because the intragranular carbides were coalesced into a secondary network when held at 950°C or higher for 10 hours (**Figure 1.24(b)**).
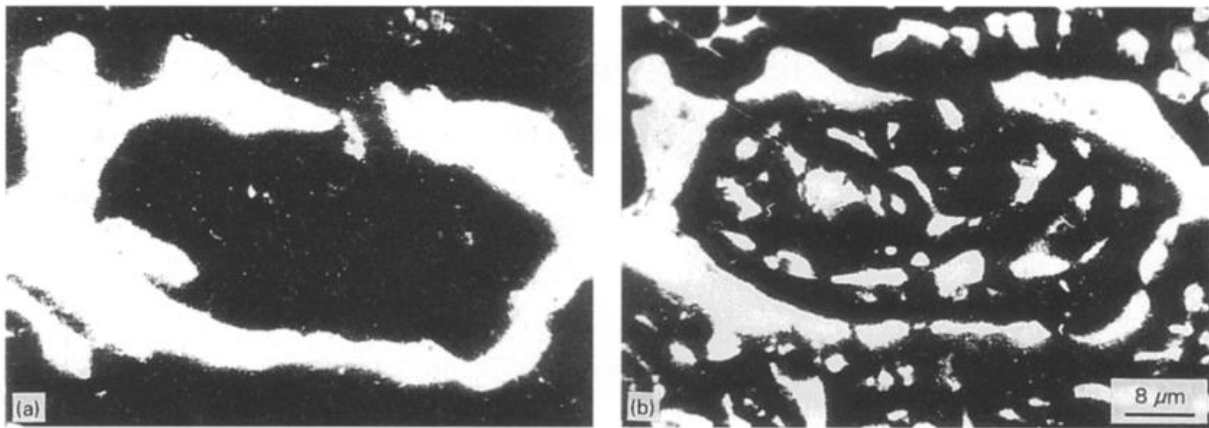
Figure 1.23 Eutectic carbides in a 2.5C-1.7Cr white cast iron (a) in the as-cast condition and (b) after holding for 2 hours at 980°C (reproduced from Liu *et al.* (*50*) with permission).
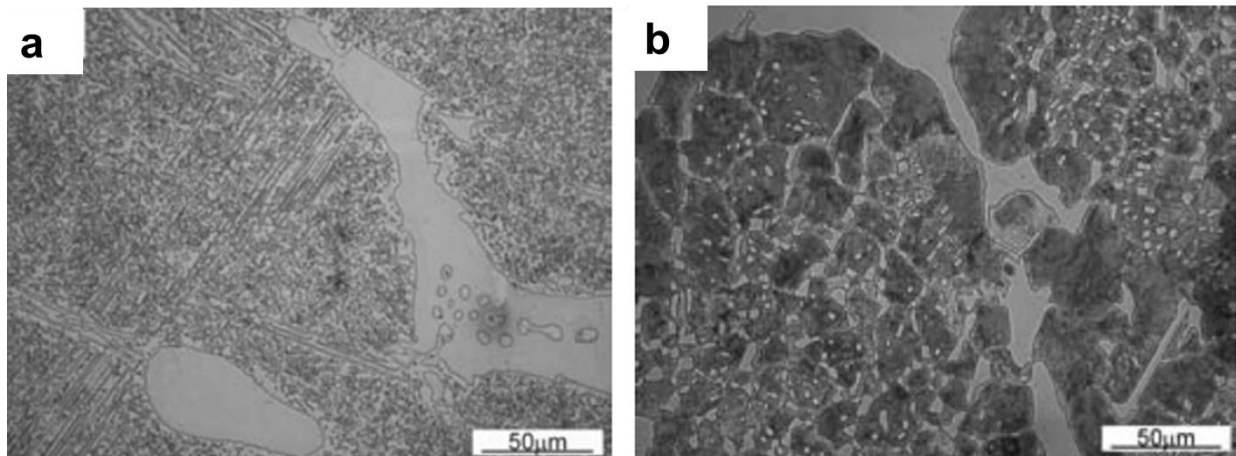
Figure 1.24 SEM micrographs showing 1.9C-1.1Cr steel in (a) as-cast condition and (b) after 10 hours at 1050°C (from Pacyna *et al.* (*51*)).

1.4 Materials Overview

The materials used for this dissertation were cut from different UHCS mill roll sections that were received from Miller Centrifugal Casting (MCC). In total, four different mill roll sections were received from MCC, and several UHCS sample were produced by re-melting at Carnegie Mellon University (CMU). The compositions of the UHCS, and the chapters in which they are analyzed, are shown in **Table 1.1**. This class of UHCS is known as "Adamite" (*32*).

Table 1.1 Compositions of UHCS used in this thesis measured by combustion-IR absorbance (C and SI) or by ICP-AES (inductively coupled plasma optical emission spectrometry).

Description	Chapters	Fe	Nb	Cr	C	Mn	Mo	Si	Ni
2C-4Cr As-Cast	2-6	Bal.	--	3.86	2.02	0.72	0.33	0.65	1.45
2C-4Cr HT	2,3, 7	Bal.	0.02	4.01	2.07	0.68	0.34	0.67	1.52
2C-1Cr As-Cast	6	Bal.	--	0.92	1.89	0.67	0.31	0.77	1.30
Nb-free Button	7	Bal.	0.02	4.13	1.93	0.83	0.37	0.73	1.54
Nb-Mod Button	7	Bal.	1.74	3.95	1.95	0.68	0.33	0.57	1.59
Nb-free Tube	7	Bal.	0.02	3.99	1.76	0.75	0.36	0.77	1.52
Nb-Mod Tube	7	Bal.	2.02	3.67	1.62	0.75	0.33	0.75	1.55
MCC AS-100 Specifications	--	Bal.	--	3.7-4.2	1.7-2.3	0.55-0.90	0.15-0.45	0.55-0.90	1.00-1.50

2C-4Cr as-cast roll

The roll was centrifugally cast by MCC and sent to us without heat treatment. In chapter 2, it is found that the as-cast microstructure consisted of a cementite network surrounded by a pearlite matrix, as well as some Widmanstätten cementite. A major objective of this dissertation (objective #2, page 28) is to develop a method to meaningfully quantify the connectivity of the cementite network. No such metric was found in the literature; typically volume fraction was the only quantitative parameter to describe the network. A connectivity index describing the network of the 2C-4Cr roll is developed chapter 3.

`

2C-4Cr industrially heat-treated (HT) roll

The roll was centrifugally cast by MCC and sent to us after their industrial heat treatment. In their technical data sheet for the AS-100 Adamite grade, MCC states that the purpose of the heat treatment was to provide optimal hardness and toughness, and that toughness was enhanced by transforming the initially lamellar pearlitic matrix to a spheroidized form. A major objective of this dissertation (objective #1, page 28) is to evaluate the microstructural mechanisms by which these properties were enhanced. Chapter 2 compares the as-cast and heat-treated UHCS microstructures to address this objective.

As shown in Chapter 2, the heat-treated microstructure contained a cementite network surrounded by a matrix containing a mixture pearlite, bainite, Widmanstätten cementite, and idiomorphic proeutectoid cementite particles. Another major objective of this dissertation objective #3, page 28) is to identify the mechanism by which the idiomorphic particles formed. Since no idiomorphs were found in the as-cast UHCS, a reasonable assumption was that the idiomorphs required pre-existing cementite in the form of spheroidized matrix pearlite laths in order to form during the heat treatment. The formation mechanism and growth kinetics of idiomorphic cementite particles is investigated in chapters 4, 5, and 6.

2C-1Cr as-cast roll

The roll was centrifugally cast by MCC and sent to us without heat treatment. As-cast microstructure was similar to the 2C-4Cr roll. Another major objective of this dissertation (objective #4, page 28) is to investigate the effects of Cr on the UHCS. The next section describes potential effects of Cr in UHCS, some of which are investigated experimentally in chapter 5.

Nb-modified and Nb-free UHCS button and tube samples (modified and recast at CMU)

The heat-treated 2C-4Cr UHCS was used as base material, and re-melted in a button melter and a tube furnace with and without an addition of Nb powder to produce four different samples. Another major objective of this dissertation (objective #5, page 28) is to investigate the effects of Nb on the UHCS. Potential effects of Nb are described in section 1.6, and the effects of the Nb modification on the network spacing and volume fraction are investigated experimentally in chapter 7.

Nb-V-Mo modified UHCS (produced by MCC)

The roll was centrifugally cast by MCC and sent to us without heat treatment. The microstructure consisted of a cementite network surrounded by a pearlite matrix. The matrix also contained NbC structures. Morphology of the network and structures is described in **Appendix C, section 2.C.**

1.5 Role of Chromium in UHCS

Chromium (Cr) is a substitutional alloying element in steels which has a significant effect on the solidification behavior and phase stability of UHCS. Cr alloying lowers the activity of carbon and decreases the maximum carbide solubility in austenite. Cr has an affinity for carbon, and decreases carbon diffusivity in austenite as shown in **Figure 1.25**. In addition, Cr alloying stabilizes a chrome-rich M_7C_3 carbide phase over a broad range of carbon contents and temperatures. The Cr content in austenite and cementite increases with the overall Cr content of the steel as shown in **Figure 1.26**. Since chromium can substitute for iron in cementite only up 17-18 wt% (*52*), Cr contents in **Figure 1.26** cementite above this amount implicitly indicate that M_7C_3 has formed. Complete dissolution of Cr-containing cementite requires redistribution of Cr

`

in the matrix (*53*). Thus, the potential effects of Cr on heat treatments of UHCS are of interest because of the influence of Cr on cementite dissolution kinetics.
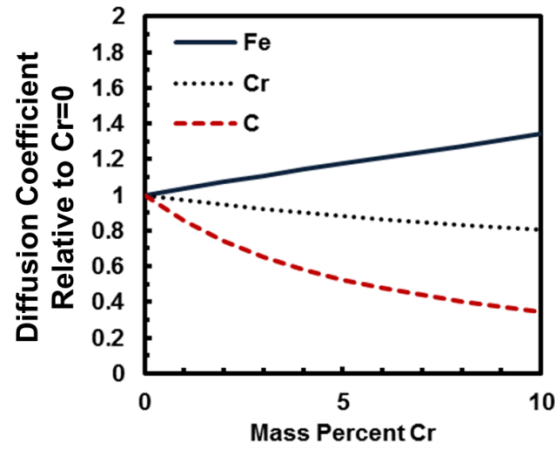
Figure 1.25 Diffusivities of Fe, C, and Cr in austenite in 2 wt% C steel as a function of Cr content in the steel, relative to the diffusivities at zero Cr. Calculated in Thermo-Calc (*54*).
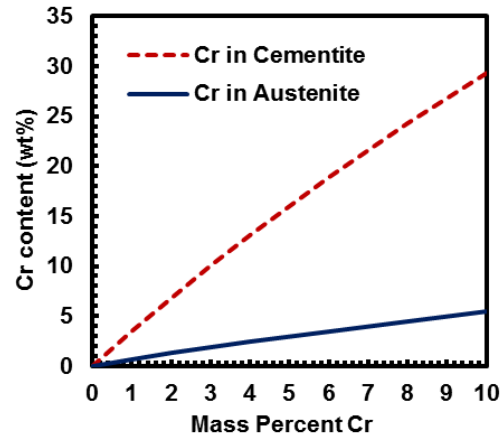
Figure 1.26 Cr content in austenite and cementite in 2 wt% C steel at 1000˚C as a function of Cr content in the steel. Calculated in Thermo-Calc (*54*).

1.6 Role of Nb in UHCS

The effects of alloying with different amounts of Nb (0.025 – 7 wt%) have been studied in hypoeutectoid steels (*55–58*), UHCS (*48, 59–61*), and cast irons (*62–70*), with a wide variety of Cr contents (0-30 wt%). In all cases, researchers found that increased additions of Nb resulted in microstructural refinement, i.e. smaller grains or carbide particles, and were generally correlated with improvements in mechanical properties such as hardness, wear resistance, tensile ductility, and/or toughness. The degree of carbide network refinement varied from a few percent

26

`

up to a factor of two, depending on the cooling rate and the amount of Nb added (*48*, *60*). Nb additions were also reported to lower the volume fraction of eutectic carbides (*48*, *60*, *63*). Even very small Nb additions in the range of 0.025-0.120 wt% (*61*) or 0.1-0.6 wt% were found to improve mechanical properties in steels with several different base compositions (*69*).

The pseudo-binary phase diagram for the 2C-4Cr UHCS composition modified by variable amounts of Nb is shown in **Figure 1.27**. The equilibirum solidification temperature of NbC is dependent on the Nb content of the UHCS; NbC solidifies before austenite above about 0.8 wt% Nb. Additions of Nb above ~1 wt%.also induce M_7C_3 formation.
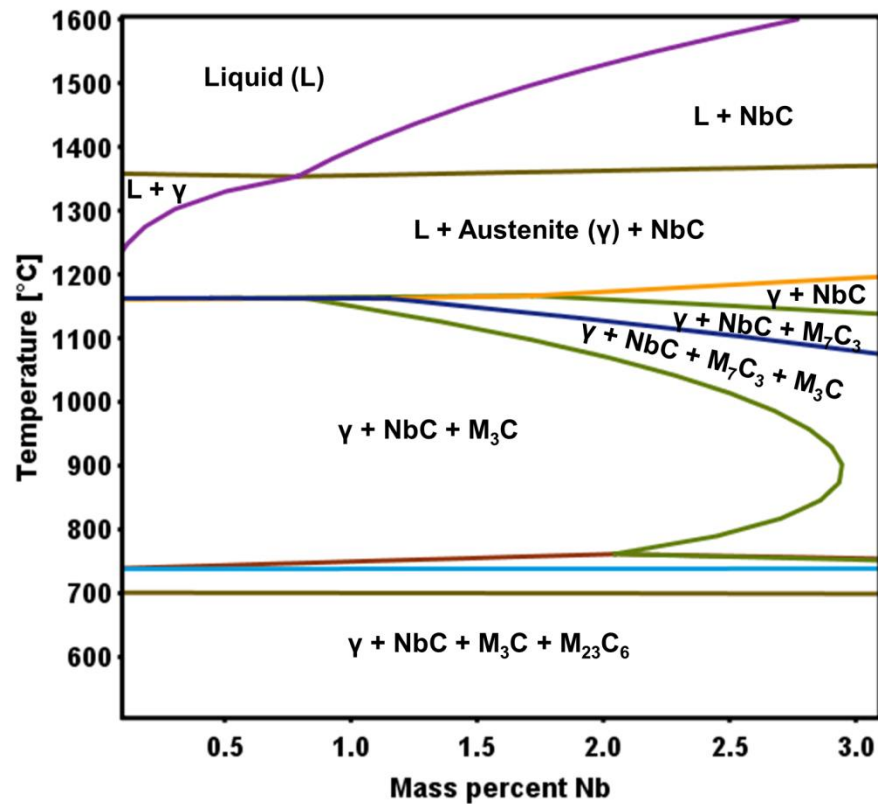
Figure 1.27 Pseudo-binary phased diagram for the 2C-4Cr composition modified by Nb. Calculated in Thermo-Calc (*54*).

`

1.7 Hypotheses and Objectives

Objectives

This work investigates the effects of heat treatments and chemical modification on the microstructure and mechanical properties of UHCS. There are five major objectives:

1.   Determine the mechanism for mechanical property enhancement by an established industrial heat treatment of an UHCS.

2.   Establish a quantitative connectivity metric for UHCS cementite network characterization and analysis.

3.   Comprehensively describe the effects of austenitizing heat treatments on UHCS microstructure.

a. Identify the mechanism for inter/intragranular carbide formation during austenitizing heat treatments of UHCS.

b. Determine what effects, if any, heat treatments of varying length and temperature have on the network carbides.

4.   Investigate the effects of Cr concentration on heat treatments and/or solidification in UHCS.

5.   Investigate the effects of Nb concentration on heat treatments and/or solidification in UHCS.

Hypotheses

Each major objective is addressed in one or more of the chapters in this thesis. In light of current understanding of UHCS, I have established major hypotheses for each of the objectives outlined above:

`

Regarding the industrial heat treatment of UHCS matrix/network effects on mechanical properties:

1.   Hardness in UHCS is largely independent of the carbide network, and instead relies on the matrix microstructure surrounding the network. For instance, a pearlitic matrix in a UHCS thatcontains a cementite network should still follow a Hall-Petch type trend relating lamellar spacing and hardness regardless of the state of the network.

2.   Toughness in UHCS is directly related to the connectivity, as opposed to the volume fraction, in the carbide network because the network provides initiation sites and pathway for crack propagation. Toughness should be at a minimum when cracks can propagate entirely along the network without involving the more ductile matrix phases. Quantification of network connectivity is possible using image analysis, and should be predictive of measured toughness in the steel after factoring in the length scale of the branches in the network.

Regarding the effects of the austenitizing heat treatment on the UHCS microstructure:

3.   Idiomorphic cementite forms in the UHCS matrix during austenitizing heat treatments due to spheroidization and coarsening of pearlite. Since coarsening is a curvature driven process, the cementite network has a perturbing effect on coarsening near the network.

Regarding the effects of Cr and Nb on cementite network and idiomorphic particle coarsening:

4.   Higher Cr contents slow down cementite dissolution and coarsening due to the requirement for Cr to diffuse through the austenite for complete cementite dissolution. Therefore, kinetics relating to cementite growth or coarsening should be faster in lower Cr UHCS.

5.   Niobium alloying produces NbC in the liquid prior to or during austenite formation (depending on the Nb content in the steel) which should have a refining effect on the cementite network by providing additional sites for austenite dendrites to nucleate. Nb pulls carbon out of

`

solution to form the NbC, which decreases the overall amount of cementite leading to a reduction in the network volume faction and connectivity. The reduction in C content of the liquid due to NbC formation can cause M_7C_3 formation by increasing the Cr/C ratio.

Chapter 2. Effects of an Industrial Heat Treatment on Microstructure and Mechanical Properties in 2C-4Cr UHCS

2.1 Abstract

This chapter examines the effects of an established industrial heat treatment on a 2C-4Cr UHCS in comparison to an as-cast UHCS of similar composition. The microstructure was characterized by using scanning electron microscopy (SEM), electron dispersive spectroscopy (EDS), focused ion beam (FIB), and X-ray diffraction (XRD). The as-cast UHCS microstructure consisted of a cementite network surrounded by a matrix of pearlite with some heterogeneously-distributed Widmanstätten cementite laths. The heat-treated UHCS microstructure consisted of a cementite network surrounded by a mixture of pearlite, bainite, retained austenite, and spheroidized cementite particles, as well as some coarsened Widmanstätten laths. The heat-treated UHCS had higher hardness, which appeared to be primarily due to refinement of pearlite interlamellar spacing consistent with a Hall-Petch type relationship (*15*, *16*). Toughness in the heat-treated UHCS was about 10% higher than in the as-cast UHCS. SEM examination of the microstructure near Vickers indentations indicated less extensive localized cracking in the heat-treated UHCS

`

roll, and fractography on the two UHCS indicated a more textured fracture surface in the heat-treated UHCS.

2.2 Introduction

Of the UHCS mill roll sections provided by Miller centrifugal casting (MCC) for this work, two were of a nominally 2C-4Cr composition (meeting MCC's specifications for the AS-100 Adamite grade). One of the sections was provided in the as-cast condition, and the other was provided in the heat-treated condition. The heat treatment involved a slow ramp-up to around 1000°C, a hold of several hours at that temperature, and then a slow cool to room temperature. In their technical data sheet for the AS-100 Adamite grade, MCC stated that the purpose of the heat treatment was to provide optimal hardness and toughness, and that toughness was enhanced by transforming the initially lamellar pearlitic matrix to a spheroidized form.

In the case of the hypereutectoid 2C-4Cr UHCS, cementite remains stable until the melting temperature as indicated in the equilibrium phase diagram for the 2C-4Cr composition in **Figure 2.1**. Thus, spheroidization of pearlite above the eutectoid temperature (intercritical spheroidization) is reasonable for this composition. A few studies have examined heat treatments in UHCS around 2 wt% C (*20–23*) , but none specifically examined pearlite spheroidization. The purpose of this chapter is to investigate the effects of the industrial heat treatment by evaluating and comparing the microstructures and mechanical properties of the heat-treated and as-cast UHCS.
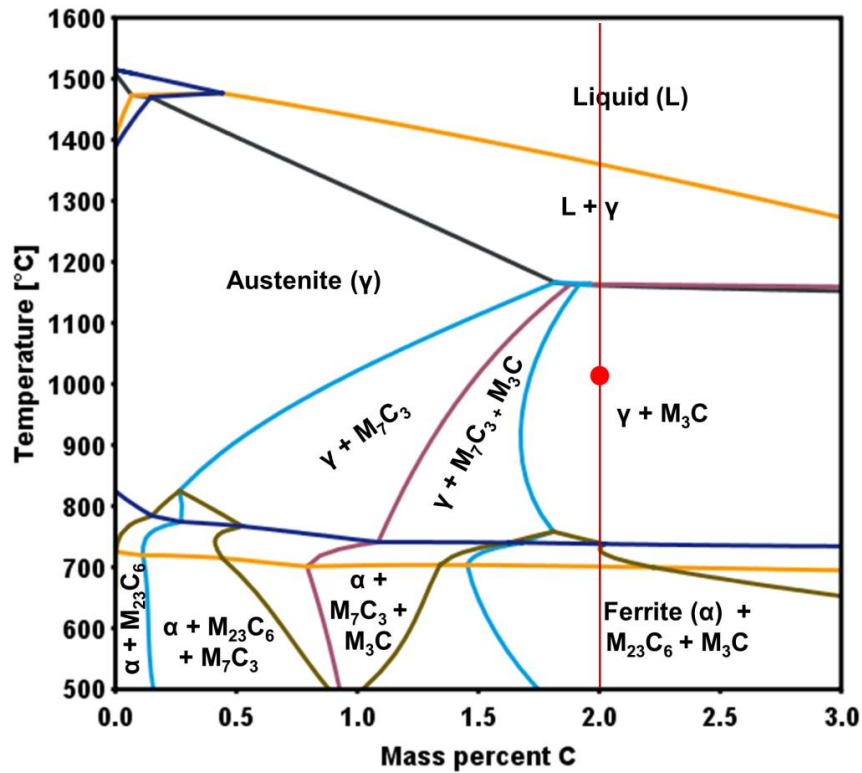
Figure 2.1 Pseudo-binary phase diagram for the 2C-4Cr UHCS composition, with carbon content and heat treatment temperature of interest indicated by a line and circular marker. (Calculated in Thermo-Calc (*71*)).

2.3 Materials and Methods

UHCS specimens consisted of half-inch cubic samples cut from as-cast and industrially heat-treated UHCS commercial roll mill castings provided by MCC. The heat treatment involved an austenetizing hold around 1000°C for about 10 hours followed by a still air cool to around 450°C. The composition of the UHCS is shown in **Table 2.1.**

Table 2.1 Compositions of UHCS used in this chapter measured by combustion-IR absorbance (C and SI) or by ICP-AES (other elements).

UHCS Description	Fe	Nb	Cr	C	Mn	Mo	Si	Ni	W
As-Cast	Bal.	--	3.86	2.02	0.72	0.33	0.65	1.45	--
Heat-Treated	Bal.	0.02	4.01	2.07	0.68	0.34	0.67	1.52	0.52

`

Samples for this study were cut using a water-cooled abrasive alumina wheel from locations at about 1, 10, and 20 cm away from the outer diameter of each roll. Samples were ground with successively finer grit SiC paper to 1200 grit, after which their hardness was evaluated using a Wilson manual Rockwell hardness tester. Hardness values were reported as an average of at least 5 measurements. Vickers indentations were also made in the samples to introduce local areas of high stress to study surface cracking behavior. Two instrumented Charpy impact tests were performed commercially by Westmoreland Mechanical Testing and Research (WMTR) for each of the as-cast and heat-treated UHCS conditions. Standard size Charpy V-notch (CVN) specimens were machined per ASTM E23 - 12c (*72*) and, due to low toughness of the samples, two instrumented Charpy tests were conducted per ASTM E2298 - 15 (*73*) for the as-cast and heat-treated steels to examine potential correlation between measured impact toughness and microstructure.

After the mechanical property evaluations, samples cut 1cm from the outer diameter of each roll were polished in 1μm alumina slurry and etched in a 4-5 % Nital (nitric acid + ethanol) solution for scanning electron microscope (SEM) characterization using a Phillips XL-30 SEM, operating at 20kV accelerating voltage. Fractography on the fractured CVN specimen surfaces was also done in the (SEM). Network and matrix compositions were measured in the SEM using an INCA X-act EDS detector. Phases were identified using X-ray diffraction (X'Pert Pro MPD XRD operated at 45 kV using Cu K_α radiation). Cross-sections from the surface of a heat-treated sample were also cut and examined using a NOVA 600 Focused ion beam (FIB) system operating at 20kV accelerating voltage to characterize idiomorphic cementite. EBSD measurements also indicated that the idiomorphic particles were made of cementite (see **Appendix A, section A.4**).

2.4 Results

2.4.1 Microstructure

Network

The largest microstructural features in these UHCS were their cementite networks, shown for the as-cast and heat-treated UHCS in **Figure 2.2**. Networks in the as-cast and heat-treated UHCS had similar appearances. Spacing of the network branches was about 100-200 μm, (the networks were just discernable to the naked eye given proper etching). Thickness of the network branches was on the order of 10-20 μm.
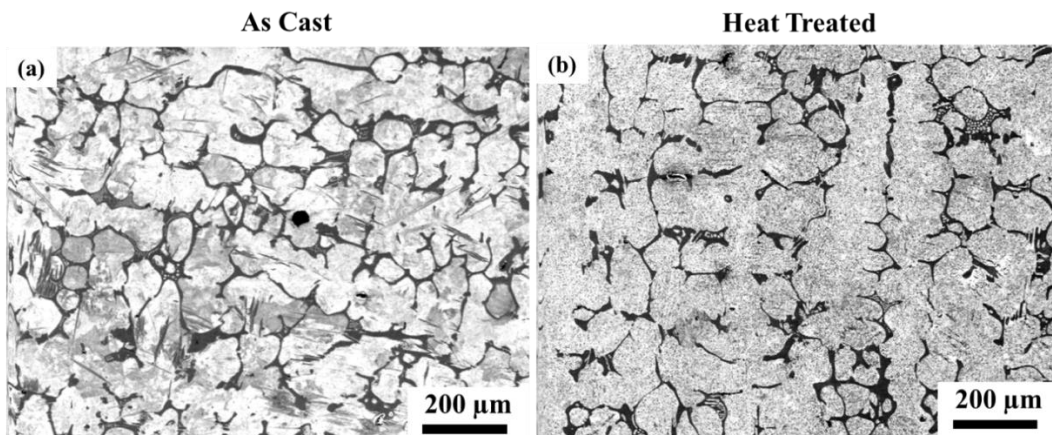
Figure 2.2 SEM micrographs of the cementite network in (a) the as-cast UHCS, and (b) the heat-treated UHCS.

Proeutectoid Cementite

At higher magnification, additional microstructural features were visible within the UHCS samples. Both the as-cast and heat-treated UHCS contained allotriomorphic cementite (network cementite) and heterogeneously distributed Widmanstätten laths as shown in **Figure 2.3 (a)** and **(b).** The matrix of the heat-treated UHCS also contained many homogenously distributed faceted carbides that were not present in the as-cast UHCS, as shown in **Figure 2.3 (d).** The faceted particles had morphologies consistent with the idiomorphic cementite in the Dubé/Aaronson

`

classification **Figure 1.5** (*10*). Idiomorphic particle were several μm in diameter, with aspect ratios varying from 1.0 to 3.4. Most Widmanstätten laths had a thickness of about 1 μm in both the as-cast and heat-treated UHCS; however, some laths in the heat-treated UHCS were considerably thicker, indicating that some had coarsening during the heat treatment.
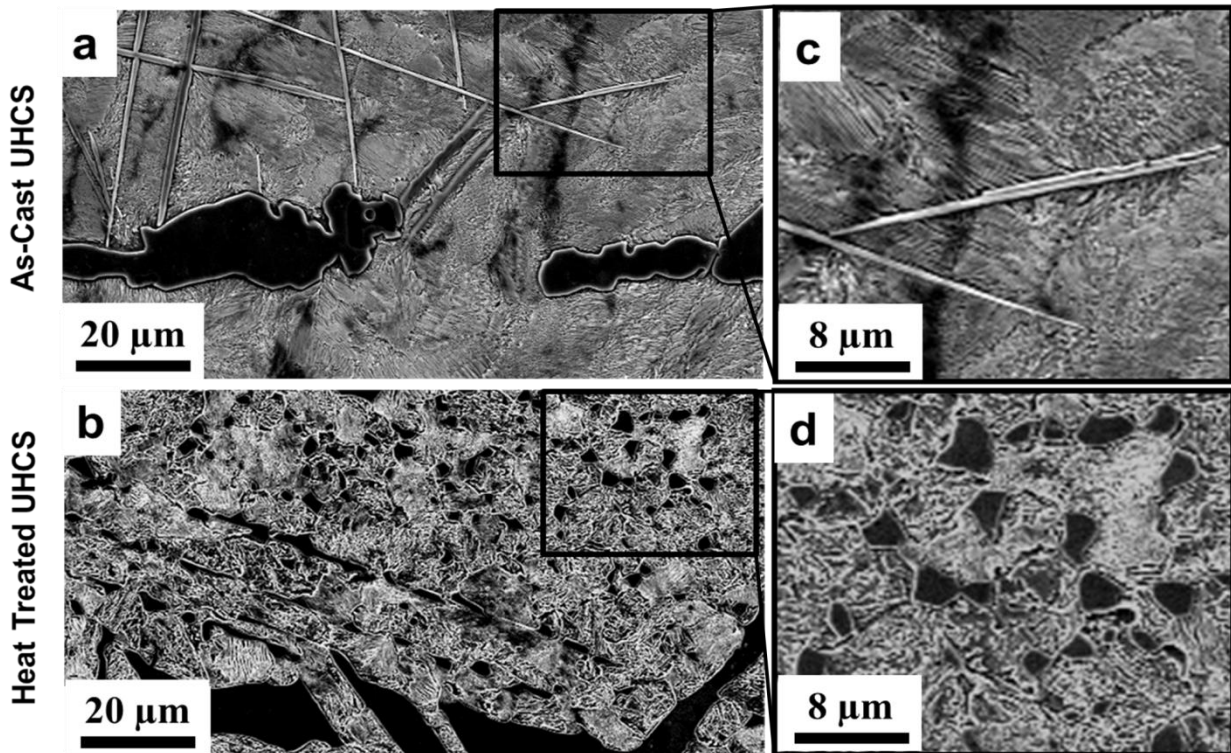
Figure 2.3 SEM micrographs of Nital etched UHCS samples comparing the microstructure (a) before heat treatment and (b) after heat treatment. Zoomed-in regions highlight (c) Widmanstätten laths and (d) faceted idiomorphic cementite particles.

Matrix Components

The finest microstructural features in the UHCS were the phases making up the matrix. The as-cast UHCS matrix was completely made up of lamellar pearlite as shown in **Figure 2.4 (a)**, whereas the heat-treated matrix was partly pearlite (about 50%) and partly made up of a jagged, more irregular phase morphology as shown in **Figure 2.4 (b)**. The morphology of the jagged matrix phase in the heat-treated UHCS most closely resembled bainite. This should be upper bainite given that it was apparently formed around the same temperatures as pearlite. The

35

pearlite lamellar structure in the heat-treated UHCS was also somewhat distorted, composed of shorter and more crooked laths than were observed in the as-cast microstructure.
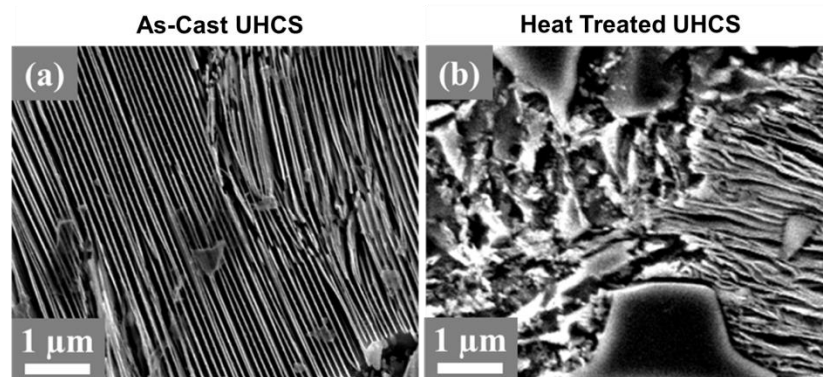
Figure 2.4 SEM micrographs of UHCS matrix microstructure show changes from (a) entirely pearlitic before heat treatment to (b) partially bainitic after the heat treatment.

2.4.2 Phase Characterization

XRD

In order to identify phases present in the UHCS samples, XRD θ-2θ scans were performed on the as-cast and heat-treated UHCS. In the θ-2θ scans, shown in **Figure 2.5**, the only phases distinguishable above the noise were austenite, cementite, and ferrite. The relative heights of the cementite and ferrite peaks were similar in both the as-cast UHCS θ-2θ scans, but only the heat-treated UHCS contained significant austenite peaks. The difference in the austenite peaks was an indication that there was more retained austenite in the heat-treated UHCS, likely due to a faster cooling rate from above the eutectoid temperature.
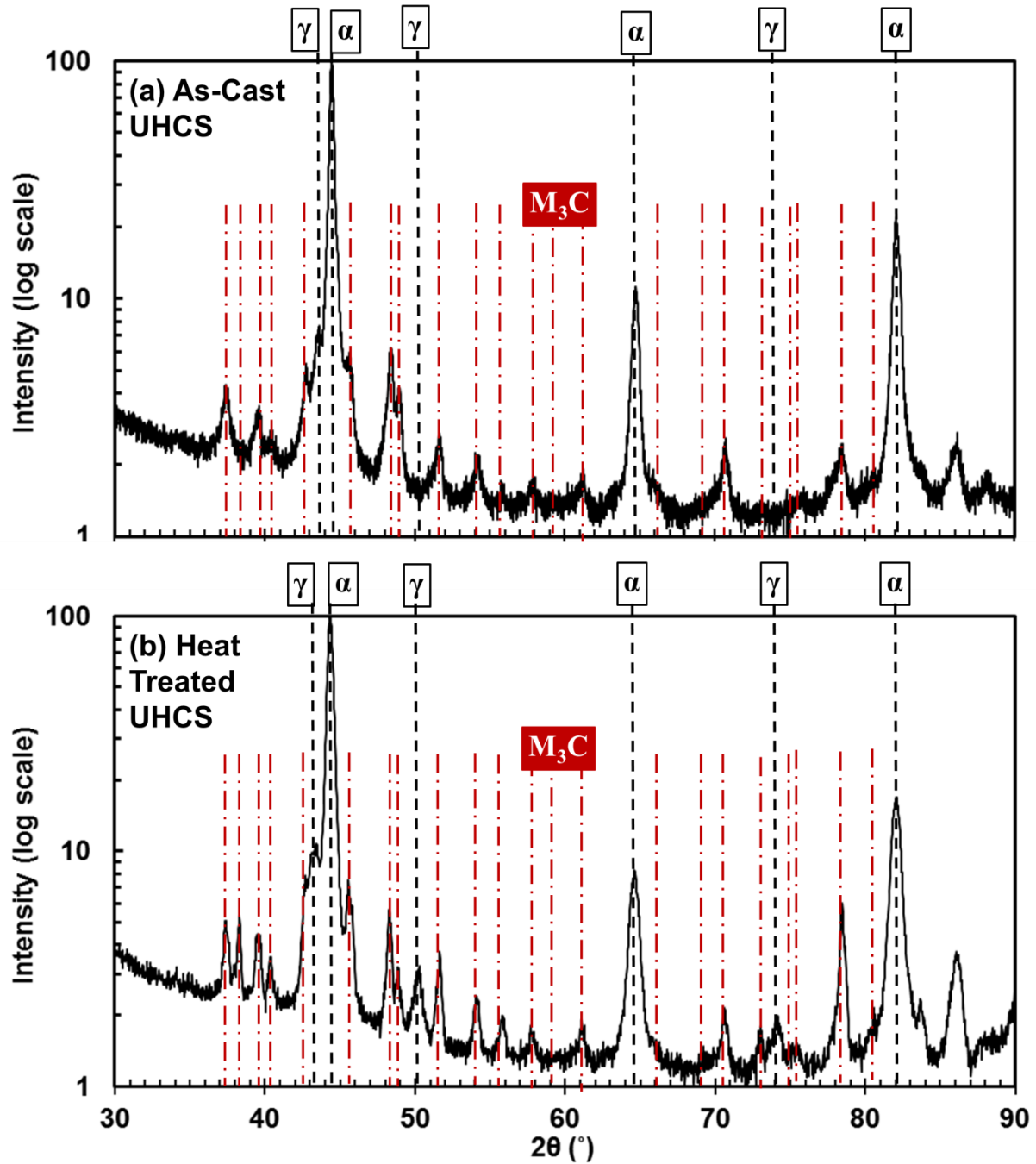
Figure 2.5 XRD θ-2θ scans indicate ferrite (α), cementite (M₃C), and retained austenite (γ) in the (a) as-cast, and (b) the heat-treated UHCS. Austenite peaks are more prominent in the heat-treated UHCS.

EDS

Compositional variations of the different regions (network proeutectoid cementite, and matrix) within the as-cast and heat-treated UHCS specimens were investigated by point and area EDS

`

analysis on polished but un-etched samples. Examples of the types of areas and points that were sampled for EDS are shown for the case of the heat-treated UHCS in **Figure 2.6**. EDS measurements of the compositions of the various phases within the base UHCS are summarized in **Table 2.2**. Overall compositions (measured over a large area) were similar in the as-cast and heat-treated samples. In both UHCS the matrix was richer in Fe, Si, and Ni relative to the cementite network/particles. The composition of the as-cast matrix was about the same as the composition of the areas of the heat-treated matrix, which included particles. Point analysis of particle-free areas of the heat-treated UHCS matrix indicated lower Cr and C. It should be noted that C measurements in EDS are very unreliable, thus the C contents in **Table 2.2** are meaningful only relative to each other.
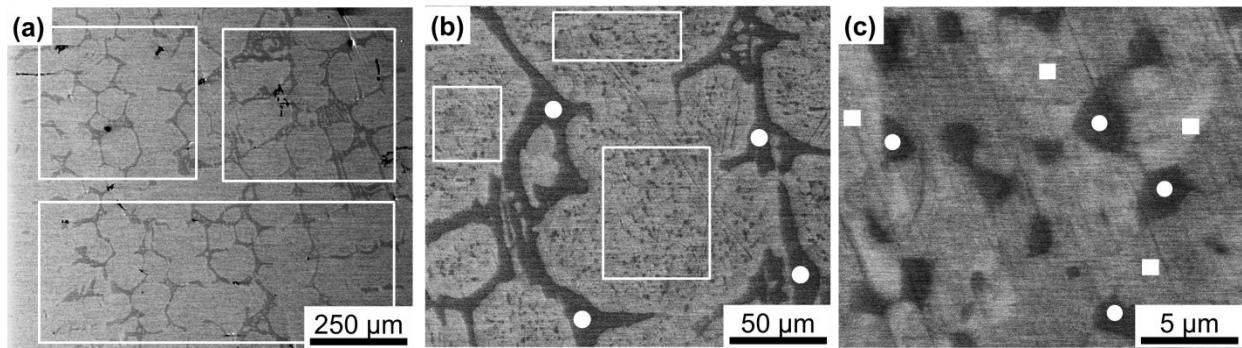
Figure 2.6 Examples of EDS point and area scans for analysis of the heat-treated UHCS. Open rectangular outlines and solid markers indicate EDS area and point scans of (a) the overall heat-treated UHCS microstructure, (b) the network and matrix with particles, and (c) the particles and matrix.

Table 2.2 Phase composition in as-cast and heat-treated (HT) UHCS measured by EDS

Overall Composition	Meas.	Fe	C	Cr	Mn	Mo	Si	Ni
As-cast UHCS	3	89	4	4.3	0.8	0.4	0.7	1.5
Heat-treated UHCS	3	87	4	4.6	0.9	0.8	0.8	1.4
Matrix Composition	**Meas.**	**Fe**	**C**	**Cr**	**Mn**	**Mo**	**Si**	**Ni**
As-cast UHCS	7	90	3	3.3	0.7	0.1	0.8	1.7
HT UHCS (no particles)	4	92	2	2.4	0.7	0.3	1	1.7
HT UHCS (with particles)	3	90	4	3.4	0.7	0.3	0.8	1.6
Network Composition	**Meas.**	**Fe**	**C**	**Cr**	**Mn**	**Mo**	**Si**	**Ni**

Cementite Particles	Meas.	Fe	C	Cr	Mn	Mo	Si	Ni
As-cast UHCS	5	77	7	12.7	1.1	1.5	0.1	0.4
Heat-treated UHCS	4	75	8	14.3	1.1	0.8	0.1	0.3
Heat-treated UHCS	4	78	8	12.2	1.1	0.9	0.1	0.3

2.4.3 Mechanical Properties

Hardness

The diameters of the Rockwell indentations used to measure hardness were about 500 μm at the sample surface as shown in **Figure 2.7(a)**. Given that the network spacing was around 100-200 μm, the sizes of the indentations were sampling large enough volumes that the local microstructure should not influence the hardness measurements. The tip of the Rockwell indenter was rounded enough to avoid hitting only a single phase as shown in **Figure 2.7(b)**.
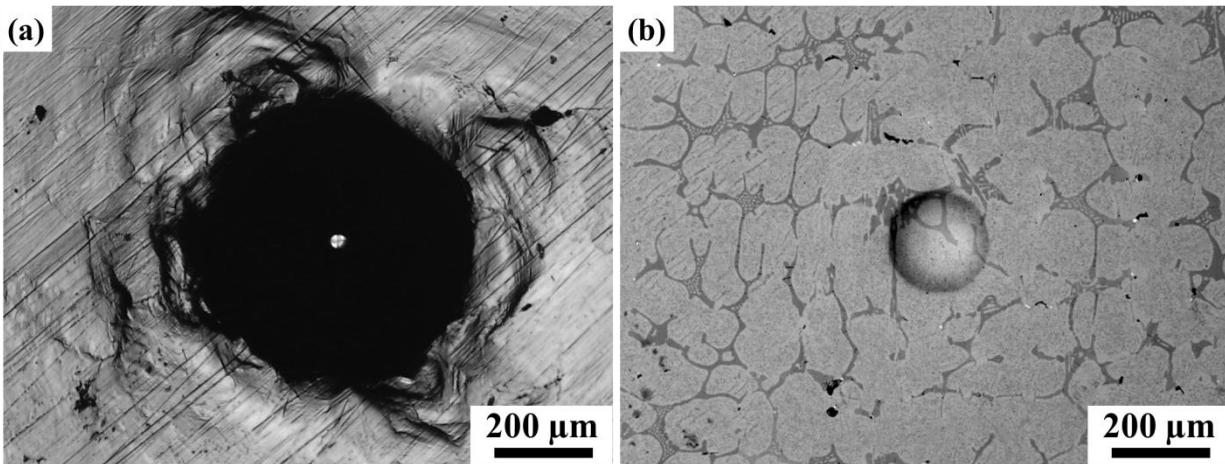
Figure 2.7 Micrographs showing (a) the unpolished surface of a Rockwell indentation imaged in an optical microscope and (b) the tip of a Rockwell indentation after a few hundred μm were ground away from the surface, imaged in backscattered electron detection mode in the SEM.

Table 2.3 shows specimen hardness and lamellar spacing data for samples cut from different positions along the roll diameters, and **Figure 2.8** plots the hardness as a function of the square root of interlamellar spacing. Hardness followed the same Hall-Petch trend as a function of interlamellar spacing regardless in both the as-cast and heat-treated UHCS regardless of the

`

fraction of non-pearlitic phases. Hardness was greatest near the roll outer diameter (OD) where cooling would have been the fastest, and decreased with distance from the outer diameter.

Table 2.3 Hardness and pearlite spacing at three distances from the roll outer diameter (OD)

Distance from OD (cm)	Hardness (HRC)		Pearlite Spacing (nm)	
	As-Cast	HT	As-Cast	HT
1	44.2 ±0.6	51.9 ±0.3	125 ± 20	70 ± 6
10	44.0 ±0.8	48.3 ±1.0	157 ± 7	91 ± 9
20	41.6 ±0.8	44.0 ±0.8	235 ±38	139 ±17
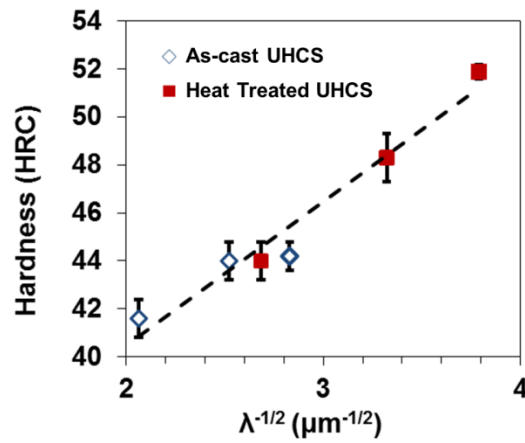
Figure 2.8 Rockwell hardness of the as-cast and heat-treated UHCS plotted as a function of the square root of the pearlite lamellar spacing (λ) exhibited a linear trend consistent with Hall-Petch relationship.

Toughness and Fractography

Two instrumented Charpy impact tests were conducted for each UHCS sample. The two as-cast UHCS CVN samples absorbed 1.82 and 1.83 J, and the two heat-treated UHCS CVN samples absorbed 1.98 and 2.06 J. Thus, toughness in the heat-treated UHCS was about 10% higher in the heat-treated UHCS. Fracture surfaces of the as-cast and heat-treated UHCS are shown at different magnifications in **Figure 2.9**.

`

As-cast UHCS   **Heat Treated UHCS**
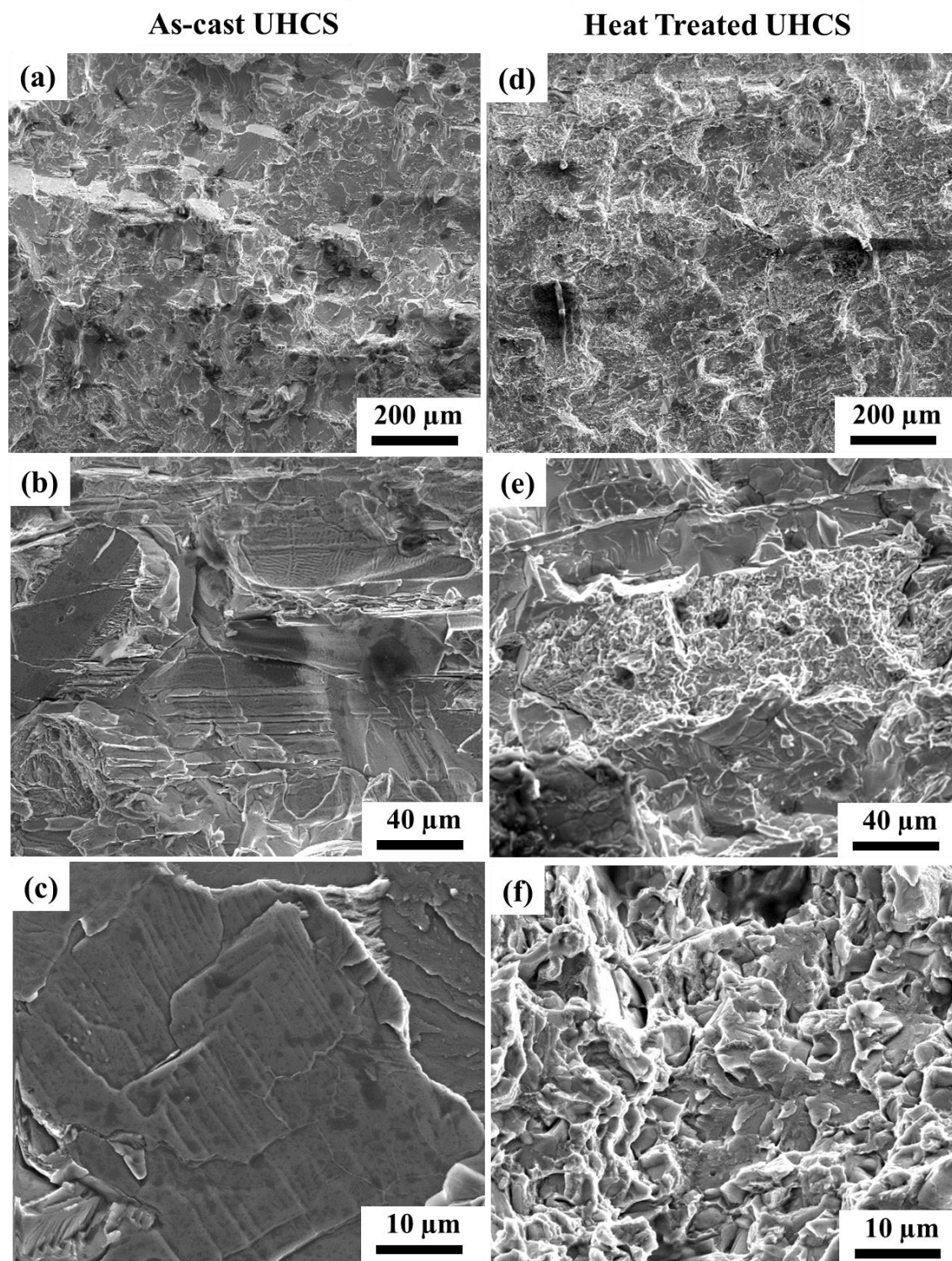
Figure 2.9 SEM micrographs of fracture surfaces of (a-c) the as-cast UHCS and (b) the heat-treated UHCS.

At low magnification, shown in **Figure 2.9 (a)** and **(d)**, faceting of the fracture surfaces was visible on the same length scales as the spacing between branches of the cementite network (100-200μm). The scale of the faceting may indicate that the network was involved in fracture. At the intermediate magnification shown in **Figure 2.9 (b)** it was apparent that the facets of as-cast UHCS fracture surface were smooth, indicating a brittle cleavage fracture. The heat-treated fracture surface shown in **Figure 2.9 (b)** contained some smooth regions and some rougher regions. The rougher regions correspond to areas where more ductile fracture occurred, perhaps due to microvoid coalescence at particle/matrix interfaces. **Figure 2.9 (c)** and **(f)** show the cleavage fracture and ductile fracture surfaces at higher magnification. The heat-treated UHCS fracture surface appeared to contain some voids of roughly the same sizes and shapes as the cementite particles noted earlier, indicating that these particles and perhaps the bainite matrix had some involvement in fracture.

To further investigate toughness in the UHCS samples, Vickers indents at 5 N load were applied at multiple locations for both as-cast and heat-treated UHCS. The sizes of the indentations shown in **Figure 2.10 (a)** were on the order of 100μm, similar to the network spacing. Contrast was enhanced in ImageJ to eliminate non-crack features from the micrographs, as seen in **Figure 2.10 (b)**. A binary summation of three such images (**Figure 2.10 (b)**) revealed that cracking was less extensive around the Vickers indentations in the heat-treated UHCS.
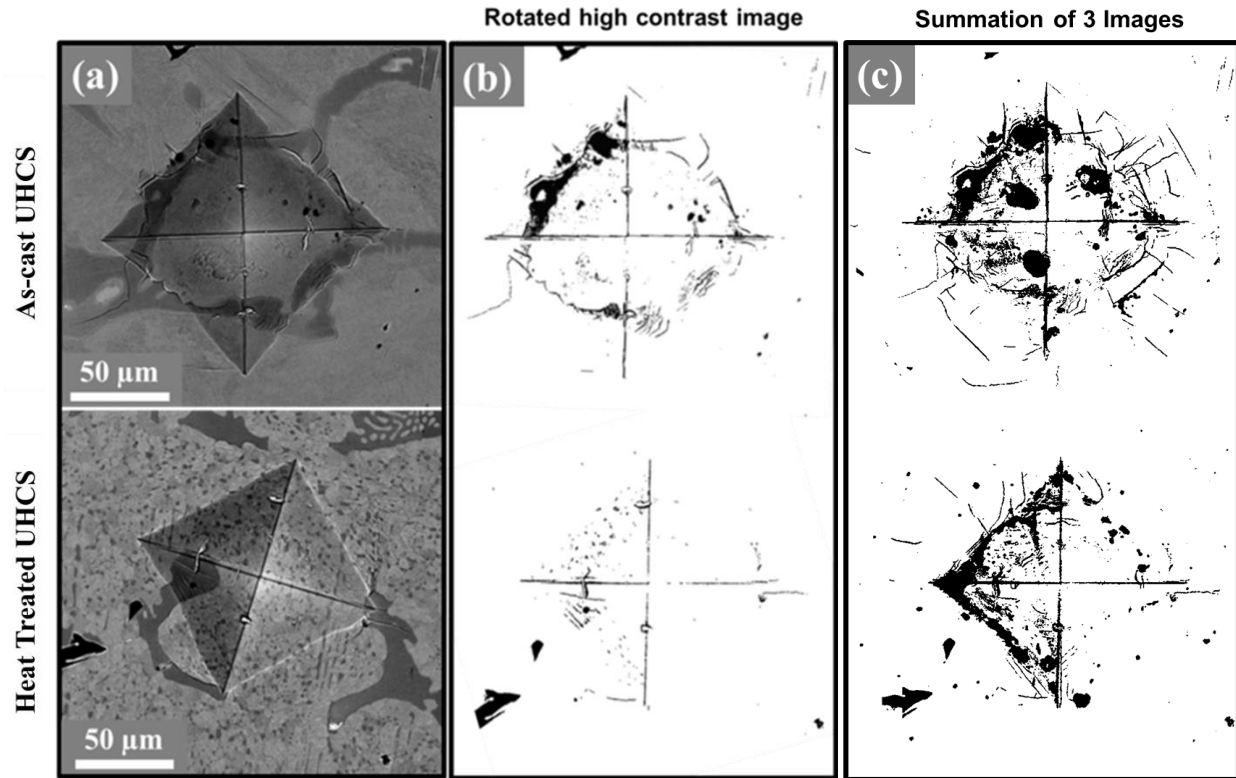
Figure 2.10 Backscattered electron micrographs of (a) Vickers indentations were (b) processed in ImageJ to enhance contrast and (c) summed with two other high contrast indentation images (binary summation operation in ImageJ) to show a cracking field.

2.5 Discussion

2.5.1 Microstructure

Network

The networks in the as-cast and heat-treated UHCS appeared qualitatively similar. Chapter 3 will propose a method for quantitatively distinguishing networks based on their connectivity.

Proeutectoid Cementite

Proeutectoid cementite in the as-cast matrix was only present in the form of Widmanstätten laths and allotriomorphic network cementite. In the heat-treated UHCS, proeutectoid cementite was present in a new form: faceted idiomorphic cementite particles. Spanos and Kral (*74*) had pointed out that it was easy to misinterpret 2D cross-sections of rods as

particles. However, in the heat-treated UHCS the distribution of idiomorphic particles appeared too homogenous compared to the distribution of the Widmanstätten laths to be a result of lath spheroidization. Therefore the apparent idiomorphic carbides were produced through spheroidization and coarsening of pearlite lamellae. Chapter 4 investigates the kinetics of this process.

To ensure that the faceted idiomorphic particles were not rods, or Widmanstätten needles, in 3 dimensions, focused ion beam (FIB) sectioning of several particles was employed to further investigate the true 3D morphology. **Figure 2.11 (a)** shows an example of the surface of an etched heat-treated sample before FIB sectioning, with a box surrounding a particle to be cross-sectioned. Lines and corresponding numbers denote the positions of cross-sections across the idiomorph, shown in **Figure 2.11 (1-4)**. These cross-sections showed no indication of rod-like morphology, confirming that the particles were truly idiomorphic.
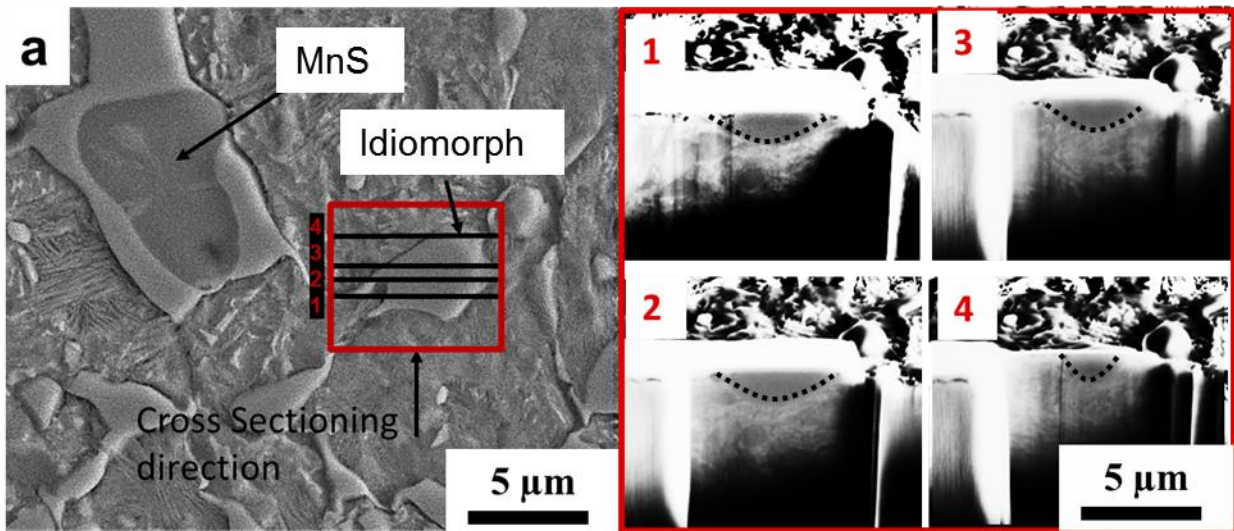
Figure 2.11 SEM micrograph of (a) an idiomorph in the heat-treated UHCS microstructure prior to cross-sectioning and (1-4) sequential cross-sections imaged during FIB milling. Particle boundaries indicated by dashed black lines.

Matrix

In conditions of equilibrium cooling, the products of the eutectoid transformation would have Cr contents equal to or less than that of the eutectoid austenite. **Figure 2.12** shows equilibrium austenite Cr composition as a function of temperature for the 2C-4Cr UHCS mill roll composition, with EDS measurements of matrix Cr contents in the UHCS samples indicated by cross markers. The as-cast matrix was purely composed of eutectoid pearlite, with a Cr content of about 3.3 wt% as measured by EDS (close to the Cr content of the equilibrium eutectic austenite). The heat-treated UHCS matrix contained some pearlite as well as a new bainite phase, which may also have contained some retained austenite. The Cr content of the heat-treated matrix pearlite/bainite/retained mixture was only about 2.4 wt%, less than that of the as-cast pearlite matrix. However, when the Cr-rich idiomorphic particles were included in area EDS measurements, the Cr content in the matrix was about equal to that of the as-cast UHCS. Thus, the EDS results indicate that both the heat-treated and UHCS rolls were far from equilibrium and their matrices were highly supersaturated in Cr. The supersaturation of the pearlite matrix in Cr (and presumable in C) prevented the complete dissolution of pearlite into austenite, which helped the idiomorphic particles to grow. Growth of idiomorphic particles, and the effects of Cr on growth kinetics, is discussed in Chapters 5 and 6.
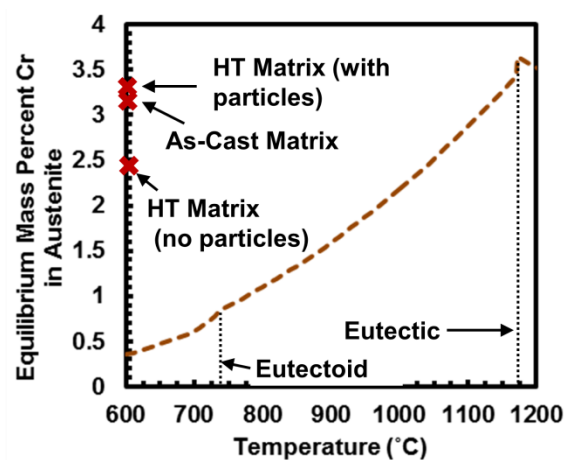
Figure 2.12 Equilibrium Cr concentration in austenite as a function of temperature, with EDS measurements from **Table 2.2** indicated by cross markers.

`

2.5.2 Mechanical Properties

Hardness

In pearlitic steels, the interlamellar spacing generally determines the strength of the steel by confining the mobility of disclocations (*75*). Pearlite lamellar spacing is known to have an inverse square relationship to yield strength in hypo-eutectic steels (*15*, *16*) and hypereutectic steels (*75*) consistent with the Hall-Petch relationship. Since yield and tensile strengths are generally related linearly to hardness (*76*), the Hall-Petch relationship is also applicable to hardness. While neither the as-cast nor the heat-treated UHCS contained fully pearlitic microstructures, variations in hardness along the diameters of both the heat-treated and as-cast UHCS rolls followed a Hall-Petch trend with pearlite lamellar spacing.

The simplest model for mechanical properties of mixed microstructures is the "rule of mixtures", which states that a property (P) of a composite material is the sum of the weighted contributions of its components:

$$P = \sum_{i=1}^{n} F_i P_i.$$

F_i is the volume fraction and P_i is the property of component *i*. For the UHCS system there were four components relating to hardness: cementite, pearlite, bainite, and austenite. Applying the rule of mixtures to the UHCS gives the following equations for hardness:

$$\text{UHCS hardness} = F_\theta \cdot H_\theta + F_P \cdot H_P + F_B \cdot H_B + F_\gamma H_\gamma.$$

F_θ, F_P, F_B, and $F\gamma$ are the volume fractions of cementite, pearlite, bainite and austenite, respectively, and H_θ, H_P, H_B, and $H\gamma$ are the hardness of cementite, pearlite, bainite and austenite, respectively. The volumes of cementite were significantly less than the matrix volume in both UHCS. The matrix in the heat-treated UHCS was roughly 50% bainite and austenite, with the remaining volume pearlite. The hardness of the cementite and austenite should have

`

been relatively constant regardless of the processing conditions. Thus, the variables which could influence hardness were the pearlite interlamellar spacing λ, the volume fractions of the various phases, and the bainite hardness H_B. If variations in the volume fractions of the phases were not very large across the roll diameter, and H_B were constant, hardness should be linear with $\sqrt{\lambda}$ with slope equal to $k \cdot F_P$. Hardness was indeed found to be linear with $\sqrt{\lambda}$ for both UHCS samples, but seemed to have the same slope regardless of F_P. Thus, it appears that the rule of mixtures was not obeyed for hardness and the pearlite controlled hardness regardless of the volume fraction of other phases. This may indicate that the hardness of the bainite was similar to that of the pearlite for each tested location, such that the volume fraction of bainite did not influence the overall hardness.

Toughness

The fracture surface of the heat-treated UHCS contained some areas indicative of ductile fracture, while the as-cast UHCS did not. However the Charpy impact toughness was only 10% higher in the heat-treated UHCS. This may be due to the effects of the brittle cementite network outweighing the small contribution of the more ductile matrix. Additionally, the ductile fracture surface appears to be a result of the interaction between cracks and the particle-matrix interface. Thus, it appears that the cracks generally followed the path of the network but may also have deviated locally into the matrix. Toughness is discussed in more detail in Chapter 3.

2.6 Conclusions

This chapter investigated the microstructures and mechanical properties of as-cast and industrially heat-treated 2C-4Cr UHCS.

1. Both as-cast and heat-treated UHCS contained a cementite network and Widmanstätten laths. The cementite networks appeared qualitatively similar, but methods to quantitatively describe

`

possible effects of the heat treatment on the network were lacking, and will be developed in the next chapter.

2. The main matrix component of both heat-treated and as-cast UHCS was pearlite. The heat-treated UHCS also contained micron-sized faceted idiomorphic proeutectoid cementite particles and pearlite in its matrix. FIB sectioning confirmed that the idiomorphic cementite 3D morphology was not rod-like.

2. Hardness in both UHCS was predominantly controlled by pearlite interlamellar spacing following a Hall-Petch trend. Pearlite spacing was finer in the heat-treated UHCS, contributing to its higher hardness.

3. Charpy impact toughness was slighly higher in the heat-treated UHCS. The fracture surface of the heat-treated UHCS had more texture, possibly due to crack interactions with cementite particles.

`

Chapter 3. Digital Image Analysis to Quantify Connectivity of Carbide Networks in Ultrahigh Carbon Steels

Note: This chapter was adapted for this thesis from a previously published article (77) with permission

3.1 Abstract

This chapter describes a method that was developed to quantify the degree of carbide network connectivity in ultrahigh carbon steels (UHCS) through digital image processing and analysis of experimental micrographs. The process involved segmenting the network and matrix into binary contrast representations via a grayscale intensity thresholding operation. Network pixels were skeletonized and grouped into braches and nodes, allowing the determination of a connectivity index for the carbide network. The method was applied to SEM micrographs from sections of two different 2C-4Cr mill rolls, one as-cast and the other heat-treated. The connectivity indices of scanning electron micrographs were consistent in both secondary and backscattered electron imaging modes, as well as across two different magnifications. Results from UHCS reported here along with other results from the literature indicated that lower connectivity indexes correlated with higher Charpy impact energy (toughness) below a critical connectivity index value. At connectivity higher than the critical value, toughness plateaued at a low value consistent with a percolation threshold for crack propagation across the network.

3.2 Introduction

A major goal in UHCS processing is modification of the network of brittle carbides distributed throughout the microstructure. Networks of proeutectoid cementite form in UHCS alloys during cooling, primarily due to precipitation in the $\gamma+Fe_3C$ phase field (depending on the steel composition and cooling rate, a small amount of eutectic solidification may also occur). The

carbide network provides crack initiation sites and pathways for crack propagation that reduce UHCS toughness/ductility (*29, 78*) by allowing cracks to circumvent the ductile matrix.

Figure 3.1 shows an example of a crack propagating preferentially within the carbide network. Breaking up the network has the potential to reduce pathways for crack propagation and force cracks to travel through the matrix, thereby increasing toughness.
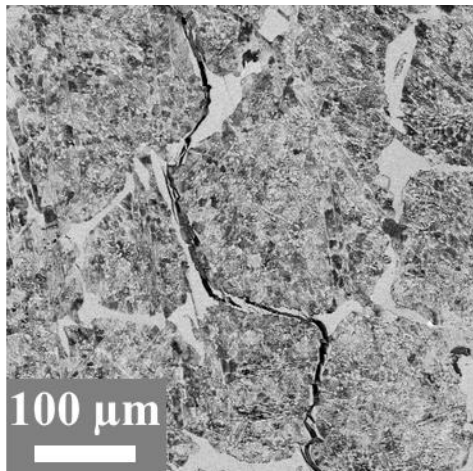
Figure 3.1 SEM micrograph of a crack propagating along the cementite network in an industrially heat-treated 2C-4Cr UHCS (BSE imaging mode).

It is possible to process UHCS so as to completely eliminate the network or significantly reduce its connectivity. In this case, toughness may depend on microstructural parameters such as the type of eutectoid transformation products and the prior austenite spacing (*79*). Successful approaches have included thermomechanical processing (*34, 37*) and chemistry modification by small additions of rare earths or niobium (*46–48*); both approaches have resulted in greatly improved mechanical properties measured at room temperature. These relatively new manufacturing methods have been not widely adopted, possibly because of additional processing difficulty and cost. Another possible processing alternative is using heat treatments alone (*21, 51, 80*). While there is interest in breaking up the network in UHCS, there currently exists no metric for quantifying the degree of network break-up beyond measuring the network volume fraction.

`

Establishing a standard method for quantifying connectivity of carbide networks would improve evaluation and comparison of proposed network modification processes.

The concept of network connectivity analysis is already well established in various fields. Percolation theory (*81–83*) provides a framework for describing networks in terms of connections between points/nodes on a grid. Transportation science (*84, 85*) defines a "connectivity index" as a ratio of streets to intersections and cul-de-sacs. Tortuosity in porous substances (*86*) is found by quantifying the ratio of distance traveled along a convoluted path to the direct point-to-point distance. Medical science describes a connectivity index in cancellous human bone (*87, 88*) in terms of the maximal number of connections needed to be broken to separate one network into two. For the case of UHCS steels, carbide networks provide a "pathway" for crack propagation from one point in the microstructure to another. Thus in this work, the transportation science metric for network quantification is leveraged to quantify carbide networks in UHCS.

The purpose of this chapter is to propose and demonstrate a potential method of analyzing micrographs of UHCS microstructures and quantifying the network connectivity. In the previous chapter, two 2C-4Cr UHCS were studied – one in the as-cast condition, and one in the heat-treated condition. In this chapter, micrographs containing cementite networks in those UHCS specimens were analyzed to produce quantified metrics for carbide network connectivity. In order to gather more data, connectivity in micrographs from the literature were also analyzed. Connectivity measurements were compared to experimental toughness measurements.

3.3 Materials and Experimental Methods

In the present study, UHCS specimens consisted of 0.5 in. x 0.5 in. x 0.5 in. samples cut from commercial roll mill castings. Specimens from two different 36 in. diameter roll mills were

`

studied, one in the as-cast condition and one after a heat treatment that involved an austenitizing hold above 1000˚C. The composition of the material is shown in **Table 3.1**.

Table 3.1 Compositions of UHCS used in this chapter measured by combustion-IR absorbance (C and SI) or by ICP-AES (other elements).

Description	Fe	Nb	Cr	C	Mn	Mo	Si	Ni	W
As-Cast	Bal.	--	3.86	2.02	0.72	0.33	0.65	1.45	--
Heat-treated	Bal.	0.02	4.01	2.07	0.68	0.34	0.67	1.52	0.52

Two instrumented Charpy impact tests were performed commercially by Westmoreland Mechanical Testing and Research for each of the as-cast and heat-treated UHCS conditions. Standard size Charpy V-notch (CVN) specimens were machined per ASTM E23 - 12c (*72*) and, due to low toughness of the samples, instrumented Charpy tests were conducted per ASTM E2298 - 15 (*73*) for the as-cast and heat-treated steels to examine potential correlation between measured impact toughness and microstructure.

The microstructure was characterized using a scanning electron microscope (Phillips XL-30 SEM, operating at 20kV accelerating voltage). For SEM analysis, specimens were cut using an abrasive alumina wheel, ground with SiC paper, polished in alumina slurry and etched for 30 seconds in 4% Nital (nitric acid/methanol) solution. The following sections describe the new approach for quantifying network connectivity in ImageJ (*89*), an image processing software program in the public domain (http://rsb.info.nih.gov/ij/index.html).

3.4. Digital Image Analysis Methods

Network analysis required deconstructing contrast features in micrographs into a collection of nodes and branches in space, illustrated in **Figure 3.2**. A node represents points in the network where branching originates or ends. *Nodes* were classified as endpoints when linked to exactly one other node, and as *internal junctions* when connected to two or more other nodes.

The average number of linkages per node, known as the *connectivity index* (*85*), expresses the average number of connections per network branch. Information such as the average link length and the probability of a given node being connected to other nodes in the network is also of interest and may be found through image analysis.
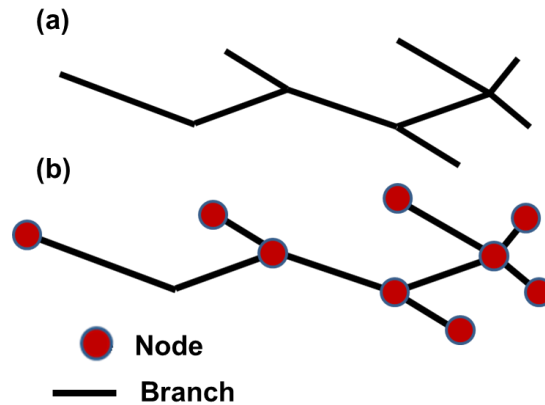
Figure 3.2 Schematic illustration of (a) a simple network and (b) the same network indicating branches and nodes in the network.

The critical image processing step allowing these parameters to be extracted is skeletonization, an operation that thins the network to a single-pixel width so that nodes and branches can be identified. The following sections describe the image processing steps developed to extract connectivity indices from digital micrographs of UHCS materials: thresholding for phase segmentation, particle size filtering for artifact removal, outlier removal for network void removal, and skeletonization for network quantification.

Thresholding for phase segmentation

The first step in extracting the connectivity index was to digitally select and isolate the carbide network from other phases present in a UHCS micrograph. For UHCS containing cementite and ferrite, the common etchant, Nital (5% nitric acid and 95% alcohol such as ethanol or methanol) was useful for ensuring clear image contrast between constituent phases in the steel microstructure under OM/SEM imaging. Nital preferentially etches ferrite, revealing

`

proeutectoid cementite as well as cementite lamellae in the pearlite. The resulting rougher eutectoid pearlite morphology produced a higher local secondary electron (SE) yield than the smoother morphology network proeutectoid cementite. Thus the proeutectoid cementite network exhibited lower grayscale intensity in the SE image.

Figure 3.3 (a) shows the typical appearance of a Nital-etched pearlitic UHCS microstructure as imaged by SEM. User-controlled gain settings ensured the proeutectoid cementite was dark and distinct from the lighter pearlitic matrix. There was some grayscale variation in the pearlite matrix due to spatial lath orientation variations. Ultimately, any suitable etchant process for the analyzed steel should yield such micrographs of distinct constituent phase contrast, whether by SEM using secondary electron (SE) or backscattered electron (BSE) detection or by OM as will be demonstrated later in this article. It should be noted that the etching process will reveal additional cementite beneath the original plane of polish. Given that etching typically does not penetrate more than a micrometer into the steel, and the UHCS microstructural feature of interest (the carbide network) has a length scale of tens to hundreds of microns, a significant deviation in measured network connectivity due to the effects of etching is not anticipated.
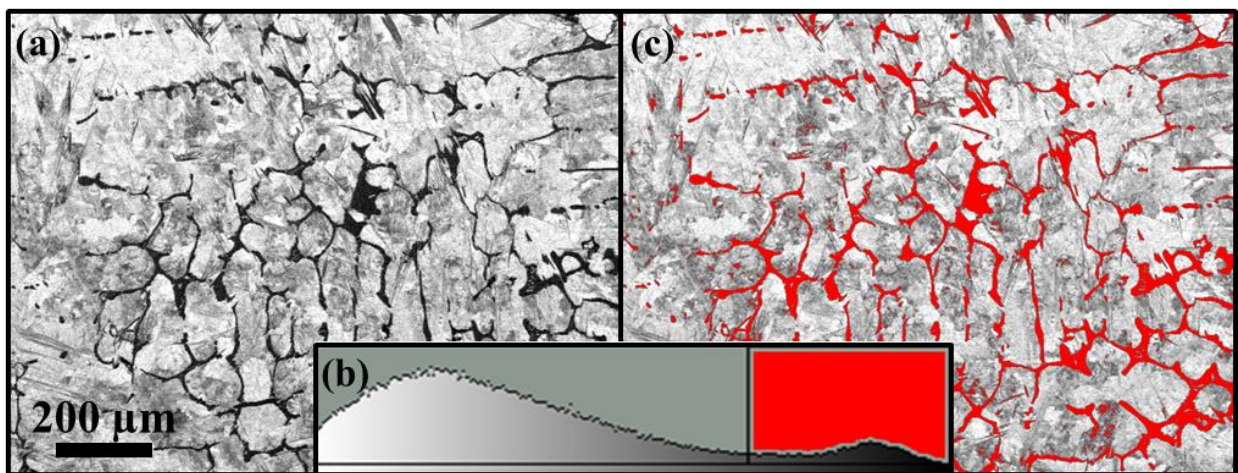
Figure 3.3 An SEM micrograph of (a) the as-cast UHCS microstructure containing a cementite network with (b) grayscale intensities plotted in a histogram; the highlighted red portion

54

`

indicates the retained grayscale intensities (c) overlaid in red on the original micrograph and denote the selected carbide network phase.

The next step was to segment phases within the micrograph. Segmentation began by establishing a grayscale intensity threshold in order to distinguish between constituent phases in the microstructure. The pixel grayscale histogram for **Figure 3.3 (a),** shown in **Figure 3.3 (b),** exhibited two peaks in grayscale intensity distinguishing the carbide network (darker grayscale) from the pearlite matrix (brighter grayscale). Intensity thresholding was used to retain only pixels below a threshold value of grayscale intensity. In **Figure 3.3 (c)** the highlighted red pixels denote pixels below the intensity threshold. The threshold intensity was chosen by fitting a Gaussian profile to the range of pixels representing the network peak and setting the threshold at either two or three standard deviations from the peak center (2 or 3σ from the maximum intensity). Taking three standard deviations ensured that most pixels in the network were included within the threshold, but substantial image noise might necessitate a 2σ selection. Simply setting the threshold at the intersection of the matrix and network peaks was not always sufficient to guarantee retention of sufficient network pixels after thresholding. The vertical black line in **Figure 3.3 (b)** denotes the threshold grayscale value at a distance of 3σ from the network peak center, and the intensity region to be retained is highlighted in red. After thresholding, a binary operation was performed to generate an 8-bit binary image where all retained pixels have one grayscale value of 0 (black) and the rest have values of 255 (white).

Particle size filtering for artifact removal

The next step in the image processing procedure was removal of noise artifacts from the binary image. Artifact pixels result from the overlap in grayscales between network and matrix phases in the histogram, as well as random fluctuations in SE signal during SEM image acquisition due to noise. Phase signal overlap was due to appreciable grayscale variation in the

`

matrix, where the darkest regions in the pearlite matrix were as low in grayscale value as the brightest regions of the carbide network and thus were not segmented out during thresholding. Random SE signal fluctuations from noise depend on beam dwell time on each pixel, and thus introduced artifacts on the order of a few pixels. Artifacts from phase signal overlap depended on the microstructure itself as well as the quality of sample preparation, and thus could be of any size. It was critical to remove as many artifacts from the image as possible while retaining the actual carbide network signal.

Artifact removal was accomplished through employment of a particle size filter. The filter only retained particles (collections of adjacent pixels) that exceeded a critical user-defined area. Since most particles on the network were elongated and most artifact particles tended to be more equiaxed in shape, filtering out particles with areas less than the square of the average network width removed few network particles while removing most artifact pixels. The average carbide network width was measured and the size filter was set to exclude areas less than the square of the network width. Network width was determined by measuring line profiles of grayscale intensity across the binary image as shown in **Figure 3.4 (a)** and plotted as a function of distance as shown in **Figure 3.4 (b)**. The peak widths for each line were averaged and the mean of the peak widths along the six lines was used as an estimation of the average carbide network widths. **Figure 3.5 (a)** shows a thresholded binary image with particles to be removed highlighted in red, and **Figure 3.5 (b)** shows the results after the filtering operation.
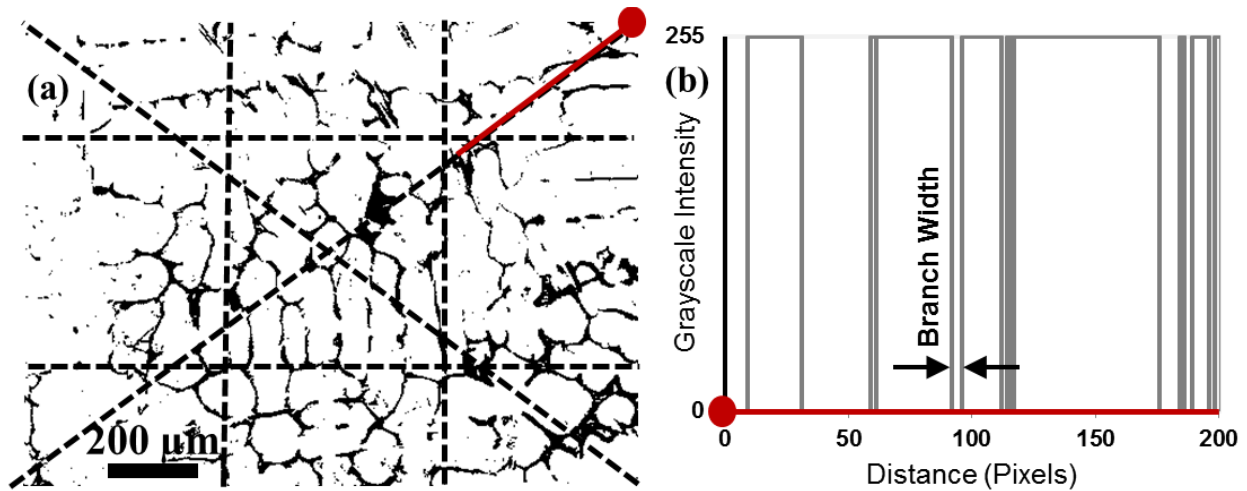
Figure 3.4 Approximate width of branches in the network was determined by (a) drawing lines across the micrograph and (b) measuring distance between peaks in grayscale intensity across the lines.
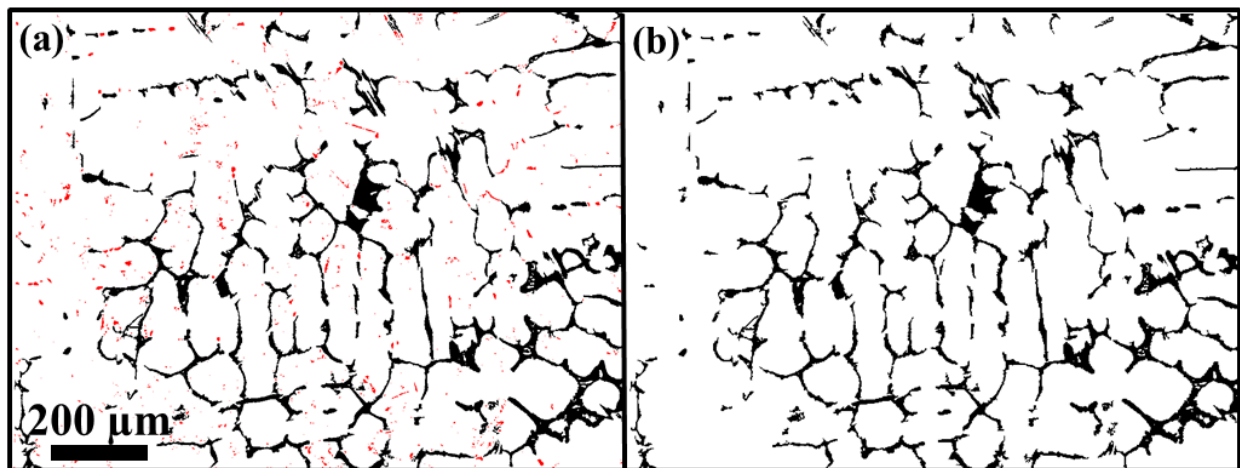
Figure 3.5 Thresholded binary micrograph (a) showing particles with area less than the square of the average network branch width highlighted in red and (b) the same binary micrograph after particles below the size threshold were removed.

Outlier removal operation for network void removal

In addition to its utility in removal of noise artifacts by size filtering, the measured network width was also employed to remove voids from the carbide network. The term "voids" refers to small pockets of matrix that existed within the branches of the network due to partially eutectic solidification. If these voids were not removed, the skeletonization step will create many artificial network pathways that were not necessarily representative of crack propagation paths

57

`

through the network. **Figure 3.6** provides an example micrograph illustrating this point, in which a crack has taken a straight path through a network carbide containing many voids. Given that voids exist entirely within the network branches, their average widths should generally be smaller than the previously measured average carbide network branch width.
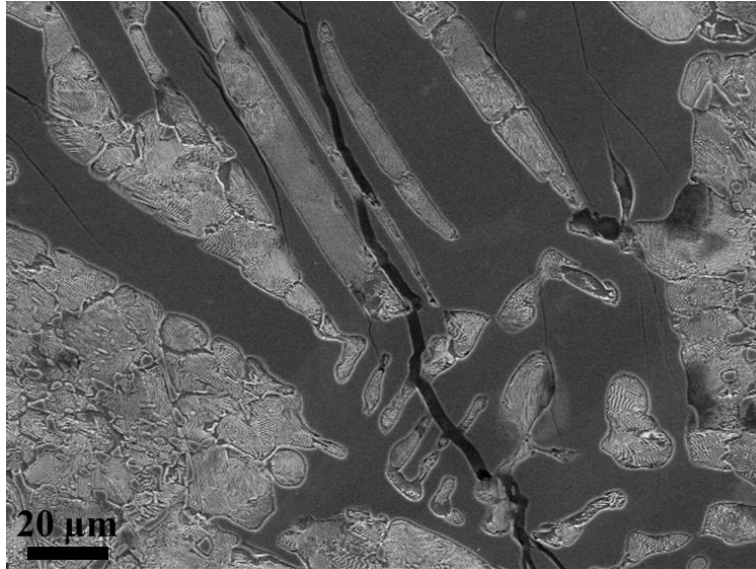
Figure 3.6 Secondary electron micrograph of a carbide network (dark gray) in an UHCS with a crack propagating across a number of voids.

To remove the voids, a "remove outliers" operation was utilized in ImageJ as demonstrated in **Figure 3.7**. For the case of void removal, the operation assessed each white pixel. If the surrounding pixels up to a user-defined radius were more black than white, that pixel was considered to be part of a void and converted to a black pixel. The radius required to remove voids was equal to or somewhat greater than the diameter of the observed voids themselves, so the average network branch width was a reasonable value to use as the user-defined radius. Comparison of **Figure 3.7 (a)** to **(c)** shows that the operation removed many voids throughout a given micrograph. Failure to remove voids from the network led to a skeleton that included many extra small loops, as shown in the unprocessed **Figure 3.7 (b)** as compared to **Figure 3.7 (d)**.

`

Inclusion of these loops in the connectivity analysis created many non-endpoint nodes, and thus contributed to an artificially larger connectivity index.
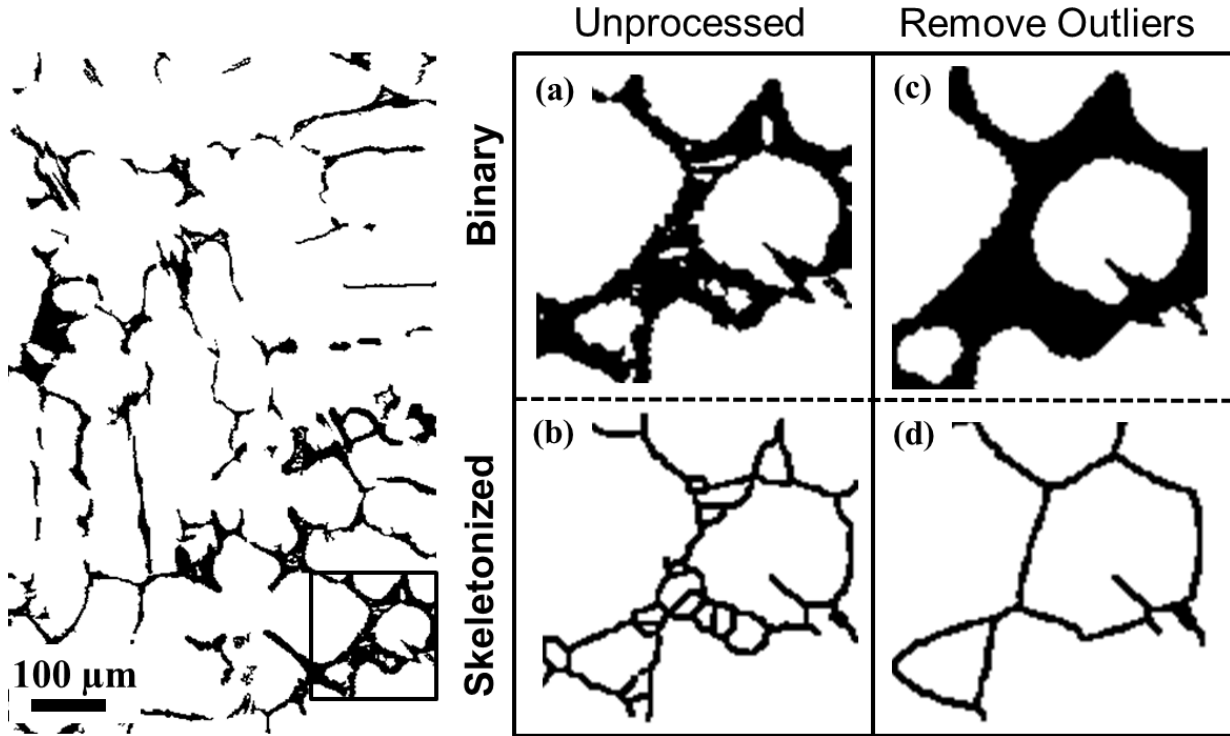
Figure 3.7 Binary micrograph of an UHCS carbide network with a region of voids in the network highlighted in the lower right corner. (a) Network segment before void removal via Remove Outliers operation in ImageJ showed (b) many small loops upon skeletonization, while (c) the same network segment after Remove Outliers operation showed (d) no small loops upon skeletonization.

Skeletonization for network quantification

The final image processing step was skeletonization. ImageJ uses a thinning algorithm for skeletonization, which iteratively removed pixels from all the edges of particles in the image, reducing thickness to one pixel. **Figure 3.8 (a)** shows a micrograph after the preliminary steps of phase segmentation by thresholding, artifact removal by particle size filter, and void filling by the remove outliers operation. Skeletonization of this image resulted in **Figure 3.8 (b)**. The longest shortest paths within each network tree, i.e. the longest distance that could be traveled

`

along the tree without doubling back, are shown in **Figure 3.8 (c). Figure 3.8 (c)** is included to help visualize the most likely crack paths through the microstructure.
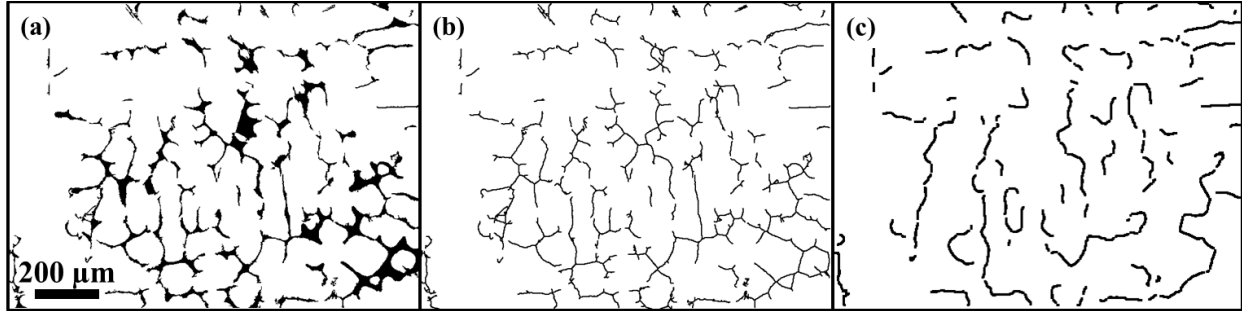
Figure 3.8 Image processing output of an SEM image (a) as a binary network representation, (b) after skeletonization and (c) after terminating branches are removed to show longest connected paths (likely in-plane crack propagation pathways).

Following skeletonization, quantitative information about the skeletonized network was extracted using the "AnalyzeSkeleton" plugin for ImageJ (*90*, *91*). AnalyzeSkeleton labels each pixel: end-point pixels are those with exactly one neighbor, slab pixels have two neighbors, and junction pixels have more than two neighbors. The plugin condensed connected slab pixels into branches (B) and connected junction pixels into junctions (J). Endpoints (E) and junctions are the nodes of the network, and branches are links between them. Relevant input and output from the Plugin is summarized in **Table 3.2**.

Table 3.2 Inputs and outputs from AnalyzeSkeleton plugin for ImageJ.

Input Pixel Type Labels:	Example (Red Pixel)	Condensed To:	Numerical Output
Endpoint Pixel		Endpoint (E)	Number of Endpoints
Slab Pixel		Branch (B)	Number of Branches, Length of Each Branch, Longest Shortest Path
Junction Pixel		Junction (J)	Number of Junctions.

`

The numerical output was useful for calculating connectivity index (ratio of links to nodes), average branch length, and probability of any node to be an endpoint. The connectivity index was defined as B/(E+J) and related to the probability of any two nodes being connected within the network. The minimum possible connectivity index value was 0.5, meaning that every branch in the network had exactly 2 endpoints. Higher values of connectivity index meant higher probability of nodes being connected, thus a more interconnected network. The probability of any node to be an endpoint was found by dividing the number of endpoints by the total number of nodes (E/(E+J)). The next sections show the application of this method to actual UHCS samples.

3.5 Results

3.5.1. Effects of magnification and imaging conditions

Examples of the image analysis approach applied to SEM micrographs of the as-cast 2C-4Cr UHCS are presented in **Figure 3.9**. Connectivity index results were found to be consistent across different magnifications and using different imaging conditions as shown in **Table 3.3**. Indexes and standard deviations from five different secondary electron SEM images of UHCS microstructure were measured for **Table 3.3**. An unsharp mask filter was applied to the BSE micrographs such as those shown in **Figure 3.9 (c)** to improve contrast. The diamond-shaped region in the center of **Figure 3.9 (c)** is an artifact from Vickers indentation, which was manually removed for connectivity index determination by selecting its pixels using the "magic wand" tool in ImageJ.

Original Micrograph   **Binary Representation**   **Skeletonized**
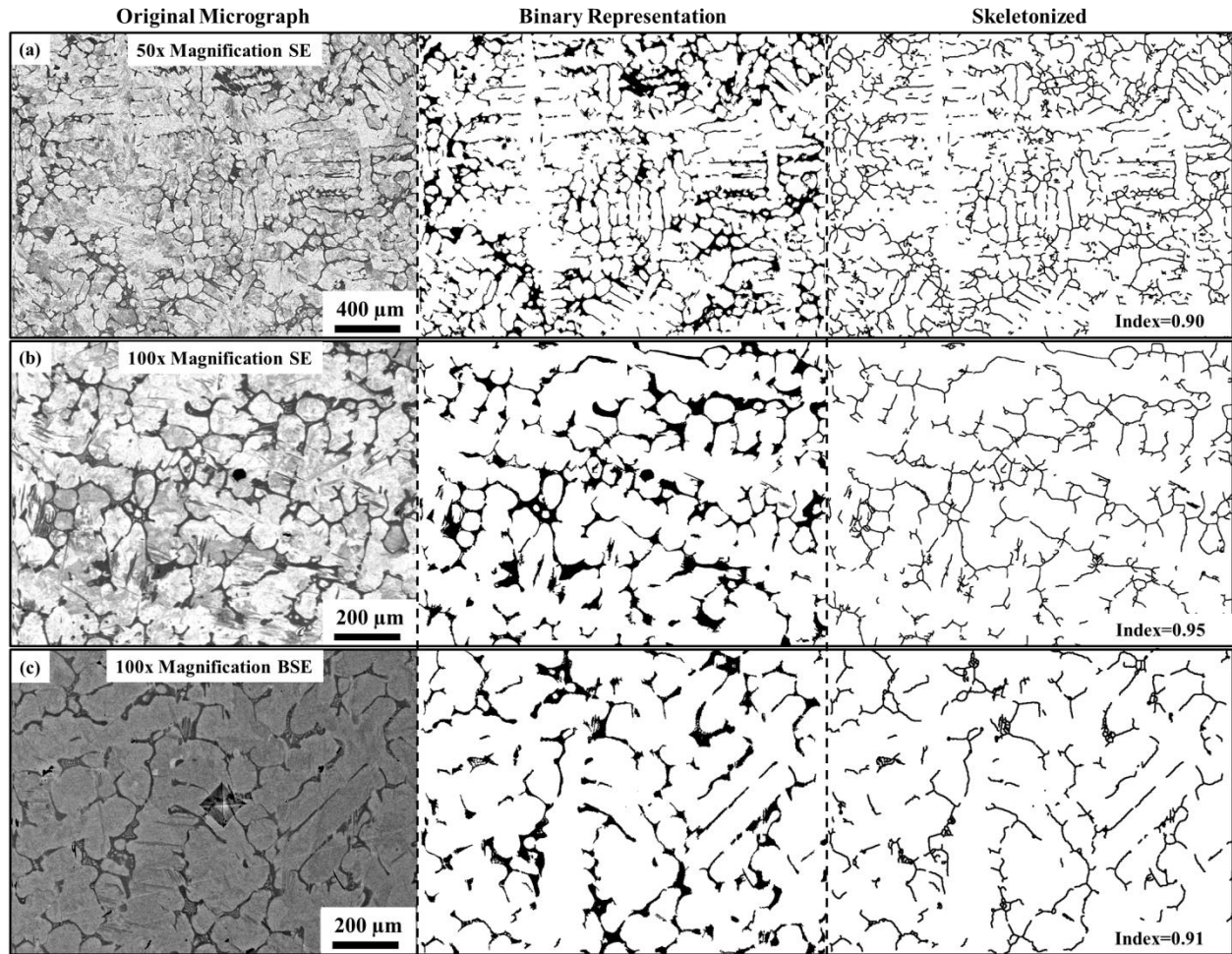
Figure 3.9 Examples of binary and skeletonization image analysis steps on SEM micrographs of as-cast UHCS (a) at 50x magnification using a SE detector, (b) at 100x magnification using a SE detector, and (c) at 100x magnification using a BSE detector. (Note that the index as shown in each figure corresponds to that micrograph alone. For mean and standard deviation of five such indexes, see **Table 3.3**.)

Table 3.3 Quantitative analysis results on images of as-cast UHCS networks

Condition	Image	Connectivity Index
Etched, as-cast, 50x magnification, SE image	**Figure 3.9 (a)**	0.91±0.02
Etched, as-cast, 100x magnification, SE image	**Figure 3.9 (b)**	0.92±0.04
Unetched, as-cast, 100x magnification, BSE image	**Figure 3.9 (c)**	0.92±0.03

`

3.5.2 Comparison of network connectivity in as-cast and heat-treated UHCS

The next objective of the study was to compare the network connectivity in the as-cast and heat-treated 2C-4Cr UHCS microstructures. **Figure 3.10** shows SEM micrographs of carbide networks and fracture surfaces in the heat-treated and as-cast UHCS samples. **Table 3.4** reports image analysis and Charpy impact testing results. Qualitatively, there was little difference in the apparent connectivity of the two UHCS conditions. Nevertheless, digital analysis of the micrographs indicates that the heat-treated UHCS had a lower connectivity index (0.84) than the as-cast sample (0.92). Fracture surfaces of the as-cast and heat-treated UHCS showed faceting on the same length scale as the spacing between branches of the cementite network, indicating that cracks did follow the network to some extent in both samples. The fracture surface of the heat-treated UHCS contained some areas indicative of ductile fracture, while the as-cast UHCS did not. There was an increase in Charpy impact energy of about 10% in the heat-treated UHCS, reflecting the additional matrix participation in cracking. However, energy absorption did not differ significantly (for the purposes of this study, a significant difference would be on the order of one to several Joules as was seen in the literature with regards to network break-up (*48*)). A standard deviation for the Charpy impact energy values is not reported because only two tests were conducted for each condition. Additional measurements from UHCS microstructures with significant differences in impact energy were desired to investigate a possible link between index and Charpy impact energy, so the image analysis method was further utilized for published micrographs in the literature.
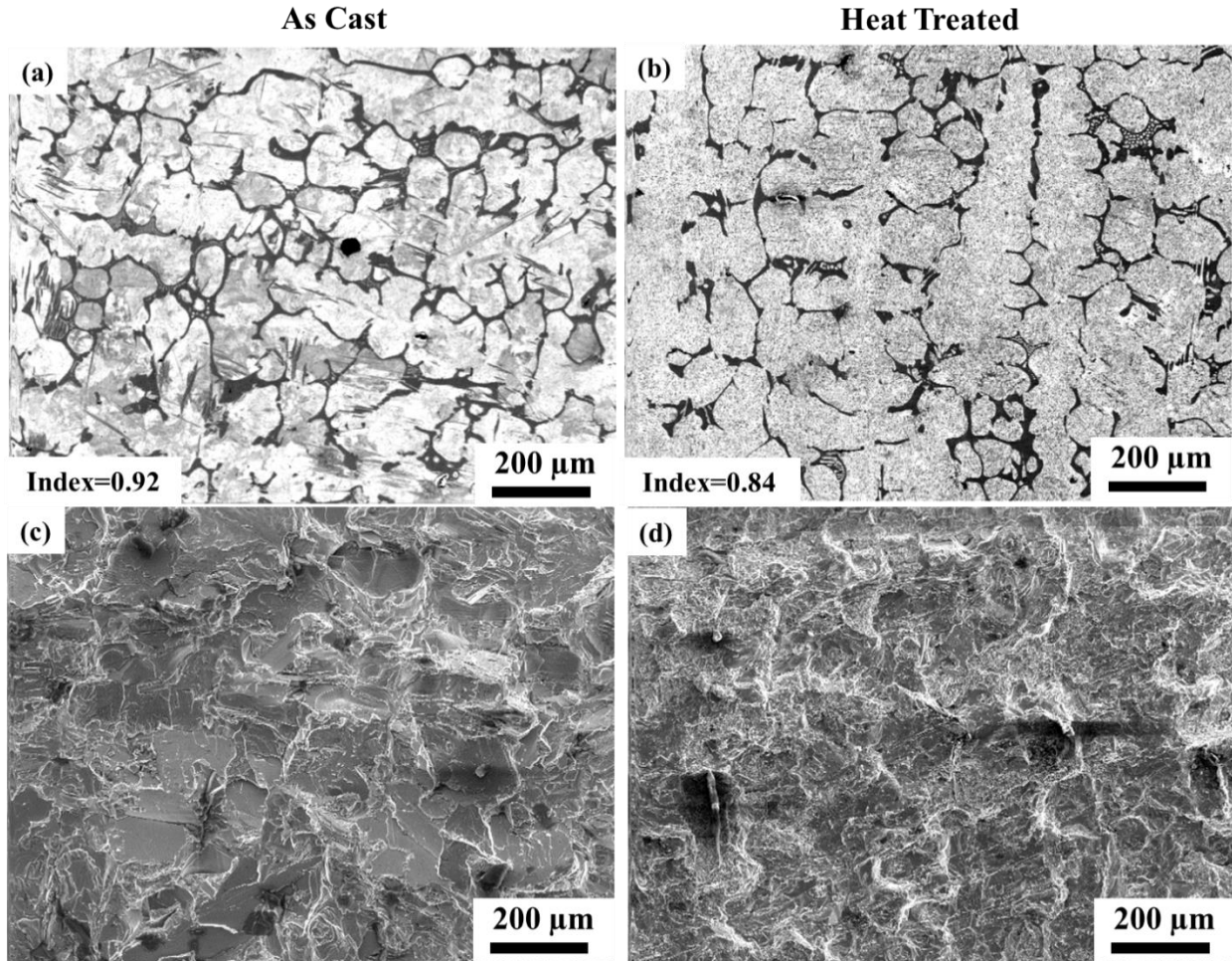
Figure 3.10 SEM micrographs of (a) the carbide network in the as-cast UHCS and (b) the carbide network in the heat-treated condition, and (c) the fracture surface of the as-cast UHCS and (d) the fracture surface of the heat-treated UHCS.

Table 3.4 Image analysis data and toughness results

Condition	As-Cast	Heat-treated
Carbon Content (Wt. %)	2.1	1.7
Network Area Fraction (%)	14 ±3	10 ±1
Connectivity Index	0.92±0.01	0.84±0.02
CVN Impact Energy (J)	1.82 and 1.83	1.98 and 2.06

3.5.3 Connectivity index at constant volume fraction

Since a major research drive for UHCS is modifying the carbide network to reduce connectivity, it would be illustrative to determine how UHCS microstructures would appear with lower

64

`

connectivity indices.   One approach is to alter an experimental micrograph of a carbide network so that the resulting connectivity is reduced. **Figure 3.11 (a)** is a binary image from an actual UHCS specimen that was then altered in a series of image processing steps to produce a new, artificial carbide network with progressively lower connectivity index values. The starting microstructure has a connectivity index of 0.95 and was altered by multiple iterations of **Erode**, **Dilate**, and **Remove Outliers** operations. **Figure 3.11 (b)** and **Figure 3.11 (c)** show binary images of the modified carbide network with progressive alteration resulting in connectivity indexes of 0.77 and 0.65. This modification process maintained consistent carbide network area fraction. The image series shows significant and obvious microstructural changes (cementite spheroidization) corresponding to substantial changes in the quantified connectivity index.   Also, this exercise demonstrates how network breakup might appear with carbide network area held constant.
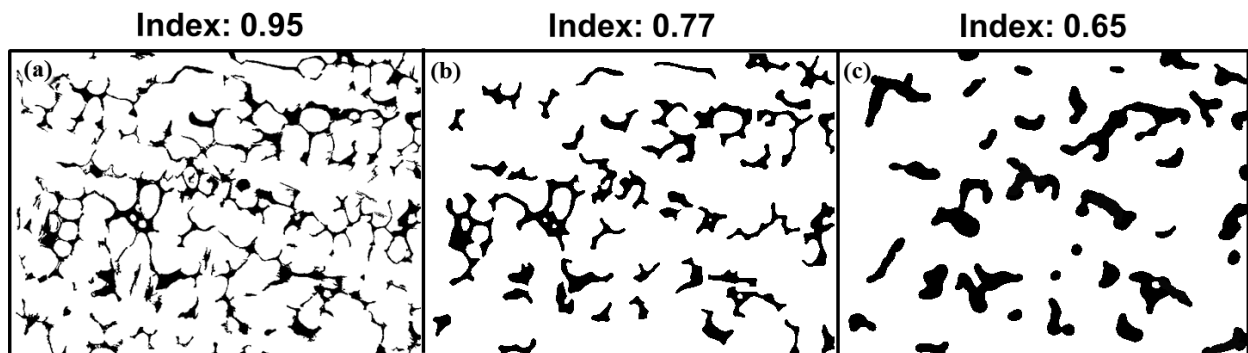
Figure 3.11 Keeping network area fraction constant, (a) a binary SEM micrograph of an UHCS with connectivity index 0.95 is processed to (b) an index of 0.77 and (c) and index of 0.65.

3.5.4 Quantifying network index in previously published research.

The image analysis methods described above were also applied to previously published studies of UHCS. Hamidzadeh (*48, 49*) and Liu (*92*) explored the effect of chemical additives on carbide network breakup and resulting toughness enhancements, measured using Charpy impact tests. Chemistries of these UHCS are shown in **Table 3.5**.

Table 3.5 Chemistries of steels in some other UHCS studies. (RE – rare earth elements added to break up carbide network)

Sample	C	Si	Mn	Cr	Nb	Mo	V	RE	Ref.
This Study	2.02	0.65	0.72	3.86	0.02	.33		-	-
Hamidzadeh A	1.45	0.18	0.37	11.45	-	0.58	0.88	-	(*48*)
Hamidzadeh B	1.44	0.18	0.39	11.30	0.48	0.61	0.89	-	(*48*)
Hamidzadeh C	1.38	0.18	0.34	11.22	1.06	0.61	0.86	-	(*48*)
Hamidzadeh D	1.35	0.18	0.33	10.95	1.54	0.60	0.80	-	(*48*)
Hamidzadeh RE	1.45	0.18	0.37	11.45	-	0.58	0.88	0.03	(*49*)
Liu Unmodified	1.94	0.53	0.47	1.43	-	-	-	-	(*46*)
Liu RE	1.93	0.58	0.49	1.46	-	-	-	>0	(*46*)

Figure 3.12 (a-c) reproduces OM micrographs of UHCS specimens previously published by Hamidzadeh *et al.*(*48*). The OM micrographs qualitatively reflect a breakup of the carbide network with increased Nb addition. The current image analysis approach was applied to quantify the carbide network connectivity index for each OM micrograph. Segmented binary images, shown in **Figure 3.12 (d-f)**, captured the carbide network for each corresponding OM micrograph **(Figure 3.12 (a-c))**. The measured connectivity index for each micrograph showed a decrease with additional Nb content. Area fraction also decreased with Nb content. The images of Liu showed little change in connectivity with the addition of rare earth modifiers, but network area fraction was increased due to the modification.
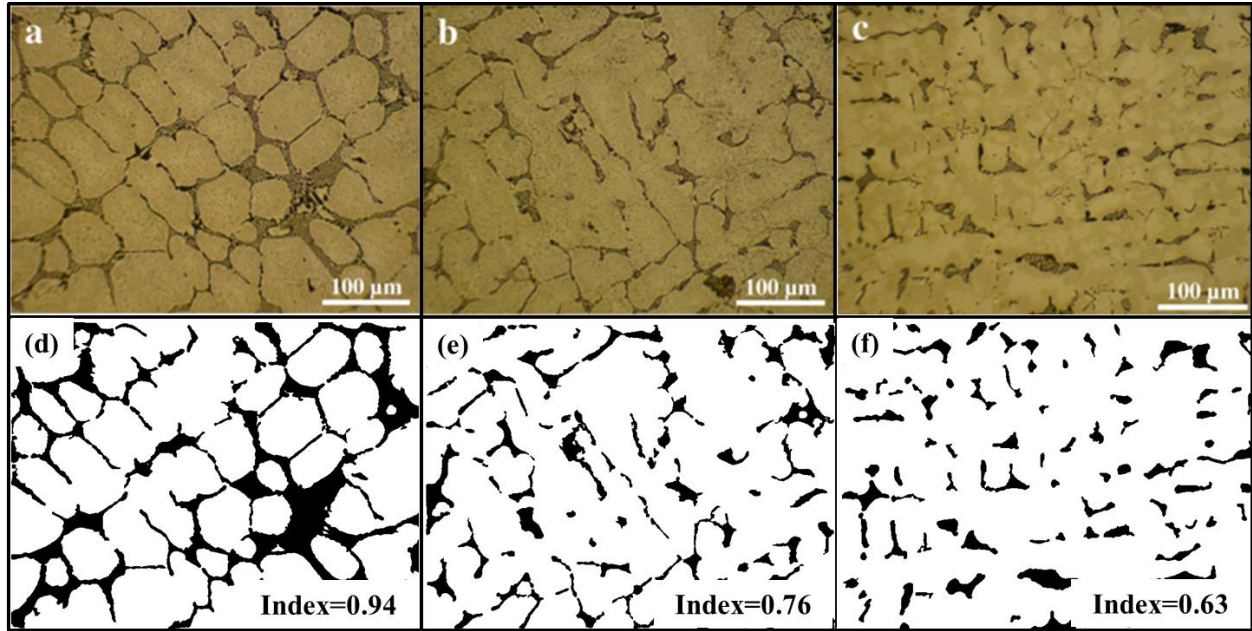
Figure 3.12 OM micrographs reproduced from Hamidzadeh et al. (*48*) show a 1.4 wt% C UHCS with chemistry modified by (a) no Nb addition, (b) 0.5 wt% Nb addition, and (c) 1 wt% Nb addition. Segmented binary images show a network connectivity change from (d) 0.94 to (e) 0.76 to (f) 0.63 upon increasing additions of niobium. Panels (a,b,c) were adapted from Hamidzadeh *et al.* (*48*), with permission from Elsevier.

3.6 Discussion

3.6.1 Relevance of connectivity index

The primary objective of this study was to develop a metric to connect UHCS microstructure and performance. Since network break-up is often associated with enhanced toughness, results from this study and published literature (*46*, *48*, *49*) were analyzed to explore possible trends in material performance (quantified by Charpy impact testing) and microstructural metrics. Comparisons for Charpy impact energy versus connectivity index and network area fraction are shown in **Figure 3.13**. Error bars are not shown for Charpy impact energy in **Figure 3.13** for the data of Liu *et al* (*46*) because no standard deviation in Charpy impact energy data was reported in their study. Charpy data measured for this study appear as a single point for each condition because the data points completely overlapped when both measurements were plotted at the scale of the figure.

67
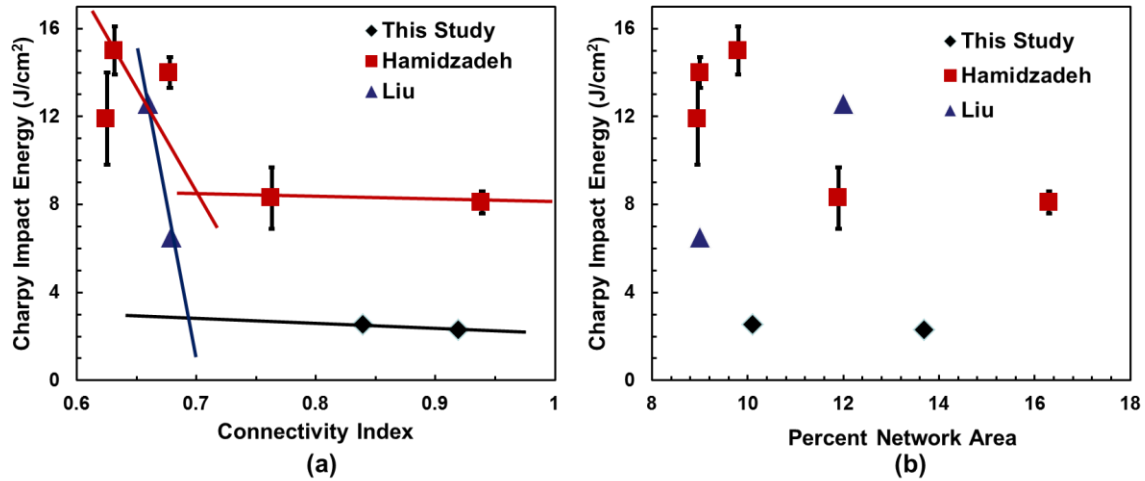
Figure 3.13 Plots of (a) connectivity index versus Charpy impact energy and (b) network area fraction versus Charpy impact energy, incorporating data from three different research studies (including the present study). Lines in (a) drawn in manually to help guide the eye to the plateau and inflection in Charpy impact energy as a function of connectivity index. Impact energy is plotted in units of J/cm^2 to be consistent with data from published literature(*46*, *48*, *49*).

Two trends were identified in **Figure 3.13 (a)** based on the grouping of UHCS samples by similar steel chemistries. Both trends show that impact energy decreased as connectivity index decreased in the lower connectivity index range (below 0.7). We noted a possible inflection point at about 0.70-0.75, above which connectivity index ceased to have an effect on impact energy (plateau region). The two different energy trends and the existence of two plateau energies in **Figure 3.13 (a)** are attributed to differences in alloy chemistry and carbide type. Hamidzadeh *et al.* (*48*, *49*) reported primarily M_7C_3 carbides in their steel (upper trend), as compared to the Fe_3C carbides reported by Liu *et al.* (*46*) and this study (lower trend). The upper trend had a plateau energy close to 8.5 J/cm^2, while the lower trend plateau energy was close to 2.5 J/cm^2. The difference in plateau energies might reflect the energy dissipation capacities of the different types of carbides. However, I have not been able to find any literature values of impact energy for M_3C versus M_7C_3.

`

Figure 3.13 (b) shows little correlation between impact energy and network area fraction across all steels, though a decreasing trend was observed in the work of Hamidzadeh. This trend was attributed to the relationship between connectivity and network area fraction as shown in **Figure 3.14**. The carbide network formed between austenite grains, so it was expected that higher amounts of carbide would correlate with a more connected network, and thus a clearer connection between network area fraction and the connectivity index.
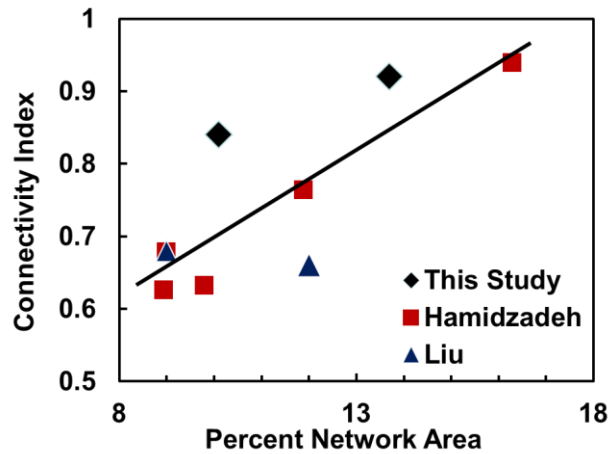
Figure 3.14 Network area fraction versus connectivity index for relevant carbide networks.

3.6.2 Crack Propagation behavior and Percolation Threshold

The plateau and inflection point in **Figure 3.13 (a)** are attributed to a possible transition in crack propagation behavior through the UHCS microstructure. The plateau region, where network connectivity does not influence toughness much, most likely corresponds to crack propagation primarily along the brittle carbide network. In this high connectivity index region, the network has sufficient connectivity to span the entire microstructure without significant discontinuities, so further increases in connectivity of the network have only a minor influence on toughness. The plateau region began when connectivity exceeds about 0.7 in the UHCS samples studied, as seen in **Figure 3.13** (a) from interpolation of trendlines for both Hamidzadeh and Liu/this study. For connectivity indexes lower than 0.7, absorbed impact energy increases as

`

index decreases, indicating that cracks must traverse greater proportions of ductile matrix to propagate across the UHCS microstructure. UHCS in which the carbide network has been eliminated should have toughness controlled by matrix microstructural parameters.

This concept of a critical connectivity level required for a network to effectively span a given length-scale is in congruence with well-established percolation theory, specifically the concept of "percolation threshold" (*81*). Percolation theory addresses connected paths of specified length within a system. Systems can be modeled as a lattice of nodes in space, with each node having a probability of being connected to its nearest neighbor(s). The percolation threshold refers to the critical connection probability required to have a greater than 50% chance of having a connected path span across the entire lattice. In systems of infinite size, the probability of spanning the lattice is a stepwise function; above the percolation threshold there will always exist a spanning path, and below it such a path will never exist. The more nodes there are in the lattice, the closer the probability of spanning approaches a stepwise function. If we envision an UHCS microstructure as a lattice of matrix and carbide nodes, the connectivity of the network of carbide nodes as a whole is related to the probability of connection between individual carbide nodes. Thus, there should be a critical network connectivity enabling the network to span the entire UHCS microstructure. Connectivity at or above this threshold should lead to cracks being able to propagate entirely within the carbide network without passing through the matrix, resulting in the observed plateaus in impact energy in **Figure 3.13 (a)**.

The 2D network sections analyzed in this work could accurately reflect the true 3D connectivity, given a sufficiently isotropic network. Analysis of different regions spanning millimeters in the UHCS specimens of this study yielded similar connectivity indices but also varying directionality in the local network structure due to dendritic solidification. With

`

sufficient statistical analysis of 2D images over many regions of a sample, the resulting microstructural properties should be adequately representative for the 3D case as well. Thus, it should be possible to estimate the true 3D connectivity of the network from 2D analysis.

3.6.3 Network length-scale

Theoretically, the connectivity index represents the likelihood of a connection existing between two points in the network. A larger length scale thus modifies the average length of connected paths in the microstructure. Thus, for a given connectivity index value below the critical threshold, the length-scale of the network will determine the average distances cracks can propagate uninterrupted along the network. Thus, smaller length scales with the same index would lead to smaller cracking paths.

Additionally, a higher number of deflections along a network correlates to higher toughness (*93*). The connectivity index is dimensionless, but a measure of network length scale can be separately quantified for the above-mentioned images by using the average distance between branches in the network along a line profile of grayscale intensities. This distance would correspond to the secondary dendrite arm spacing of the primary austenite and thus depend on cooling rate and chemistry (*48*, *94*). For the UHCS tested in this report, average network branch spacing was slightly larger (within a factor of two) than those of Hamidzadeh and Liu. Therefore a higher amount of crack path deflections occurring in the more closely spaced networks could also account for some of the energy absorption differences.

3.7 Conclusions

This chapter presents a method for quantitatively assessing carbide network connectivity in UHCS based on the connectivity index used in transportation science (analogous to crack propagation along a "pathway" of carbide networks in UHCS). The method involves a series of

71

`

standard image processing steps that common commercial software programs, such as ImageJ, can perform. Experimental micrographs were segmented by phase using grayscale intensity thresholding. Artifacts in the segmented images were removed by filtering out particles with area less than the square of the average network branch width. Voids inside the carbide branches were filled and then the networks were skeletonized to convert them into systems of links and nodes for determining connectivity index. The method was applied to determine connectivity index values from SEM and OM micrographs in order to gain insight on crack propagation and toughness for UHCS microstructures.

Connectivity index values were consistent with respect to two different magnifications (50x and 100x) and imagining conditions for the same UHCS samples. Toughness was correlated with connectivity index below a critical value of around 0.7 and plateaued above that value. This observation was attributed to connectivity index exceeding a percolation threshold. In general, the connectivity index shows promise as a useful metric to evaluate whether toughness will be affected by processing designed for network modification.

`

Chapter 4. Kinetics of Cementite Particle Coarsening and Denuded Zone growth in a 2C-4Cr Ultrahigh Carbon Steel

Note: this chapter was adapted from a previously published paper (95)

4.1 Abstract

This chapter examines spheroidization and coarsening of cementite in an initially pearlitic 2C-4Cr ultrahigh carbon steel (UHCS) containing a cementite network at 800˚C, 900 ˚C, and 970˚C for durations of 5 minutes up to 85 hours. Coarsening kinetics of spheroidized cementite particles and growth of denuded zones adjacent to the cementite network were investigated by quantitatively analyzing particle sizes from digital micrographs of water-quenched steel etched with Nital. Denuded zone widths grew at a rate proportional to $t^{1/4}$ - $t^{1/5}$. Spheroidization of pearlite was completed within 90 minutes at 800˚C and 900˚C, and within 5 minutes at 970˚C. Bimodal particle size distributions were identified in most of the samples and were more pronounced at higher temperatures and hold times. Peaks in the bimodal particle size distributions were attributed to the coarsening of intragranular and grain boundary particles in the steel. A third, non-coarsening peak of particles was present at 800˚C only and was attributed to a small volume fraction of particles existing prior to the heat treatment. Particle sizes were plotted versus time to investigate possible coarsening mechanisms. The coarsening exponent for the growth of grain boundary carbides was close to 4, indicating grain boundary diffusion control. The coarsening exponent was close to 5 for intragranular carbides, indicating suppression of volumetric diffusion (possibly due to reduced effective diffusivity because of Cr alloying) to rates comparable to diffusion along dislocations.

4.2 Introduction

4.2.1 Ultrahigh Carbon Steels

In Chapter 2 of this dissertation an as-cast 2C-4Cr UHCS mill roll was compared to an industrially heated roll of similar composition. The as-cast matrix was fully pearlitic while the heat-treated matrix contained a homogenous distribution of faceted idiomorphic cementite particles. The idiomorphic particles may have contributed to a 10% increase in Charpy impact toughness in the heat-treated UHCS. This chapter investigates the kinetics of idiomorphic cementite particle growth through a series of heat treatment experiments of the as-cast UHCS.

UHCS are typically heat-treated after casting to improve mechanical properties. Heating an initially pearlitic matrix to near or above the eutectoid temperature will cause spheroidization of cementite lamellae into equiaxed particles. Further time at temperature will result in curvature-driven particle coarsening. Carbide particle size distribution influences fracture toughness (*96*) and yield strength (*97*), and potentially also the proeutectoid network volume fraction and connectivity in UHCS. Gurland (*98*) noted that cracking in tension and torsion in spheroidized pearlite tended to occur in the largest cementite particles. A smaller mean free path between particles, i.e. a smaller particle size, typically improves both toughness and hardness, so processing to produce a finer distribution of particles is usually beneficial. On the other hand, a partially pearlitic microstructure might be desirable for increased wear resistance (*99*). Closely spaced particles are more likely to lead to a non-lamellar divorced eutectoid transformation upon cooling from the austenite (*19*). Thus, understanding particle coarsening behavior is desirable for improving the tailoring of mechanical properties via heat treatment processes for UHCS.

Intercritical spheroidization is intimately related to austenite formation, so understanding the nucleation of austenite and dissolution of cementite is important. The nucleation and growth

rate of austenite is strongly dependent on transformation temperature. Molinder (*100*) studied the transformation of a spheroidized microstructure of ferrite and cementite to austenite in a 1.27 wt% C, 0.8 wt% Cr steel and noted that the transformation to austenite took seconds at 800˚C and higher, and about 15 minutes at 750˚C. Cementite dissolution was rapid, but slower than would have been expected by carbon diffusion alone, and cementite continued to dissolve until the equilibrium austenite carbon concentration was reached. Shtansky (*101*) found that additions of Cr delayed the onset of austenite nucleation in a 1C-2.6Cr steel. Austenite took 8s to nucleate austenite at 800˚C, while a 1C-8.2Cr alloy took 20s at 850˚C. Speich (*102*) studied austenite nucleation in plain carbon steels, and concluded that austenite nucleates at the intersection of two pearlite colonies in pearlitic steels, and at the intersection of ferrite grains and cementite particles or laths.

4.2.2 Kinetics of Particle Coarsening

In 1961, Lifshitz and Slyozov (*103*) and Wagner (*104*) independently derived a mathematical treatment describing coarsening of small volumes of dilute second-phase particles by bulk diffusion (LSW theory). In LSW theory, each particle sees a concentration gradient field based on the curvature of all other particles. The radius of curvature *r* of a particle affects the concentration of solute in the matrix C_r immediately surrounding it according to the Gibbs-Thomson Equation (*105*):

$$C_r = C_\infty + C_\infty 2\sigma V_m / rTR$$

where C_∞ is the equilibrium matrix concentration, V_m is the molar volume of the precipitate, R is the gas constant and T is the temperature. Differences in particle curvatures result in concentration gradients from small particles to larger particles. The result is that particles above

a critical radius grow and those below it shrink. In a random and dilute distribution of particles, the critical radius is the mean particle size.

The general form of the coarsening equation is:

$$r^n - r_o^n = k_n(t - t_o)$$

where r is the mean particle radius at time t, r_o and t_o are the mean radius and time at the start of steady state coarsening, and k_n is a temperature (T) dependent constant and n depends on the diffusive mechanism controlling particle coarsening: $n=3$ for bulk/volume diffusion; $n=4$ for grain boundary diffusion; $n=5$ for dislocation-mediated diffusion.

The LSW derivation considered bulk diffusion only, and predicted that particle coarsening would proceed according to time to the 1/3 power, such that:

$$r^3 - r_o^3 = k_3(t - t_o).$$

The constant k_3 in this equation includes the diffusion coefficient D, surface energy γ, equilibrium solute concentration C_o, and molar volume V_m of the coarsening phase:

$$k_3 = \frac{8\gamma D C_o V_m^2}{9RT}$$

Speight (*106*) extended the theory to include microstructures where two-dimensional diffusion along grain boundaries was dominant:

$$r^4 - r_o^4 = k_4(t - t_o).$$

k_4 is similar to k_3 but depends on grain boundary energies and diffusion coefficient. Ardell (*107*) extended the theory to include systems where diffusion along dislocations was dominant:

$$r^5 - r_o^5 = k_5(t - t_o).$$

Particle diameter (*d*) may be used instead of particle radius (*r*) in these equations if an extra factor of 2^n is multiplied into k. It has been theorized (*108*) that systems may have combined diffusion mechanisms in operation such that

$$r \propto (at+bt^{3/4}+ct^{3/5})^{1/3}.$$

The constant a, b, and c scale the contribution of each diffusive mechanism. Thus, the coarsening exponent n might take on non-integer values between 3 and 5 depending on the contributions of each mechanism to the overall coarsening process.

Identifying the n value for a given coarsening process can pose a challenge. Typically, mean particle diameters are plotted versus time on a log-scale plot, and n and k are extracted from the equation for the best-fit line:

$$\log(d) = \frac{1}{n} \cdot \log(kt)$$

This procedure is applicable if the initial particle size d_o is negligible. If d_o is not negligible, then unless $k \cdot t_o = d_o{}^n$, the apparent value of n will be different from the true n value when extracted from a log-log plot.

The literature regarding cementite coarsening in steel considers two general cases: coarsening of cementite produced during tempering of supersaturated martensite (*13, 109, 110*) and coarsening of spheroidized pearlite particles (*111–113*). The n values for various steels ranged in the literature from about 2 to 6 (see **Table 4.1**). Some literature n values may be erroneously high due to failure to correct for a non-negligible d_o, especially in cases dealing with coarsening of the products of spheroidization.

Table 4.1 Literature references for n values in cementite coarsening

Year	C and Cr	Temperatures	n value	Reference
1968	0.3C	948 K (675°C), 993 K (720°C)	3 to 4	(*113*)
1982	0.33C	903 K (630°C)-963 K (690°C)	2.7 to 3.0	(*109*)
1995	1C-1.5Cr	973 K (700°C)-1013 K (740°C)	2.9 to 3.0	(*111*)
1998	0.2 to 1.4C	963 K (690°C)	4.3 to 5.0	(*108*)
1999	0.45-C	973 K (700°C)	3.7 to 4.4	(*110*)
2008	0.8C	973 K (700°C)	4.1 to 6.1	(*112*)
2008	0.8C-1Cr	973 (700°C)	2.0 to 6.3	(*112*)

The literature generally uses an effective diffusion coefficient in describing coarsening derived by Li *et al.* (*114*) for plain carbon steel reflecting constraints that cementite composition and volume remain constant during coarsening:

$$D_{eff} = \frac{C_{Fe}D_{Fe}D_C V_{Fe}^2 + C_C D_{Fe}D_C V_C V_{Fe}}{C_{Fe}D_{Fe}V_{Fe}^2 + C_C D_C V_C^2}$$

C_{Fe} and C_C refer to the concentrations of iron and carbon, respectively. V_{Fe} is the atomic volume of Fe and V_C is the difference between the volume of one molecule of Fe_3C and three atoms of iron in ferrite (or austenite). In steels with significant Cr alloying, Cr is reported to substitute for Fe in cementite up to about 18 wt% (*52*). Due to the constant composition constraint, the expression for the effective diffusion coefficient should be modified to hold the Cr composition constant. While the diffusion coefficient of Cr in Fe is very close to the self-diffusion coefficient of Fe, the concentration of Cr is overall significantly lower. Cr alloying has also been suggested to increase the activation energy of iron self-diffusion, though its effect is not well understood (*115*). Thus, the effective diffusion coefficient controlling cementite coarsening might be significantly lowered by Cr alloying, leading to substantially slower coarsening. Zhang *et al.* (*116*), in a study of an initially pearlitic steel with 1 wt% C observed that "the addition of substitutional alloying elements (Mn, Si, Cr) can remarkably retard the coarsening of cementite particles".

Brown and Kraus (*117*) studied spheroidization in a 52100 bearing steel with a nominal composition of 1C-1.5Cr. Their heat treatment consisted of a 1 hour hold at 850 ˚C followed by an oil quench to room temperature. They noted that large (~1 μm diameter) spheroidized cementite particles formed on austenite grain boundaries, while smaller (mostly finer than 0.25 μm) particles formed inside austenite grains. Luzginova *et al.* (*118*) heated 1wt% C and 0.5-3.5 wt% Cr steels to about 800˚C for 2-3 hours and cooled slowly to about 720 ˚C, then air-cooled to

`

room temperature. They reported a similar bimodal distribution of spheroidized cementite in all samples with two mean sizes, 0.15 μm and 0.41 to 0.47 μm. The bimodal distribution was also attributed to grain boundary (larger mean size) versus non-boundary carbides (smaller mean size).

Similarly, some authors found changes in the slope of particle diameters versus time. Day and Barford (*113*) noted an abrupt change in slope in their *r* versus *t* data corresponding to a change in *n* values from 3 to 4 at about 20000s at 675˚C, which they attributed to a change in the dominant coarsening mechanism from bulk diffusion to grain boundary diffusion. Cree *et al.* (*111*) noted a change in slope from *n* values very high to about 3 after about 3600s at 740˚C and 10000s at 700˚C, which they attributed to bulk diffusion controlled coarsening after an initial "transient" period of slower apparent growth. Nam and Bae (*110*) reported that grain boundary particles coarsened with *n*~4.5, while intragranular particles coarsened with *n*~3.7.

In the existing literature on cementite coarsening in steels, the maximum carbon concentration studied was 1.4 wt% C, the maximum chromium concentration studied was 1.5 wt% Cr, and the maximum temperature studied was 740˚C. The present study analyzes cementite coarsening kinetics in a new regime of chemistry and temperature: 2 wt% carbon, 4 wt% Cr between 800°C and 970°C. The high chromium content is of interest because it might lead to slower coarsening kinetics by lowering the effective diffusion coefficient. The high carbon concentration is of interest because it contributes to the presence of the cementite network. The effects of the network on coarsening kinetics have not been studied previously.

4.3 Materials and Methods

Different samples of as-cast UHCS (composition shown in **Table 4.2)** were placed in a preheated box furnace at 800, 900, and 970˚C for times of 5 min, 90 min, 3 hours, 8 hours, or 24

`

hours, and then quenched to room temperature in water. Furnace temperature calibration curves are shown in **Appendix A, Section A.2.** An additional water-quenched heat treatment of 85 hours at 800˚C was also conducted. Several samples were also cooled in air or were furnace cooled (for further details see **Appendix A, Section A.2**). All of these heat treatments were in the two-phase austenite + $(M,Cr)_3C$ phase field according to Thermo-Calc calculations (version 2016b, TCFE8 database) (*54*).

Table 4.2 As-cast UHCS composition. Carbon content was measured by combustion analysis, and other elements by ICP-OES (inductively coupled plasma optical emission spectrometry).

	Fe	Nb	Cr	C	Mn	Mo	Si	Ni	W
As-Cast UHCS	Bal.	--	3.86	2.02	0.72	0.33	0.65	1.45	--

Since heat treatments were conducted in air, we ensured microstructural analysis avoided the decarburized region. The greatest potential depth of decarburization for these heat treatments was calculated at about 3 mm for 24 hours at 970˚C (*119*). All samples were more than twice as large as this depth and the decarburized zone was avoided during microstructural characterization by imaging close to the center of the samples.

Heat-treated samples were cross-sectioned along the midline with a water-cooled alumina cutoff wheel, then were polished with 1 μm alumina and etched for 25-30s in 4-5% Nital (nitric acid in ethanol). Microstructural phases were investigated in several samples using X-ray diffraction (X'Pert Pro MPD XRD operated at 45 kV, Cu K_α radiation). Only cementite, ferrite, martensite and austenite phases were identified. Etched samples were imaged using a Phillips XL-30 scanning electron microscope (SEM) at 20 kV accelerating voltage in secondary electron imaging mode. The resulting micrographs were then analyzed using the public domain ImageJ software (*120*).

To investigate coarsening kinetics, a specialized particle analysis methodology was developed to quantify particle sizes from multiple digital micrographs. The core steps of the

method are shown in **Figure 4.1**. This method was used for all samples except for the 5 minute

holds at 800 and 900˚C. The method was not suitable for those two samples because they were

partially pearlitic; particles could not be properly targeted and isolated by the edge detection

filter because of the cementite lamellae. At least 2000 particles were analyzed per heat treat

condition except in the case of the aforementioned 2 samples, for which 102 particles (800˚C, 5

minute hold) and 321 particles (900˚C, 5 minute hold) were measured by manually fitting

ellipses to particles. Particle areas (A) were measured in all cases, and diameters were calculated

assuming spherical particles such that $d = 2\sqrt{A/\pi}$. Corrections for stereology were made

according to Saltikov's procedure (*121*): logarithms of the diameters were taken, then sorted into

bins (size classes) of 0.1 log (µm), from -1.2 (0.06 µm) to 0.8 (6.3 µm). The number of particles

within each bin was then corrected to account for stereology according to the following

expression:

$$N_{Vi} = \alpha_1 N_{Ai} - \sum_{j-1}^{i-1} \alpha_{j+1} N_{A(i-j)}$$

where N_{vi} is the number of particles in the *i*th bin corrected for stereology, N_{Ai} is the number of

particles in the *i*th bin before correction, and α_i are constants. Errors due to the assumption of

perfectly spherical particles should not be significant since the aspect ratios of the particles were

not large (*122*).
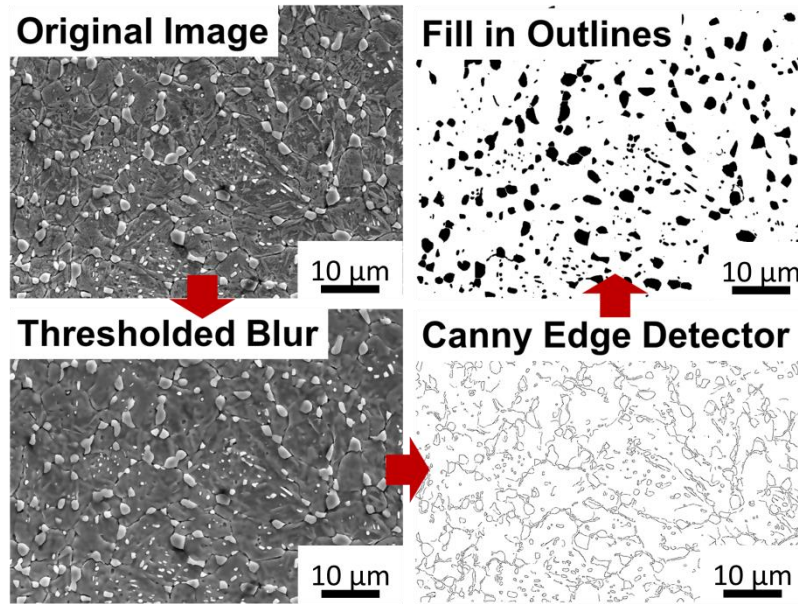
Figure 4.1 Steps in the particle analysis methodology using ImageJ to quantify carbide particle sizes. First a thresholded blur filter was applied to the original digital SEM micrograph to smooth contrast outside the particles. Next, application of a Canny edge detection algorithm identified particle edges. Finally, particle outlines were filled in and a 2 pixel width median filter was applied to remove non-particle edges.

4.4 Results

The initial (as-cast) microstructure consisted of a network of cementite surrounded by a matrix of pearlite as shown by the SEM micrograph in **Figure 4.2.** Upon heating, the pearlite matrix spheroidized into discrete particles that coarsened over time at rates dependent on temperature. Particles were uniformly distributed in the matrix, with the exception of denuded zones free of particles adjacent to the cementite network. These zones were found to grow in size with greater annealing time.
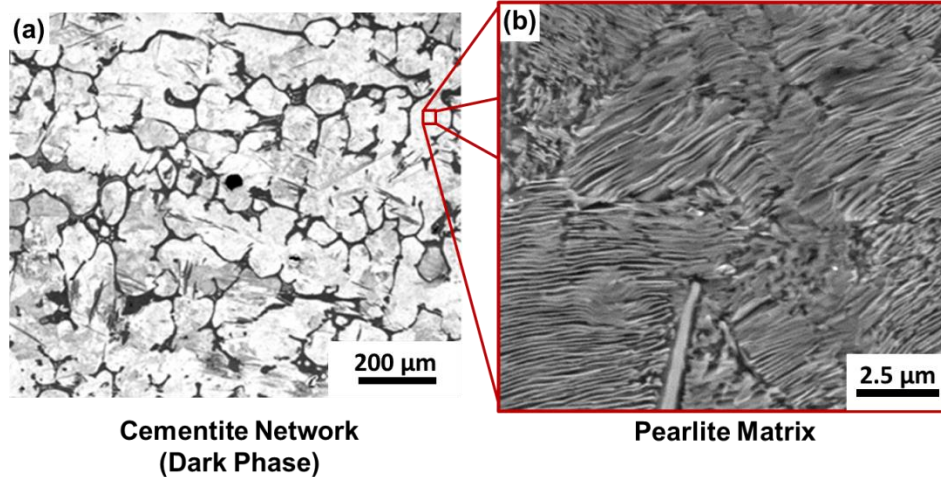
Figure 4.2 SEM micrographs of the initial UHCS microstructure showing (a) a cementite network on prior austenite grain boundaries surrounded by (b) a pearlite matrix.

4.4.1 Denuded zone widths next to cementite network

Denuded zone widths next to network branches were measured for various times and temperatures. **Figure 4.3 (a)** shows an example of a branch of the cementite network with a denuded zone, and **Figure 4.3 (b)** shows the method used to quantify zone widths (boundaries of the denuded zones were traces, then lines were drawn perpendicular to the network branches). For each time and temperature combination, zone widths next to five different branches in different areas of the network were measured. Average network branch widths and area fractions remained about the same over time, indicating that the denuded zones were not caused by network dissolution. **Figure 4.4** shows the time evolution of denuded zone widths, which demonstrated an apparent power law relation with time: $d^n = kt$.

The values of n for denuded zone growth are summarized in **Table 4.3**. n values appeared to be around 4 or 5 for 970°C or 900°C. An n value in the range of 4-5 was found at 800°C for times up to 24 hours (800°C (a) entry in **Table 4.3**), but inclusion of data from a measurement at 85 hours at 800°C changed n to around 9 for that temperature (800°C (b) entry in **Table 4.3**; $n=5$ was still within the range of error).
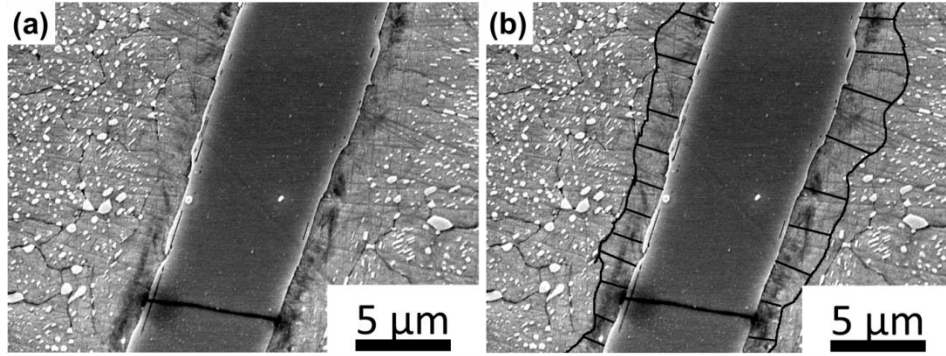
Figure 4.3 SEM micrograph of (a) a branch of the cementite network on an original austenite grain boundary, which was (b) analyzed to find the average width of the denuded zone around it.
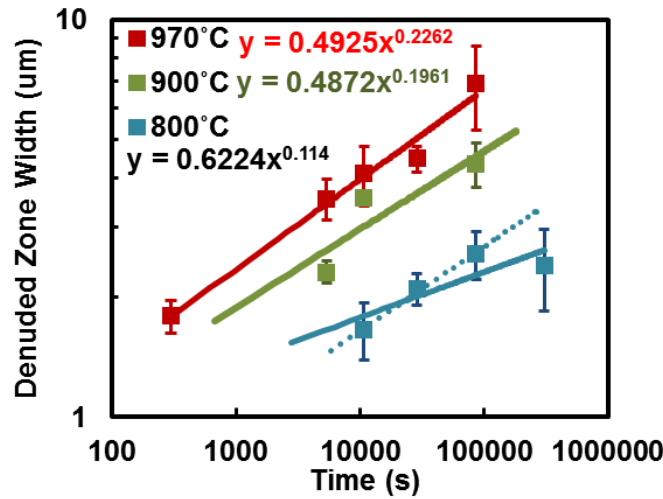
Figure 4.4 Denuded zone widths versus time for heat treatments at three temperatures. The dotted trend line for the 800˚C data (entry 800 (a) in **Table 4.3**) neglects the data point at 85 hours which might be affected by decarburization. The line includes the 85 hour data point (Entry 800 (b) in **Table 4.3**).

Table 4.3 *n*-values for growth of denuded zones.

Temperature	*n*
970˚C	4.4±0.4
900˚C	5±3
800˚C (a)	4.7±0.4
800˚C (b)	9±4

4.4.2 Particle size distributions

Representative SEM micrographs of the UHCS microstructures resulting from each hold time and annealing temperature combination are shown in **Figure 4.5**.
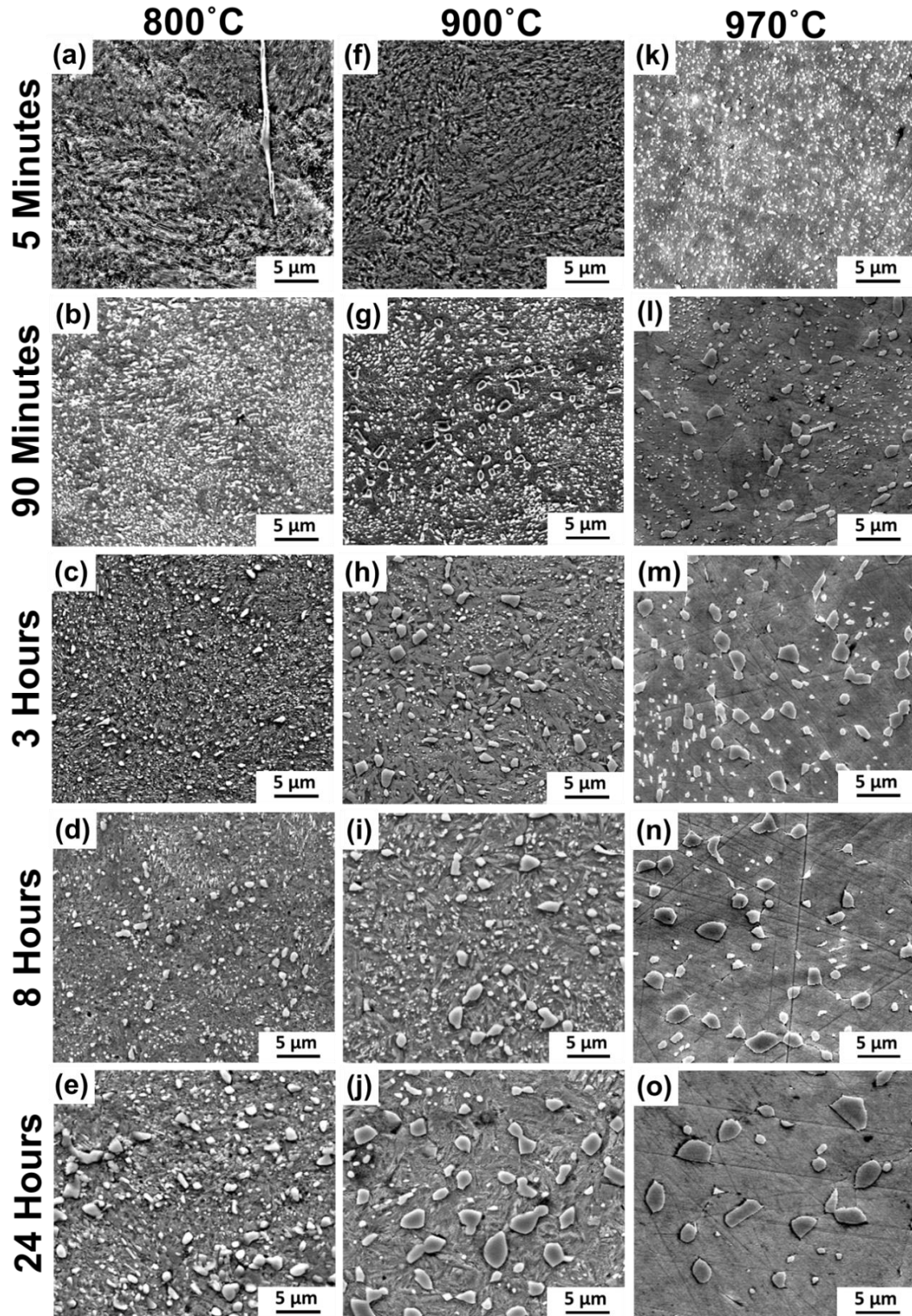
Figure 4.5 SEM micrographs of UHCS microstructures of (a-o) each time and temperature combination ranging from 800-970°C and 5 minutes to 24 hours.

The micrographs in **Figure 4.5** show the spheroidized microstructures well away from the proeutectoid cementite network and associated denuded zones discussed in the previous section. It was apparent that cementite particle sizes increased with temperature and hold time. There also appeared to be a bimodal particle size distribution at moderate annealing times, most readily apparent in **Figure 4.5 (h)** and **(l)**. Pearlite spheroidization was fully completed within 5 minutes at 970˚C as shown in **Figure 4.5 (k),** and within 90 minutes at 800˚C and 900˚C as shown in **Figure 4.5 (b)** and **(g)**. Particles grew larger over time at each hold temperature.

Digital micrographs of the UHCS microstructures shown in **Figure 4.5** were quantitatively analyzed to find particle sizes using the methodology outlined in **Figure 4.1**. Plots of particle size distributions corrected for stereology are shown in **Figure 4.6**. Particle size distributions were log-normal in all cases, as is common for particle analysis (*123*, *124*). Gaussian peak profiles were fit to the data by manually adjusting peak amplitude, width, and position to match the data as closely as possible. Nearly all of the measured distributions required at least two separate Gaussian profiles to fit the data. This was consistent with the distribution of particles observed in, e.g. **Figure 4.5 (m)**. A vertical dashed line denotes the peak position of each component distribution on the plots. The vertical line in **Figure 4.6 (a)** is at the position of the mean of the particle size data since a Gaussian peak could not be fitted for the 5 minute at 800°C data.
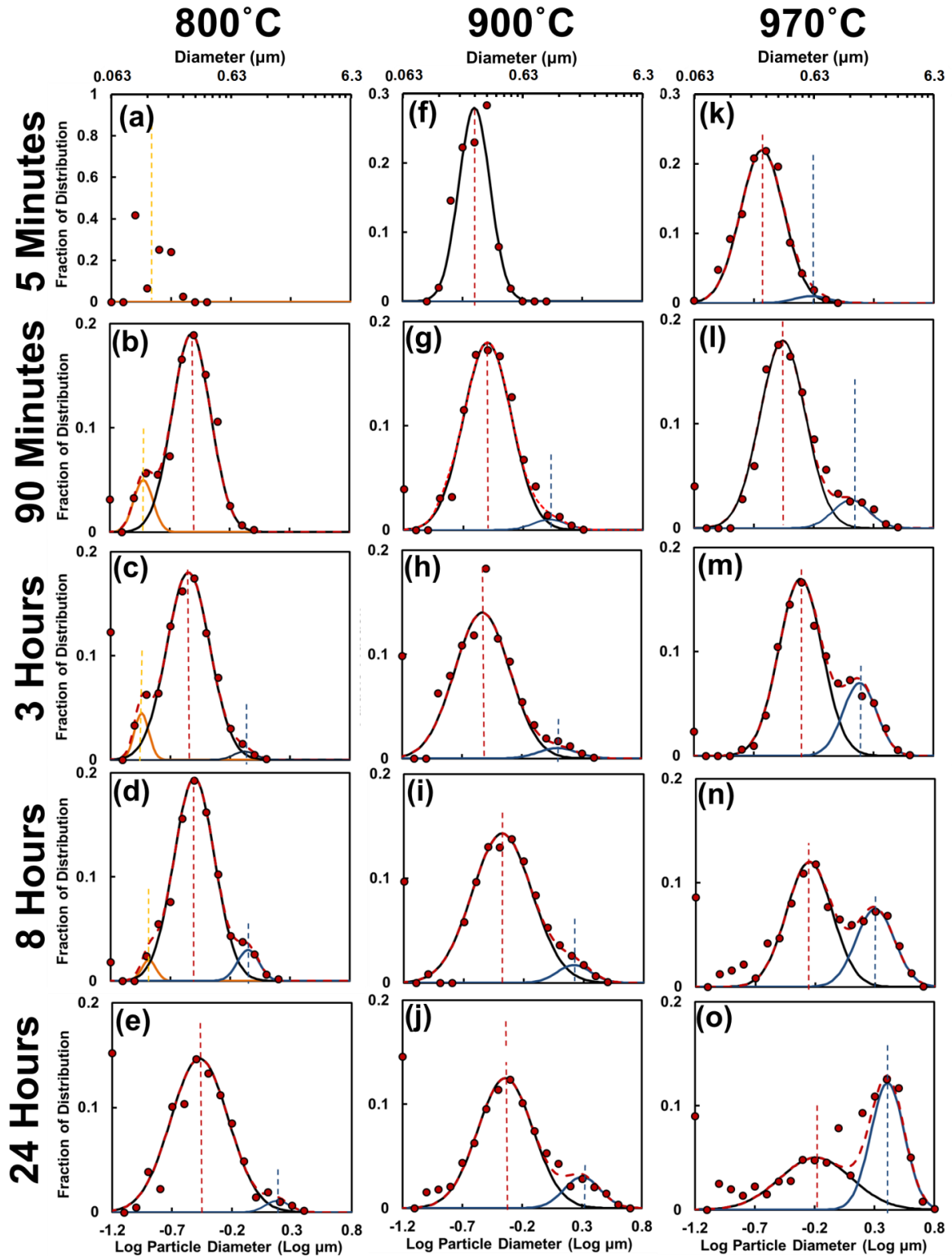
Figure 4.6 Log particle size distributions of each (a-o) time and temperature combination ranging from 800-970°C and 5 minutes to 24 hours. Multiple peaks within the distributions were fitted with Gaussian profiles. The dashed vertical lines in the figures denote the positions of the Gaussian profiles.

The feature common to every plot except for 5 minutes at 800˚C was a central distribution with its peak located around -0.5 log (µm), or about 0.3 µm. The position of that peak shifted to the right (larger particle sizes) over time at 900˚C and 970˚C, but stayed fixed with time at 800˚C. Two other peaks appeared in some of the samples: one to the left of the central distribution at about -0.9 log (µm), or 0.13 µm, that was fixed in time and one to the right of the central distribution that shifted further to the right (larger particle sizes) with longer annealing time. The left peak was only observed in samples annealed at 800°C, **Figure 4.6 (a-d)**.

4.4.3 Identifying component distributions

The central distribution was produced directly by the spheroidization of pearlite inside the austenite grains. The only plot in which this peak did not appear was **Figure 4.6 (a)**. The absence of a central peak in the **Figure 4.6 (a)** plot indicated that spheroidization had not progressed to the point where particles were distinguishable among the spheroidizing pearlite lamellae. Central peak particles will be termed intragranular particles (IG) for the remainder of this chapter.

The left distribution consisted of the smallest particles, and only appeared at the lowest temperature studied. The left distribution was present in **Figure 4.6 (a)** even though pearlite spheroidization had not completed, so the distribution apparently corresponded to particles that were already present in the initial microstructure prior to the heat treatment. For instance, **Figure 4.7** showed that some regions of the initial as-cast pearlite microstructure contained particles. Left peak particles will be termed leftover particles (LP) for the remainder of this chapter.

`
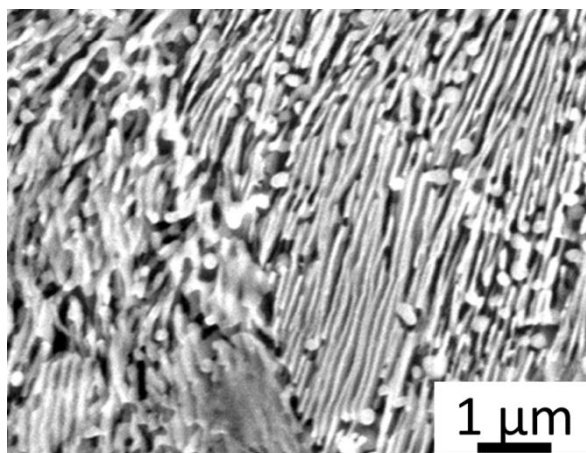
Figure 4.7 SEM micrograph of as-cast UHCS showing a region of pearlite containing particles, termed as leftover particles (LP).

There were two possible explanations for the presence of the LP particles. First, they could have been spheroidized eutectoid cementite that formed via the divorced eutectoid transformation along with pearlite (*19*) during cooling of the steel after casting. The particles may also have been $(Fe,Cr)_{23}C_6$, which Thermo-Calc predicted was thermodynamically stable below the eutectoid temperature in equilibrium with cementite and ferrite. The gradual disappearance of the LP could be due to dissolution of the unstable $M_{23}C_6$ or divorced eutectoid cementite phase slowly dissolving at 800˚C. The absence of LP at 900 and 970˚C was likely due to faster dissolution kinetics at those higher temperatures.

The right distribution was attributed to intergranular particles coarsening on austenite grain boundaries. **Figure 4.8(a)** shows a micrograph of UHCS heat-treated for 8 hours at 970˚C. The shapes of the cementite particles as well as some prior austenite grain boundaries revealed by the Nital etch enabled manual interpolation of the austenite grain boundary network shown in **Figure 4.8 (b)**. The size distribution of all particles in seven such micrographs is shown in **Figure 4.8 (c)**, while the size distribution of the particles only at the grain boundaries in seven micrographs is shown in **Figure 4.8 (d).** While the positions of the peaks did not change from **Figure 4.8 (c)** to **(d)**, the relative heights of the peaks changed significantly so as to nearly

`

eliminate the central peak in the distribution. This indicated that particles on the grain boundaries contributed far more to the right distribution. The particles that comprise this right distribution will be termed grain boundary (GB) particles for the remainder of this article.
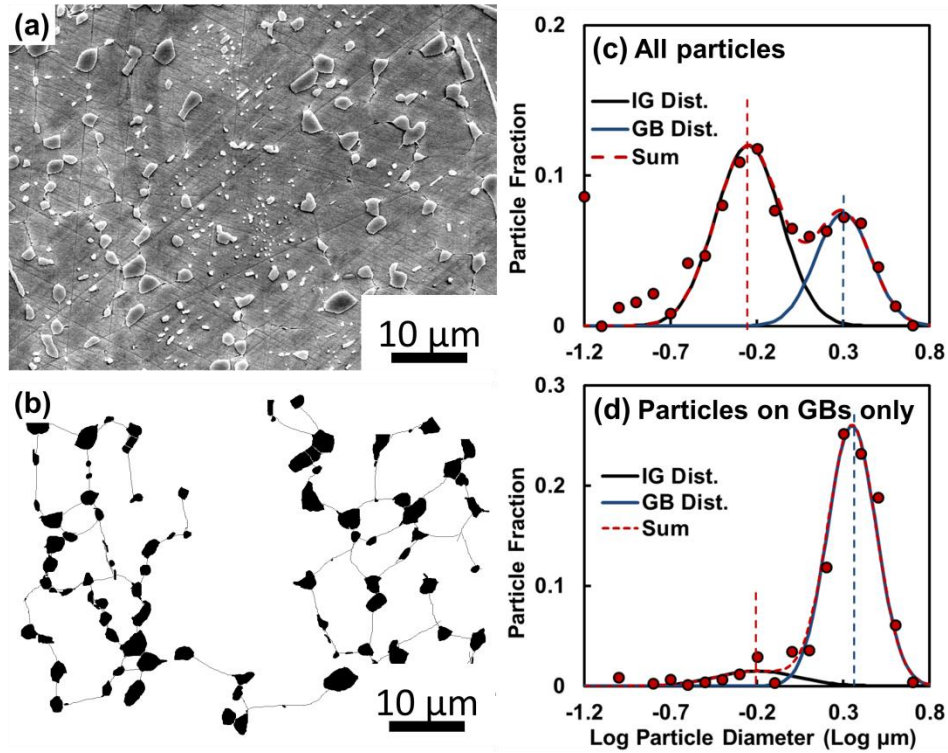
Figure 4.8 Grain boundaries in (a) a micrograph of UHCS heat-treated for 8 hours at 970˚C were (b) traced to isolate particles on grain boundaries. Particle size distributions are shown for (c) all particles and (d) only particles at the identified grain boundaries.

In some cases, grain boundary particles were present without showing an obvious second peak in the particle size distribution. **Figure 4.9 (a)** shows a micrograph of a sample held at 970˚C for 5 minutes. Only particles intersecting prior austenite grain boundaries were retained in **Figure 4.9 (b).** Before grain boundaries were traced, only a central peak was identified in the full particle size distribution in five such images as indicated in **Figure 4.9 (c).** When the distribution was modified to include only particles intersecting the grain boundaries, the result was a distribution shifted to larger sizes as shown in **Figure 4.9 (d)**. It was not always possible to trace

`

grain boundaries in every image, so some of the distributions with only a central peak potentially also contained an overlapped right peak.
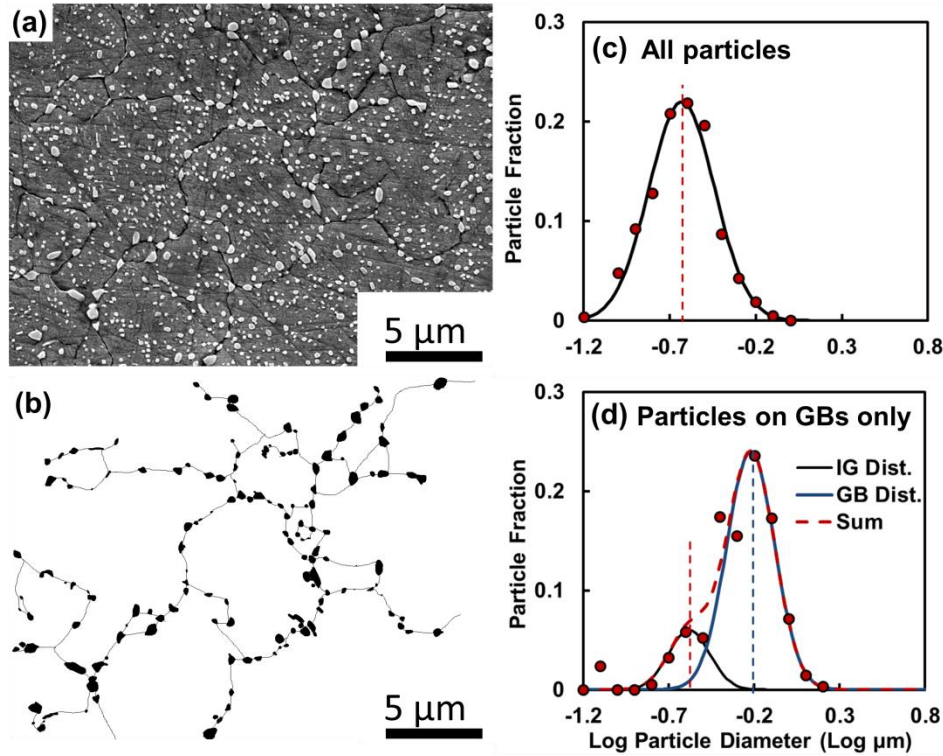
Figure 4.9 Grain boundaries in (a) a micrograph of UHCS heat-treated for 5 minutes at 970°C were (b) traced to isolate particles on grain boundaries. Particle size distributions are shown for (c) all particles and (d) only particles at the identified grain boundaries.

4.5 Discussion

Annealing UHCS specimens above the austenitizing temperature caused a process of pearlite spheroidization into small size cementite particles followed by growth over time. The growth of the cementite particles over time showed evidence of coarsening at two different rates, resulting in a bimodal distribution of particles. These particles could be distinguished by their position relative to the prior austentite grain boundaries. As such, the dominant particle type by size transferred from intragranular (IG) particles within grains to intergranular (GB) particles on grain boundaries. Concurrent to this observed particle coarsening behavior, cementite particles in the vicinity (< 10 μm) of the proeutectoird cementite network dissolved to produce a

`

"denuded" zone. This denuded zone extended further from the network boundary with longer annealing time. All of these observed carbide particle coarsening and dissolution processes exhibited a power law relationship. The associated kinetics of these processes are further discussed in the context of LSW theory. The phase diagram for the UHCS composition used in this study is shown in **Figure 4.10** for reference in the following discussion.
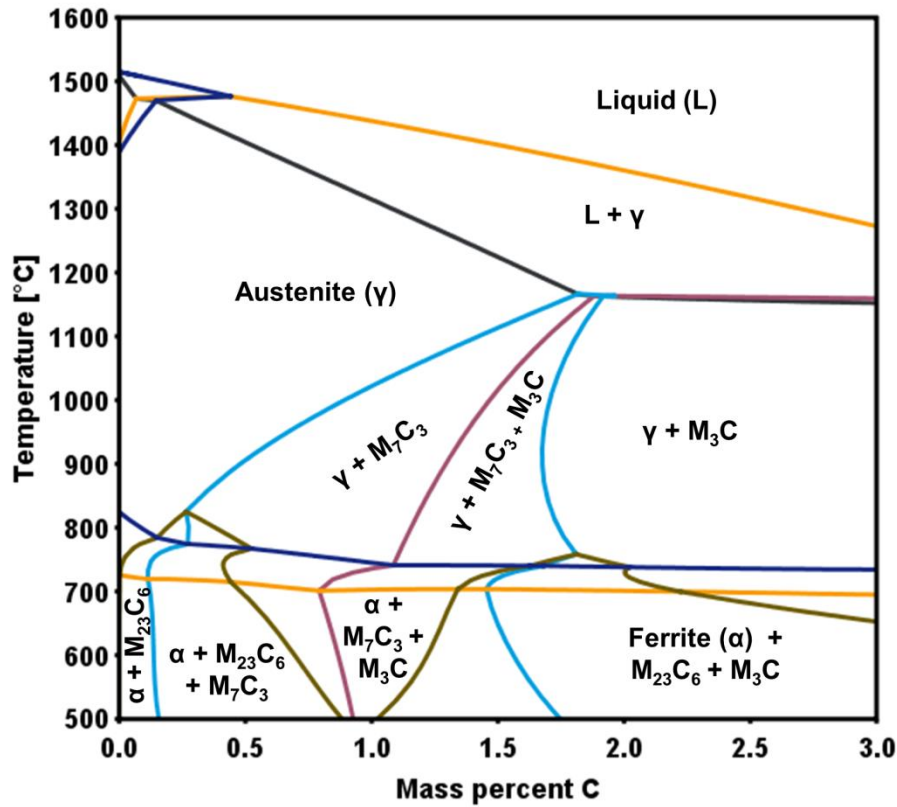
Figure 4.10 Pseudo-binary phase diagram for the UHCS composition used in this study (from Thermo-Calc).

4.5.1 Coarsening and denuded zone growth kinetics

As noted in section 4.4.1, denuded zones free of carbide particles formed adjacent to branches of the proeutectoid cementite network proportional to $t^{1/4}$-$t^{1/5}$. In the literature, precipitate free zones (PFZ) next to normal grain boundaries grew at rates proportional to $t^{1/2}$ (*125*, *126*). The growth of the denuded zones in this study was consistent with the particle

`

coarsening kinetics. In UHCS, the branches of the proeutectoid cementite network may be viewed as very large particles with essentially zero curvature compared to cementite particles formed during the heat treatment. Therefore, a curvature driven concentration gradient from cementite particles towards the network cementite existed throughout the entire coarsening process. I attribute the growth of the denuded zones to the dissolution of small particles in the network vicinity due to this gradient.

Diffusion length and denuded zone widths

Table 4.4 shows the chemical diffusion coefficients of C, Cr, and the tracer diffusion coefficient of Fe calculated in Thermo-Calc. **Table 4.4** also shows the constants used to calculate D_{eff} , which was described in **section 4.2.2**. **Figure 4.11** shows the denuded zone widths compared to volumetric diffusion lengths for C, Cr, Fe, and the calculated effective diffusing species. Diffusion lengths were calculated by taking the square root of the diffusion coefficient multiplied by time. The measured denuded zone widths were closest to the effective diffusion length at shorter times and lower temperatures, but eventually approached the diffusion length of Cr after long times at 970˚C. This result indicates that the contributions of C diffusion to denuded zone growth (and by extension, to particle coarsening) became less important compared to Cr and Fe diffusion at longer times and higher temperatures. Since the diffusion coefficients were calculated for volumetric diffusion, the diffusion lengths might not be accurate if other diffusion mechanisms, such as GB or dislocation-mediated diffusion, were involved in denuded zone growth. However, the above discussion should be valid as long as non-volumetric diffusivities were within an order of magnitude of volumetric diffusivities. The Cr content within the denuded zones themselves was the same as that of the matrix away from the zones, as demonstrated in **Section A.3** of Appendix A.
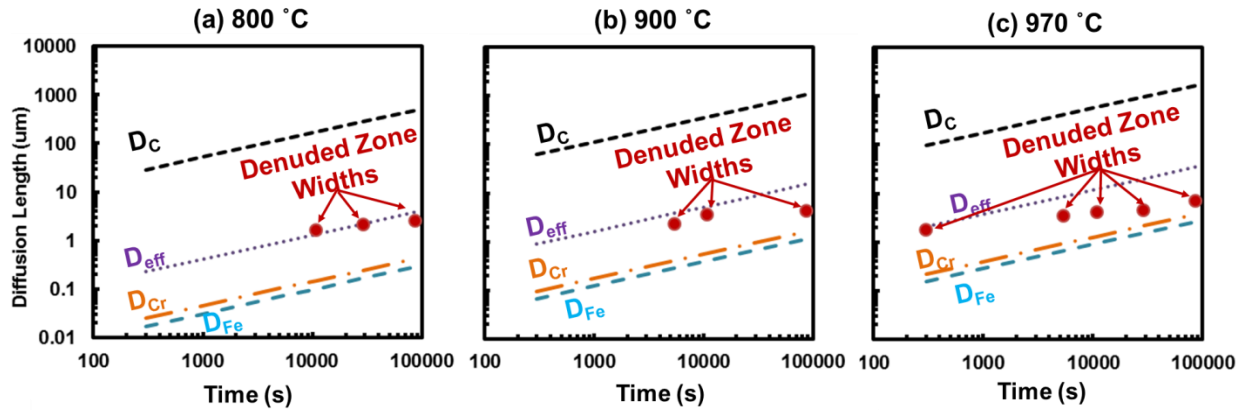
Figure 4.11 Denuded Zone widths plotted as a function of time at (a) 800˚C, (b) 900˚C, and (c) 970˚C. Denuded zone widths are compared with calculated diffusion lengths based on the diffusion coefficients of carbon (D_C), iron (D_{Fe}) chromium (D_{Cr}), and a calculated effective coefficient of iron and carbon (D_{eff}).

Table 4.4 Volumetric diffusion coefficients of C, Cr, and Fe, as well as constants needed to calculate D_{eff}. D_C, D_{Cr}, and D_{Fe} were calculated in Thermo-Calc.

Constants		Coefficient	800˚C	900˚C	970˚C
V_{Fe} (cm^3/atom)	$1.2 \cdot 10^{-23}$	D_C (cm^2/s)	$2.8 \cdot 10^{-8}$	$2.3 \cdot 10^{-7}$	$3.2 \cdot 10^{-7}$
C_{Fe} (atoms/cm^3)	$8.1 \cdot 10^{22}$	D_{Cr} (cm^2/s)	$2.1 \cdot 10^{-14}$	$3.1 \cdot 10^{-13}$	$1.6 \cdot 10^{-12}$
Vc (cm^3/atom)	$3.7 \cdot 10^{-24}$	D_{Fe} (cm^2/s)	$9.5 \cdot 10^{-15}$	$1.5 \cdot 10^{-13}$	$7.9 \cdot 10^{-13}$
C_C (atoms/cm^3)	$4.7 \cdot 10^{21}$	D_{eff} (cm^2/s)	$1.4 \cdot 10^{-10}$	$2.7 \cdot 10^{-11}$	$1.7 \cdot 10^{-12}$

4.5.2 Average particle size versus time

The average particle diameter far away from the denuded zones appeared to follow a power-law relationship with time as shown in **Figure 4.12**. The trend lines for 970˚C and 900˚C passed through a common point at around 0.2μm after 300s of heat treatment. If the data point for 300s at 800˚C, which did not contain an IG distribution, was ignored (dotted line in **Figure 4.12**), the power law trend line for the 800s data also passed near 0.2 μm at that time.

As shown previously, there were multiple types of particles present in the steel samples (GB, IG, and LP). Thus, power law fits reflected apparent n values (n_{app}) relating to the fractions of each type of particle at a given time, rather than true n values relating to diffusion kinetics. Apparent n values (summarized in **Table 4.5**) from the power law trend lines in **Figure 4.12**

were 3.0±0.3 at 970˚C, 5.6±0.8 at 900˚C, and 10±2 at 800˚C. n_{app} values did not actually indicate

coarsening mechanisms because they did not account for the effects of the multimodal particle

size distribution. The next sections assess the growth kinetics for each particle type individually.
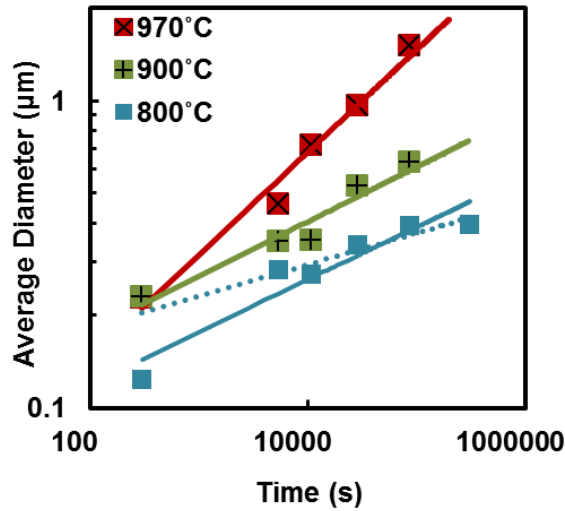
Figure 4.12 Average particle diameter versus time. The dotted blue line shows the trend of average particle size at 800˚C excluding the data point at 300s, which did not contain an IG peak.

4.5.3 Power law fits of multimodal distributions

The average values (peaks in the distributions) for the leftover (LP), intragranular (IG),

and grain boundary (GB) particle size distributions were separated and plotted individually on

log-log axes in **Figure 4.13**. Each point in **Figure 4.13** was the center of one of the peaks in

Figure 4.6. The power law fits to the data did not show any abrupt changes in slope. The

exponents of the power law fits are labeled "*m*" and shown next to the corresponding power law

fit trend lines. Apparent *n*=1/*m* values (summarized in **Table 4.5**) varied from 4 to 30. The

apparent *n* values were only truly indicative of a rate controlling diffusion mechanism if the

effect of $d_o{}^n$ was negligible for all data points. Extremely large values of *n* at 800˚C and for the

intragranular particle data at 900˚C indicated that this was not the case at least for those datasets.

Thus, *n* and *k* values from **Figure 4.13** were also labeled n_{app} and k_{app} in **Table 4.5**. The power

law fit to the data at 970°C, having the fastest coarsening kinetics, should be least affected by d_o and thus have n_{app} and k_{app} closest to the true values (presumably n~5 for intragranular particles and n~4 for grain boundary particles). These n values were both similar to the n=4-5 identified for denuded zone growth.
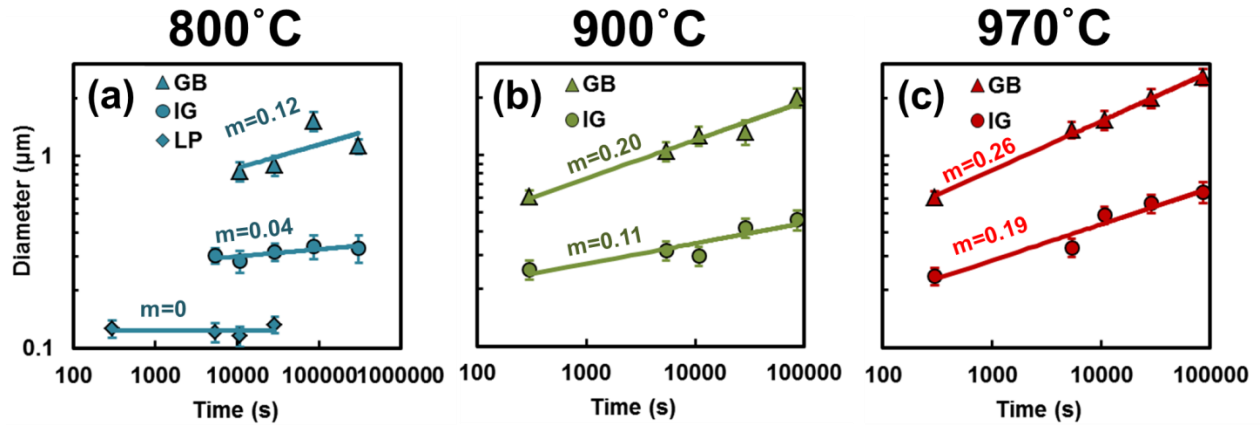
Figure 4.13 Power law relationship of GB, IG, and LP particle diameters versus time. m=exponent of the power law fit.

Table 4.5 Apparent n and k values from **Figure 4.12** and **Figure 4.13** (power law fits).

Temp	IG Particles k_{app} [$\mu m^n/s$]	n_{app}	GB Particles k_{app} [$\mu m^n/s$]	n_{app}	All Particles k_{app} [$\mu m^n/s$]	n_{app}
970°C	1.2 x 10⁻⁶	5.3±0.8	5.1 x 10⁻⁴	3.9±0.1	3.1 x 10⁻⁵	3.9±0.1
900°C	4.5 x 10⁻⁹	9±2	2.5 x 10⁻⁴	4.9±0.8	6.2 x 10⁻⁷	5.6±0.8
800°C	5.3 x 10⁻¹⁹	30±10	3.0 x 10⁻⁵	8±7	3.8 x 10⁻⁸	10±2

4.5.4 Accounting for initial particle diameter

In order to find true n and k values, the effects of initial particle size d_o on apparent rate of particle growth were addressed. d_o and t_o in the coarsening equation refer to the diameter and time at which steady state coarsening begins. Since there were no apparent changes of slope in any of the power law fits in **Figure 4.13**, d_o and t_o were set based on the earliest time each type of distribution could be distinguished. With d_o and t_o thus defined, the equation $d^n - d_o^n =$

$k_n(t - t_o)$ incorporated only two variables, n and k. For a prescribed n value (3, 4, or 5) it was possible to determine a corresponding k by finding the slope of the line defined by d^n-$d_o{}^n$ versus t-t_o.

Figure **4.14 (a)** shows the possible k values for the intragranular particles coarsening at 970˚C, determined by setting n equal to 3, 4 and 5. **Figure 4.14 (b)** shows different k values for the grain boundary particles coarsening at 970˚C determined by setting n equal to 3, 4 and 5. The coupled n and k values were also used to predict the mean particle size as a function of time, based on the equation:

$$d(t) = [k_n(t - t_0) + d_0^n]^{1/n}$$
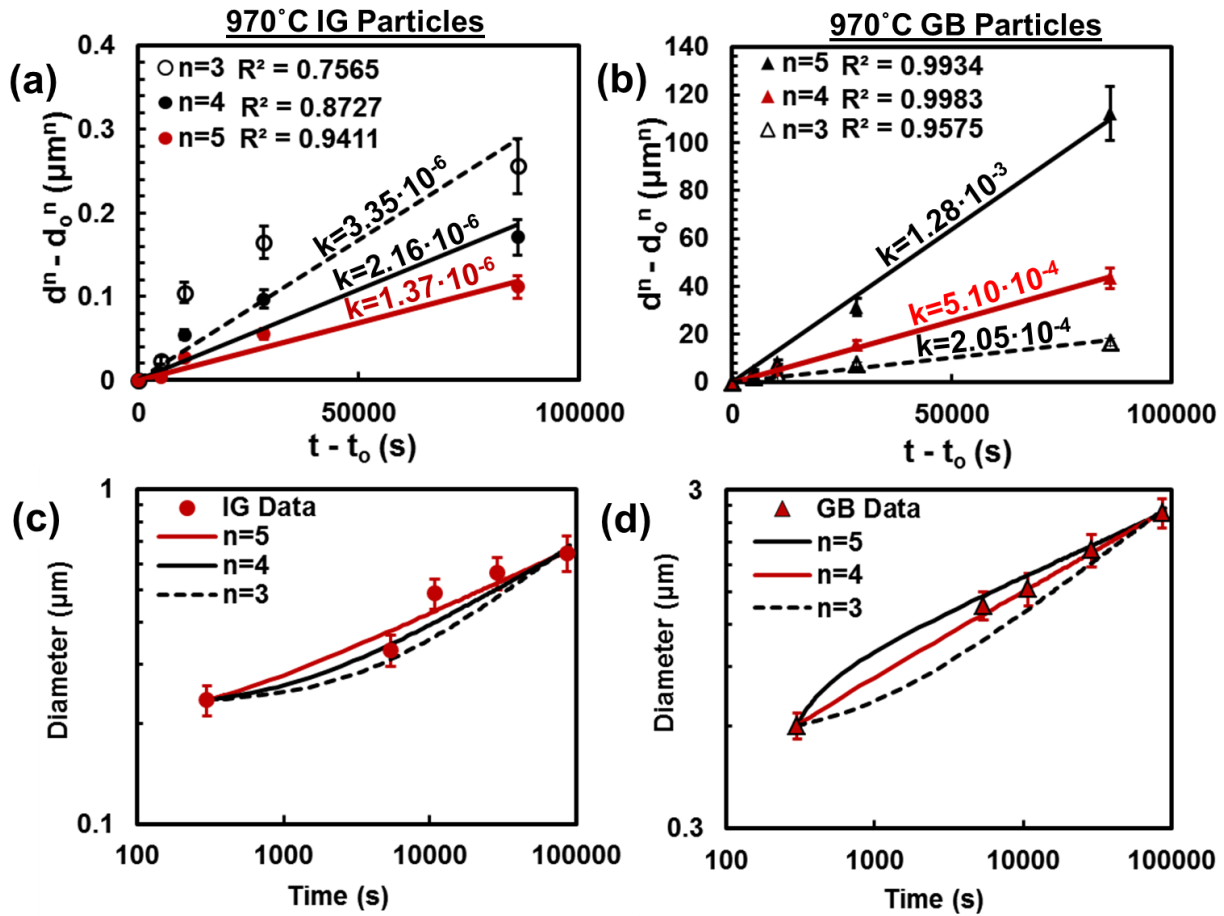
Figure 4.14 970˚C plots of particle diameter and time to calculate k for (a) IG particles and (b) GB particles. Subsequently, k values were used to construct plots of theoretical d versus t for (c) IG and (d) GB particles.

The $d(t)$ values calculated in this manner were compared to the experimental datasets in log-log plots in **Figure 4.14 (c)** and **(d)**. Comparison of the values in **Figure 4.14** showed that $n=5$ provided the best fit to the measured data for IG particles, and $n=4$ provided the best fit for GB particles (the red lines in **Figure 4.14 (c)** and **(d)**. Volume diffusion appeared to be inhibited as a transport mechanism for coarsening inside the grains and on the grain boundaries, as $n=3$ did not provide as good a fit to the data in both IG and GB cases.

Figure 4.15 (a) and **(b)** show the possible k values for the IG and GB particles coarsening at $900°C$ determined by setting n equal to 3, 4 and 5. The difference between the theoretical intragranular $d(t)$ lines calculated from each n and k combinations was smaller than at $970°C$, and the relative effect of the scatter in the IG data was higher because the IG particle sizes were closer together. Nevertheless, $n=5$ still appeared to be the best fit to the data. In **Figure 4.15 (d)**, no GB data point could be determined at 300s, so d_o and t_o were set at 5400s instead. If GB particles existed in the samples at $900°C$ after 300s, they should certainly not be bigger than the size of the $970°C$ GB particles at the same size. This size is indicated by an arrow **Figure 4.15 (d).** Note that the line which intersects the red point is closest to $n=4$. Thus an n value close to 4 is most likely for the GB particle coarsening at $900°C$.
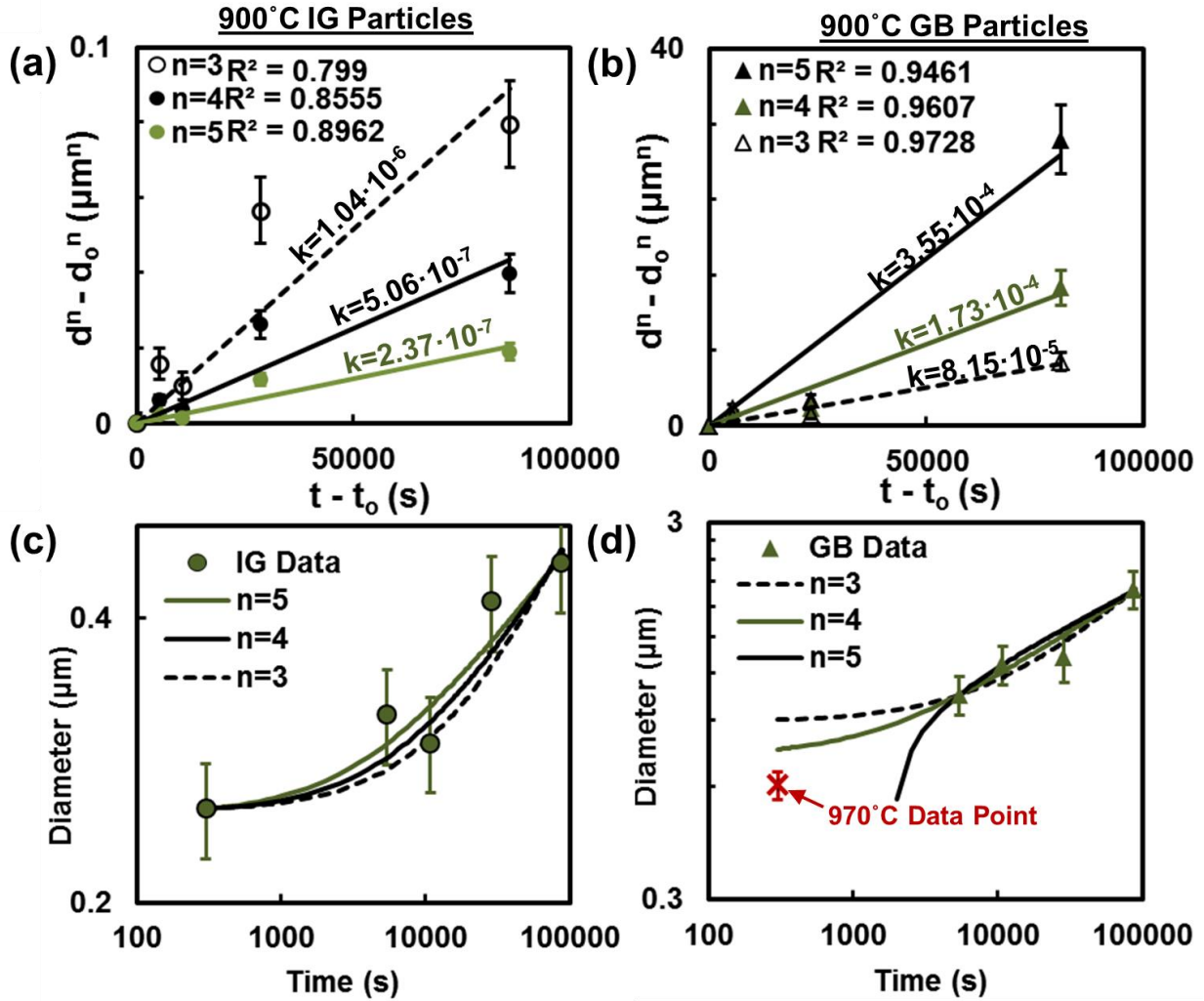
Figure 4.15 900˚C plots of particle diameter and time to calculate k for (a) particles in the central peak (intragranular particles/IG) and (b) particles in the right peak (intergranular particles/GB). k values were used to construct plots of theoretical d versus t for (c) IG and (d) GB particles.

Figure 4.16 (a) and **(b)** show the possible k values for the IG and GB particles coarsening at 800˚C determined by setting n equal to 3, 4 and 5. The relative amount of scatter in the data in this case was high. The IG and GB k values were so small that there was very little difference in the $d(t)$ predictions based on the different n values. For this reason, **Figure 4.16 (c)** and **(d)** show only one $d(t)$ line for $n=3,4,5$. Since all mechanisms ($n=3,4,5$) were compatible with the data, it was impossible to determine the most likely coarsening mechanism at 800˚C for both IG and GB particles. Though compatible with low k coarsening mechanisms, IG coarsening

`

was still negligible at 800˚C over the time scale studied. GB coarsening on the other hand was non-negligible. Since the GB particles at higher temperatures (900˚C and 970˚C) coarsened by a grain boundary mechanism ($n=4$), we anticipate that the same mechanism was in operation at 800˚C.
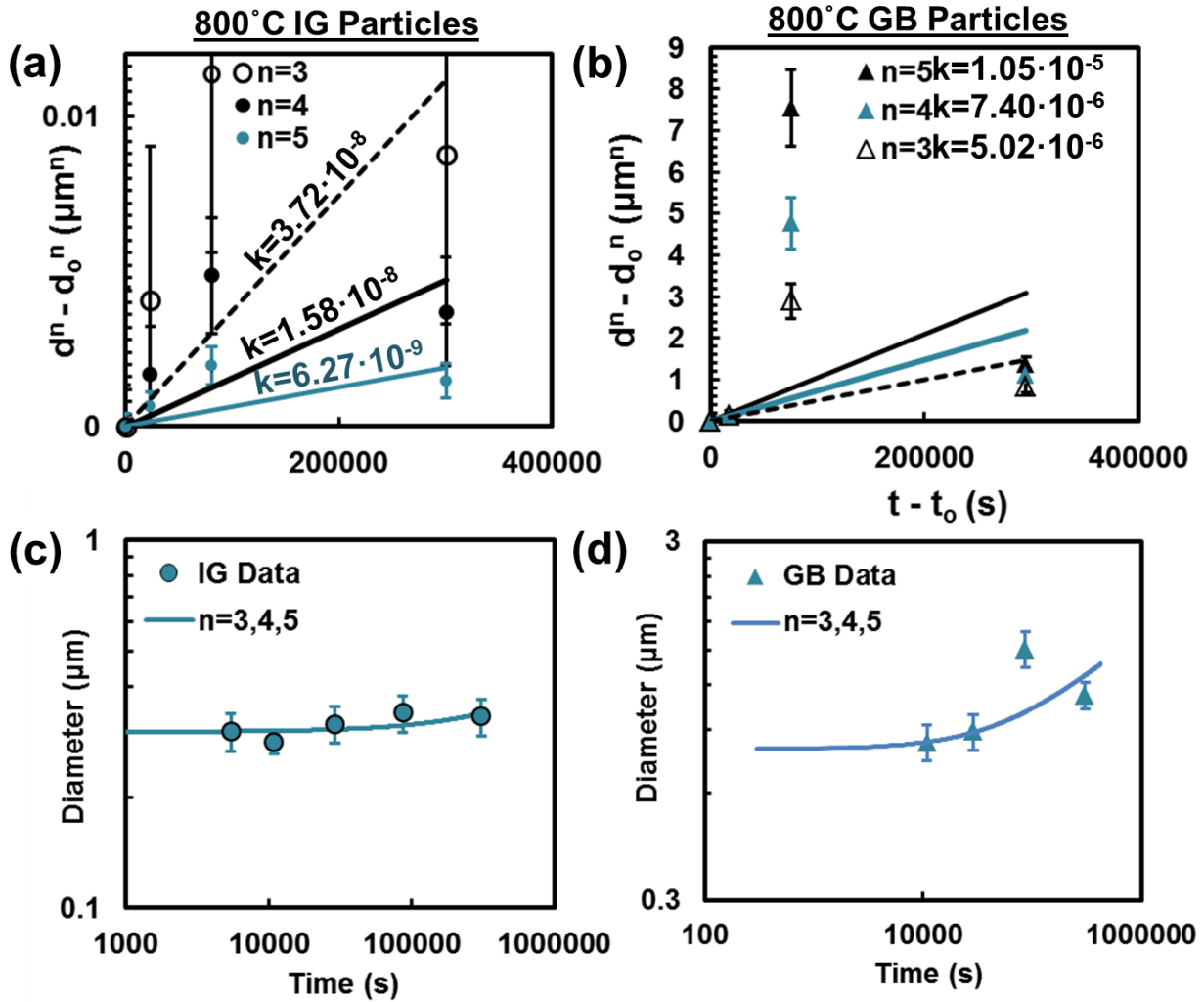
Figure 4.16 800˚C plots of particle diameter and time to calculate k for (a) particles in the central peak (intragranular particles/IG) and (b) particles in the right peak (intergranular particles/GB). k values were used to construct plots of theoretical d versus t for (c) IG and (d) GB particles.

In summary, coarsening kinetics were analyzed assuming that intragranular particles and intergranular particles coarsened independently. The values of coarsening exponent and rate constants are summarized in **Table 4.6**. The data at all temperatures was consistent with $n=4$ for

GB particle coarsening, and $n=5$ for IG particle coarsening, both of which are similar to the $n=4$-5 observed in denuded zone growth adjacent to the cementite network. The values of the coarsening exponents at 800˚C have asterisks because any n of 3-5 was consistent with the data, and n values for IG and GB coarsening at that temperature were chosen assuming that the coarsening mechanism did not change over the temperature range studied. The n and k values at 970˚C in **Table 4.6** are very similar to the n_{app} and k_{app} values at 970˚C from **Table 4.5** derived directly from log d versus log t plots, while values from the other temperatures differ significantly. Again, this is because d_o became negligible quickly at 970˚C compared to the other temperatures. The coarsening exponent values for both IG and GB particles were consistent with the $n=4$-5, which controlled denuded zone growth rate. Denuded zone growth should have involved both mechanisms, as both IG and GB particles near the proeutectoid cementite network would have to dissolve to form the denuded zones.

Table 4.6 n and k values from **Figure 4.14**, **Figure 4.15**, and **Figure 4.16**.

	IG Particles		GB Particles	
Temp	$k\ [\mu m^{-5}s]^{-1}$	n	$k\ [\mu m^{4}\cdot s]^{-1}$	n
970˚C	1.4×10^{-6}	5	5.1×10^{-4}	4
900 ˚C	2.4×10^{-7}	5	1.7×10^{-4}	4
800 ˚C	*6.2×10^{-9}*	5*	*7.4×10^{-6}*	4*

*The data was consistent with any $n=3$-5 for coarsening at 800˚C. n values were assumed to stay consistent with the other n values in the range of temperatures studied.

The coarsening exponent values of 4 and 5 found in this study were within the range seen in the literature, which reported n values from 3 to 5 at lower temperatures, lower carbon content, and lower chromium content. Lu *et al.* (*112*) reported n values between 2 and 6 (including 5), but did not account for the possibility of multimodal particle distributions or possible effects of d_o on the slopes of their log-log plots. In the literature, $n=3$ was always

`

associated with coarsening of intragranular particles controlled by bulk diffusion and $n=4$ was always associated with coarsening controlled by grain boundary diffusion. Nam and Bae (*110*) observed directly, and Day (*113*) observed indirectly, that in simultaneous coarsening of IG and GB particles, IG particles coarsened with $n=3$ and GB coarsened with $n=4$. Excluding the study of Lu *et al*, $n=5$ was only observed in one study by Lindsley and Marder (*108*), who theorized that it was associated with particles coarsening primarily on grain boundaries by a combined grain boundary and dislocation diffusion mechanism.

That n did not equal 3 for IG particles in this study was unexpected, especially since the temperatures investigated were higher than the literature temperatures. The reduced diffusivity of carbon in austenite relative to ferrite may have contributed to the suppression of bulk diffusion. The higher chromium content compared to the steels in the other literature studies might also have been a factor leading to sluggish bulk diffusion. The high Cr composition may have lowered the effective diffusion coefficient for particle coarsening sufficiently for bulk diffusion to become slower than dislocation or grain boundary diffusion. We were unable to reliably calculate diffusion coefficients in this study based on the measured k values to compare with the literature or Thermo-Calc calculations because of the high uncertainty in k values at 900°C and especially at 800°C.

4.5.5 Time dependent contributions of each coarsening mechanism to mean particle size

Figure 4.17 shows the fraction of GB and LP particles in this study plotted as a function of time. IG particle fractions are not shown because they can be found by subtracting GB and LP fractions from 1. Particle fractions were found by dividing the area under the corresponding peak by the sum of the areas under all peaks for a given time/temperature combination. Particle fractions exhibited a power law relation with time, consistent with Heckel's equations (*127*) and

102

`

observations (*128*) relating the number of particles per volume N to a power of the coarsening time. The decrease in LP particle fraction with time, $f_{LP}=64t^{-0.7}$ was due to LP particle dissolution as well as IG particle formation from pearlite spheroidization. The increase in GB particle fraction with time, $f_{GB}=kt^{0.4-0.5}$, was primarily due to IG particle dissolution.
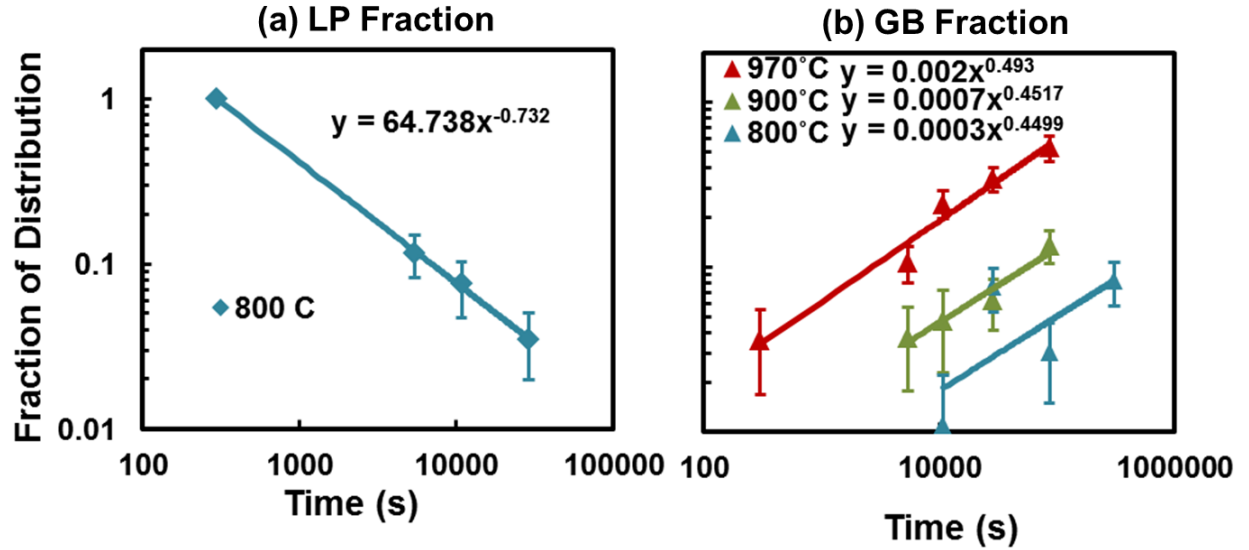
Figure 4.17 Time evolution of the fractions of particles which make up (a) preexisting particle (LP) peak at 800˚C, and (b) the grain boundary (GB) particle peaks at 800˚C, 900˚C, and 970˚C.

The contribution of each particle distribution to the mean particle size in the steel was determined using the fractions of the distributions made up of IG and GB particles. The contributions of each particle distribution A were determined as follows:

$$C_A(t) = f_A(t) \cdot [k_A(t - t_{0A}) + d_{0A}^n]^{1/n}.$$

For example, at 970˚C the two contributions would be:

GB contribution: $(0.002 \cdot t^{0.493}) \cdot [\, 5.1 \times 10^{-4} \cdot (t-300) + 0.60^4\,]^{1/4}$

IG contribution: $(1-0.002 \cdot t^{0.493}) \cdot [\, 1.4 \times 10^{-6} \cdot (t-300) + 0.23^5\,]^{1/5}$

Contributions from each particle distribution were calculated for 800, 900 and 970˚C. The sums of the contributions were then compared to the measured mean particle size data in

`

Figure 4.18. At 800˚C, IG particles were the main contributors to mean particle size except for short heating times when the LP particle contribution was important (less than ~5400s). At long heating times (greater than about 8 hours) the GB contribution to mean particle size had become noticeable. By extrapolation, GB particles should become the primary contributors to mean particle size after holding around 500 hours at 800˚C. At 900˚C, IG particles were the main contributors to mean particle for the entire time range that was studied. The influence of GB particles on the mean particle diameter became noticeable after around 3 hours of heat treatment. GB particles should become the primary contributors to mean particle size after around 58 hours of heating at 900˚C. At 970˚C, the contribution of GB particles to mean particle size was noticeable after only 90 minutes. GB particles became the primary contributors to mean particle size after about 3 hours of heat treatment at 970˚C.
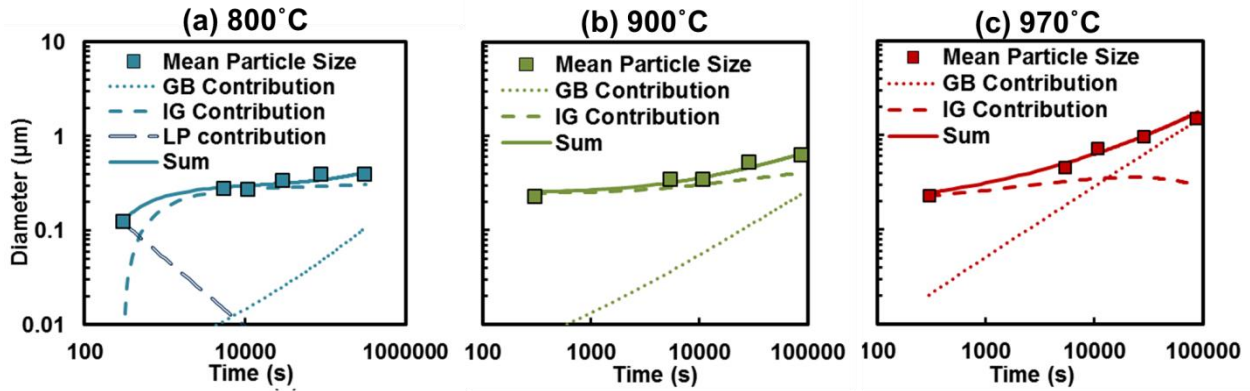
Figure 4.18 Contributions from IG, GB, and LP particle distributions at (a) 800˚C, (b) 900˚C and (c) 970˚C were summed to find a theoretical mean particle size as a function of time, which was compared to the measured mean particle sizes.

The results of this study show how elevated temperature annealing could be used as a tool to modify room temperature UHCS microstructures. Longer heat treatments and higher temperatures increased the particle fraction and mean size of large GB particles as well as the size of the denuded zones next to the cementite network. Both effects would promote pearlite

`

formation after the heat treatment by increasing the particle spacing and making the divorced eutectoid transformation less likely. Shorter heat treatment times at lower temperatures would have the opposite effect and promote a finer particle distribution with less pearlite.

4.6 Conclusions

An initially pearlitic UHCS containing a cementite network was heat-treated at 800°C, 900°C, and 970°C for times of 5 minutes to 24 hours. The pearlite quickly spheroidized into carbide particles, which then coarsened over time. A denuded zone devoid of particles developed adjacent to branches of the preexisting proteutectoid cementite network. Denuded zone width evolved with time described by the equation $d^{4-5}=kt$ (d in µm). The exponent for growth of the denuded zone was apparently related to the exponents controlling particle coarsening.

Away from the denuded zone, particle size distributions were clearly multimodal. Three component distributions were identified, corresponding to different types of particles: medium sized intragranular (IG) particles >0.2 µm produced by pearlite spheroidization inside austenite grains; larger grain boundary (GB) particles >0.6 µm; and very small leftover particles (LP) ~0.13 µm in size that formed in the cast UHCS prior to annealing. GB particle distributions were confirmed by tracing along prior austenite boundaries and retaining only the GB distribution. LP distributions were attributed to preexisting divorced pearlite or possibly to pre-existing $M_{23}C_6$.

Plotting the mean diameter of all particles within each sample versus time on log-scale axes resulted in apparent power law relations that were without meaning due to the multimodal distributions. When the individual IG and GB distributions were plotted on log-log axes, apparent n values were much larger than the true n values for the distributions at 900°C and 800°C due to the influence of the initial particle size d_o. 970°C n and k values were close to the true values because k was large enough that d_o became negligible very quickly. In order to

`

identify the true n and k values for the distributions, k was fixed for each n value by plotting d^n-d_o^n versus t-t_o for n values of 3,4, and 5. The resulting $d(t)$ lines for each n and k pair were compared to the data.

The most likely value of n for IG particles was 5 at all three temperatures studied, indicating coarsening comparatively slow as diffusion along dislocations. Chromium alloying in the steel may have significantly decreased the effective diffusion coefficient, retarding volumetric diffusion. IG particles at 800°C displayed negligible coarsening. The most likely value of n for GB particles was 4 at all temperatures studied, indicating coarsening controlled by diffusion along grain boundaries. Coarsening exponents of IG and GB particles were consistent with the n=4-5 range found in the power law rate of denuded zone growth.

The fraction of the distribution corresponding to the GB particles at all temperatures and LP particles at 800°C was determined to be power law functions of time. The GB fraction increased with time according to $f_{GB}=kt^{4.5-5}$. The LP fraction decreased with time according to $f_{LP}=64t^{-0.7}$. GB and LP fractions were used to calculate contributions of each type of particle to the overall mean particle sizes. It was determined that GB particles became the primary contributors to overall mean particles sizes at about 500 hours of heat treatment at 800°C (projected), 58 hours at 900°C, and 3 hours 970°C. Overall, carbide particle size quantification from digital micrographs in relation to existing microstructural features, like prior austenite grain boundaries and proeutectoid cementite network, allowed evaluation of multimodal carbide particle coarsening kinetics.

`

Chapter 5. Effects of Cr on Particle Coarsening and Denuded Zones in Ultrahigh Carbon Steel

5.1 Abstract

In this chapter the effects of Cr concentration on cementite coarsening kinetics in 2C-4Cr ultrahigh carbon steel (UHCS) are investigated. The focus is on comparing particle distributions in a low Cr (about 1 wt% Cr) UHCS to a higher Cr (about 4 wt% Cr) UHCS after a series of heat treatments at 800°C, 900°C, and 970°C for times up to 24 hours. Both UHCS contained a cementite network at austenite grain boundaries that formed during casting. The 4Cr UHCS contained a homogenous spatial distribution of particles away from the network branches, but a particle-denuded zone close to the network branches. The spatial distribution of particles found in the 1Cr UHCS was skewed towards clustering near network branches, with lower particle density away from the network branches. The differences in particle distributions may be related to differences in diffusion gradient steepness due to the different Cr contents.

5.2 Introduction

In chapter 4 of this dissertation, it was determined that cementite particles within the matrix of a 2C-4Cr UHCS coarsened with an exponent closest to 4 for GB particles and 5 for IG particles. It was noted that bulk diffusion was inhibited, and attributed this to the effects of Cr lowering the effective diffusion coefficient for cementite coarsening. This study investigates a steel of similar composition but with a much lower Cr content (2C-1Cr) using the same heat treatment conditions, in order to further investigate the effects of Cr on the kinetics of cementite particle coarsening.

`

Heat treatments of 10 hours in 2C-1Cr steel followed by slow cooling were previously studied by Krawczyk *et al.* (*22*). They noted many spheroidized cementite particles distributed homogenously in the matrix, as well as subgrain boundaries in the matrix outlined by cementite. The subgrains corresponded to boundaries of the original pearlite colonies in the as-cast UHCS. In the present study the effects of cooling rate were avoided by quenching samples, so as to study only the effects of the isothermal hold.

5.3 Materials and Methods

Sections of 36 inch diameter centrifugally cast UHCS mill rolls cut by band saw were provided for this study by Miller Centrifugal Casting (MCC). For this study, two different UHCS rolls were studied – one with a lower Cr content (2C-1Cr) and one with a higher Cr content (2C-4Cr). The compositions of the two rolls are shown in **Table 5.1**. Different samples about 1cm on each side were placed in a preheated box furnace at 800°C, 900°C, or 970°C for times of 5 min, 15 min, 90 min, 3 hours, 8 hours, or 24 hours, and subsequently water quenched.

Table 5.1 Compositions of the UHCS used in this study.

	Fe	Cr	C	Mn	Mo	Si	Ni
High Cr (2C-4Cr UHCS)	Bal.	3.86	2.02	0.68	0.33	0.65	1.45
Low Cr (2C-1Cr UHCS)	Bal.	0.92	1.89	0.67	0.31	0.77	1.30

Since the heat treatments were conducted in air, we ensured microstructural analysis avoided the decarburized region. The greatest potential depth of decarburization for these heat treatments was calculated at about 3 mm for 24 hours at 970°C (*119*). All samples were more than twice as large as this depth and the decarburized zone was avoided during microstructural characterization by cross-sectioning samples and imaging close to the center. Vickers hardness measurements were also used as to check for signs of decarburization. The most significant

`

decarburization would have occurred in the sample heat-treated at the highest temperature for the longest time. Thus, hardness across the cross-sectioned 2C-1Cr UHCS sample which had been heated at 970°C for 24 hours was measured. Hardness in a sample which had only been heated for 15 minutes at 970°C, in which little to no decarburization was expected, was also measured as a control. **Figure 5.1** shows hardness variations across the centerline of the two samples, from one edge to the other. For the sample heated for 24 hours at 970°C, where the most decarburization was expected, two different hardness regions were identified: a high hardness (650-800 HV) region within 1 mm of the sample edges, and a low hardness (500-550 HV) region away from the sample edges. In the sample heated for just 15 minutes at 970°C, hardness fluctuated randomly. The high hardness regions in the 24 hour sample were attributed to increased amounts of martensite formed during quenching due to decarburization (higher carbon contents tend to promote formation of retained austenite over martensite (*129*)). The uniform lower hardness region appeared to be sufficiently unaffected by decarburization to avoid excessive martensite formation.
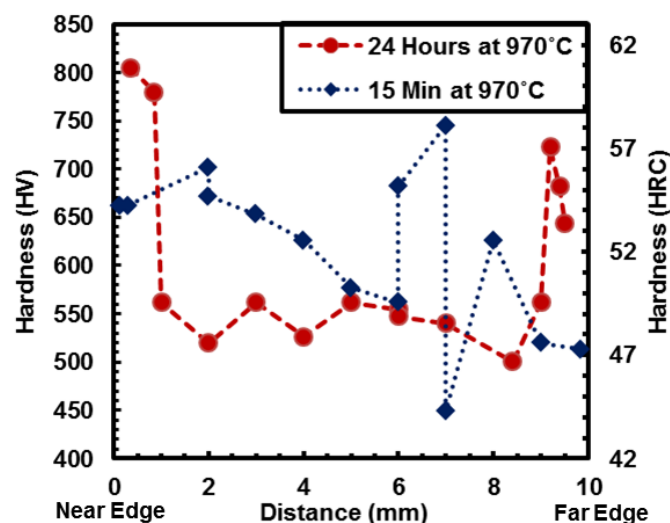
Figure 5.1 Hardness as a function of distance measured across the centerline of two samples from one edge to another (one after heat treatment for 15 minutes at 970°C and one after 24 hours at 970°C).

`

Heat-treated samples were cross-sectioned along the midline with a water-cooled alumina cutoff wheel, then were polished with 1 μm alumina and etched for 25-30s in 4-5% Nital (nitric acid in ethanol). Etched samples were imaged using a Phillips XL-30 scanning electron microscope (SEM) at 20 kV accelerating voltage in secondary electron imaging mode, and also with a Leica series 750 optical microscope (OM). Compositions of different phases in the microstructure were analyzed in the SEM using an Oxford Instruments INCA X-act electron dispersive spectrometer (EDS). Expected equilibirium phase compositions and diffusivities were calculated in the Thermo-Calc 2017a package (including DICTRA) using the TCFE9 and MOBFE4 databases.

Particles in some of the OM micrographs were analyzed using the public domain ImageJ software (*120*). Particle areas (A) were measured in all cases, and diameters were calculated assuming spherical particles such that $d = 2\sqrt{A/\pi}$. Corrections for stereology were made according to Saltikov's procedure (*121*): logarithms of the diameters were taken, then sorted into bins (size classes) of 0.1 log (μm), from -0.4 (0.4 μm) to 0.8 (6.3 μm). The number of particles within each bin was then corrected to account for stereology according to the following expression:

Equation 5.1 $N_{Vi} = \alpha_1 N_{Ai} - \sum_{j-1}^{i-1} \alpha_{j+1} N_{A(i-j)}$

where N_{vi} is the number of particles in the *i*th bin corrected for stereology, N_{Ai} is the number of particles in the *i*th bin before correction, and α_i are constants. Errors due to the assumption of perfectly spherical particles should not be significant since the aspect ratios of the particles were not large (*122*).

5.4 Results

5.4.1 SEM

The starting (as-cast) microstructure of the 1Cr UHCS consisted of a cementite network, (the dark phase in the **Figure 5.2 (a))**, surrounded by a matrix of lamellar pearlite. This microstructure was very similar to that of the 4Cr UHCS we studied previously in chapter 4. The cementite network was formed on austenite grain boundaries during cooling after solidification, and the pearlite colonies were nucleated from the austenite grains during cooling below the eutectoid temperature. After heat treatment, both the 1Cr and 4Cr microstructure consisted of a cementite network, matrix, and particles. **Table 5.2** shows the compositions of the phases in the two UHCS after heat treatment measured by EDS after the heat treatment.

Table 5.2 Compositions of phases (in wt%) in the heat-treated and quenched 1Cr and 4Cr UHCS measured by EDS. The 1Cr UHCS EDS sample was heat-treated or 24 hours at 970˚C, and the 4Cr UHCS EDS sample was heat-treated for 8 hours at 970˚C.

Overall Composition	Meas.	Fe	C	Cr	Mn	Mo	Si	Ni
1Cr UHCS	3	84	8	0.9	0.7	0.6	0.7	1.2
4Cr UHCS	3	88	4	4.4	0.9	0.6	0.8	1.5
Matrix Composition	**Meas.**	**Fe**	**C**	**Cr**	**Mn**	**Mo**	**Si**	**Ni**
1Cr UHCS	3	88	6	0.6	0.6	0.4	1.0	1.4
4Cr UHCS	5	92	2	2.8	0.7	0.3	0.9	1.7
Network Composition	**Meas.**	**Fe**	**C**	**Cr**	**Mn**	**Mo**	**Si**	**Ni**
1Cr UHCS	5	87	6	3.6	1.3	1.5	0.1	0.3
4Cr UHCS	5	76	7	14.5	1.2	0.8	0.1	0.3
Particle Composition	**Meas.**	**Fe**	**C**	**Cr**	**Mn**	**Mo**	**Si**	**Ni**
1Cr UHCS	5	84	9	3.3	1.2	1.1	0.2	0.3
4Cr UHCS	5	79	7	12.0	1.2	0.6	0.1	0.4
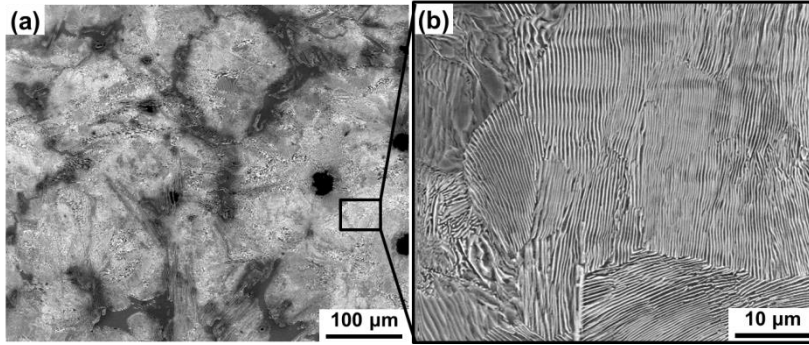
Figure 5.2 SEM micrographs of 1Cr UHCS as-cast microstructure showing (a) cementite network and matrix at low magnification and (b) lamellar pearlite at high magnification.

970˚C Heat Treatments

Figure 5.3 compares the local microstructure around the network branches and the microstructure in the matrix away from the network branches in the 1Cr and 4Cr UHCS after heat treatments of 5 minutes to 24 hours at 970˚C.

Three differences were observed between the microstructures of the 1Cr and 4Cr UHCS after the series of 970˚C heat treatments: (1) the matrix far away from the network branches was almost devoid of particles in the 1Cr UHCS (almost all particles were only observed very close to the network branches); (2) particles were larger in the 1Cr microstructure; (3) there was no longer a denuded zone next to the network branches in the 1Cr UHCS. The comparison of areas near and far from the network branches in **Figure 5.3** is meant to highlight observation (1), as it is clear from the figure that areas far from the network branches contained far fewer particles in the 1Cr UHCS than the 4Cr UHCS.
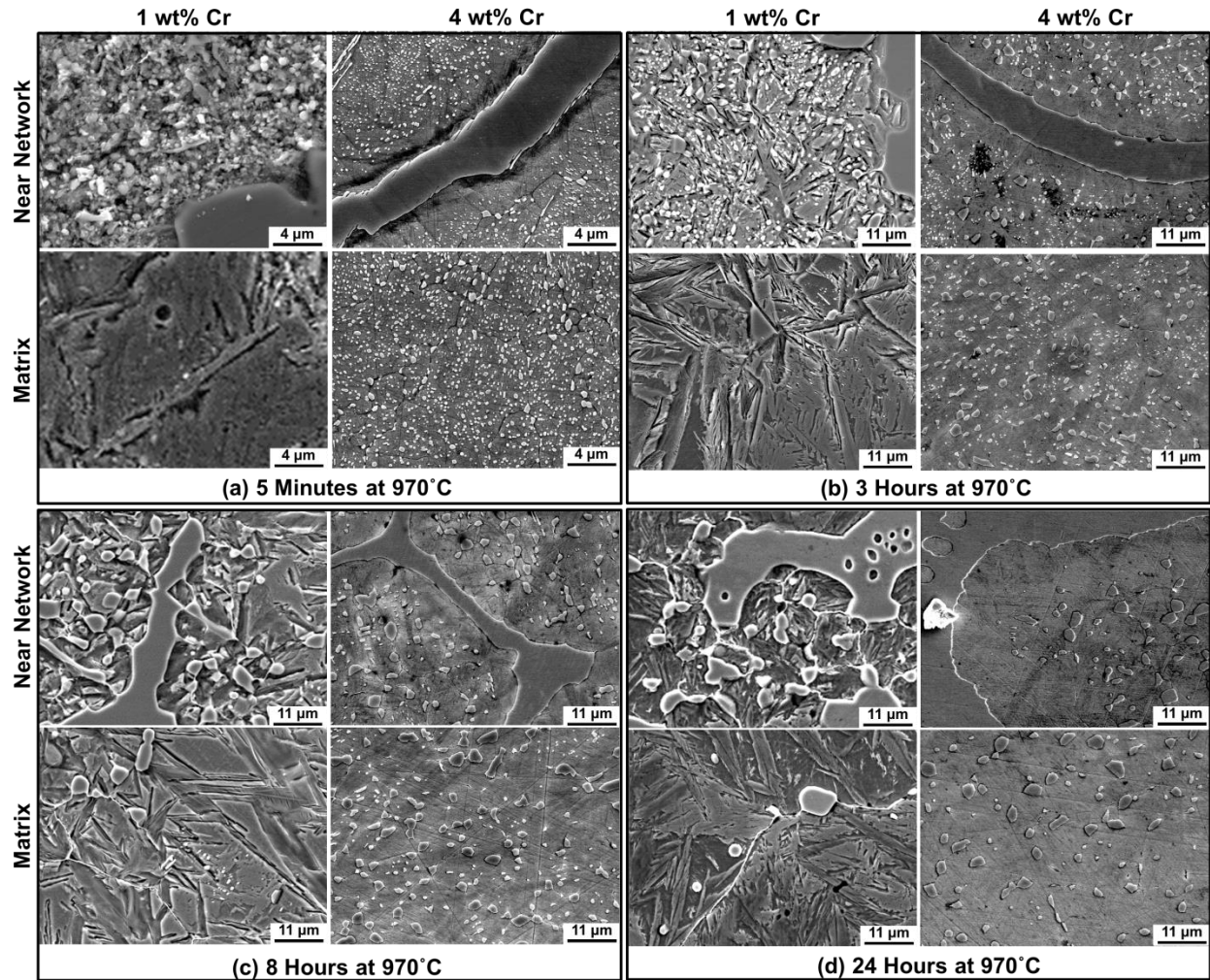
Figure 5.3 SEM micrographs of microstructure at locations near the network branches and in the matrix in both 1Cr and 4Cr UHCS heat-treated at 970˚C for (a) 5 minutes, (b) 3 hours, (c) 8 hours, and (d) 24 hours.

Observation (2) is supported by **Figure 5.4,** which shows some typical regions near the network branches in both the 1Cr and 4Cr UHCS samples. Black lines were manually drawn onto the micrographs to denote boundaries between regions with high and low particle density. In the 4Cr UHCS, the low density particle denuded zone region was found between the black lines and the network branches, while the opposite was found in the 1Cr UHCS. The denuded zones in the 4Cr UHCS grew steadily in a power-law relation with time, but no such relation was found for the regions of high particle density next to the network branches in the 1Cr UHCS.

113
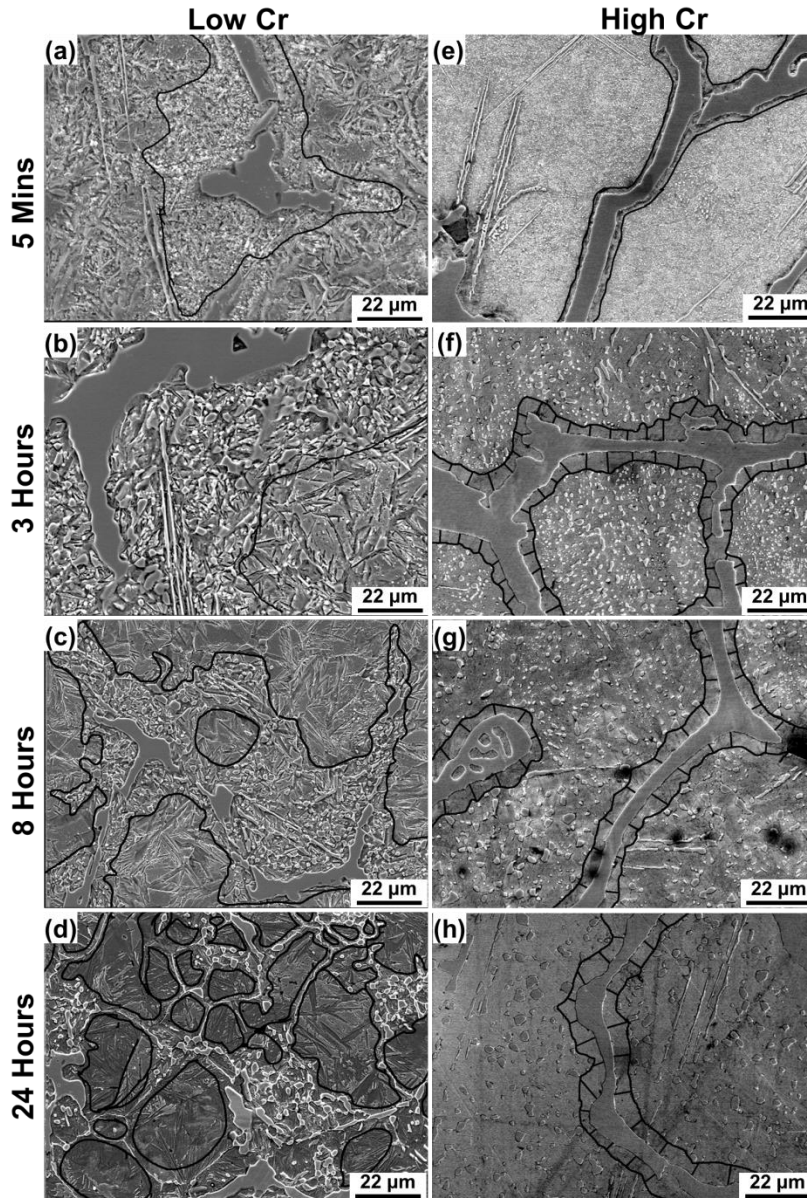
Figure 5.4 SEM micrographs of the (a-d) 1Cr and (e-h) 4Cr UHCS microstructure after heat treatments of 5 minutes through 25 hours at 970°C at locations near the network branches. Dark lines manually drawn onto the micrographs show the boundaries between regions which contain many particles and regions which were mostly particle-free.

800°C and 900°C Heat Treatments

Heat treating the 1Cr UHCS at 800°C or 900°C resulted in increased spatial densities away from the network branches compared to the 970°C heat treatments. For instance, as shown in **Figure 5.5** and **Figure 5.6**, the j1Cr UHCS matrix contained particles after heat treatments of

114

`

various times at 900°C and 800°C, while the matrix in the 1Cr UHCS heated at 970°C did not contain particles. However, particle densities near the network branches were still higher than in the matrix at both 800°C and 900°C. Particle sizes within the 1Cr UHCS microstructure appeared larger than particles within the 4Cr UHCS after heat treatments for corresponding lengths of time at 800°C and 900°C. While particle size distributions in the 4Cr UHCS were determined through quantitative image analysis of SEM micrographs, contrast between particles and matrix in the SEM micrographs of the 1 Cr UHCS microstructure was not sufficient for similar particle analysis. Therefore, particle sizes were measured using optical microscopy (OM) instead.
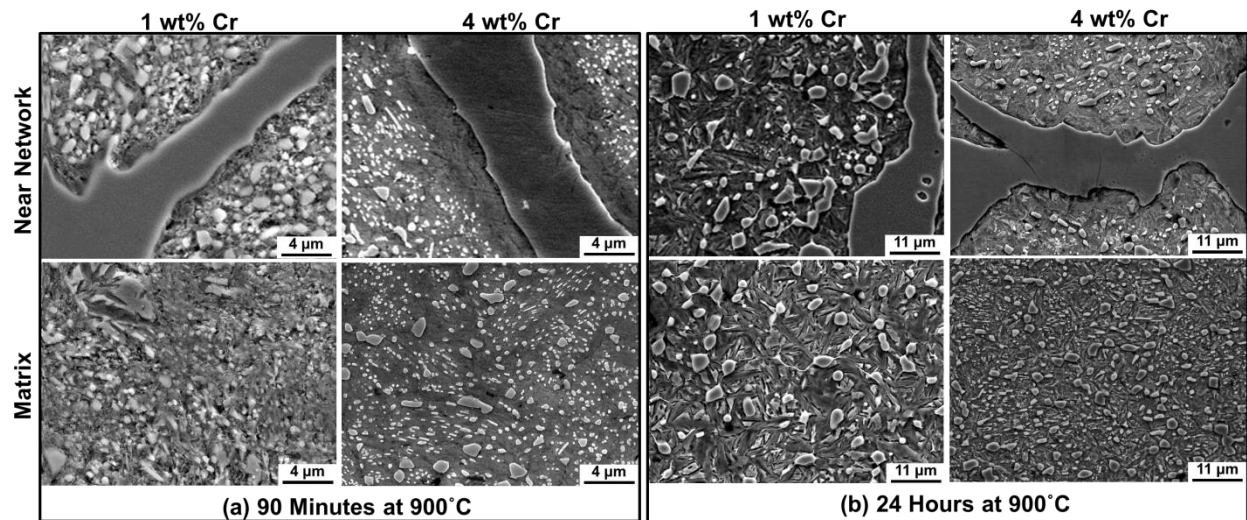
Figure 5.5 SEM micrographs of microstructure at locations near the network branches and in the matrix in both 1Cr and 4Cr UHCS heat-treated at 900°C for (a) 90 minutes and (b) 24 hours.
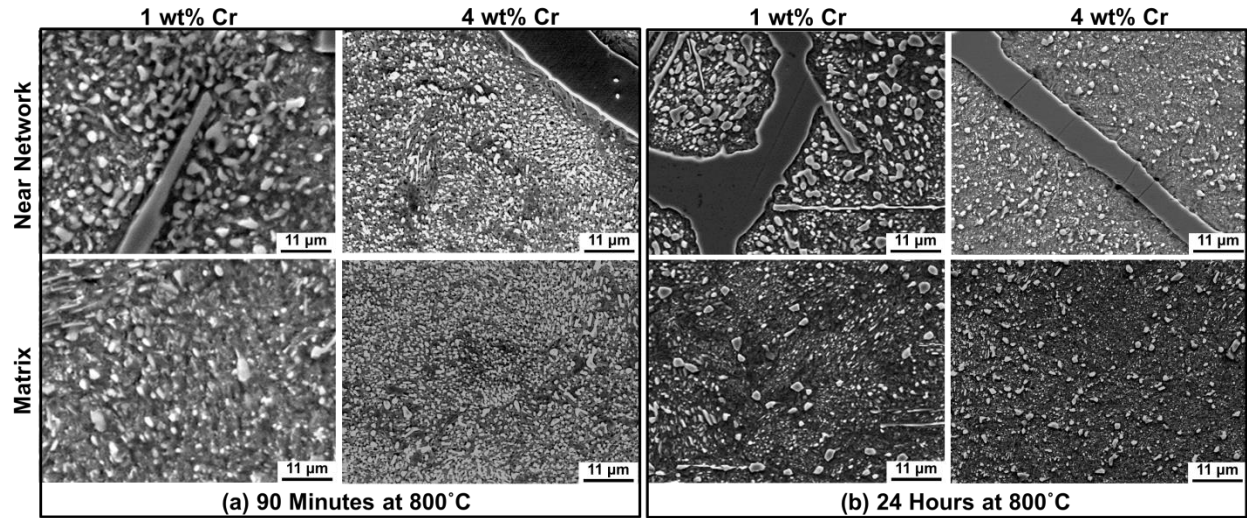
Figure 5.6 SEM micrographs of microstructure at locations near the network branches and in the matrix in both 1Cr and 4Cr UHCS heat-treated at 800˚C for (a) 90 minutes and (b) 24 hours.

5.4.2 OM

Figure 5.7 shows a comparison of OM micrographs of the low Cr microstructure after 8 hours of heat treatment at 800˚C, j900˚C, and 970˚C. Unlike the SEM micrographs, cementite is the bright phase in the OM micrographs. The micrographs show examples pf the previously noted increase in particle size and spatial inhomogeneity with increasing temperature of the heat treatment.
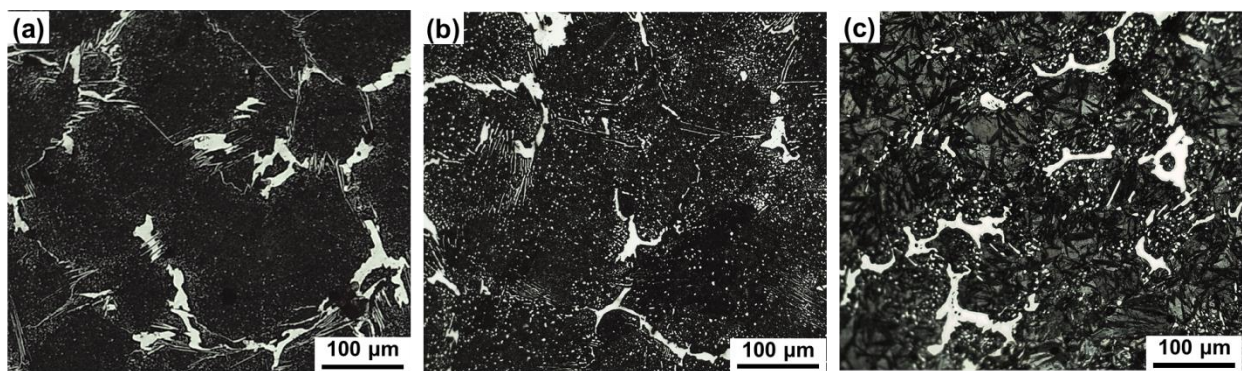
Figure 5.7 OM micrographs of the 1Cr UHCS microstructure after heat treating for 8 hours at at (a) 800˚C, (b) 900˚C, and (c) 970˚C.

`

800˚C

OM micrographs of samples heat-treated at 800˚C are shown in **Figure 5.8**. Cementite particles coarsened over time, and became large enough to be resolved in the OM micrographs between 15 minutes and 90 minutes at 800˚C. The OM images showed significant clustering of particles around the network branches, but the areas further away from the network still contained many cementite particles. Smaller particles tended to be dimmer than larger particles, so some areas in the OM matrix which appeared mostly devoid of particles still contained many small particles that were not bright enough to be distinguished from their surroundings.
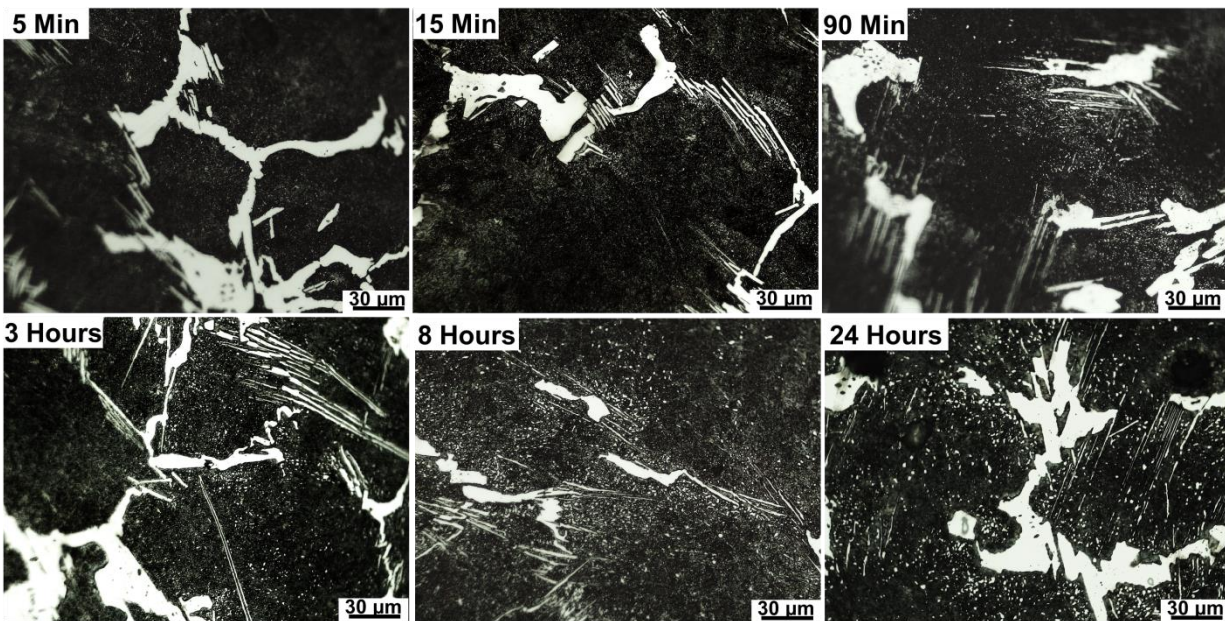
Figure 5.8 OM micrographs of 1Cr UHCS microstructure near branches of the network after heat treating at 800˚C for 5 minutes to 24 hours.

900 ˚C

Figure 5.9 shows a series of OM micrographs of 1Cr UHCS heated treated at 900˚C for times of 5 minutes to 24 hours. Particles first became resolvable between 5 and 15 minutes of heat treatment at 900˚C. Once again, significant clustering of particles near network branches was evident in the micrographs.
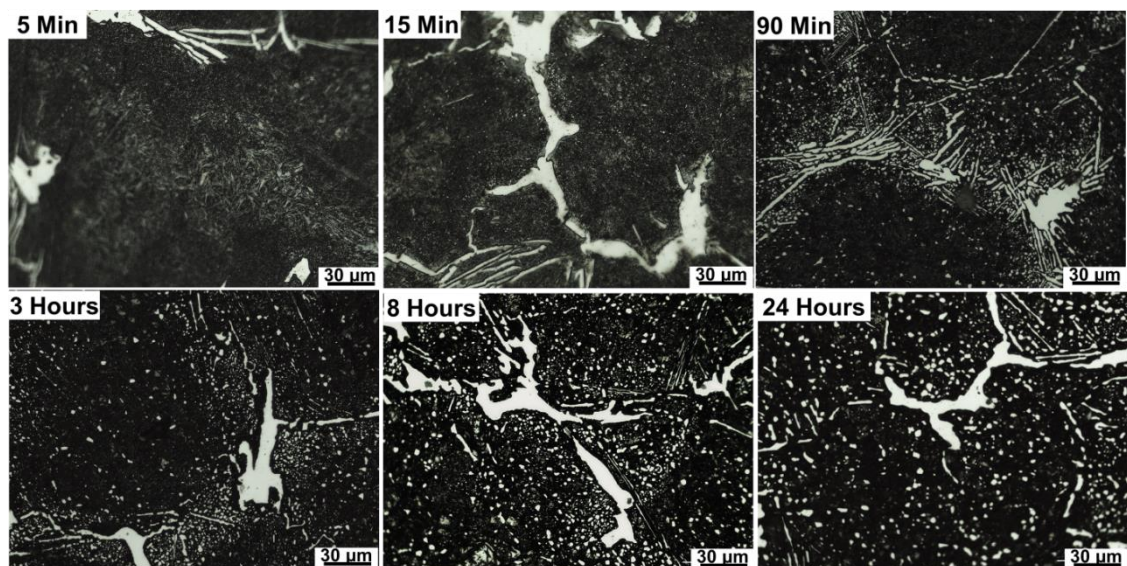
Figure 5.9 OM micrographs of 1Cr UHCS microstructure near branches of the network after heat treating at 900˚C for 5 minutes to 24 hours.

970˚C

Figure 5.10 shows a series of OM micrographs of 1Cr UHCS heated treated at 970˚C for times of 5 minutes to 8 hours. Particles were already resolvable in OM micrographs after 5 minutes of heat treatment. Particle clustering was again evident near network branches, but unlike the other temperatures the matrix was denuded of particles at 970˚C.
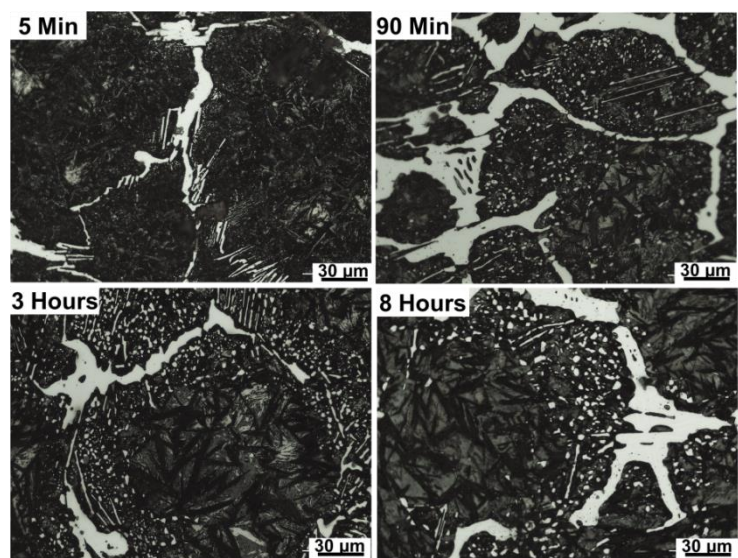
Figure 5.10 OM micrographs of the 1Cr UHCS microstructure near branches of the network after heat treating at 970˚C for 5 minutes to 8 hours.

5.4.3 Quantitative Analysis of OM Micrographs

In Chapter 4, particle size distributions were found through analysis of SEM images. Particle/matrix contrast in the 1Cr SEM micrographs was too poor for digital image processing and particle analysis, so OM micrographs such as those shown in **Figure 5.8, Figure 5.9**, and **Figure 5.10** were utilized instead. Contrast in the OM micrographs was sufficient for segmentation by setting a pixel intensity threshold. The downside to analyzing the OM micrographs was limited resolution; while the minimum resolvable particle size in the 4Cr UHCS SEM micrographs was about 0.06 μm, the minimum resolvable particle size in the 1Cr OM micrographs was about 0.4 μm, an order of magnitude larger. Some of the particles in the 0.4-0.5 μm range may have been noise artifacts, as these sizes approach the optical limit. The limited OM resolution meant that a portion of the 1Cr particle size distribution histogram, indicated in **Figure 5.11 (a)** was not resolvable. In order to plot the two distributions together with the correct particle fractions, the 4Cr distribution was truncated at -0.4 log (μm) and particle fractions were recalculated based on the number of particles after truncation, as shown in **Figure 5.11 (b) and (c).**
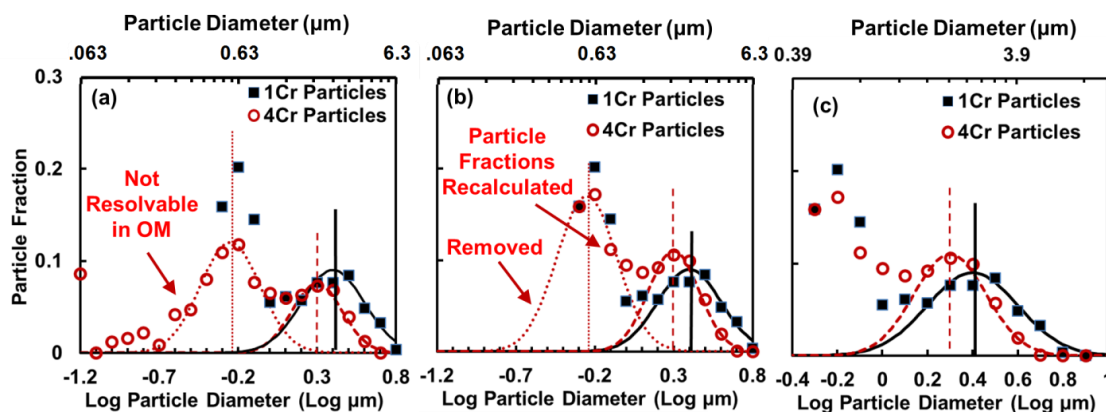
Figure 5.11 Log-log particle size distributions for the 1Cr and 4Cr UHCS heat-treated for 8 hours at 970˚C. The (a) complete range of measured particle sizes in the 4Cr UHCS contained a portion that was too small to be resolved in OM. This portion was (b) removed, and the remaining portion of the distribution was re-scaled and (c) re-plotted over a smaller range of particle sizes.

Particle size distribution histograms for the series of heat treatment times and temperatures in this study are shown in **Figure 5.12**. Gaussian peak profiles were fit manually to the data. Although bimodal distributions were still evident in many of the histograms, only the GB distributions were complete enough to be fit with Gaussian peaks. As shown in **Figure 5.13**, average particle sizes in both 1Cr and 4Cr UHCS GB exhibited a power law relation with time. However, average 1Cr UHCS GB particles sizes were consistently greater than 4Cr UHCS GB particles sizes at corresponding times and heat treatment temperatures. It should be noted that the 1Cr particle sizes were measured in the vicinity of network branches where clustering of particles occurred, while the 4Cr particle sizes were measured away from the network branches to avoid the denuded zones.

In order to describe and compare coarsening behaviors in the UHCS samples, the power law trend lines in **Figure 5.13** were used to extract parameters of the coarsening equation:

$$d^n - d_o^n = k(t - t_o).$$

In this equation, d is the average particle diameter, n is the coarsening exponent, k is a constant, t is the time, and d_o and t_o reflect the initial conditions. Generally an assumption is made that d_o is negligible at the start of coarsening ($t_o=0$), so the equation simplifies to $d^n = kt$, corresponding to the equations for the power law trend lines shown in **Figure 5.13**. This assumption can lead to errors if d_o is not negligible.
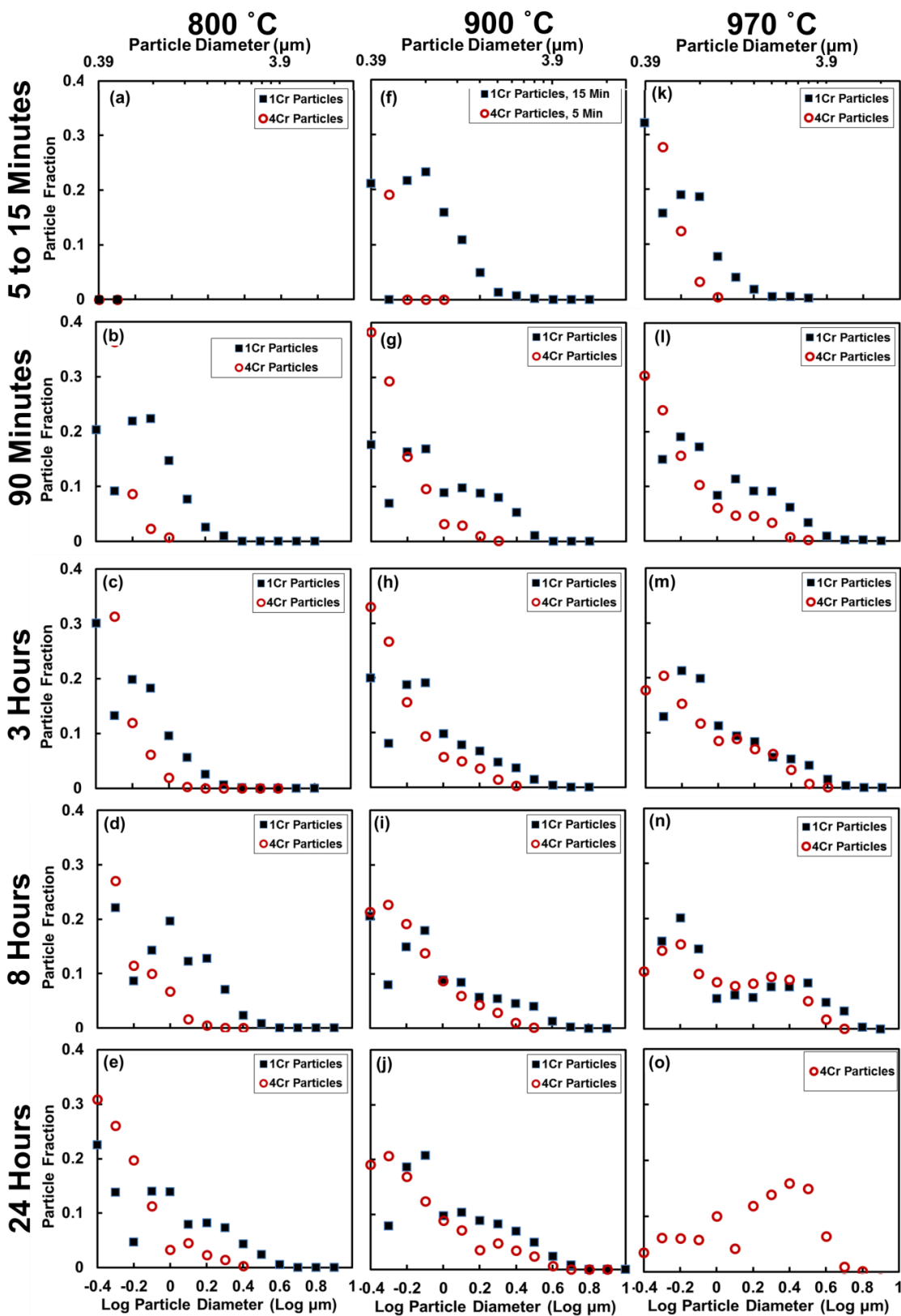
Figure 5.12 Log-log particle size distributions for the 1Cr and 4Cr UHCS heat-treated for 5 minutes to 24 hours at (a-e) 800°C, (f-j) 900°C, and (k-o) 970°C.

121
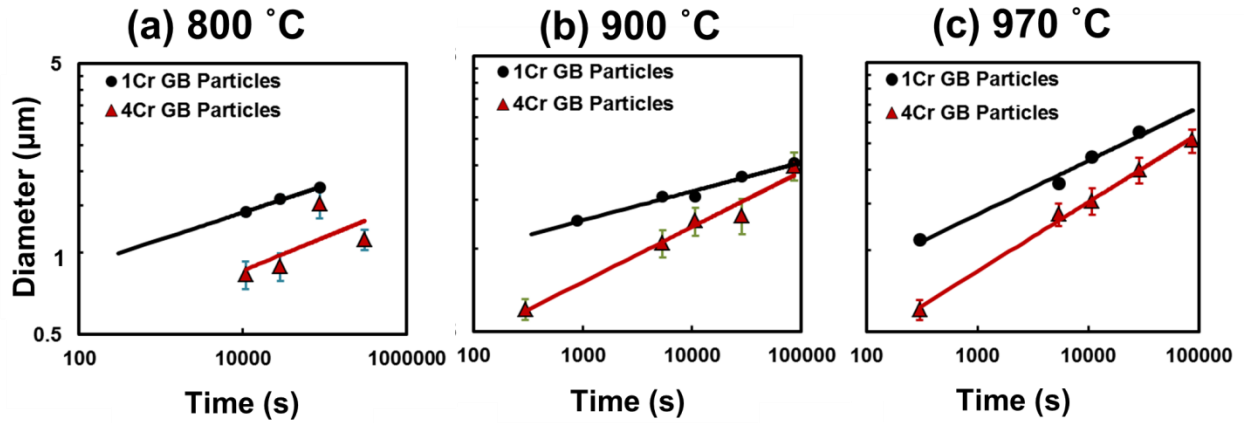
Figure 5.13 Average GB particle diameters exhibited a power law relation with time for both 1Cr and 4Cr UHCS at (a) 800°C, (b) 900°C, and (c) 970°C.

The apparent n and k values based on the power law trend lines assuming negligible d_o are tabulated in **Table 5.3**. At all temperatures n_{app} and k_{app} were higher for the 1Cr UHCS, reflecting a somewhat slower rate of coarsening but a larger particle size over the range of times and temperatures studied. The high values of n_{app} for particle coarsening probably reflected a strong influence of the initial particle size d_o, and were not indicative of diffusive mechanisms. Using the same procedure outlined in our previous study of the 4Cr UHCS, k_n values were determined for n=3,4,5, and used them to calculate theoretical particle sizes for the different coarsening mechanisms. The curves generated by this method are shown in **Figure 5.14**. The curves for n=3,4, and 5 were all consistent with the experimental data, such that they could not be used to narrow down the coarsening mechanism. Thus, in this study we were not able to determine whether or not the coarsening diffusion mechanism changed due to the lower Cr content.

Table 5.3 Apparent n and k values (neglecting d_o) calculated from the power law trend lines in **Figure 5.13**.

Temp [°C]	Low Cr GB Particles		High Cr GB Particles	
	k_{app} [μm^n/s]	n_{app}	k_{app} [μm^n/s]	n_{app}
970	4.7×10^{-3}	5.0 ± 0.5	5.1×10^{-4}	3.9 ± 0.1
900	1.8×10^{-3}	9.5 ± 0.9	2.5×10^{-4}	4.9 ± 0.8
800	3.1×10^{-3}	10 ± 1	3.0×10^{-5}	8 ± 7
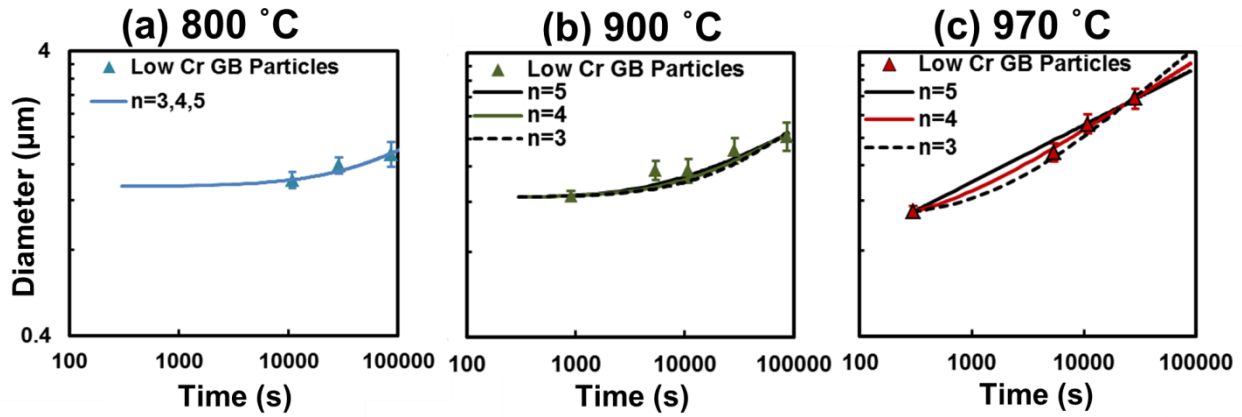
Figure 5.14 Calculations of expected particle sizes calculated based on n=3,4,5 compared to the experimental results at (a) 800°C, (b) 900°C, (c) 970°C.

5.5 Discussion

5.5.1 Phase Diagrams

As the series of experimental heat treatments was identical for the 1Cr and 4Cr UHCS, differences in the resultant microstructures can be attributed to the differences in composition. Thermo-Calc was used to predict the pseudo-binary phase diagrams for both compositions, which are shown in **Figure 5.15**. The diagrams show that the M_7C_3 phase was possible in the 4Cr UHCS if carbon was low. However, the carbon content in the 4Cr UHCS was sufficient to avoid formation of M_7C_3. Below the eutectoid temperature, the phase diagrams indicate that the stable phases were ferrite (α), M_3C, and M_7C_3 in the 1Cr UHCS, and α, M_3C, and $M_{23}C_6$ in the

`

4Cr UHCS. The existence of M_7C_3 or $M_{23}C_6$ phases in any of sample was unlikely, as the rapid quenching from the γ+M_3C dual phase region probably did not allow time for their formation.
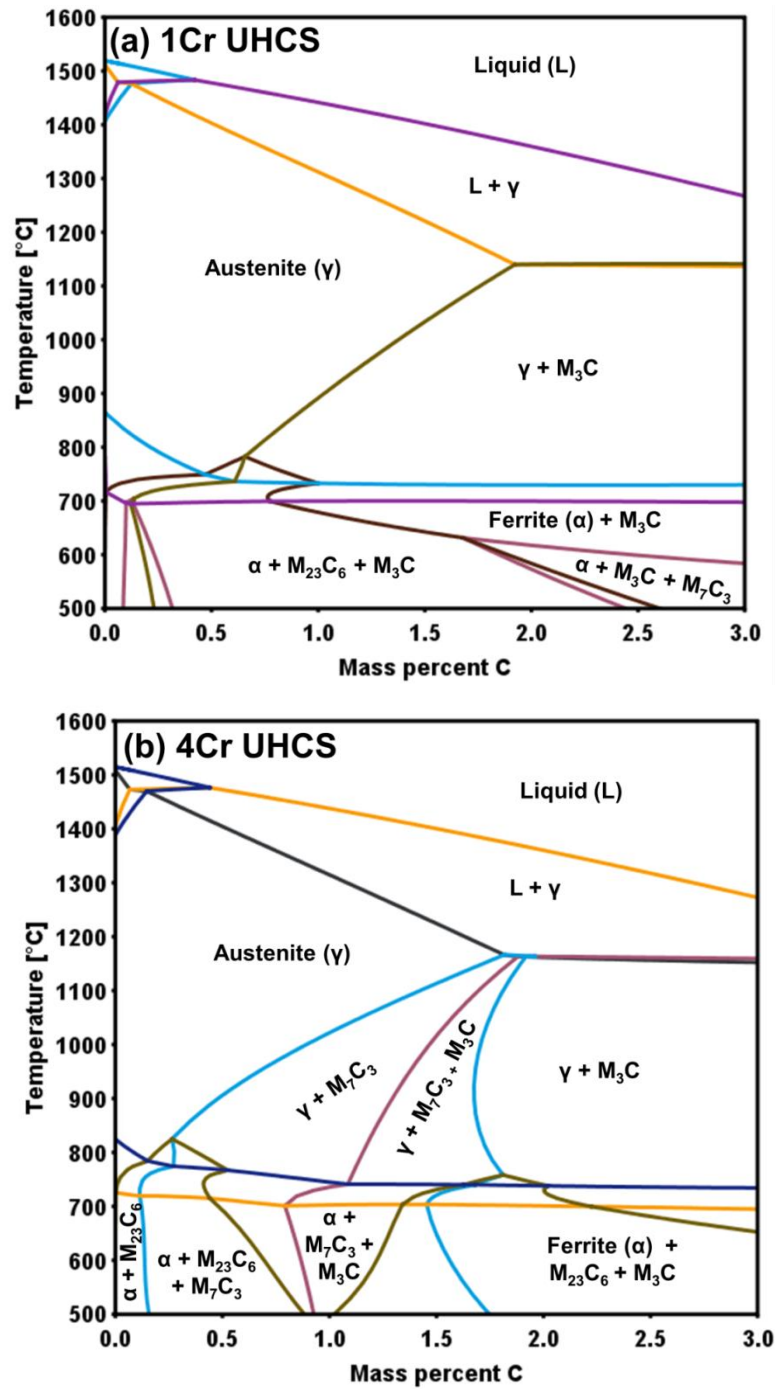
Figure 5.15 Pseudo-binary phase diagrams of (a) the 1Cr UHCS composition and (b) the 4Cr UHCS composition (from Thermo-Calc).

124

Figure 5.16 shows calculated equilibrium volume fractions as a function of temperature for the 1Cr and 4Cr UHCS compositions, with dashed lines denoting the temperatures used in this study and the corresponding calculated equilibrium cementite volume fractions. The low Cr UHCS had about a cementite volume fraction about 0.04 lower than the high Cr UHCS at 800°C and 900°C, and about 0.07 lower than the high Cr UHCS at 970°C. Assuming that the total cementite volume fraction reached equilibrium during the heat treatment experiments, and that cementite was present only in the particles and network, and that no additional cementite formed during the water quenching, the volume of cementite available for particle formation was equal to the network volume fraction subtracted from the equilibrium cementite volume fraction.
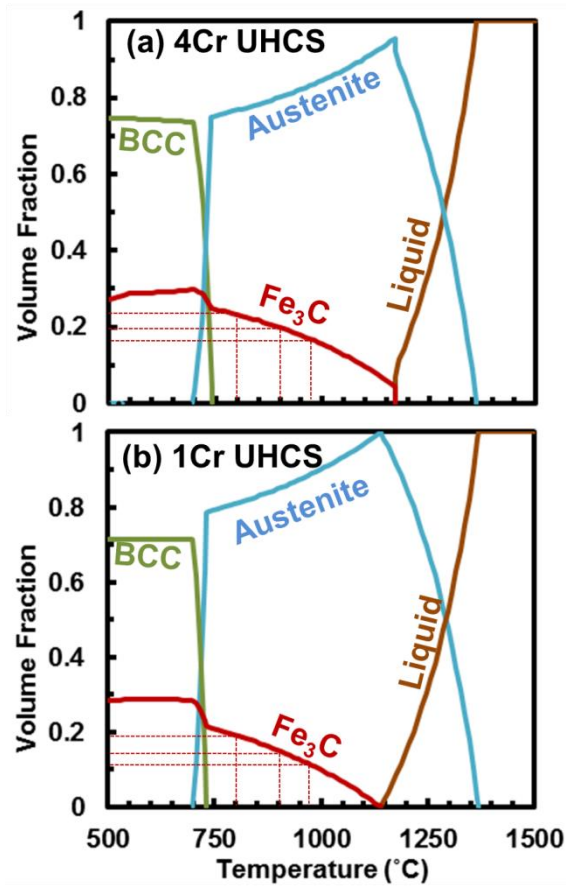
Figure 5.16 Volume fractions plotted versus temperature for the (a) 4Cr and (b) 1Cr UHCS. Dotted lines indicate equilibrium cementite volume fractions at 800°C, 900°C, and 970°C.

5.5.2 Network Volume Fractions

Figure 5.17 shows volume fractions of the cementite network, which were measured from OM micrographs, at different times and temperatures for both the 1Cr and the 4Cr UHCS. No clear trend was observed in network volume fraction as a function of temperature, so the average network volume fraction value for the entire time range at each temperature was used to calculate the amount of cementite left over for particles, as shown in **Table 5.4**. Despite higher equilibrium cementite fractions in the high Cr UHCS, the total amount of cementite available for cementite particle formation did not change much as a function of C or Cr content at 800˚C or 900˚C. However, much less cementite was available for particle formation at 970˚C in both the 1Cr UHCS. This difference in available cementite, together with the clustering behavior seen in all the low Cr UHCS samples, was probably responsible for the denuded matrix at 970˚C in the 1Cr UHCS. The matrix of the 4Cr UHCS, which had similar amounts of cementite available for particle formation at 970˚C, did not become denuded of particles because there was no clustering near network branches. Thus, it appears that a high Cr content can inhibit particle clustering near the network branches and help ensure a more homogenous particle distribution in UHCS microstructure.
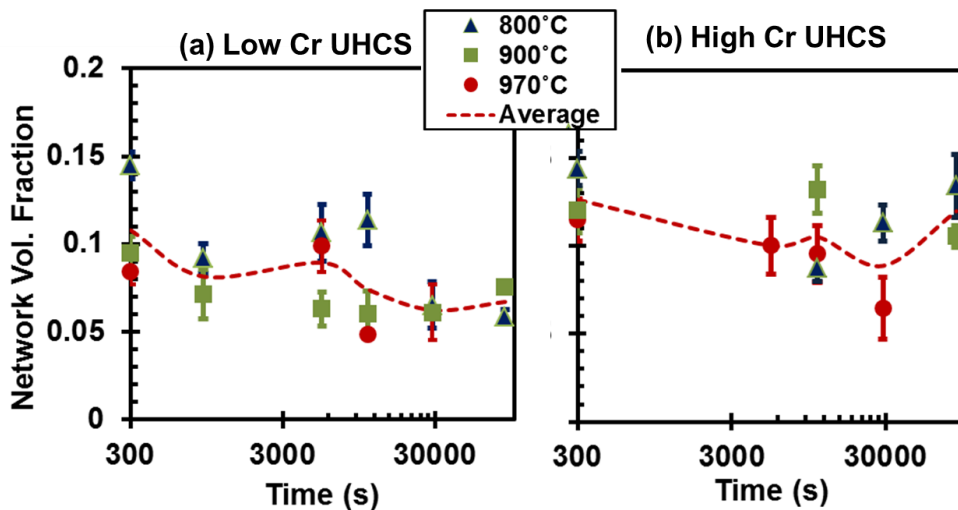
Figure 5.17 Network volume fractions versus time for (a) low Cr UHCS and (b) high Cr UHCS.

Table 5.4 Cementite available for particle formation at different temperatures.

1Cr UHCS	800°C	900°C	970°C
Equilibrium Vol. Fraction Fe$_3$C	0.19	0.15	0.11
- Avg. Fe$_3$C Network Fraction	0.10±0.03	0.07±0.01	0.07±0.02
= Fe$_3$C for Particles	0.09±0.03	0.08±0.01	0.04±0.02
4Cr UHCS	**800°C**	**900°C**	**970°C**
Equilibrium Vol. Fraction Fe$_3$C	0.24	0.20	0.18
- Avg. Fe$_3$C Network Fraction	0.12±0.03	0.12±0.01	0.09±0.02
= Fe$_3$C for Particles	0.12±0.03	0.08±0.01	0.09±0.02

5.5.3 Particle Clustering and Denuded Zones

The particle clustering phenomenon was unexpected in the 1Cr UHCS, given that no such effect was reported by Krawczyk *et al.* in steel of a similar composition (*22*). Additionally, no cementite subgrain boundaries were observed. Instead, discreet GB particles decorated the grain boundaries. The main difference in processing between this study and that of Krawczyk was the cooling rate. It is possible that the subgrain boundaries only formed during slower cooling, or that clustering became obscured during slow cooling.

In chapter 4, the cause of the denuded zones near the network carbides was tentatively identified as an effect of a concentration gradient of Cr directed towards the low-curvature cementite network. The direction of the concentration gradient in coarsening should depend only on curvature, and not on composition. **Figure 5.18** shows that the equilibrium Cr content in the matrix and cementite was higher by about a factor of 3-4 in the 4Cr UHCS as compared to the 1Cr UHCS. The Gibbs-Thompson equation indicates that the concentration at particle/matrix interfaces is equal to the matrix concentration scaled by a curvature-dependent factor. Thus assuming that the curvature factor is about the same in the 1Cr and 4Cr UHCS, the difference in concentration at the matrix/particle interfaces would be about four times higher in the 4Cr UHCS. Thus the higher Cr in the austenite in the 4Cr UHCS may be responsible for a steeper

solue gradient towards the network. The Cr might also influence the diffusivity of chemical species in the steel. **Figure 5.19** shows that increasing Cr concentration in the UHCS composition decreased C and Cr chemical diffusion, and increases iron self-diffusion. If Cr diffusion is the bottleneck for cementite coarsening, then the decrease in Cr diffusivity might be a factor affecting denuded zones and clustering.
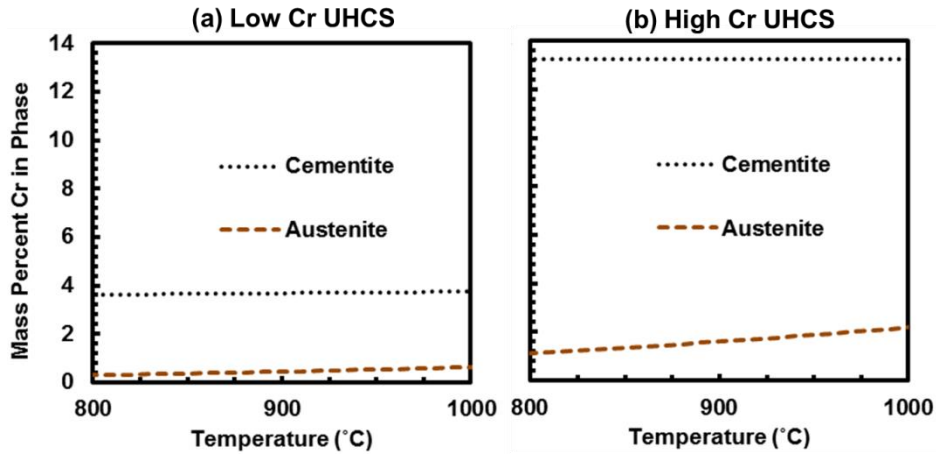
Figure 5.18 Equilibrium Cr contents in cementite and austenite calculated in Thermo-Calc for (a) the 1Cr UHCS and (b) the 4Cr UHCS.
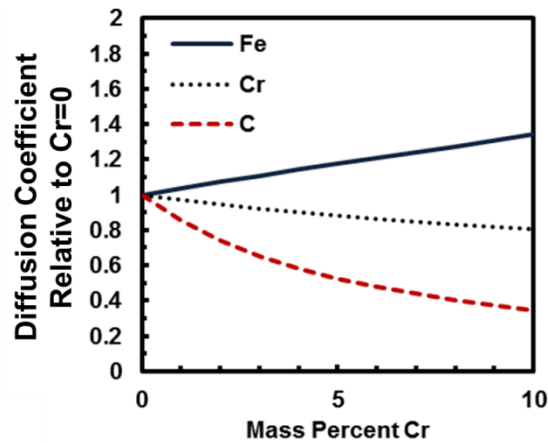
Figure 5.19 Effect of Cr concentration on chemical diffusion coefficients of Cr and C, and tracer diffusion of Fe calculated in the Thermo-Calc and Dictra package.

`

Another factor that might have influenced diffusivity was stress developed during heating due to mismatched thermal expansion coefficients of cementite and austenite.[1] Umemoto *et al.* (*130*) found that adding 0.2 wt% Cr to bulk cementite increased the coefficient of thermal expansion considerably at and below 400˚C (they did not report on the thermal expansion of pure cementite above 400˚C). They also reported that the Cr-containing cementite's linear expansion coefficient of $2.5 \cdot 10^{-5}$/K did not change as a function of temperature over a range of about 100˚C to 1000˚C. For this study, volumetric thermal expansion of cementite and austenite were calculated in Thermo-Calc for a 2wt% C UHCS containing variable amounts of Cr. **Figure 5.20 (a)** shows the variation with Cr content in volumetric thermal expansion coefficient of austenite and cementite at 970˚C, and **Figure 5.20 (b)** shows the ratio of the expansion coefficients of cementite and austenite at 970˚C. The thermal expansion of austenite peaked at about 1wt% Cr while the expansion of cementite only changed slightly with Cr content. The calculated volumetric expansion coefficient of cementite matched well with Umemoto's experimentally measured linear expansion value. The net result was that the mismatch in thermal expansion coefficients of austenite and cementite was about 11% higher for the 1Cr UHCS than for the 4Cr UHCS, meaning that the 1Cr UHCS experienced a larger compressive stress during heating. It is difficult to predict exactly the effect of stress on diffusivity in a given system (*131*), but others have shown that increased compressive stress led to increased self-diffusivity in α-iron (*132*) and increased interstitial diffusivity in austenite (*133*).

---

[1] This line of reasoning was suggested by Professor Chris Pistorius at Carnegie Mellon University.

`
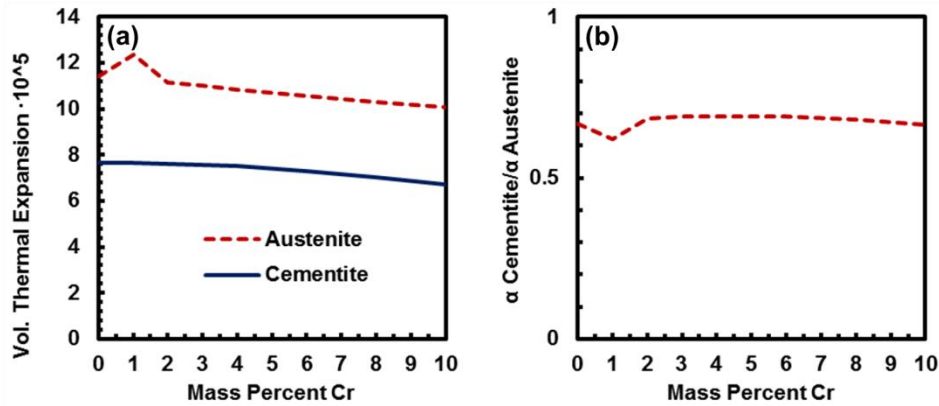
Figure 5.20 Variation with Cr content of (a) volumetric thermal expansion coefficients of austenite and cementite and (b) the ratio of the cementite and austenite coefficients at 970˚C (from Thermo-Calc).

5.6 Summary and Conclusions

In this chapter, an initially pearlitic 2C-1Cr UHCS was heat-treated at 800˚C, 900˚C, and 970˚C for comparison with a 2C-4Cr UHCS studied previously. During the 1Cr UHCS heat treatments pearlite spheroidized into cementite particles that subsequently coarsened over time. Unlike the 4Cr UHCS, which exhibited particle denuded zones near network branches, cementite particle densities in the low Cr UHCS were highest in clusters near network branches. At 970˚C, the 1Cr UHCS matrix became denuded of particles completely. Particles in these clusters were consistently larger than the homogenously distributed particles previously measured in the 4Cr UHCS. We were not able to determine whether any rate-controlling diffusion mechanisms had changed due to the lower Cr content.

Although equilibrium amounts of proeutectoid cementite differed in the 1Cr and 4Cr UHCS, the volume fraction available for particle formation was about the same at both Cr contents after accounting for the cementite network volume. The denuded matrix of the 1Cr UHCS at 970˚C was a result of particle clustering and the lower cementite volume fraction available for the particles at that temperature. We explained the particle clustering and denuded zones as phenomena related to the steepness and depth of the solute gradient established by the

130

`

cementite network branches. A steep gradient with little depth, indicated in the 4Cr UHCS, could theoretically result in denuded zones. A shallow gradient with high depth, indicated in the 1Cr UHCS, could result in increased particle stability and clustering near the cementite network branches.

`

Chapter 6. In Situ Confocal Laser scanning Microscopy (CLSM) Heat Treatments

6.1 Abstract

This chapter describes several heat treatment experiments which were observed *in situ* in a confocal laser scanning microscope (CLSM). Thermal grooving, particle coarsening, and oxidation were observed *in situ* for all four experiments. Particles coarsened on the surface consistent with a mechanism controlled by dislocation-mediated diffusion. Two of the CLSM sample surfaces and cross-sections were subsequently examined by SEM. Particles on the surface tended to be larger than in the bulk, possibly due to elongation along the free surface. The CLSM samples also contained particle-free and particle-dense regions, which appeared to be distributed randomly in the microstructure.

6.2 Introduction

In Chapter 2 of this dissertation, an industrial heat treatment was found to create micron-sized faceted idiomorphic cementite particles in the matrix of the UHCS sample. In chapter 4, a series of box furnace heat treatments demonstrated that the faceted idiomorphic particles coarsened at different rates depending on whether they were on grain boundaries (GB particles, *n=4*) or intragranular (IG particles, *n=5*). In this chapter, *in situ* confocal laser scanning microscopy (CLSM) was utilized to observe the particle coarsening processes in real time.

Imaging samples *in situ* at high temperatures poses a challenge because heated materials emit incandescent radiation above ~500˚C that can obscure surface features. CLSM (*134*) avoids the issue by utilizing a small aperture to detect radiation only from a very small area of the sample surface at a time. The technique has been very successful at filtering excess radiation in fluorescent samples, (*134*) and is similarly effective at filtering excess INCAndescent radiation in samples at high temperature.

6.3 Experimental Methods

CLSM *in situ* heat treatment experiments were conducted on four different initially as-cast 2C-4Cr UHCS samples at temperatures of about 1000˚C, 1050˚C, and 1100˚C. The composition of the samples is shown in **Table 6.1**.

Table 6.1 As-cast UHCS composition

	Fe	Cr	C	Mn	Mo	Si	Ni
As-Cast UHCS	Bal.	3.86	2.02	0.72	0.33	0.65	1.45

Figure 6.1 shows a schematic of the CLSM setup. In each experiment, a flat cylindrical UHCS sample of about 3 mm diameter and 1 mm height was placed in an alumina crucible inside an ellipsoidal gold plated chamber. The chamber walls reflected radiation from a halogen lamp onto the samples, allowing heating in a controlled manner. A laser beam sensitive to surface topography was scanned across the sample surface to form an image on a computer screen. Argon gas was pumped through the system to inhibit sample oxidation. Contrast in the CLSM was a result of variations in surface topography; rougher surfaces, and points higher or lower than the exact plane of focus, appeared darker due to the confocal optics.
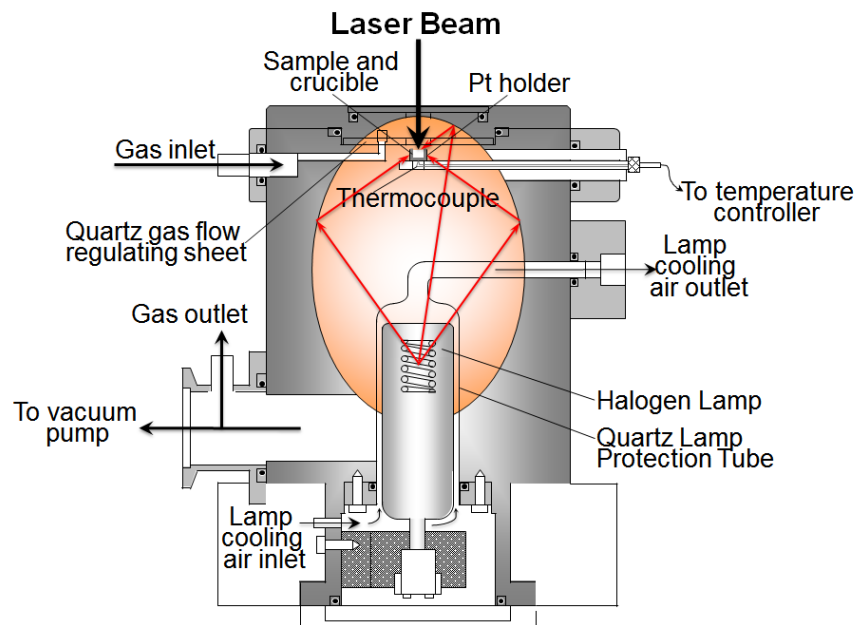
Figure 6.1 Confocal setup [Figure from J. Zhu, private communication].

Time and temperature plots for the four different CLSM experiments are shown numbered from 1-4 in **Figure 6.2**. The numbering represents the chronological ordering of the experiments and has no other significance. **Figure 6.2 (a)** shows only the first three minutes of heating, and **Figure 6.2 (b)** shows the entire duration of the heat treatments. A reference temperature of 500°C was assigned to t=0. Heating rates varied from about 6°C/to 12°C/s. Samples 1 and 2 were held at about 1000°C for 45 minutes each; sample 3 was held at about 1050°C for one hour; and sample 4 was heated to 1100°C, then immediately quenched by switching from argon gas to helium and turning off the halogen lamp. Additional details of the CLSM experiments, including heating rates, isothermal holding temperatures and times, and average cooling rates, are shown in in **Table 6.2**.
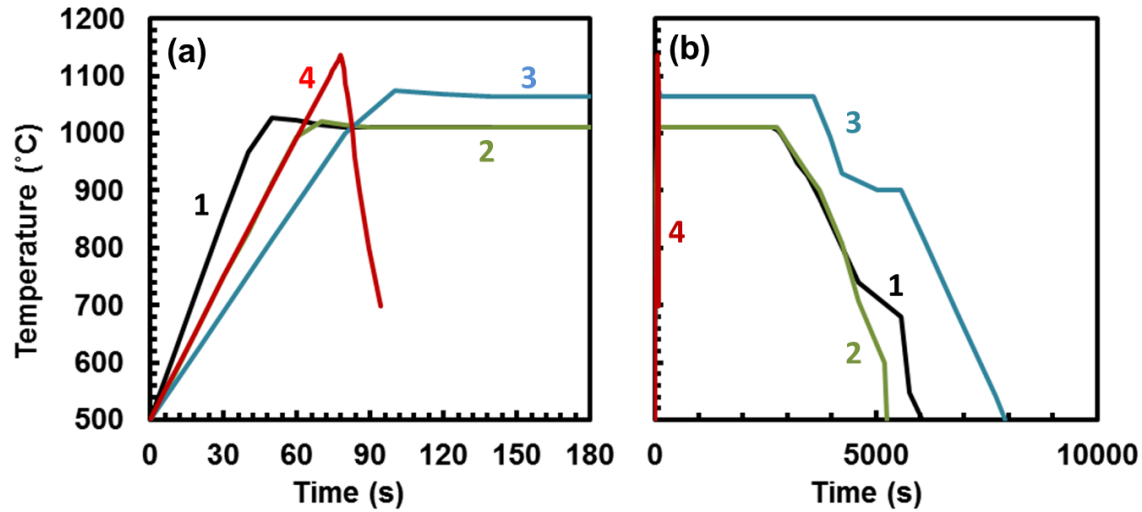
Figure 6.2 Time versus temperature profiles of (a) the first 3 minutes and (b) the full heating cycles for the four CLSM *in situ* heat treatments.

Table 6.2 Details of the four CLSM experiments.

Experiment #	Isothermal Hold Temp	Heating Rate	Isothermal Hold Time	Cooling Rate
1	1000 °C	12 °C/s	45min	7-8 °C/min
2	1000 °C	8 °C/s	45min	7-16 °C/min
3	1050 °C	6 °C/s	60min	7-8 °C /min
4	1125 °C	8 °C/s	Quench	27 °C/s

After the heat treatments, sample surfaces were examined using a Phillips XL-30 scanning electron microscope (SEM) at 20 kV accelerating voltage in secondary electron imaging mode. Electron dispersive spectroscopy (EDS) was used to identify compositions of different phases. To compensate for potential surface effects, samples were subsequently cross-sectioned, etched with 5% Nital (nitric acid in ethanol) for 20-30s, and imaged again by SEM and optical microscopy (OM) on a plane perpendicular to the original CLSM sample surface as shown in **Figure 6.3**.

(a) Surface   (b) Cross Section
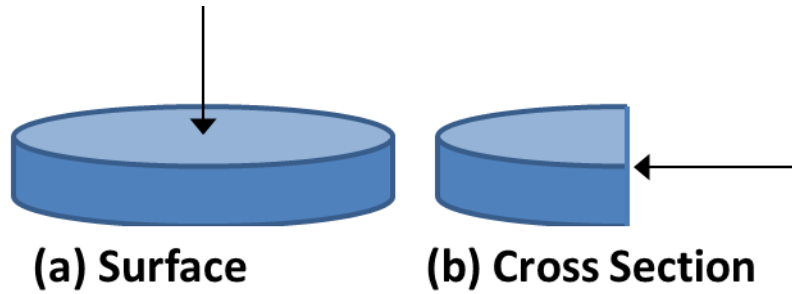
Figure 6.3 Schematic of CLSM samples showing the (a) surface and (b) cross-section views.

6.4 Results

Initial Microstructure

The initial microstructure of the jas-cast 2C-4Cr UHCS consisted of a cementite network surrounded by a pearlite matrix as shown in **Figure 6.4**.

Cementite Network
(Dark Phase)   Pearlite Matrix
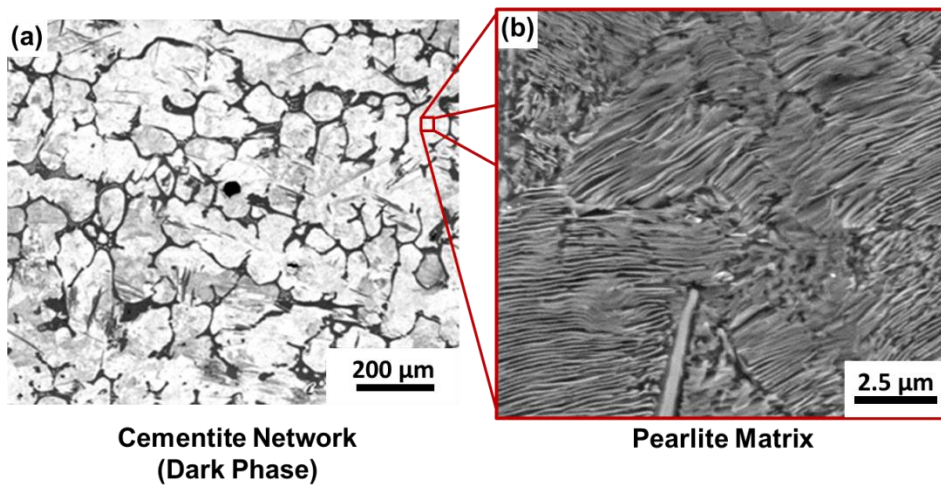
Figure 6.4 SEM micrographs of the initial UHCS microstructure showing (a) a cementite network on prior austenite grain boundaries surrounded by (b) a pearlite matrix.

6.4.2 Experiment 1: 12°C/s heating, 45 minute 1000°C isothermal hold, 7-8°C/min cooling

Heating

During heating, the cementite network became outlined due to thermal grooving. **Figure 6.5** shows individual video frames during the heating step in the first CLSM heat treatment. Below the eutectoid temperature, only branches of the cementite network and a few

`

Widmanstätten laths were visible as shown in **Figure 6.5 (a).** As heating progressed, thermal grooving began to slightly delineate branches of the network as observed in **Figure 6.5 (b).** The amount of thermal grooving around the network branches reached its maximum soon after reaching the isothermal hold temperature of 1000˚C as shown in **Figure 6.5 (c).**
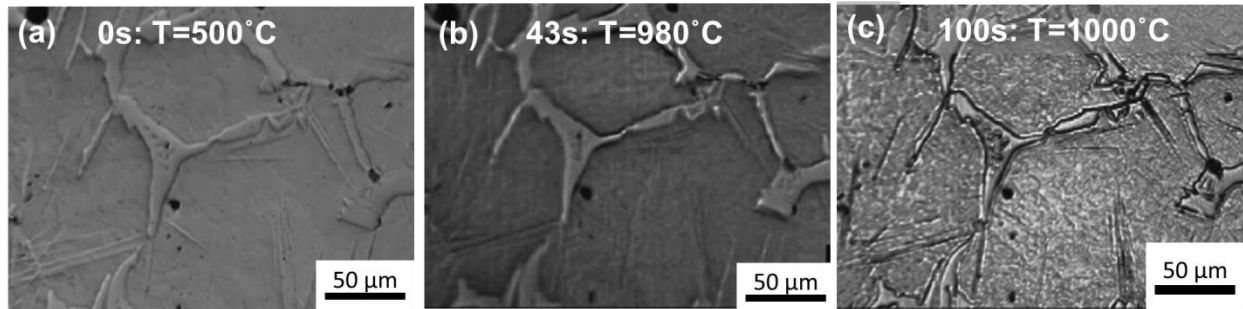
Figure 6.5 CLSM video frames from the heating step in experiment 1showing microstructure at (a) the reference starting time of 0s at 500˚C, (b) 43s into the heating, and (c) 100s into heating. Thermal grooving next to the network developed within the first 100s of the heat treatment.

Isothermal hold at ~1000˚C

During the isothermal hold, particles appeared in the microstructure and coarsened; additionally, the network may have thinned or broken up to some degree. Particles were first resolvable in the microstructure near the start of the isothermal heat treatment, around 112 seconds after reaching 500˚C. Particles grew steadily over time as seen in **Figure 6.6** (b-f). Certain particles, indicated by arrows in **Figure 6.6** (e-f), grew much faster than other particles (the circled region in **Figure 6.6 (e)** denotes slower growing particles). After a few minutes of isothermal heating, thermal grooving became evident within the matrix as shown in **Figure 6.6 (c) and (d).** There may also have been thinning and/or breakup of the network during the isothermal heat treatment in experiment 1. Arrows in **Figure 6.7** show points on the network that may have been thinned during the heat treatment. Edge detection processing in ImageJ was used to better visualize the potential thinning.

137
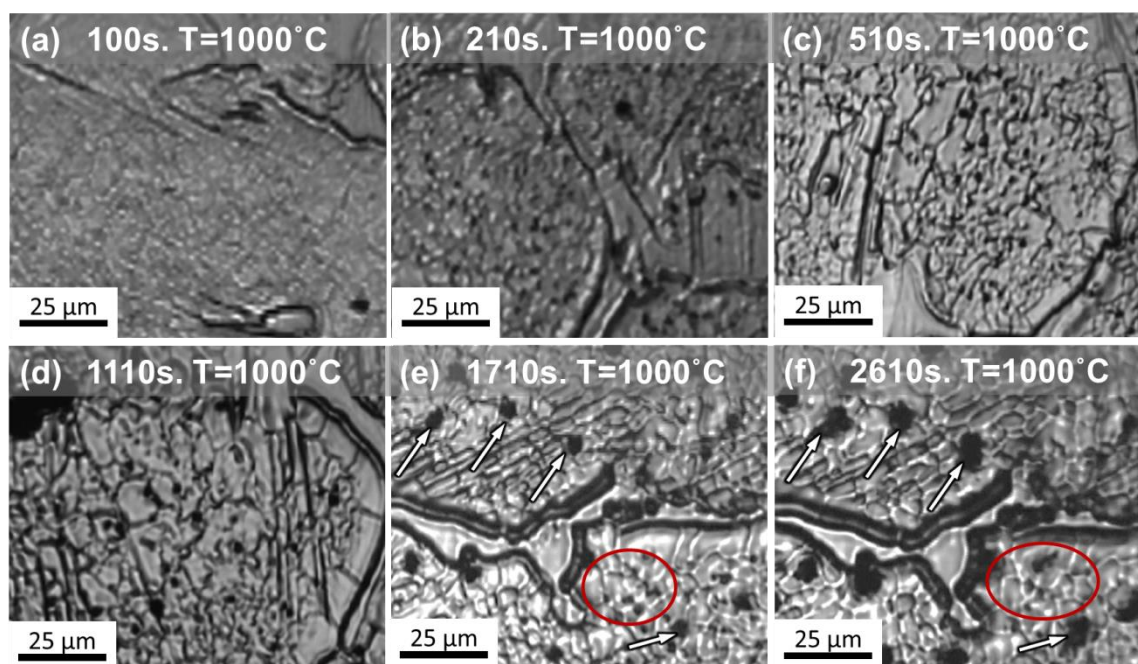
Figure 6.6 CLSM video frames from the isothermal hold at 1000°C during experiment 1 showing (a) the matrix free of resolvable particles after 100s followed by progressive coarsening of particles at (b) 210s, (c) 510s, (d) 1110s, (e) 1710s, and (f) 2610s. Arrows denote rapidly growing particles and the circled region denotes slower growing particles.
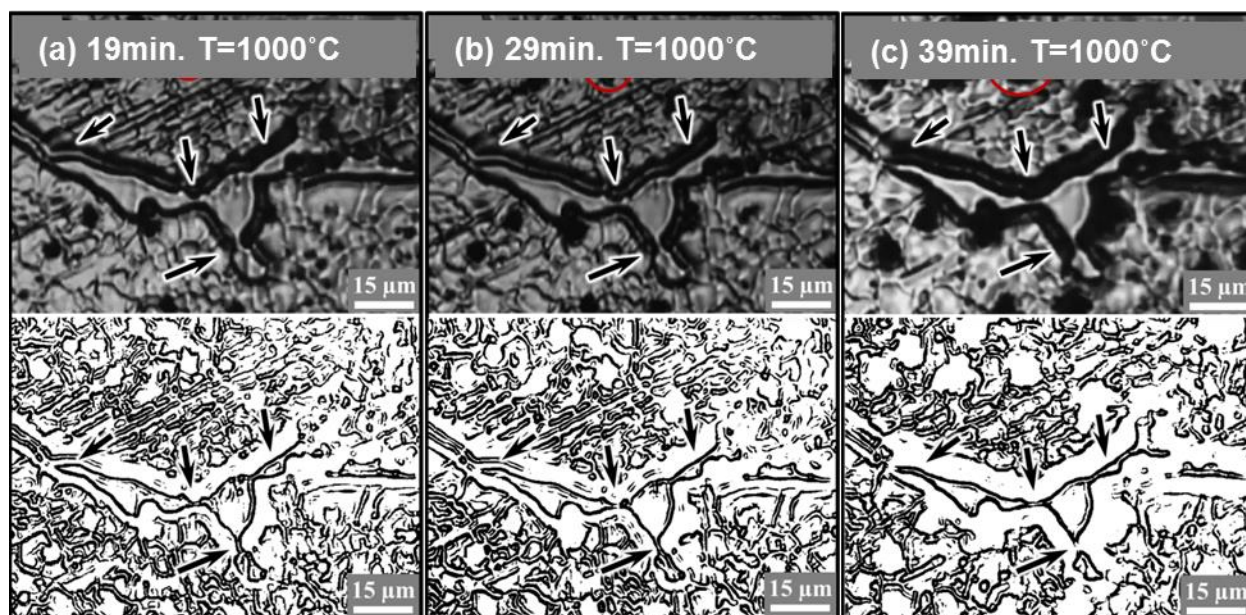
Figure 6.7 CLSM video frames from the isothermal hold at 1000°C during experiment 1 showing network at (a) 19 minutes, (b) 29 minutes and (c) 39 minutes. ImageJ was used to detect edges in the CLSM frames to show possible points of network separation (bottom images).

`

Cooling

There was significant roughening of the surface during cooling, as shown in **Figure 6.8**. The entire sample surface grew more textured, especially the cementite network. The smaller particles (circled in the figure) were obscured. Larger particles sizes (denoted by arrows) became less distinct but were still discernable.
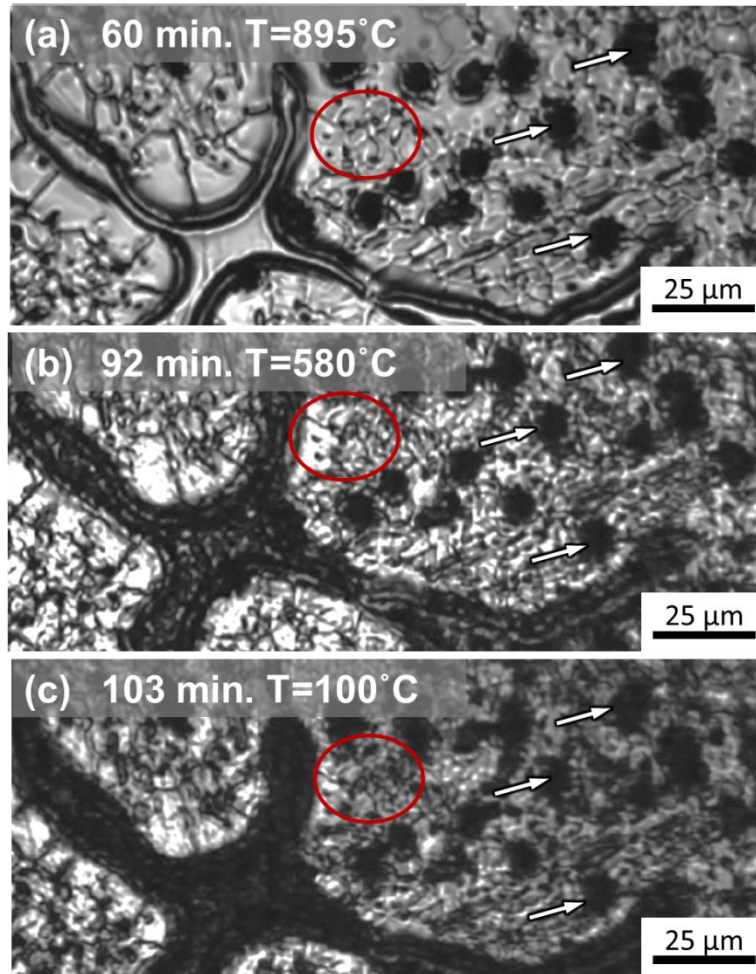
Figure 6.8 CLSM video frames from experiment 1 showing the microstructure during cooling at (a) 895°C, (b) 580°C, and (c) 100°C.

SEM

Two distinct particle morphologies, corresponding to oxides and cementite, were observed when the CLSM sample surface was examined in the SEM after the CLSM experiment. Larger particles denoted by arrows in **Figure 6.9 (a)** were of similar sizes and shapes to the

larger particles in the CLSM video. Smaller particles had much higher relative areal density than larger particles, as seen in **Figure 6.9 (b)**. When viewed at higher magnification in **Figure 6.9 (c)**, it was apparent that the larger particles had an indistinct and nodular morphology characteristic of oxide particles. Smaller particles, denoted by arrows in **Figure 6.9 (c),** had a smoother faceted morphology characteristic of cementite particles. In cross-section, no particles with the characteristic oxide morphology were found deeper than the immediate surface sample.
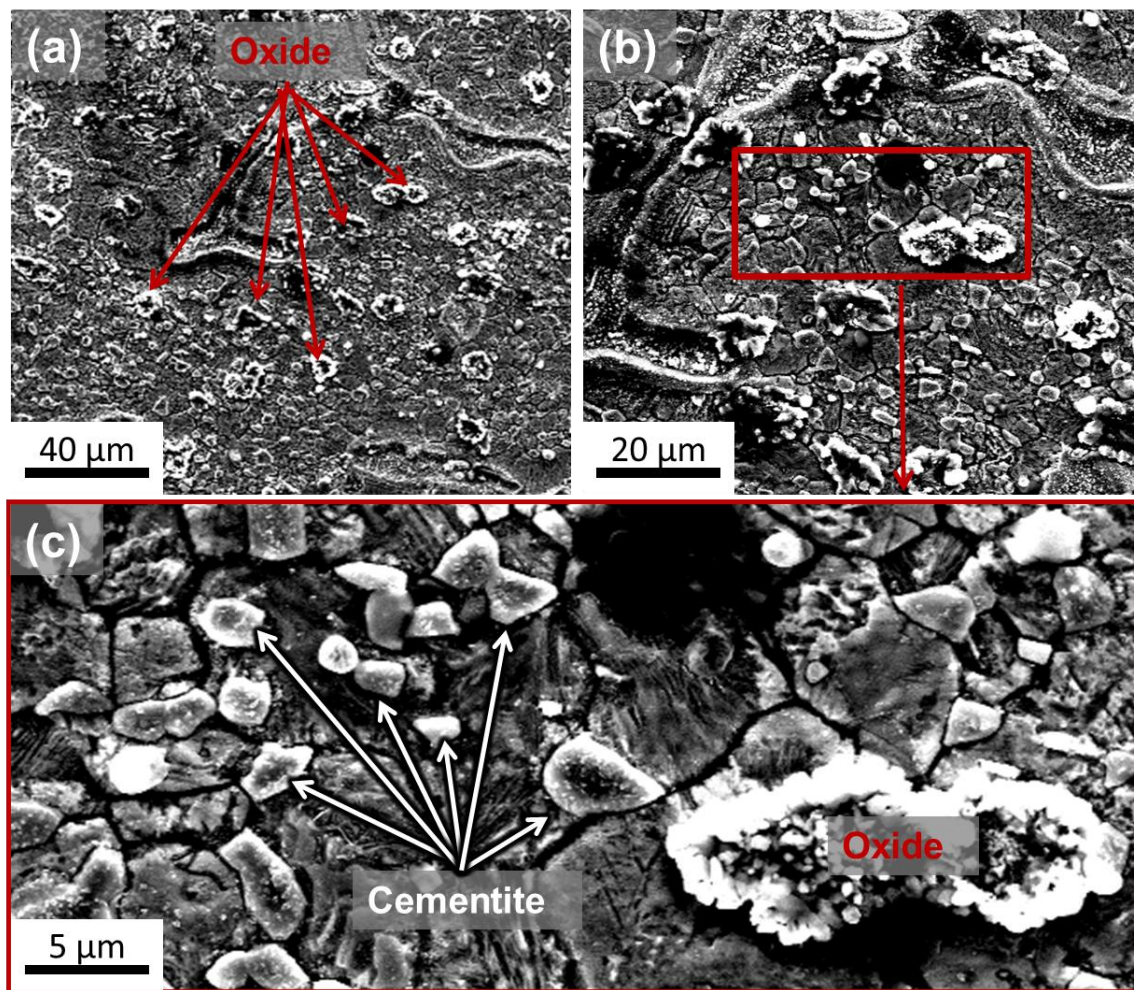
Figure 6.9 Secondary electron SEM micrographs of the CLSM sample surface from experiment 1 at progressively higher magnifications showing (a) distribution of larger oxide particles, (b) relative distributions of oxide particles and cementite particles, and (c) details of oxide and cementite particle morphologies.

In the etched cross-sectioned surface shown in **Figure 6.10 (a)**, particle-containing regions and particle-free regions were found. An example of a particle-free region is shown in

Figure 6.10 (b); these smooth and featureless regions were apparently distributed randomly throughout the microstructure. Cementite particles sizes and morphologies in the etched cross-sectioned surface were very similar to the original untreated CLSM sample surface, with the exception that particles with the characteristic oxide morphology were not observed in cross-section.
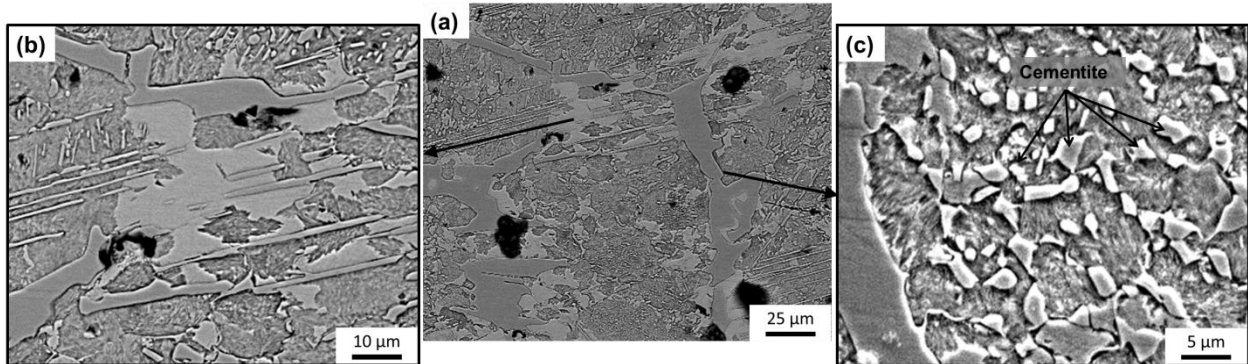
Figure 6.10 SEM micrographs about 500 μm deep into the cross-section of the CLSM sample from experiment 1 showing (a) the over-all microstructure which contained (b) particle-free areas and (c) particle-containing areas. Cementite particles had morphologies and sizes similar to the cementite particles on the original surface.

6.4.3 Experiment 2: 8°C/s heating, 45 minute 1000°C isothermal hold, 7-16°C/min cooling

Isothermal Hold at ~1000°C

Particles in experiment 2 were first resolvable in the microstructure after about 83 seconds of heating above 500°C. Particles grew steadily over time as seen in **Figure 6.11 (b-f).** It is apparent in the figure that particle distributions were not homogenous. For instance, in **Figure 6.11 (f)** the left portion of the micrograph contained few particles, while the right portion of the micrograph contained many particles. The particle density appeared to be correlated to the density of grain boundaries in the region, or grain size. In **Figure 6.12** the small-grained right half of the figure contained a high particle density, and the larger-grained left half of the figure contained a lower particle density. Particles coarsened over time, and consequently the particle density in both regions decreased over time. Certain particles on the grain boundaries in the

141

lower density region appeared to grow abnormally quickly. For instance, the boxed region in **Figure 6.12 (a) and (b)** contained only a small particle at 11 and 20 minutes of isothermal heating, which developed into a very large particle (compared to the sizes of particles in the high density region) after 47 minutes of isothermal heating in **Figure 6.12 (c).**
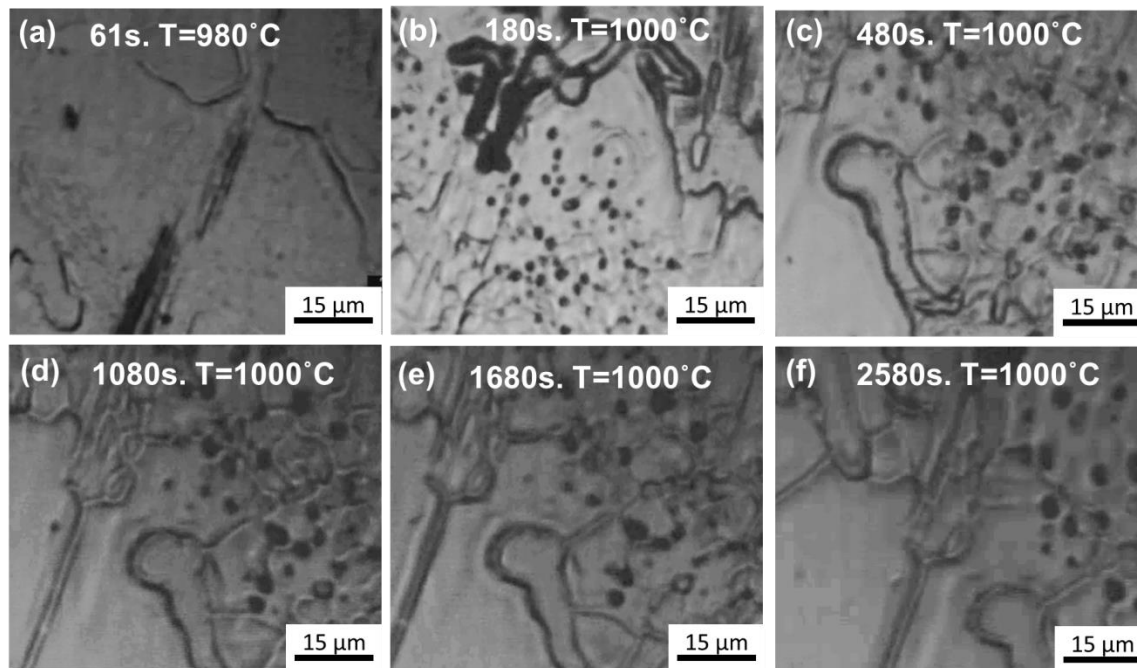
Figure 6.11 CLSM video frames from the isothermal hold at 1000˚C during experiment 2 showing (a) the matrix free of resolvable particles after 61s followed by progressive coarsening of particles at (b) 180s, (c) 480s, (d) 1080s, (e) 1680s, and (f) 2580s.
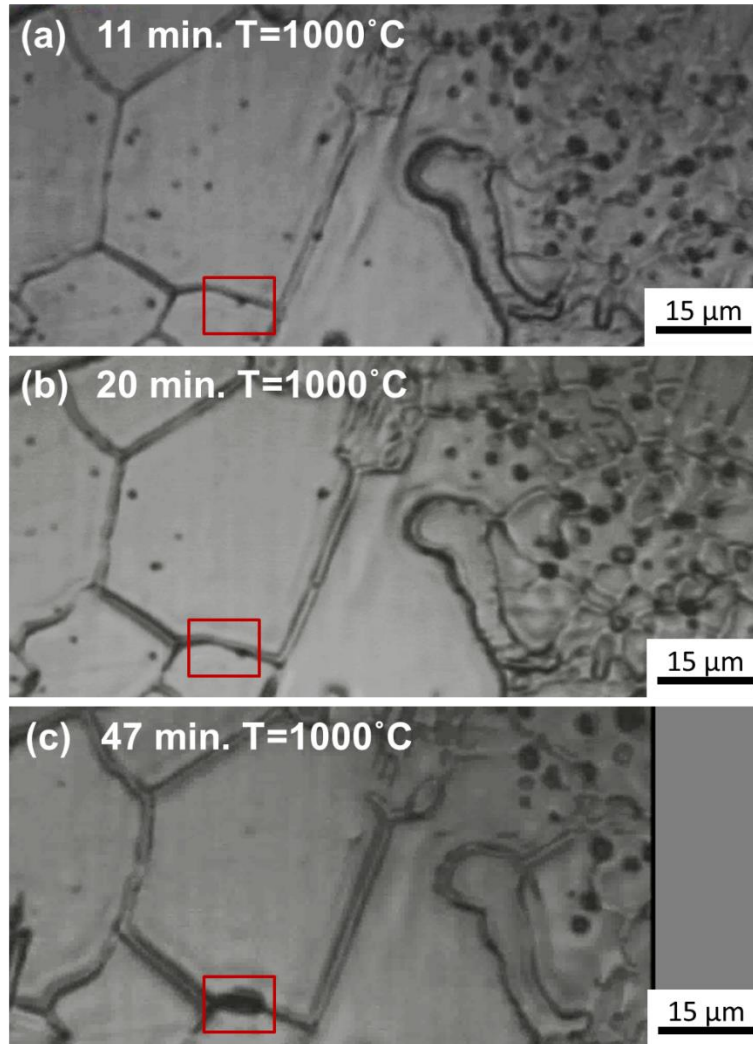
Figure 6.12 CLSM video frames from the isothermal hold at 1000°C during experiment 2 showing a region with a non-uniform distribution of particles after (a) 11 minutes, (b) 20 minutes and (c) 47 minutes of heating. Red boxes indicate a growing grain boundary particle.

Cooling

As cooling progressed, particles grew larger and the samples surface roughened. Particle sizes in the low particle density region increased significantly during cooling as indicated by white arrows in **Figure 6.13 (a-c)**. Some of the apparent change in size could be due to additional thermal grooving in response to the mismatched thermal expansions of austenite and cementite during cooling (see **Figure 5.20**). The cementite network carbides appeared smooth during the isothermal hold as shown in **Figure 6.13 (a)**, but roughened during cooling, as shown

in **Figure 6.13 (b)**. Grain boundary particle size growth over time during the (a) isothermal hold

and (b) cooling process is shown in **Figure 6.14**.
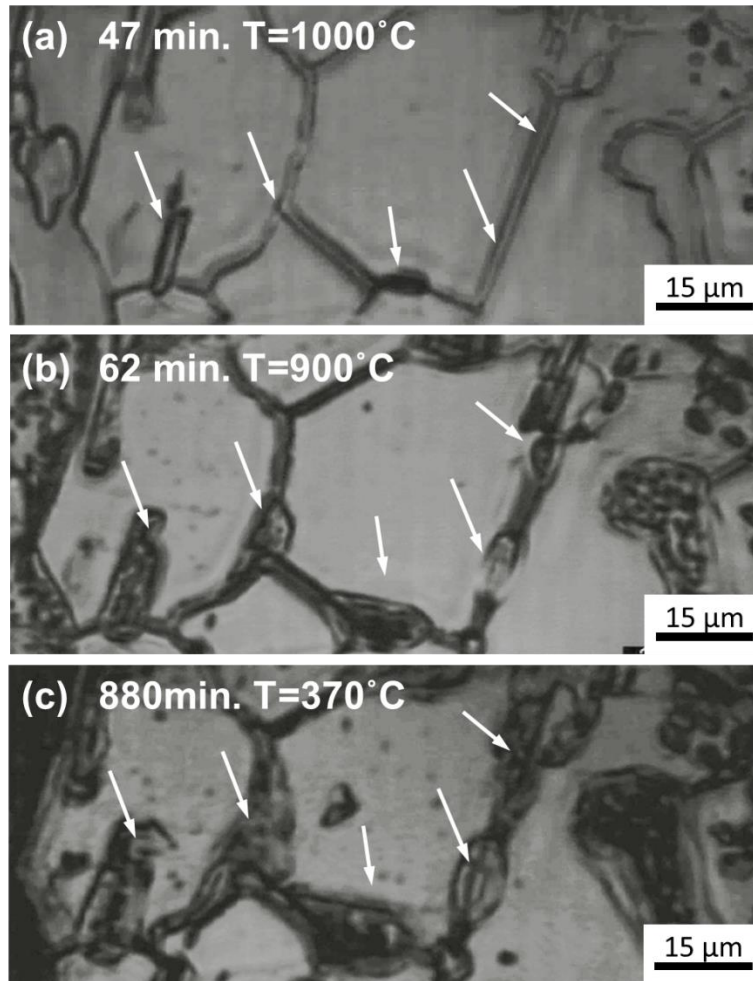
Figure 6.13 CLSM video frames from experiment 2 showing the microstructure during cooling at (a) 1000˚C, (b) 900˚C, and (c) 370˚C. White arrows indicate growing grain boundary particles.
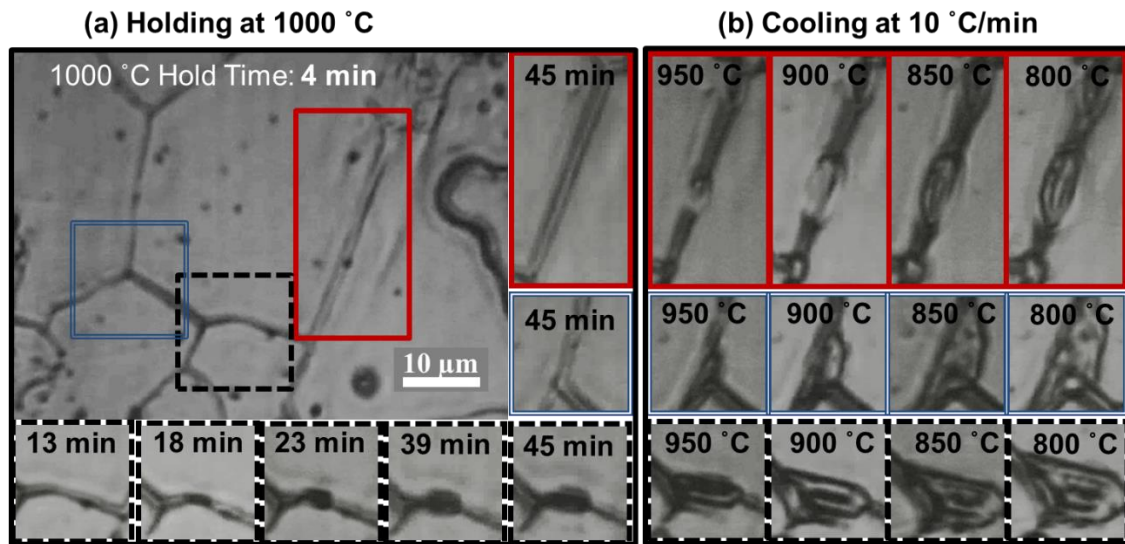
Figure 6.14 CLSM frames showing growth of carbide particles on austenite grain boundaries (a) while holding at 1000 ˚C and (b) while cooling at 10 ˚C/min.

SEM and EDS

High and low particle density regions observed in the CLSM were verified in the SEM. **Figure 6.15** shows areas with different particle densities on the untreated CLSM sample surface. Particle morphologies in the CLSM and SEM micrographs appeared very similar. Particles in the low density regions were several times larger than particles in the high density regions. EDS measurements were used to confirm that all particles were cementite, by comparing their composition to EDS measurements of cementite in previous chapters. EDS on the CLSM sample surface showed no oxygen concentration within the matrix, as indicated in **Figure 6.16 (a)**. However the network carbides were studded with small particles which contained oxygen, as indicated in **Figure 6.16 (b).**
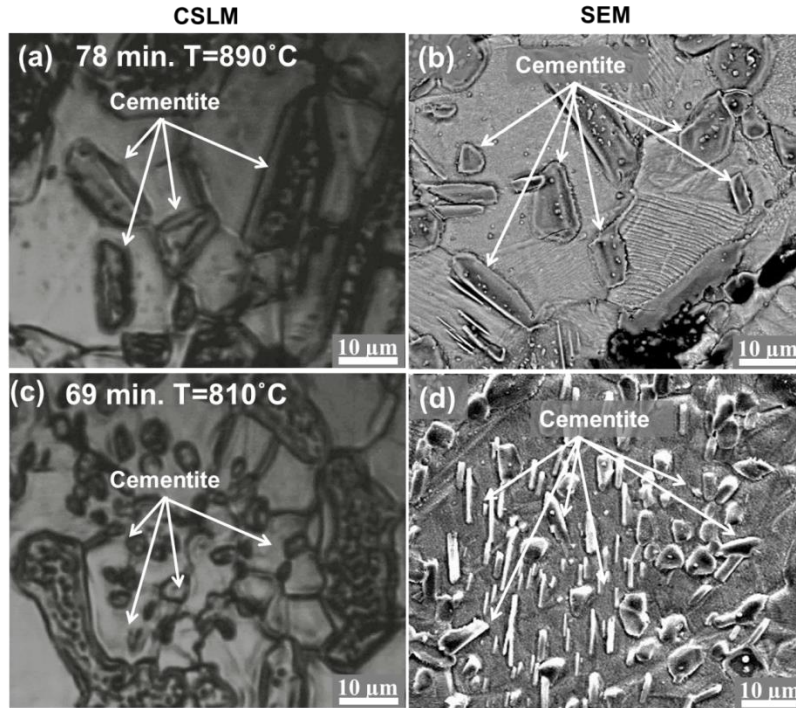
Figure 6.15 Example of carbides created by the heat treatment in low (a,b) and high (c,d) particle density areas on the surface of the UHCS sample, imaged by (a,c) *in situ* CLSM, (b,d) *ex situ* backscattered electron SEM imaging. EDS confirmed that the particles were cementite.
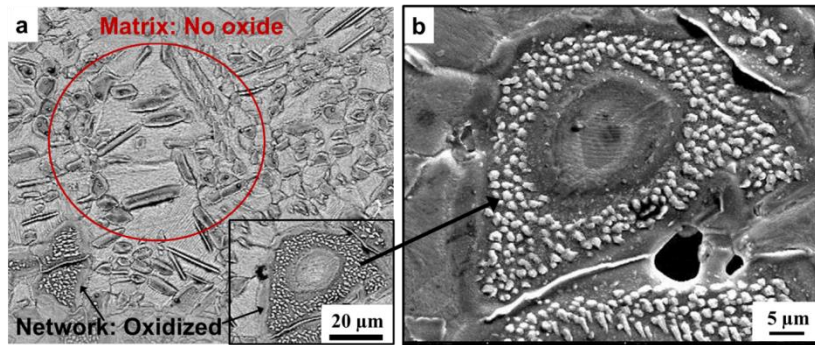
Figure 6.16 BSE SEM micrographs showing (a) unoxidized matrix and oxidized network carbides and (b) oxide particles on the network carbides.

The cross-sectioned morphology showed particle-dense regions and particle-free regions, as were seen in experiment 1 and in the surface observed by CLSM. **Figure 6.17 (a)** shows that the cross-sectioned microstructure exhibited regions with and without a high density of particles. **Figure 6.17 (b)** shows a region with a relatively high particle density, and **Figure 6.17 (b)** shows

a region with low particle density. Cementite particles in the high particle density region of the cross-sectioned sample were smaller than the carbides on the surface.
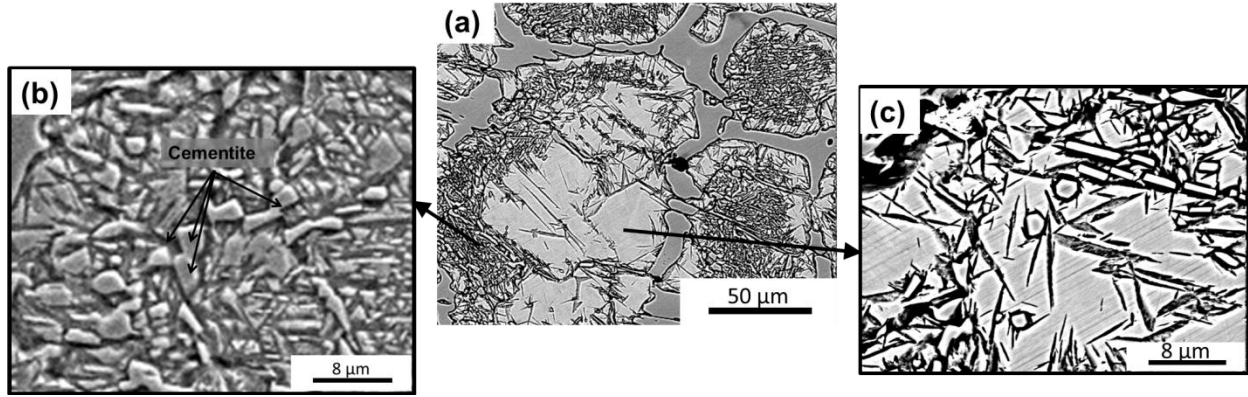
Figure 6.17 SEM micrograph of (a) a cross-section of the CLSM sample from experiment 2 showing (b) regions with high particle density and (c) regions with low particle density.

6.4.4 Experiment 3: 6°C/s heating, 60 minute 1050°C isothermal hold, 8°C/min cooling

Heating and Isothermal Hold at ~1050°C

Particles appeared and coarsened during experiment 3. The isothermal holding temperature for experiment 3 was higher than experiments 1 or 2. **Figure 6.18** shows a series of images from different times during the isothermal hold at ~1050°C. Particles sizes were larger as a function of time than the first two experiments.

Cooling

Particles grew larger during cooling as in the previous experiments. Surface roughening during cooling was not localized to the network as in experiment 2, but rather was widespread over the entire surface as in experiment 1. There may have been precipitation of new particles at around 800°C as shown in the circled regions in **Figure 6.19 (a) and (b)**. It is also possible that the circled particles were becoming visible by coming into better alignment with the CLSM focal plane.
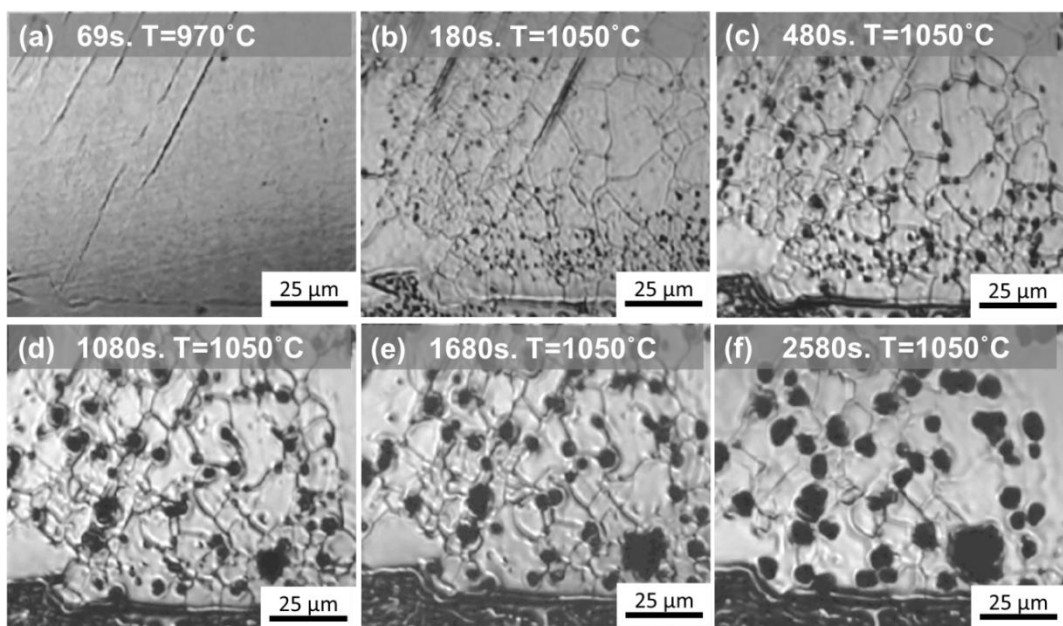
Figure 6.18 CLSM video frames from the isothermal hold at around 1000°C during experiment 3 showing (a) the matrix free of resolvable particles after 69s followed by progressive coarsening of particles at (b) 180s, (c) 480s, (d) 1080s, (e) 1680s, and (f) 2580s.
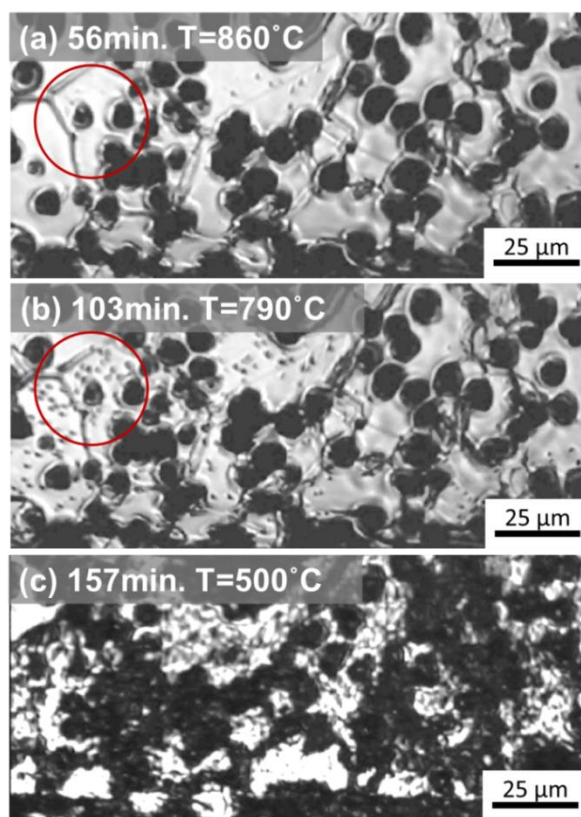
Figure 6.19 CLSM frames from experiment 3 showing the microstructure during cooling at (a) 860°C, (b) 790°C, and (c) 500°C. Circled regions indicate possible precipitation of new particles.

6.4.5 Experiment 4: 8°C/s heating, 1125°C Max Temperature, no Isothermal hold, 27°C/s cooling

Heating and Cooling

Experiment 4 involved rapid heating and rapid cooling. As shown in **Figure 6.20 (a),** particles were not discernable in the matrix at 78s when the maximum temeprature was reached. Particles appeared abruptly within seconds of the start of cooling, and grew rapidly as cooling progressed.
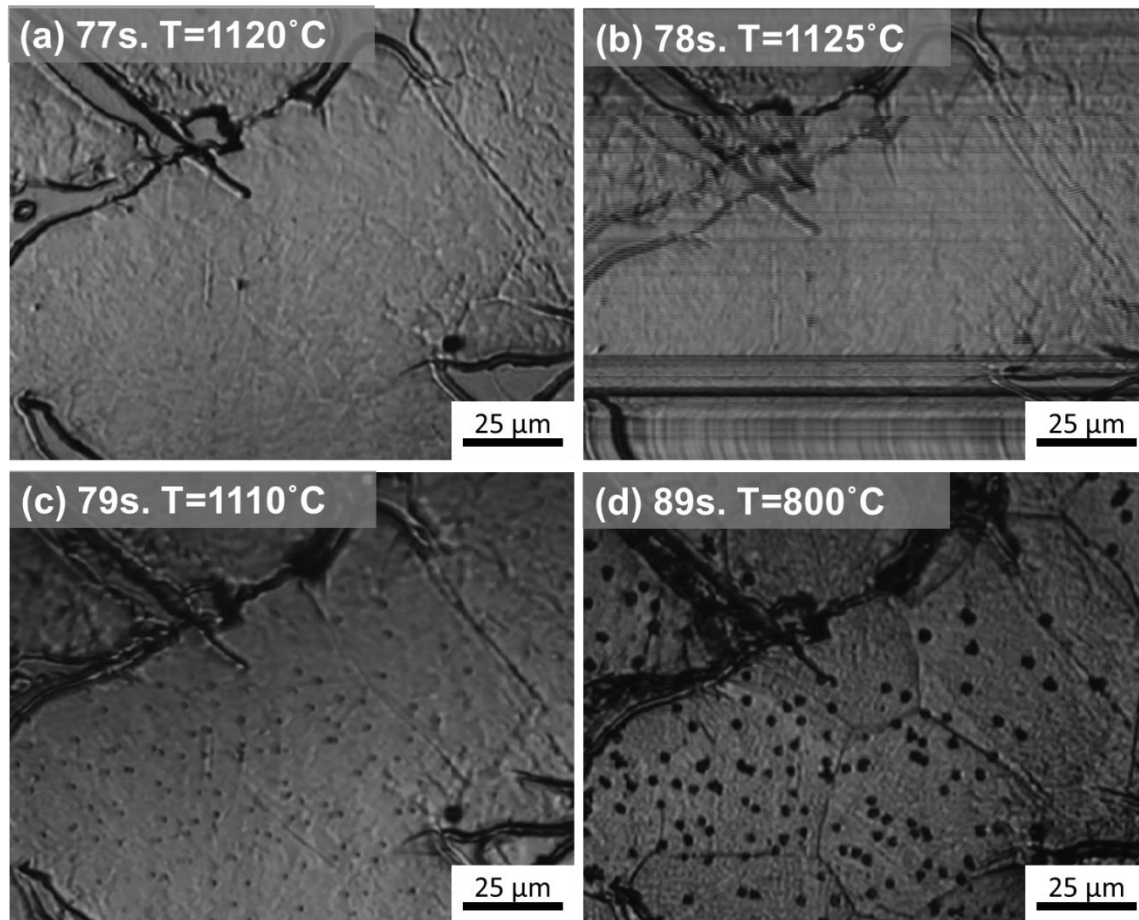
Figure 6.20 CLSM video frames from experiment 4 showing the microstructure after heat treating for (a) 77s, (b) 78s, (c) 79s, and (d) 89s. Cooling began at 78s.

SEM and EDS

Figure 6.21 shows SEM micrographs of the surface of the CLSM sample heat-treated in experiment 4. EDS measurements at the points and areas indicated in **Figure 6.21** are summarized in **Table 6.3.** The EDS measurements indicated that the particles visible in the CLSM were chromium oxide particles, rather than cementite.
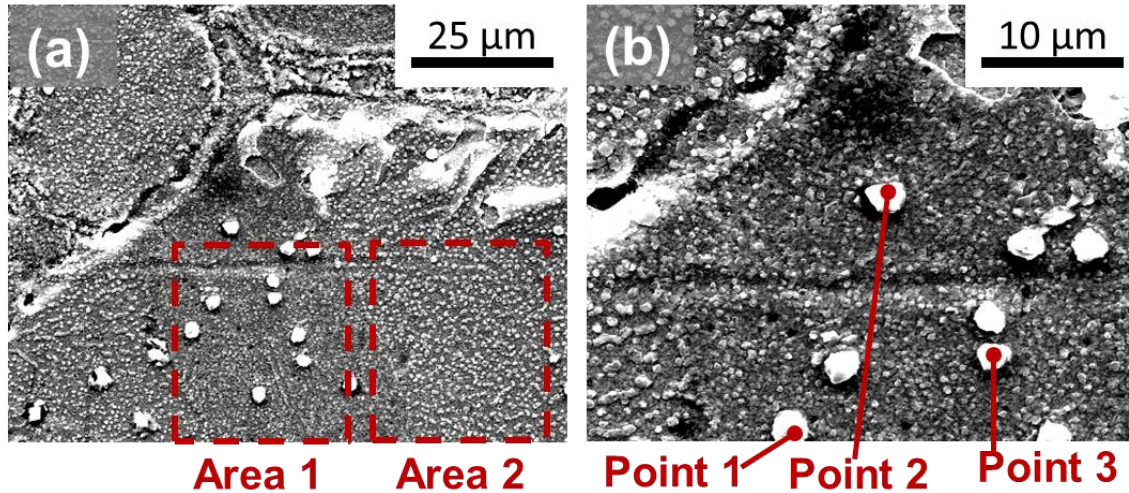
Figure 6.21 SEM micrographs of the sample surface from experiment 4 at (a) lower magnification and (b) higher magnification. Locations of point and area EDS scans are indicated on the figures.

Table 6.3 EDS compositional analysis results.

EDS	O	Si	Cr	Mn	Fe	Ni
(a) Area 1	11.16	0.67	3.10		83.65	1.43
(a) Area 2	12.63	0.74	2.59	1.12	81.58	1.34
(b) Point 1	29.02	1.56	19.10	13.65	36.67	--
(b) Point 2	35.01	2.46	15.34	13.89	30.21	--
(b) Point 3	35.97	2.27	20.17	16.25	25.34	--

6.5 Discussion

6.5.1 Thermal Grooving

`

Much of the additional contrast that developed in the CLSM videos during heating was a result of thermal grooving. Thermal grooving is a well-understood phenomenon (*135*) whereby free surface energies and grain boundary energies reach a balance by forming a groove of angle governed by the equation:

$$2\gamma_s\sin\beta=\gamma_b$$

where γ_s is the surface energy, γ_b is the grain boundary energy, and β is the angle of the groove with respect to the plane of the grain boundary. Thus, every grain boundary or interface in the CLSM sample developed a thermal groove during heating. Due to the CLSM optics, both ridges and grooves appeared to be dark; thus, the thermal grooving effect might cause some particles to appear larger than their actual sizes due to the inability to distinguish particle edges from the grooves surrounding them.

6.5.2 Heating

During heating of all four CLSM samples, the cementite network/matrix interfaces quickly developed thermal grooving. Thermal grooving also eventually developed in the matrix at austenite grain boundaries. The reason that the network/matrix interface developed grooving before the matrix/matrix interfaces may have been due to the requirement for pearlite to transform into austenite. The ongoing pearlite to austenite reaction may have disturbed the interfaces between pearlite colonies sufficiently to prevent thermal grooving until the completion of the transformation.

6.5.3 Isothermal Holds

Oxidation

The four CLSM experiments were affected by oxidation to different extents. In experiment 1, the largest particles observed during the isothermal hold were determined to be

`

oxides when examined later in the SEM. In experiment 2, the matrix was free of oxides but the network became oxidized during cooling. The extent of oxidation in experiment 3 is unknown, as that sample was not investigated in the SEM after the CLSM heat treatment. In experiment 4, all particles observed in the CLSM were oxides. There was no way to differentiate oxide particles from cementite particles in the CLSM video. Consequently, only experiment 2 was suitable to quantitatively investigate particle coarsening in the CLSM.

Cementite Particle Coarsening

The sizes of particles at different times during the isothermal hold of experiment 2 were measured in ImageJ from CLSM video frames such as those shown in **Figure 6.22**. Only about 100 particles were contained in each frame. **Figure 6.23** shows a log-log plot of average particle sizes versus time for experiment 2. The equation for the trend line indicated a coarsening exponent n of about 5, which was similar to the value found for IG particles in the box furnace experiments in chapter 4. The k value for coarsening in the CLSM was about 0.08 $\mu m^{1/5}$, which was larger than the k values found in Chapter 4. Consequently, particle sizes measured in the CLSM were several times larger than IG or GB particles measured in chapter 4 for a given time.

This difference in particle size between CLSM and box furnace studies might be a result of several different factors: (1) the limited resolution of the CLSM could not capture the smallest particles; (2) the free surface might have led to faster diffusion; (3) the free surface might have altered the carbide morphology from globular to disc-shaped. The minimum particle size measured in the CLSM was about 0.2 μm, while the minimum particle size measured by SEM was about 0.06 μm. However, excluding particles less than 0.2μm from the SEM measurements did not affect the positions of the IG or GB distributions. If the free surface diffusion was controlling coarsening then the coarsening exponent should be closer to 2 than 5, which was not

the case. Thus it appeared that the contribution of surface diffusion to particle coarsening was relatively small. Therefore, the most likely explanation for the larger sizes of particles in the CLSM sample was probably that the particle shapes were elongated along the plane of the free surface. This explanation also accounts for the factor of 2-3 difference in size between particles on the surface and particles in cross-section for CLSM experiment 2.
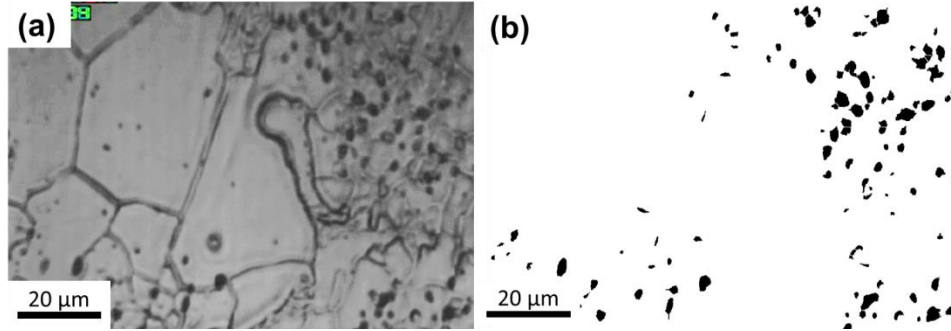
Figure 6.22 (a) An individual frame from CLSM video of experiment 2 was (b) analyzed in ImageJ to find particle sizes.
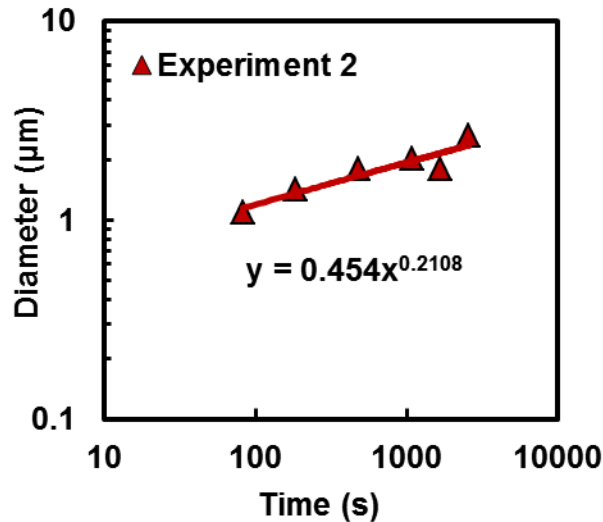
Figure 6.23 Plot of average particle sizes versus time for experiment 2.

Particle Distributions

The microstructures of experiment 1 and experiment 2 both contained regions of high and low particle density. These regions were found hundreds of microns below the top surface as well as after cross-sectioning the samples. In Chapter 4, particle-free denuded zones in the 2C-4Cr

`

UHCS were found consistently adjacent to the cementite network. In chapter 5, particles in the 2C-1Cr UHCS clustered near the branches of the cementite network. However, in the CLSM samples, denuded zones appeared to be distributed more randomly through the microstructure. The difference in heat treatment temperature might play a role; CLSM experiments were conducted at around 1000°C, while the box furnace experiments were at most 970°C. Decarburization of the CLSM sample might also have been a factor.

6.6 Summary and Conclusions

Four CLSM experiments were conducted in this study in order to observe cementite particle coarsening *in situ*. The experiments all showed particles which appeared early on in the first few hundred seconds of heating past 500°C, and coarsened over time as isothermal heating continued. All experiments were impacted by oxidation to different degrees; oxide particles formed in the matrix of experiment 1, experiment 4 and possibly experiment 3. The oxide particles could not be distinguished from cementite particles in the CLSM videos, thus those experiments were not suitable for investigating coarsening kinetics. Only the matrix of experiment 2 was oxide-free. The coarsening exponent of particles in experiment 2 was about 5, which was the same as the coarsening exponent of the IG particles in chapter 4, indicating control of coarsening by diffusion along dislocations. However, CLSM particles were several times larger for any given time. The size difference might have been a result of an elongated disk shape of particles at a free surface.

Experiments 1 and 2 showed regions of high and low particle density at the surface and in cross-section. These regions were similar to the denuded zones identified in chapter 4, but were not generally adjacent to the cementite network branches.

`

Chapter 7. Effects of Nb Modification and Solidification Rate on Microstructure in an 2C-4Cr Ultrahigh Carbon steel

7.1 Abstract

In this chapter changes to the microstructure of an ultrahigh carbon steel (UHCS) caused by Nb addition are investigated at two solidification rates. Parameters of interest were carbide network volume fraction, branch spacing, and connectivity. First, rapidly cooled Nb-free and Nb-modified UHCS samples were produced by melting and re-solidifying industrially-produced base UHCS in a button melter with and without an addition of Nb powder. Sections of the button melted samples were then re-melted and solidified in a tube furnace with much slower cooling rate. Microstructures were characterized using scanning electron microscopy, X-ray diffraction, and electron dispersive spectroscopy, and compared with computed equilibrium phase fraction and composition. The Nb addition had a significant effect on the UHCS microstructure. Nb combined with C to form NbC structures before and during austenite solidification, reducing the effective amount of carbon available for the other phases. Network spacing was also strongly influenced by the sizes of the NbC structures. Network spacing in the Nb-free samples without NbC structures was controlled by the solidification rate (faster solidification led to a more refined network).

7.2 Introduction

Allotriomorphic carbide phases in UHCS tend to form a network on austenite grain boundaries, providing undesired sites for crack initiation and propagation. Hence, the network is very deleterious for toughness and reducing network connectivity is of interest for improving mechanical properties. In Chapter 3 of this dissertation, a method was developed to quantify network connectivity in terms of a connectivity index. Other parameters of interest regarding the

`

network are volume fraction and branch spacing. The carbide network in UHCS is surrounded by a matrix, which could be pearlite (lamellar eutectoid cementite + ferrite), bainite, martensite, and/or retained austenite depending on the processing conditions. While the matrix always strongly affects steel hardness, its effects on toughness are limited once the network exceeds a critical connectivity index (*77*).

Two methods of network break-up have achieved success in UHCS: thermomechanical processing (*36, 37, 42*) and chemistry modification (addition of high temperature carbide/oxide forming elements to the melt) (*46–49*). Thermomechanical processing aims to break connections within an existing network through heavy mechanical deformation, while chemistry modification seeks to prevent the network from forming as a highly interconnected structure in the first place. In this work we have opted to study chemistry modification. Chemical modifiers which have seen success in network break-up, or connectivity reduction, are rare earths such as Ce/La (*47, 49*) or Nb (*48, 63*). Ce and La were reported to form oxides in the melt that serve as heterogeneous nucleation sites for eutectic carbides, resulting in a finer and less connected structure overall. Similarly, Nb forms NbC that is speculated to serve as austenite and eutectic carbide nucleation sites. The objective of this chapter is to further investigate mechanisms by which Nb modifies the microstructure, specifically to quantify and explain any reduction of network connectivity caused by Nb addition.

The effects of alloying with different amounts of Nb (0.025 – 7 wt%) have been studied in hypoeutectoid steels (*55–58*), UHCS (*48, 59–61*), and cast irons (*62–70*), with a wide variety of Cr contents (0-30 wt%). In all cases, researchers found that increased additions of Nb resulted in microstructural refinement, i.e. smaller grains or carbide particles, and were generally correlated with improvements in mechanical properties such as hardness, wear resistance, tensile

156

ductility, and/or toughness. The degree of carbide network refinement (reduction in network/eutectic dendrite secondary arm spacing) varied from a few percent up to a factor of two, depending on the cooling rate and the amount of Nb added (*48*, *60*). Nb additions were also reported to lower the volume fraction of eutectic carbides (*48*, *60*, *63*). Even very small Nb additions in the range of 0.025-0.120 wt% (*61*) or 0.1-0.6 wt% were found to improve mechanical properties in steels with several different base compositions(*69*).

Few studies directly addressed the effects of Nb on steel toughness. Fiset *et al.* (*63*) reported a fracture toughness enhancement of about 7% in a 3C-17Cr white cast iron after alloying with 2 wt% Nb. Hamidzadeh *et at*. (*48*) reported an 85% enhancement in Charpy impact toughness in a 1.5C-11Cr UHCS after alloying with 1.5 wt% Nb. Both studies contained M_7C_3 as their primary cabide phase. In chapter 3, the Charpy impact toughness enhancement reported by Hamedzadeh was attributed to a network breakup sufficient to reduce the network below a critical connectivity value. This chapter explores the effects of a similar Nb modification on network and matrix microstructure.

7.3 Materials and Methods

Sections of a centrifugally casted and industrially heat-treated UHCS mill roll were provided by Miller Centrifugal Casting (MCC). Two melting methods were employed to examine the effects of cooling rate on microstructure development. First, two samples from the roll were re-melted in a Cianflone Scientific Instruments Corp model 2701 electric arc button melter. One sample was modified by an addition of pure niobium powder (Nb-modified button) and the other was an unmodified control (Nb-free button). Each sample was re-melted four times to ensure homogenous mixing of the Nb powder into the liquid. The button melter utilizes a

water-cooled copper mold, so the cooling rate of the button melted samples was very rapid due to the high thermal gradient at the mold walls.

After button melting and rapid cooling, the samples were cut in half. One half of each sample was retained for microstructural analysis, and the other halves of the samples (about 20g each) were placed in separate zirconia crucibles and simultaneously re-melted in a tube furnace. The tube furnace reached a maximum temperature of 1600°C, then was slowly cooled at a rate of 2°C/min to 1200°C, 1°C/min to 800°C, and 3°C/min to room temperature. **Figure 7.1** shows a schematic of the sequential melting steps and **Table 7.1** shows the compositions of all the samples. Samples were shipped to IMR labs in New York for compositional analysis. At IMR, Carbon and silicon contents were measured by combustion-infrared absorbance, and the other elements by ICP-AES per ASTM 1090-11. There was some decarburization of samples remelted in the button melter, and further decarburization of samples remelted in the tube furnace. The Nb-free compositions contained a very small amount of Nb (0.02 wt%), but this was considered negligible in comparison to the Nb contents of the Nb-modified samples.
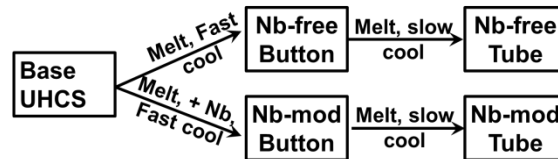
Figure 7.1 Schematic diagram of experiments.

Table 7.1 Composition of UHCS samples (in wt%).

Sample	Fe	Nb	Cr	C	Mn	Mo	Si	Ni
Base UHCS	Bal.	0.02	4.01	2.07	0.68	0.34	0.67	1.52
Nb-free Button	Bal.	0.02	4.13	1.93	0.83	0.37	0.73	1.54
Nb-Mod Button	Bal.	1.74	3.95	1.95	0.68	0.33	0.57	1.59
Nb-free Tube	Bal.	0.02	3.99	1.76	0.75	0.36	0.77	1.52
Nb-Mod Tube	Bal.	2.02	3.67	1.62	0.75	0.33	0.75	1.55

Samples from the base UHCS, button melter, and tube furnace were cross-sectioned and polished with 1μm alumina solution. The polished cross-sectioned sample surfaces were examined using a FEI XL-30 field emission gun (FEG) SEM at 20 keV accelerating voltage in backscatter electron (BSE) imaging mode, which enhanced compositional contrast to aid in differentiating various phases. Compositions of different phases in the microstructure were analyzed in the SEM using an Oxford Instruments INCA X-act electron dispersive spectrometer (EDS). Microstructural phases present in the sample were also characterized by a Panalytical X'Pert Pro MPD X-ray diffractometer (XRD) using Co K_α radiation over a θ range of 30-100° with a three hour scan time and 0.05° step size. Samples were then etched in Nital and examined again using OM and SEM. Quantitative analysis of micrographs was done using the open source program ImageJ (https://imagej.nih.gov/ij/) (*89*).

Equilibrium pseudo-binary phase diagrams and the compositions and volume fractions of phases identified by XRD were calculated in Thermo-Calc (*71*) version 2017a using the TCFE9 and MOBFE4 databases to assist in interpreting the experimental results.

7.4 Results

7.4.1 Base UHCS and button melted samples

BSE SEM

The starting base UHCS sample was compared against its button melted derivatives (Nb-free button and Nb-modified button) to investigate the effects of Nb modification on the microstructure in the case of very rapid cooling. BSE SEM micrographs of the starting base UHCS microstructure and button remelted samples are shown in **Figure 7.2**. The micrographs all contained a network phase (darker features) and a matrix phase (brighter features). The base

UHCS network branches were about 10-20 μm thick, and spacing between parallel branches was on the order of 100-200 μm. Button melted sample network branches were about 5 μm thick with spacings of 25-50μm. The base UHCS also contained many faceted particles (also darker features) around 5μm in diameter homogeneously distributed within the matrix as shown in **Figure 7.2 (b).** Analysis in previous research on UHCS microstructures of similar composition to the specimens used in this study suggested that the network and particles were composed of cementite (M_3C; M=(Fe,Cr)) while the matrix was composed of ferrite, austenite, pearlite, bainite, martensite, or a mixture thereof (*77, 95*).
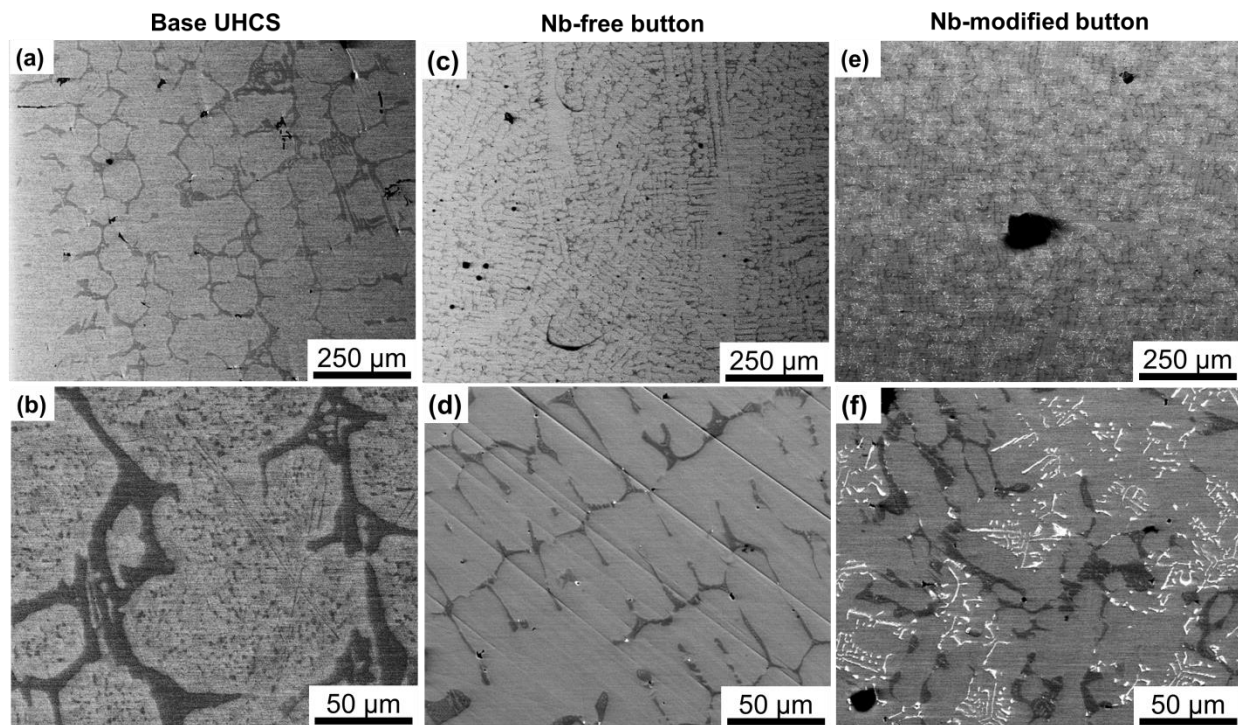
Figure 7.2 SEM BSE micrographs of UHCS specimen microstructures at lower and higher magnification, including (a,b) the base UHCS microstructure, (c,d) the Nb-free button microstructure, and (e,f) the Nb-modified microstructure.

The Nb-modified button sample contained complex structures (brightest features) about 20-50 μm in size within the matrix shown in **Figure 7.2 (f)**. Compositional variations produce BSE contrast, so the high brightness of the complex features relative to the network and matrix

160

`

indicated a higher average atomic mass ($\bar{Z}$). NbC has a $\bar{Z}$ of about 37 while pure iron and cementite have $\bar{Z}=26$ and 24.6, respectively. Thus, it is to be expected that NbC would appear brighter than austenite or cementite in BSE images.

XRD

In order to identify the phases present within the base UHCS and button specimens, samples were analyzed using XRD. Data from θ-2θ scans for all samples are shown in **Figure 7.3**. Phases identified in the scans were austenite (γ), ferrite/martensite (α), cementite (Fe_3C), and NbC. All samples contained many unique peaks belonging to Fe_3C. The base UHCS θ-2θ scan shown in **Figure 7.3 (a)** contained prominent α peaks, while the button scans shown in **Figure 7.3 (b)** did not. Both button and base UHCS θ-2θ scans had perceivable γ peaks, but the austenite phase was much more prominent in the buttons. Thus, the button melting process increased the relative amount of retained austenite in the UHCS microstructure. The Nb-modified button θ-2θ scan shown in **Figure 7.3 (b)** contained prominent NbC peaks while the two Nb-free scans did not. Thus, the XRD measurements confirmed that Nb modification produced NbC in the Nb-modified button microstructure.
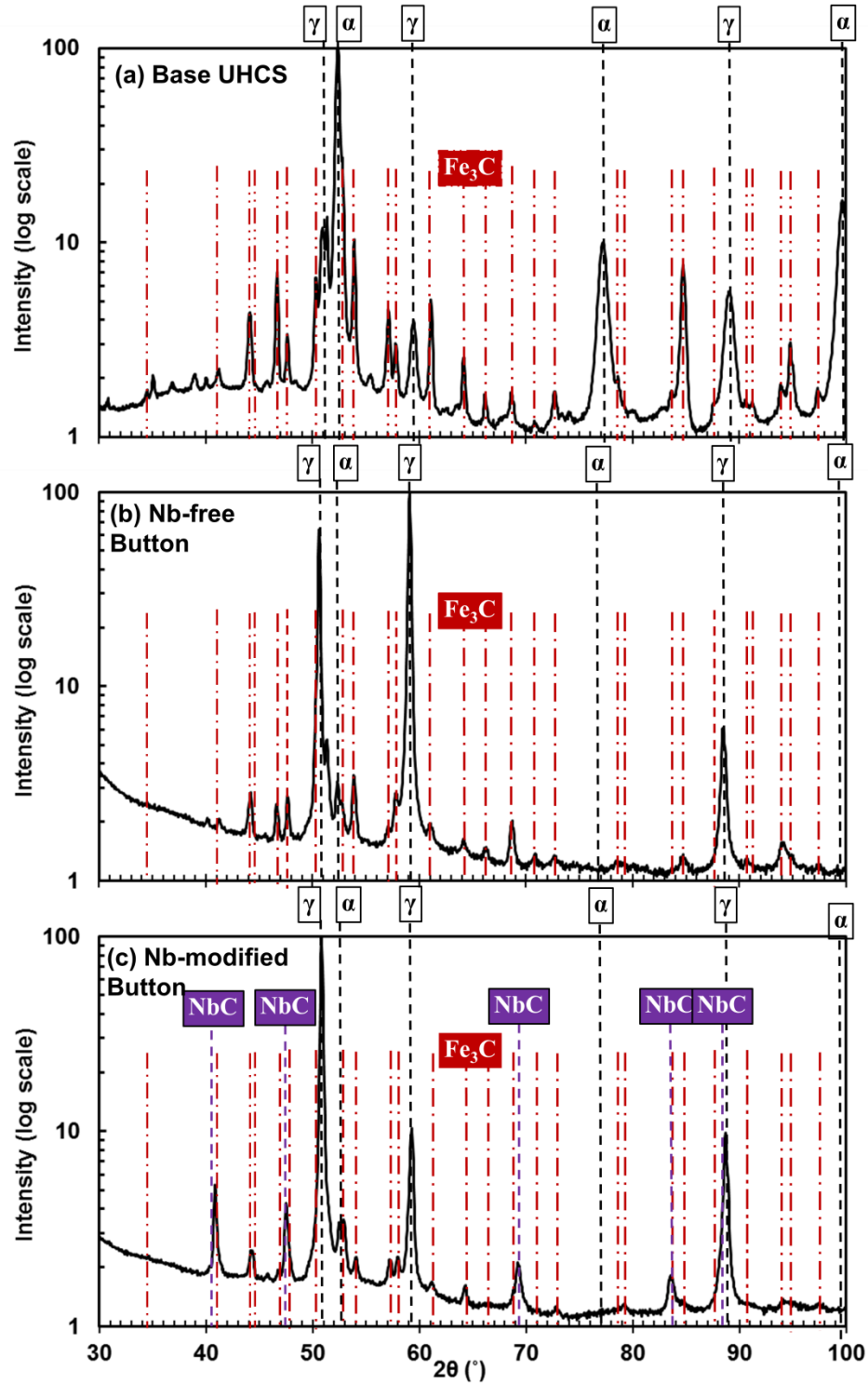
Figure 7.3 XRD θ-2θ scan with peaks identified for (a) the base UHCS, (b) the Nb-free button, and (c) the Nb-modified button specimen.

EDS

Compositional variations of the different regions within the specimens were investigated by point and area EDS analyses. Examples of the types of areas and points that were sampled for EDS are shown for the case of the base UHCS in **Figure 7.4**. EDS measurements of the compositions of the various phases within the base UHCS are summarized in **Table 7.2**. In all specimens the matrix was richer in Fe, Si, and Ni relative to the cementite network/particles and cementite was richer in C, Cr, Mn, and Mo relative to the matrix. The brightest features in the Nb-modified samples were found to contain high Nb levels and there was no Nb detected in the matrix or the network.
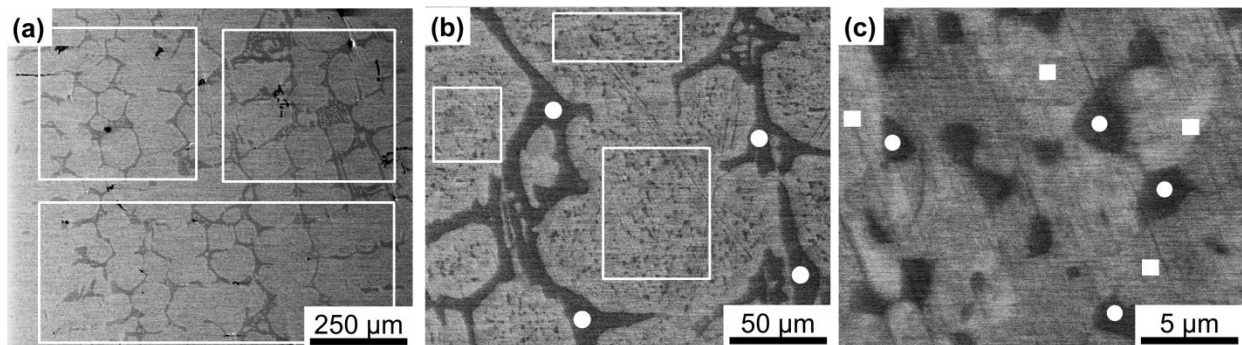
Figure 7.4 BSE SEM micrographs of the base UHCS microstructure. Open rectangular outlines and solid markers indicate EDS area and point scans on (a) the overall base UHCS microstructure, (b) the network and matrix with particles, and (c) the particles and matrix.

Table 7.2 Composition of phases (in wt%) in base UHCS and button samples measured by EDS

Overall Composition	Meas.	Fe	C	Nb	Cr	Mn	Mo	Si	Ni
Base UHCS	3	87	4	0	4.6	0.9	0.8	0.8	1.4
Nb-free Button	6	88	4	0	4.5	0.8	0.5	0.8	1.4
Nb-modified Button	3	85	4	3	4.4	0.9	0.6	0.8	1.3
Matrix Composition			C	Nb	Cr	Mn	Mo	Si	Ni
Base UHCS (with particles)	3	94	4	0	3.4	0.7	0.3	0.8	1.6
Nb-free Button	3	95	3	0	3.1	0.6	0.1	0.8	1.6
Nb-modified Button	7	94	3	0.1	3.3	0.7	0.2	0.8	1.6
Network Composition			C	Nb	Cr	Mn	Mo	Si	Ni
Base UHCS	4	75	8	0	14.3	1.1	0.8	0.1	0.3
Nb-free Button	3	75	9	0	14.6	1.1	0.9	0.1	0.4
Nb-modified Button	9	74	8	0.1	15.5	1.2	1.1	0.1	0.3

`

Segmented micrographs

One objective in this study was to investigate the effect of Nb on the cementite network connectivity. Network features were digitally segmented and then quantified to determine network area fractions and connectivity indexes. In the process of digital image segmentation, the network phase was isolated from the other phases in ImageJ using unsharp masking, thresholded blurring, and intensity thresholding. The results of the segmentation process were binary contrast images such as those shown in **Figure 7.5** (note that the magnification of **Figure 7.5 (a)** is different from **Figure 7.5 (b)** and **(c)**). Network area fractions (F_A) and connectivity indices (*77*) for the Nb-free specimens were then each calculated from 3-5 segmented images such as those in **Figure 7.5** and tabulated in **Table 7.3**. The Base UHCS and button melted UHCS all had similar network area fractions. Both Nb-free and Nb-modified buttons samples had lower network connectivity than the base UHCS. The Nb-modified button network appeared qualitatively more broken up than the Nb-free button network. This was not reflected in the measured connectivity index because network/matrix contrast in the BSE images was very poor.
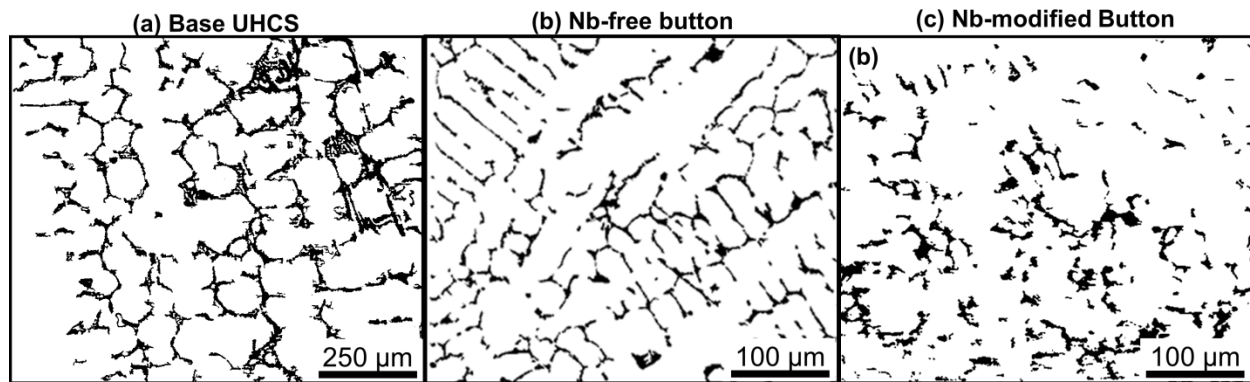
Figure 7.5 Segmented networks for (a) base UHCS, (b) Nb-free button, (c) Nb-modified button.

Table 7.3 Network area fractions and connectivity in base UHCS and button samples.

Ref. Figure	Sample	F_A	Connectivity index
Figure 7.5 (a)	Base UHCS	0.10 ± 0.01	0.90 ± 0.01
Figure 7.5 (b)	Nb-free button	0.09 ± 0.01	0.7 ± 0.1
Figure 7.5 (c)	Nb-modified button	0.09 ± 0.01	0.8 ± 0.1

`

7.5 Tube furnace remelted samples

SEM

To further understand the effect of Nb on this microstructure, additional heat treatments were performed using a tube furnace where cooling was much slower and thus more relatable to cooling after casting of large scale parts. BSE SEM micrographs of the Nb-free and Nb-modified tube specimens are shown in **Figure 7.6**. As in the base UHCS and button melted cases, the micrographs all contained a network phase (darker features) surrounded by a matrix phase (brighter features). The Nb-free tube network appeared similar to the base UHCS, with branches about 50 µm thick, and spacing between parallel branches on the order of 100-250 µm. In contrast, the Nb-modified tube network had a reticulated (web-like) rather than a solid morphology, with branches 100 µm thick and 250-600 µm spacing. As shown in **Figure 7.7**, reticulated Nb-modified tube branches also contained a homogenous distribution of very small particles (bright features within the darker network regions) which were identified as NbC particles via EDS in **Figure 7.7 (c).**

The Nb-modified tube sample also contained complex NbC structures (brightest features) within the matrix phase with similar morphology to those in the Nb-modified button sample. However, the Nb-modified tube NbC structures were much larger than those of the Nb button sample, with sizes ranging from about 100-600 µm in size. The increased size of the NbC structures was attributed to the slower cooling rate. While the Nb-containing tube network was frequently connected to the edges of NbC structures, branches of the network never cut through the Nb structures. Additional OM micrographs of the Nb-modified tube microstructure are shown in **Appendix C, Section C.2** to provide a better sense of the scales and morphologies of the microstructural features.
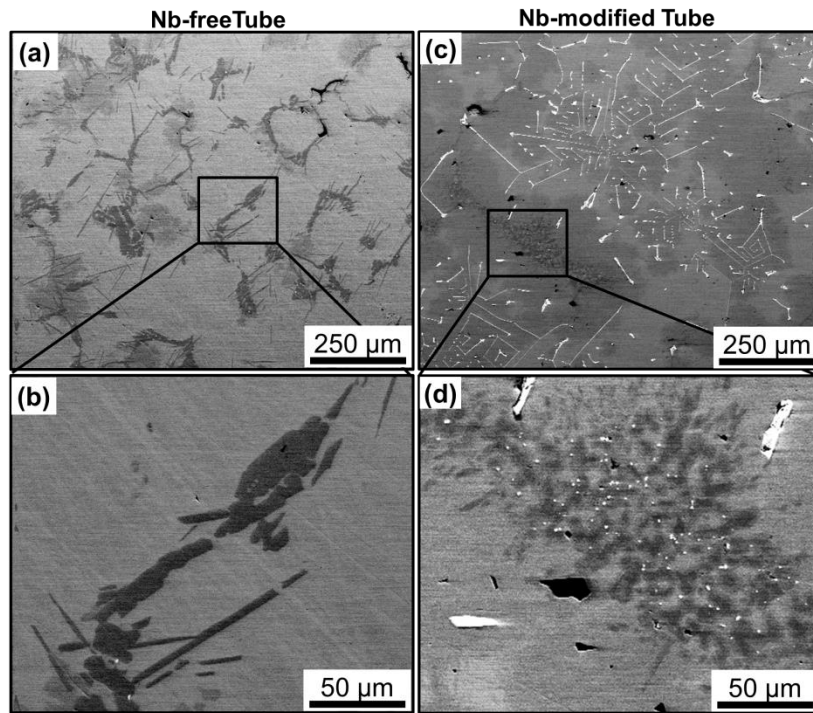
Figure 7.6 SEM BSE micrographs of (a,b) the Nb-free tube microstructure, and (c,d) the Nb-modified tube microstructure.
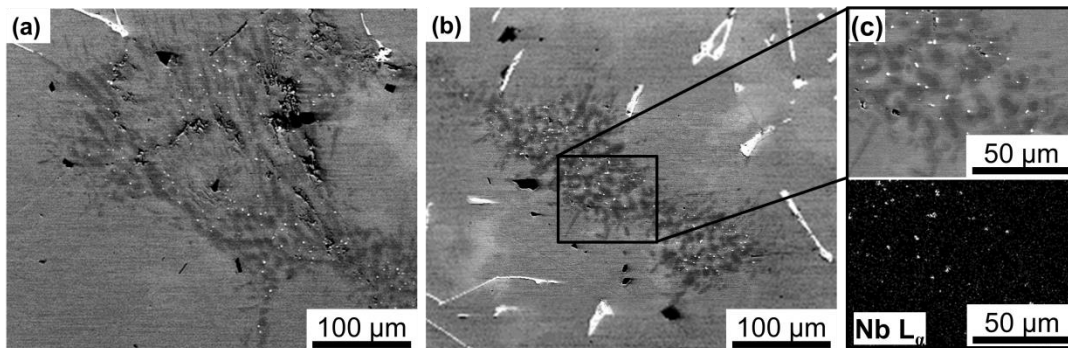
Figure 7.7 SEM BSE micrographs of (a,b) two different reticulated carbide network branches containing small very bright particles which were identified as NbC by (c) EDS element mapping.

XRD

Phases in the tube samples were also analyzed using XRD. Data from θ-2θ scans for both tube samples are shown in **Figure 7.8**. Both tube samples contained austenite (γ), ferrite (α), cementite (Fe$_3$C), and the Nb-modified tube sample additionally contained NbC.

166
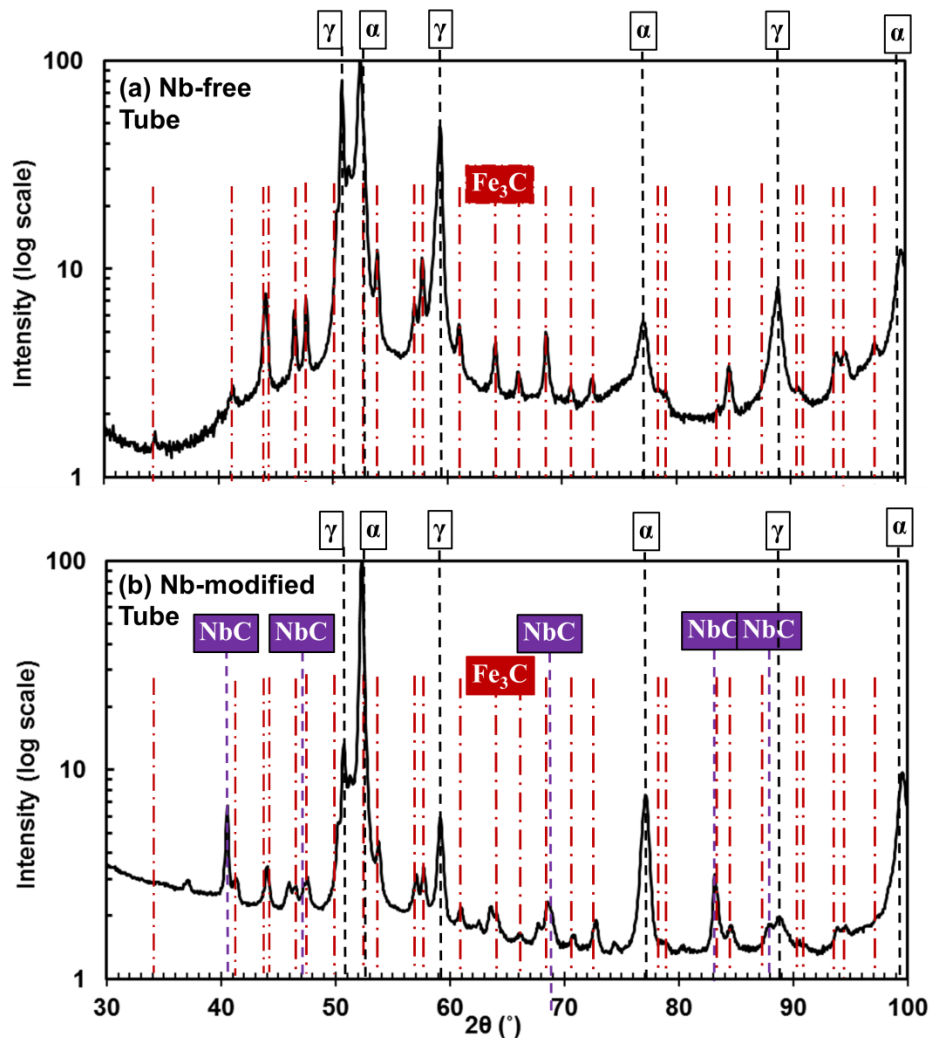
Figure 7.8 XRD θ-2θ scans with peaks identified for (a) the Nb-free tube and (b) the Nb-modified tube specimens.

EDS

Compositional variations of the different regions within the tube specimens were investigated by point and area EDS analysis. EDS measurements of the compositions of the various phases within the base UHCS are summarized in **Table 7.4**. In both tube specimens the matrix was richer in Fe, Si, and Ni relative to the cementite network/particles. NbC in the Nb-modified tube sample was rich in C and Nb and especially poor in Cr. The network in both tube samples was found to be richer in C, Cr, Mn, and Mo relative to the matrix. Although most of the

`

Nb-modified tube network had the same composition as the Nb-free tube, some areas such as those shown in **Figure 7.9** were richer in Cr (approx. 25 wt% Cr vs. 14 wt% Cr). Cr rich regions were distributed randomly throughout the network, and could not be distinguished using BSE or SE imaging.
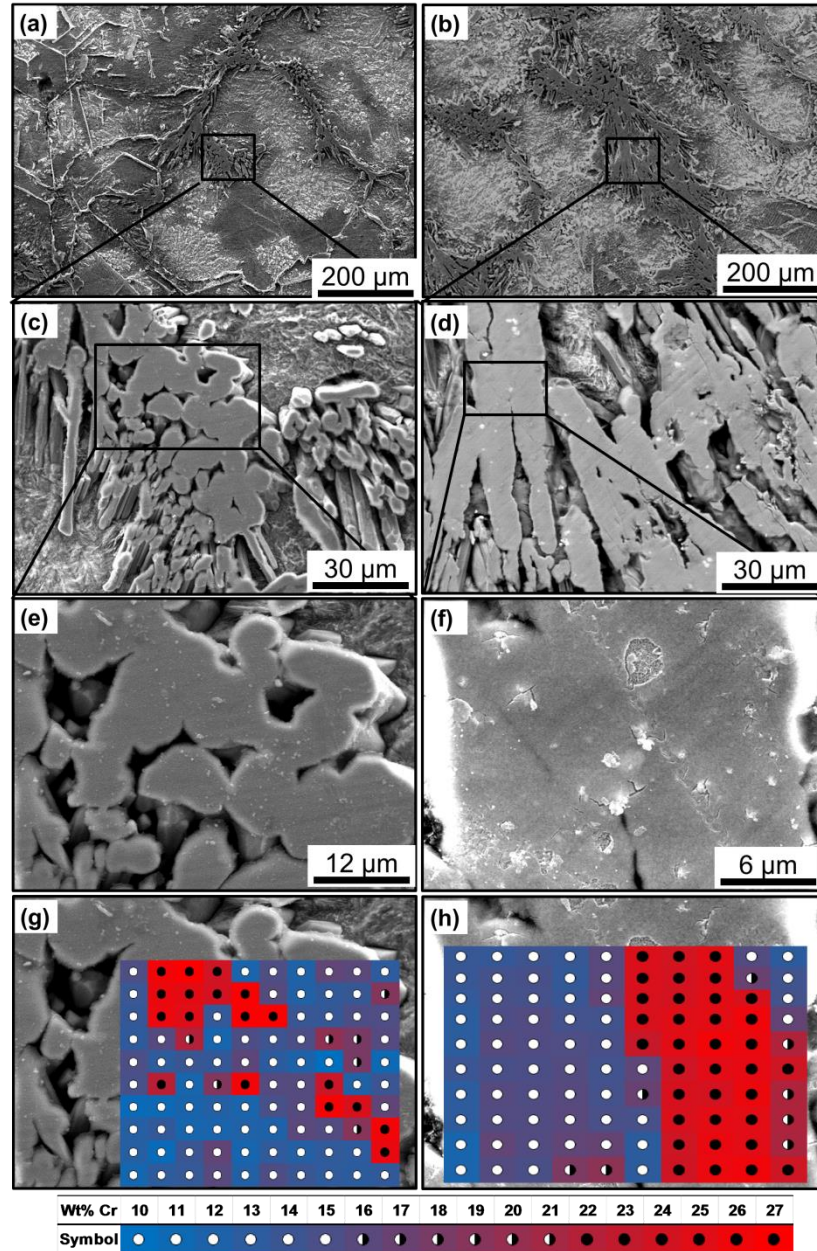
Figure 7.9 BSE SEM micrographs of (a-f) sequentially higher magnification images of two different sections of the Nb-modified tube network. Normal Cr and high Cr regions in (e,f) highly magnified network regions were differentiated using (g,h) a 10x10 array of EDS scans.

Table 7.4 Composition of phases in Nb-containing UHCS samples measured by EDS

Overall Composition	Meas.	Fe	C	Nb	Cr	Mn	Mo	Si	Ni
Nb-free Tube	3	88	4	0	4.2	0.9	0.6	0.8	1.5
Nb-modified Tube	3	85	5	3	4.1	0.8	0.6	0.7	1.4
Matrix Composition	**Meas.**	**Fe**	**C**	**Nb**	**Cr**	**Mn**	**Mo**	**Si**	**Ni**
Nb-free Tube	7	90	3	0	3.5	0.7	0.3	0.8	1.6
Nb-modified Tube	4	91	3	0	3.6	0.7	0.2	0.8	1.6
Network Composition	**Meas.**	**Fe**	**C**	**Nb**	**Cr**	**Mn**	**Mo**	**Si**	**Ni**
Nb-free Tube	9	76	8	0	13.4	1.1	1.4	0.1	0.3
Nb-modified Tube	7	76	6	0	14.8	1.0	1.7	0.2	0.4
Nb-modified Tube (High Cr)	10	62	9	0	25.0	1.3	2.5	0.2	0.2

Segmented micrographs

Network features of the tube samples were digitally segmented to produce binary images shown in **Figure 7.10**. Network area fractions were then each calculated from 3-5 segmented images and tabulated in **Table 7.5**. Network connectivity was also calculated for the Nb-free tube, but could not be quantified for the Nb-modified tube sample because of the extremely large network length scale. The Nb-free tube sample network made up about 12% of the micrograph area – slightly higher than the base UCHS and button samples connectivity was also similar to the other Nb-free samples. On the other hand, the measured area fraction of the Nb-modified tube sample network was only about 5%, which was lower than all the other samples including the Nb-modified button sample.
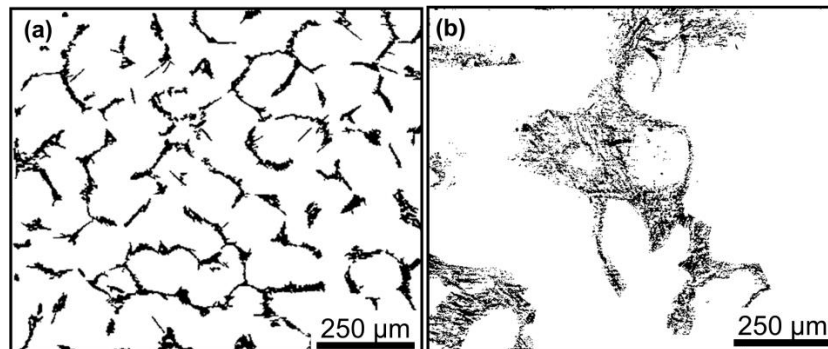
Figure 7.10 Segmented networks for (a) Nb-free tube and (b) Nb-modified tube.

`

Table 7.5 Network area fractions and connectivity in base UHCS and button samples.

Ref. Figure	Sample	F_A	Connectivity index
Figure 7.10 (a)	Nb-free tube	0.12 ± 0.01	0.98 ± 0.03
Figure 7.10 (b)	Nb-modified tube	0.05 ± 0.03	Undetermined

7.6 Hardness and Matrix

High surface hardness is a desirable property of UHCS, so preservation of hardness after Nb modification was of interest. As discussed in **Section 2.4.3**, the carbide phases were naturally very hard, but made up only a small volume fraction (typically around 10-20%) of the microstructure; hence, the matrix was the most important component determining steel hardness. Measured Rockwell hardness, network phases, and matrix phases identified through XRD are tabulated for all specimens in **Table 7.6**. Button remelting decreased hardness by around 16 Rc from the base UHCS in both the Nb-free and Nb-modified button samples. The Nb-free tube was around 3 Rc harder than Nb-free button, and Nb-modified tube was around 12 Rc harder than Nb button.

Table 7.6 Matrix and Carbide Phases and Hardness Measurements.

Sample	Matrix	Carbide Type	Hardness (Rc)	Meas.
Base UHCS	Pearlite+bainite	Fe_3C	51.5 ± 0.3	6
Nb-free Button	Austenite	Fe_3C	36 ± 2	5
Nb-modified Button	Austenite	Fe_3C+NbC	36.7 ± 0.8	6
Nb-free Tube	Austenite+ Ferrite	Fe_3C	39.7 ± 0.7	5
Nb-modified Tube	Austenite+ Ferrite	$Fe_3C+M_7C_3+NbC$	49 ± 2	6

Figure 7.11 shows the matrices of the samples after etching. The Nital etchant attacked α (ferrite/martensite) matrix phases, but left γ (austenite) and Fe_3C relatively untouched. Thus lamellar pearlite, and bainite, which gave the base UHCS its hardness, could be distinguished in **Figure 7.11 (a).** Button sample matrices, which were composed entirely of γ, appeared smooth and featureless even after etching as shown **Figure 7.11 (b) and (c)**. γ is the softest matrix phase

due to its FCC lattice. The Nb-free tube shown in **Figure 7.11 (d)** contained mostly γ, but XRD indicated at least some α, giving it slightly more hardness than the button samples. The Nb-modified tube matrix shown in **Figure 7.11 (e)** contained a significant amount of α as evidenced by the increased surface roughness after etching, which provided a hardness almost equaling that of the base UHCS.
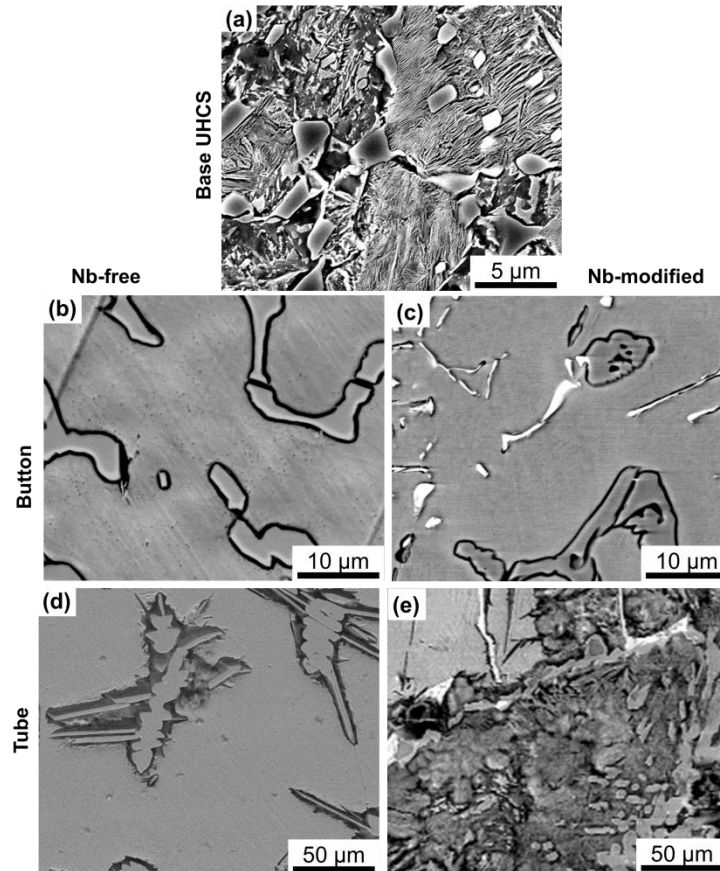
Figure 7.11 SEM micrographs of the etched matrices of (a) the base UHCS, (b) the Nb- free button sample, (c) the Nb-modified button sample, (d) the Nb-free tube samples, and (e) the Nb-modified tube sample.

7.7 Discussion

In summary, three microstructural constituents were identified in the Nb-modified UHCS: cementite network, matrix, and NbC structures. The industrial processing that produced the base UHCS microstructure included a centrifugal casting step which produced the cementite

171

`

network and initially pearlitic eutectoid microstructure, followed by a heat treatment step and furnace cool from around 1000°C that produced the final γ+α+pearlite matrix. Cementite particles were produced during the heat treatment by spheroidizing and coarsening of an initially pearlitic microstructure as described in Chapters 2 and 4. The following sections will explain the effects of cooling rate and Nb modification on the variations in the network parameters and matrix constituents found in the UHCS samples.

The base UHCS and button melted UHCS samples contained networks with similar volume fractions, but button branch spacing and thickness were both highly refined compared to the base UHCS. The Nb-modified button network had thicker branches and appeared less connected than the Nb-free button network. The Nb-free tube network area fraction and connectivity were similar to the base UHCS, but the Nb-modified tube network had a smaller network volume fraction and greater branch spacing and thickness. Unlike the other samples, the Nb-modified tube network branch morphology was reticulated and contained Cr-rich regions and small NbC particles. The base UHCS matrix phase was made up of pearlite, α, and γ; button matrix phases were mostly γ, while tube matrix phases were a mixture of α and γ. The Nb-modified tube matrix had a higher proportion of α to γ compared to the Nb-free tube matrix. Hardness values decreased as the matrix γ content increased. Complex NbC structures were found within the matrix of the Nb-containing samples, with sizes on the order of the network branch spacings.

Thermo-Calc

Thermo-Calc was used to predict the equilibrium solidification microstructure of the Nb-free and Nb-modified UHCS in order to establish context for evaluation of the effects of Nb and different cooling rates on network spacing and volume fractions. **Figure 7.12** shows pseudo-

binary phase diagrams for the base UHCS composition, with and without a modification of 2wt% Nb. When Nb was present and the composition contained above about 1 wt% C (as was the case for the Nb-modified UHCS samples in this study), NbC was the first solid to form from the liquid. At lower temperatures, NbC and austenite solidified together. The Nb addition also stabilized austenite and M_7C_3 at the expense of cementite. Cooperative eutectic solidification of NbC and austenite may account for the intricate NbC structures observed in the Nb-containing samples; Haddad *et al.* (*70*) showed very similar eutectic NbC morphologies in their study of cast irons containing 1-2 wt% Nb.

In the experimental UHCS samples, the network was formed from eutectic cementite and/or M_7C_3 between austenite dendrites, as well as additional proeutectoid cementite during cooling. Thus, the network volume fraction depended on the growth kinetics of carbide on the austenite grain boundaries. In the case of equilibrium cooling, the equilibrium volume fraction of $M_3C + M_7C_3$ just prior to the formation of bcc Fe should be equal to network volume fraction. Thermo-Calc plots of equilibrium phase fractions versus temperature were calculated for each of the different UHCS samples in **Figure 7.13**. The measured network area fractions for each sample are indicated in **Figure 7.13** for comparison with the equilibrium calculations. Measured 2D network area fractions should be equivalent to volume fractions assuming an isotropic 3D microstructure (*136*). Equilibrium and measured network and NbC volumes are tabulated in **Table 7.7**. Measured network volume fractions were consistently lower than the 750˚C equilibrium carbide volume fractions, indicating departures from equilibrium cooling for all UHCS samples. Network area/volume fractions in samples processed in the tube furnace were closer to equilibrium than the button samples, indicating that the slower tube furnace cooling was allowing more time for proeutectoid carbides to form on the austenite grain boundaries.
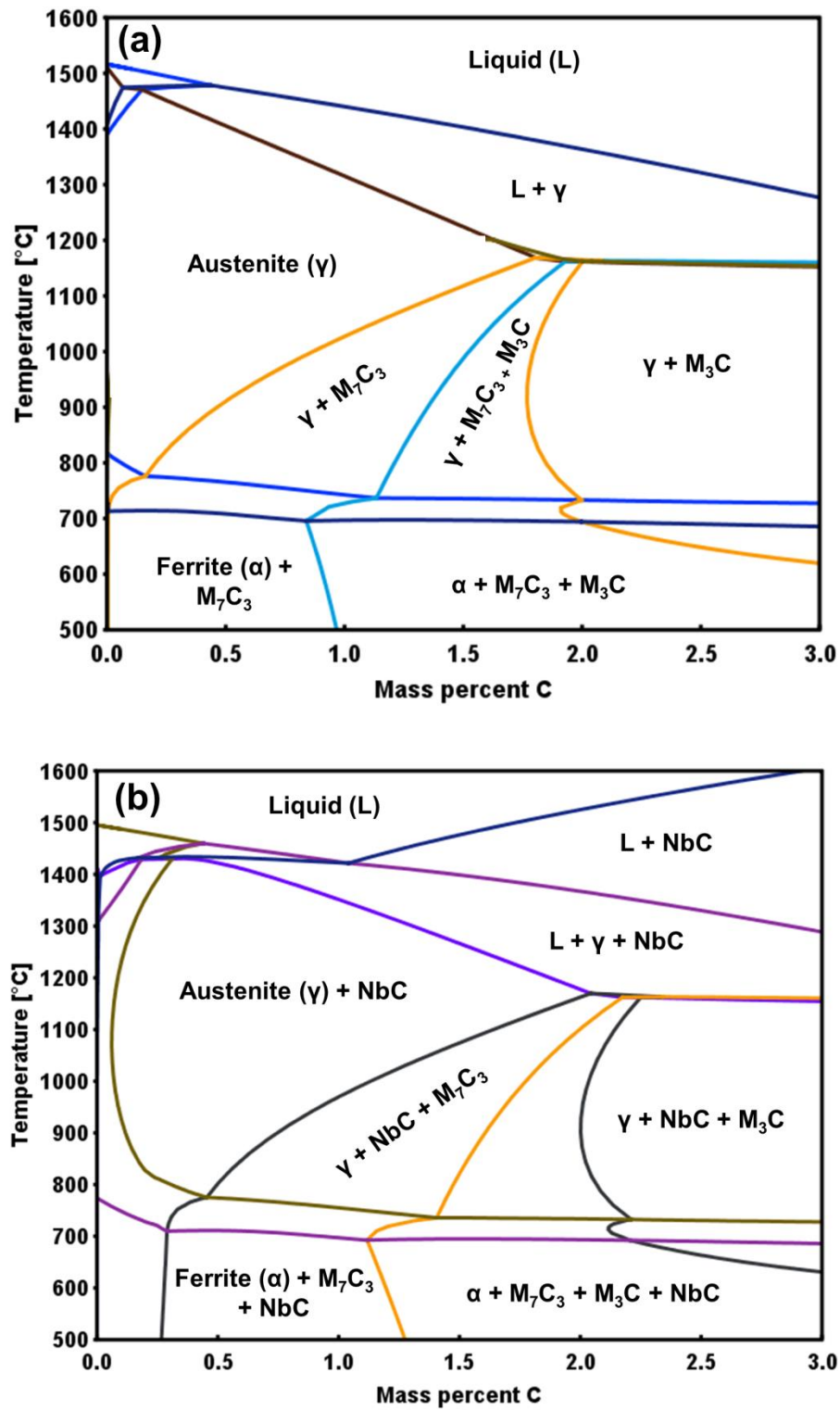
Figure 7.12 Pseudo-binary phase diagrams for the (a) the base UHCS microstructure and (b) base UHCS + modification by 2 wt% Nb (Thermo-Calc).
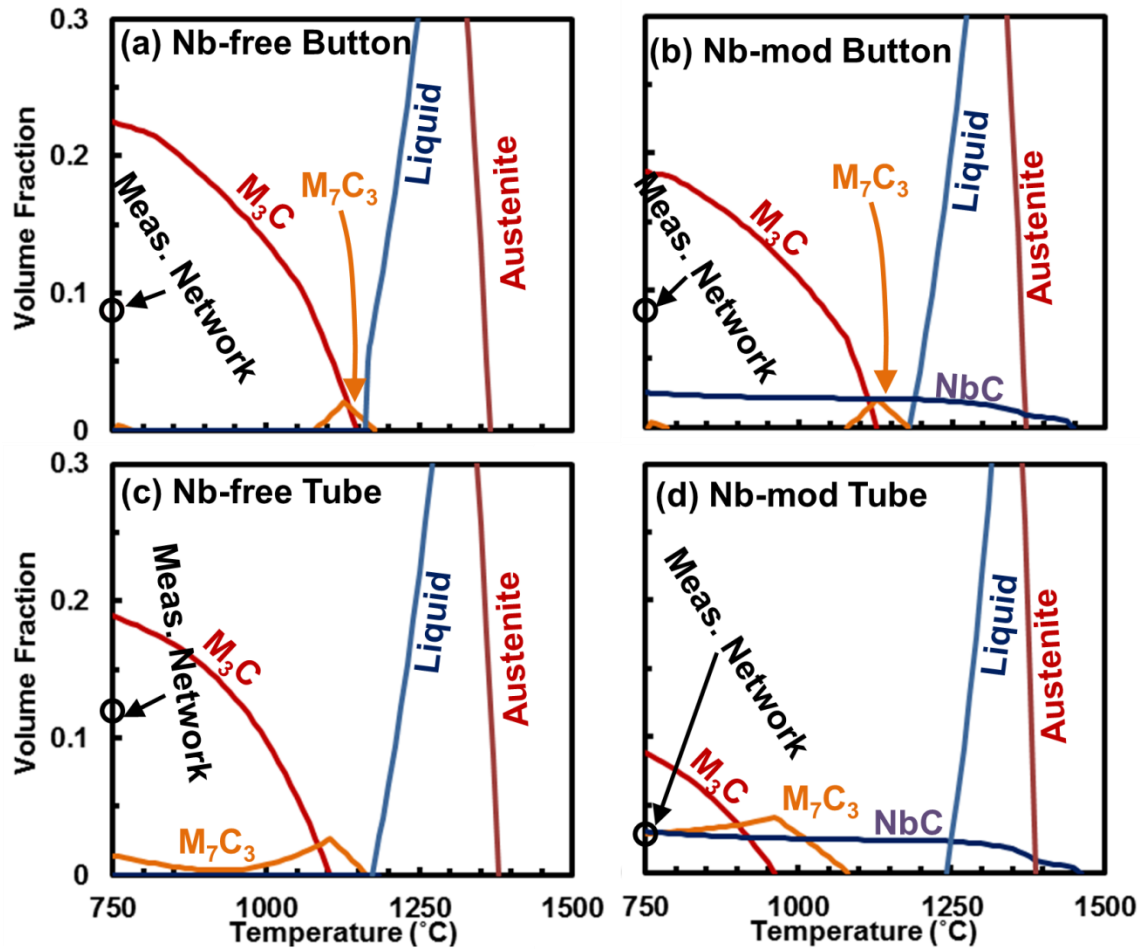
Figure 7.13 Volume fractions of equilibrium phases versus temperature for (a) the Nb-free UHCS composition and (b) the Nb-modified UHCS composition (Thermo-Calc). Measured volumes of the cementite network are indicated by open circles in the figure.

Table 7.7 Comparison of equilibrium calculations and measured network and NbC volume fractions.

Sample	Equilibrium Network V_f	Measured Network V_f	Equilibrium NbC V_f	Measured NbC V_f
Base UHCS	0.23	0.10 ± 0.01	--	--
Nb-free button	0.23	0.09 ± 0.01	--	--
Nb-mod button	0.19	0.09 ± 0.01	0.03	0.07 ± 0.01
Nb-free tube	0.19	0.12 ± 0.01	--	--
Nb-mod tube	0.11	0.05 ± 0.03	0.03	0.03 ± 0.01

EDS measurements indicated that the matrix Cr contents in the UHCS samples were also far from equilibrium, as shown in **Figure 7.14**. This was reasonable given the measured volume of

`

network cementite.   To maintain the correct mass balance, an UHCS low in network cementite

must contain an austenite matrix highly enriched in C and Cr. Both C and Cr lower the

martensite start temperature in steels (*129*), so the high concentration of C and Cr accounted for

the retained austenitic matrix microstructures and consequently the low hardness found in the

experimental UHCS samples.
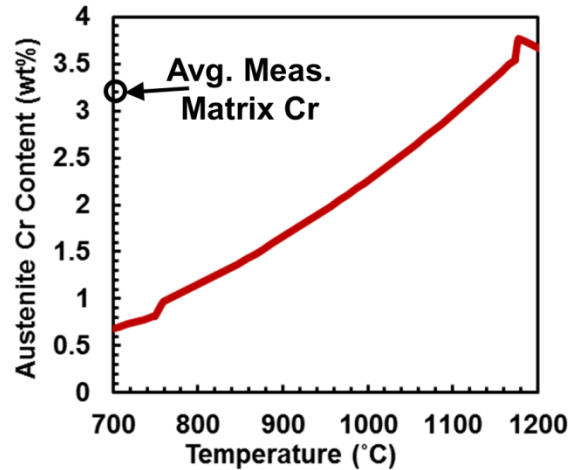
Figure 7.14 Equilibrium Cr content for the austenite in the base UHCS composition (Thermo-Calc). The average matrix Cr content in the UHCS samples (measured by EDS) is indicated in the figure.

Network Spacing

Network spacing in the UHCS samples depended on the austenite dendrite secondary arm

spacing that eventually formed the grain boundaries at their intersections. In the samples studied

here, network spacing and network branch thicknesses were smaller for the button-melted

samples compared to the base UHCS and the tube samples. This was consistent with a smaller

austenite secondary dendrite arm spacing (λ_{SDAS}) and faster cooling rates during solidification.

Correlations such as those developed by Won and Thomas (*7*) show an exponential relationship

between cooling rate and λ_{SDAS}. These expressions are dependent on steel C content (*7*) and

were developed for lower C steels, therefore this discussion is only qualitative. The difference in

C content between the tube and button samples might have contributed to the difference in

176

`

network spacing, but this contribution is expected to be much smaller than the effect of cooling rate. Previous studies have indicated that Nb additions refined the network by providing additional nucleation sites for austenite dendrites. Kheirandish *et al* (*60*) noted that both Nb alloying and faster cooling due to smaller section sizes caused decreases in network spacing (eutectic cell size) in a Nb-containing steel. The degree of carbide network refinement varied from a few percent up to a factor of two, depending on the amount of Nb added (*48, 60*). Nb additions were also reported to lower the volume fraction of eutectic carbides (*48, 60, 63*). In this study we found that Nb modification caused no measurable changes in the network of the fast-cooled button sample. In the slow-cooled tube sample, Nb modification increased the spacing of the network, in contrast to the refinement seen in previous studies.

In the Nb-modified samples, there was evidence of cooperative growth of γ+NbC with the "Chinese script" morphology. The sizes of the Chinese script NbC structures were on the order of the network spacing, indicating that they formed before any of the network carbide. The structure of the network carbide was very different between the Nb-modified button and tube samples. This was attributed to the effect of cooling rate on the multicomponent eutectic reactions occurring in the system. The Nb-modified button network branches appeared somewhat thicker and less connected than those of the Nb-free button, possibly due to NbC interfering with austenite grain boundaries. The Nb-modified tube network branches were about twice the width of the Nb-free tube branches, exhibited a reticulated structure interspersed with small NbC particles. The reticulated network structures with embedded NbC particles were similar to those reported by Haddad *et al.*(*70*) in the Fe-Nb-C system, who had described them as the result of a ternary eutectic reaction such as $L = \gamma + NbC + M_3C$. In the literature where refinement due to Nb modification was reported, NbC structures did not reach sizes comparable to those seen in the

177

`

Nb-modified tube sample (*48*, *55–58*, *60*, *62*, *63*, *65–67*). The NbC structures noted by Haddad *et al* were of similar length scales to those seen in this study, but the effect of those structures on network spacing was not investigated or compared to a control. .

High Cr Regions

Of the UHCS studied in this chapter, the Nb-modified tube network branches were also the only ones to contain high Cr regions, as indicated in **Figure 7.15**. These high Cr regions of the network were apparently M_7C_3 produced as part of a ternary eutectic L $L = \gamma + NbC + M_3C$ reaction, which should contain a higher Cr content than M_3C according to calculations in Thermo-Calc. The ternary eutectic and resultant reticulated network structure was not seen in the Nb-modified button sample, which might be due to the higher C content or suppression due to the faster cooling rate.
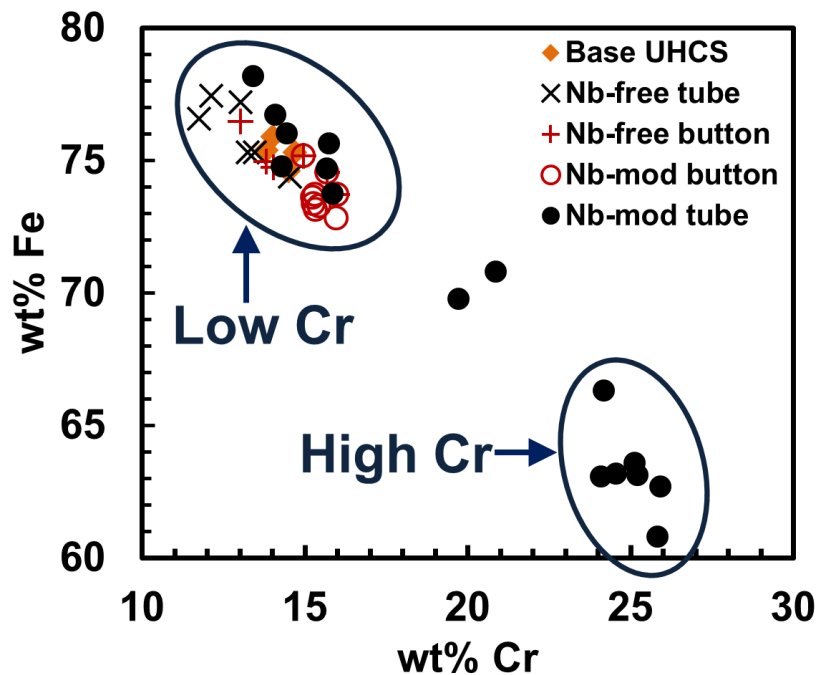
Figure 7.15 Point EDS measurements of cementite network are plotted as a function of Fe and Cr wt%. Cr-rich regions in the Nb-modified tube network (labeled high Cr in the diagram) were clustered around 25 wt% Cr, while the normal network was clustered around 14 wt% Cr (labeled low Cr in the diagram). Of all samples that were examined, only the Nb-modified tube sample contained high Cr network regions.

`

Chinese Script and Block NbC Structures

NbC morphologies in the literature have been identified either as 'blocky/nodular' or 'Chinese script'. Typically only one of the two morphologies was reported for a given steel composition. Studies with the hypoeutectoid compositions all reported Chinese script morphologies regardless of Nb content, but there was no clear trend in NbC morphology type for hypereutectoid steel compositions. Fiset *et al.* (*63*) showed that increasing the Nb content in a hypereutectoid steel above about 1 wt% changed the morphology from Chinese script to blocky, but other authors reported the blocky morphology at Nb contents well below 1wt% (*67*, *69*) in other hypereutectoid steels. Judging from micrographs in the literature studies, NbC structures with the Chinese script morphology were typically about 10-20 µm in size (*55*, *58*, *74*), and blocky NbC particles were typically about 5µm in size (*63*, *67*). In this study, both the Chinese script and blocky morphologies were found in the Nb-modified button and tube samples, as shown in

Figure 7.16. Chinese script and blocky NbC in the Nb-modified button sample had similar sizes to those found in the literature, but the Nb-modified tube had much larger sizes for both morphologies. Although we have found no reports in the literature of other steels containing both morphologies, it is possible such microstructures existed and that one type of NbC morphology was not noticed or the authors did not specifically report it.
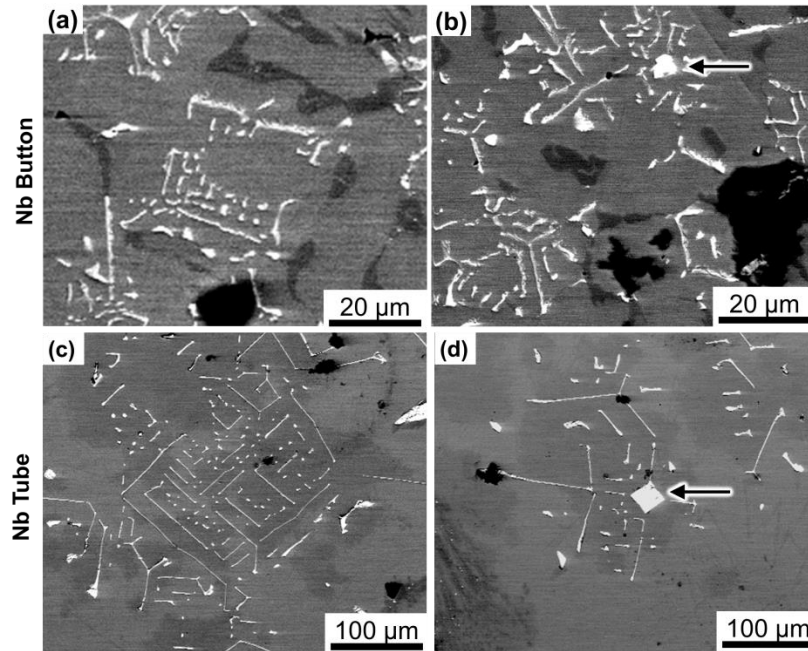
Figure 7.16 BSE SEM micrographs of NbC with the Chinese script morphology and the blocky morphology in (a,b) the Nb-modified button UHCS and (c,d) the Nb-modified tube UHCS. Arrows indicate the blocky morphology.

The blocky NbC morphology is likely formed in the liquid prior to the start of austenite solidification, and the Chinese script NbC morphology is likely formed in cooperation with the solidifying austenite. The presence of blocky NbC in a steel would then depend on the melting point of NbC being higher than the austenite melting point in the steel. This would account for the lack of blocky morphology reported in the hypereutectoid steels, since austenite in hypoeutectoid steel solidifies at a higher temperature than hypereutectoid austenite. Furthermore, increasing the Nb content of the steel increases the Nb solidification temperature as shown in **Figure 7.17**, which accounts for the observation of Fiset *et al.* that increasing the Nb content could promote formation of the blocky NbC morphology. However, the question of why some Nb-modified steels were reported having the blocky NbC morphology without the Chinese script remains.

`
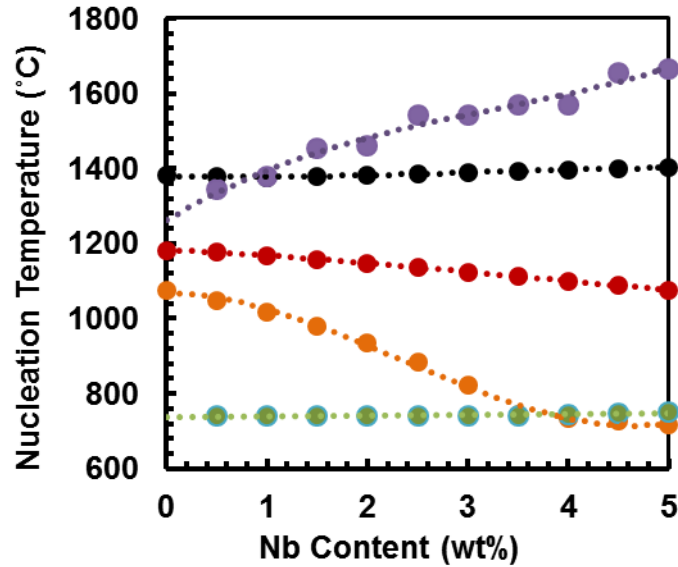
Figure 7.17 Effects of increasing Nb content on equilibrium nucleation temperature for phases in the base UHCS (Thermocalc equilibrium calculations).

Croker *et al.* (*137*) reported that the morphology of a cooperatively growing eutectic phase should depend on its entropy of solution (ΔS_α) and volume fraction. For a growth velocity of $5 \cdot 10^{-4}$ cm/s, the morphology closest to the Chinese script was found when entropy of solution was greater than about 6 cal/K·mol and volume fraction of the phase was greater than about 0.08. Using Thermo-Calc, we found that the formation entropy of formation of NbC was about 8 cal/K·mol during austenite solidification. However, the equilibrium volume fraction of NbC was only about 0.03, which was expected to solidify with austenite as a broken lamellar morphology. The NbC in the Nb-modified tube UHCS was cooled at a rate of approximately 5˚C/min, so given approximately the 200˚C range during which NbC and austenite were solidifying together, and the 100-600 μm NbC Chinese script size, the NbC growth velocity in the tube furnace would be about 3 μm/min, or about $5 \cdot 10^{-6}$ cm/s. Thus, it is possible that the growth velocity of NbC was different enough from the $5 \cdot 10^{-4}$ cm/s used in Croker *et al.* to change the boundaries of volume fractions that would produce the Chinese script morphology. It is also possible that the observed Chinese script NbC morphology was all produced during the approximately 10˚C

temperature window wherein the NbC volume fraction relative to austenite was greater than 0.08, as highlighted in **Figure 7.18**. In that case, the NbC growth velocity would be about $3 \cdot 10^{-4}$ cm/s for the Nb-modified tube furnace, close to the value used by Croker *et al.* Since the network spacing in the Nb-modified UHCS samples depended on the length scales of the NbC structures with the Chinese script morphology, it is anticipated that controlling the growth time of the NbC structures allows a degree of control over the network spacing.
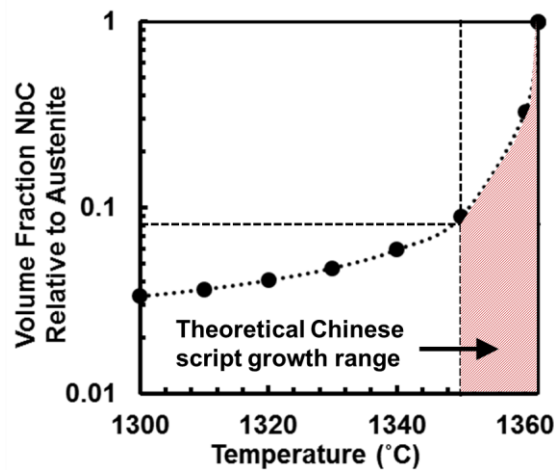
Figure 7.18 Thermo-Calc equilibrium volume fraction of NbC relative to austenite as a function of temperature. The shaded region shows temperature and volume fraction range over which the Chinese script NbC might have formed.

7.8 Conclusions

In this Chapter, effects of Nb modification and cooling rate on UHCS microstructure were investigated. Nb modification affected the UHCS network microstructure in two ways: by forming NbC structures, and by decreasing the effective amount of carbon available in the matrix for carbide formation. NbC structures had the potential to alter cementite network spacing if given sufficient time to grow large enough, as was seen in the Nb-modified tube network spacing. However if the cooling rate was too fast, as it was in the Nb-modified button spacing, the NbC structures did have time to grow large enough to alter network spacing.

`

Nb alloying apparently caused a ternary eutectic rection L-> $M_7C_3 + \gamma + NbC$ to occur in the Nb-modified tube sample, which was responsible for the reticulated network structure. The reaction did not take place in the Nb-modified button sample, either because of a higher Cr content or faster cooling that acted to suppress the reaction.

In the Nb-free samples, solidification rate alone determined the network spacing by controlling the growth kinetics of austenite dendrites. The Nb button samples had the finest network spacing, followed by the base UHCS followed by the tube samples.

`

Chapter 8. Conclusions and Suggestions for Future Work

8.1 Addressing Objectives and Hypotheses

Objective 1: Determine the mechanism for mechanical property enhancement by an established industrial heat treatment of an UHCS.

In chapter 2, the microstructures of as-cast and industrially heat-treated 2C-4Cr UHCS were investigated using SEM, EDS, XRD, and FIB. Rockwell hardness and Charpy impact energy were measured for both UHCS conditions. Both hardness and toughness were around 10% higher in the heat-treated UHCS. The purpose of the study was to address objective 1 by identifying microstructural features affected by the heat treatment, and determining the influence of those features on mechanical properties.

Two main features were identified: network and matrix. The network was identified as cementite through EDS and XRD characterization, while the matrix was a more complicated mixture of component phases. The network appeared qualitatively similar in both heat-treated and as-cast UHCS. The primary matrix phase in both heat-treated and as-cast UHCS was pearlite. The as-cast UHCS matrix was made up entirely of pearlite, with some interspersed elongated Widmanstätten cementite. The matrix of the heat-treated UHCS contained a mixture of pearlite, Widmanstätten cementite, bainite, and micron-sized faceted idiomorphic proeutectoid cementite. FIB serial sectioning confirmed the equiaxed idiomorphic cementite morphology. These microstructural observations regarding network, matrix, and idiomorphic particles directly relate to the first three hypotheses for this work.

Hypothesis 1: Hardness in UHCS is largely independent of the volume fraction or connectivity in the carbide network, and instead relies on the matrix microstructure surrounding the network.

`

Hypothesis 2: *Toughness in UHCS is directly related to the connectivity in the carbide network. Quantification of network connectivity is possible using image analysis, and should be predictive of measured toughness in the steel after factoring in the length scale of the branches in the network.*

The main microstructural factor contributing to higher hardness was the pearlite interlamellar spacing, which followed a Hall-Petch trend. The effects of the network and idiomorphic cementite on hardness, if any, were negligible compared to the pearlite lamellar spacing. This finding supports hypothesis 1, since hardness changed significantly independent of the network or other non-pearlitic cementite.

The 10% increase in Charpy impact toughness in the heat-treated UHCS appeared to be a result of changes to the matrix due to the heat treatment. The fracture surface of the heat-treated UHCS had a texture with voids with sizes and shapes reminiscent of the idiomorphic cementite particles, which indicated crack-particle interactions. Hypothesis 2 predicted that major improvements in toughness would only be possible through changing the connectivity of the cementite network. However, the heat treatment did appear to improve toughness somewhat, in contrast to the claim of hypothesis 2. In order to investigate the hypothesis further, it was necessary to quantitatively define network connectivity, and also to determine what effects the network connectivity might have on UHCS toughness. No such connectivity metric was found in the literature with regards to cementite networks, which led to objective 2 of the study.

Objective 2: *Establish a quantitative connectivity metric for UHCS cementite network characterization and analysis.*

In order to test hypothesis 2, a new method for quantitatively assessing carbide network connectivity in UHCS was developed based on the connectivity index used in transportation

`

science (analogous to crack propagation along a "pathway" of carbide networks in UHCS). Steps of the method are described in chapter 3, and involve a series of standard digital image processing steps that common commercial software programs, such as ImageJ, can perform. The new method was applied to the as-cast and heat-treated UHCS described in chapter 2 to determine if the heat treatment had modified the connectivity index values of the networks in those samples. The method was also applied to micrographs of UHCS samples in the literature which showed a much wider range of Charpy impact toughness values.

In the literature studies cited in chapter 3, Charpy toughness only varied significantly (on the order of 1 or more Joules) when the connectivity index was less than ~0.7. When the index was less than 0.7, toughness increased significantly as connectivity decreased. This observation was attributed to connectivity index exceeding a percolation threshold. Above the threshold of connectivity, cracks could span the microstructure without much deviation from the network paths, and thus the more ductile matrix apparently only contributed slightly to toughness. Both the heat-treated and as-cast UHCS studied in chapter 2 had network connectivity indices greater than 0.7. The 10% increase in Charpy impact toughness of the heat-treated UHCS was only on the order of a few tenths of a Joule, and thus was not a significant increase on the order of the increases seen in the literature when connectivity was decreased below the critical value. Hypothesis 2 has been adjusted to reflect these observations and is restated as follows:

Adjusted Hypothesis 2: *Toughness in UHCS is related to the connectivity in the carbide network. Quantification of network connectivity is possible using image analysis, and should be predictive of measured toughness in the steel after factoring in the length scale of the branches in the network. When connectivity exceeds a critical value related to a percolation threshold, the*

toughness will not change significantly. Minor changes in toughness (differences of less than a Joule in absorbed Charpy impact energy) are still possible with changes in matrix morphology.

The analysis in chapters 2 and 3 indicated that the idiomorphic particles in the matrix interacted with the propagating crack front, increasing toughness slightly, even though the network was above the critical connectivity. The literature also indicated that the sizes and distributions of particles would influence toughness. The mechanism and kinetics of the process by which the idiomorphic particles formed was unknown, however. Thus, the next objective and related hypothesis in this dissertation follows:

Objective 3: *Comprehensively describe the effects of austenitizing heat treatments on UHCS microstructure.*

a. Identify the mechanism for idiomorphic carbide formation during austenitizing heat treatments of UHCS.

b. Determine what effects, if any, heat treatments of varying length and temperature have on the network carbides.

Hypothesis 3: *Idiomorphic cementite forms in the UHCS matrix during austenitizing heat treatments due to spheroidization and coarsening of pearlite. Since coarsening is a curvature driven process, the cementite network has a perturbing effect on coarsening near the network.* Chapters 4, 5, and 6 address this objective and hypothesis.

In Chapter 4, the formation mechanism and growth kinetics of the idiomorphic particles was investigated using annealing experiments combined with quantitative analysis of SEM micrographs. Samples of the as-cast 2C-4Cr UHCS were heat-treated at 800˚C, 900˚C, and

970˚C for times of 5 minutes to 24 hours. Examination of the different isothermal holding times revealed that the initially lamellar pearlitic cementite transformed entirely into cementite particles after a certain amount of time at each temperature. At 800˚C and 900˚C the complete transformation took between 5 and 90 minutes, and at 970˚C all pearlite lamellae were transformed into particles in less than 5 minutes. These observations indicated that the pearlite was undergoing spheroidization during the isothermal holds. The average particle size increased with isothermal holding time at each temperature. The particle growth mechanism was identified as coarsening because the total number of particles decreased with isothermal holding time. Thus, the idiomorphic particles noted in the heat-treated 2C-4Cr UHCS in chapter 2 were spheroidized pearlite particles which had coarsened during the industrial heat treatment.

A denuded zone devoid of particles developed adjacent to branches of the cementite network. Denuded zone width evolved with isothermal hold time described by the equation $d^{4-5}=kt$ (d in µm). The denuded zones supported the hypothesis that the cementite network would have a perturbing effect of the network cementite on the idiomorphic cemenetite particle coarsening.

Particle sizes in many SEM micrographs were analyzed in ImageJ to determine particle size distributions. The particle size distributions were multimodal, with three component distributions corresponding to different types of particles: medium sized intragranular (IG) particles inside austenite subgrains; larger grain boundary (GB) particles and very small leftover particles (LP) found only at 800˚C. GB particle distributions were confirmed by tracing along prior austenite boundaries and retaining only the GB distribution.

The coarsening parameters, n and k were determined for each temperature and type of particle. n was closest to 4 for the GB particles and 5 for the IG particles, indicating grain

`

boundary and dislocation controlled diffusion, respectively. Fractions of the total distribution corresponding to each type of particle were also determined as functions of temperature and time. Extrapolation/interpolation of *n* and *k,* together with the fractions of the total distribution, should allow prediction of particle sizes and distributions for any given austenitizing heat treatment of that particular 2C-4Cr composition. Bulk diffusion appeared to be inhibited even at high temperatures in the samples; this might have been due to a need for Cr diffusion in cementite coarsening. The next objective of this dissertation follows:

Objective 4: *Investigate the effects of Cr concentration on heat treatments and/or solidification in UHCS.*

Hypothesis 4: *Higher Cr contents slow down cementite dissolution and coarsening due to the requirement for Cr to diffuse through the austenite for complete cementite dissolution. When the ratio of Cr to C exceeds a certain amount, M_3C (cementite) transforms to M_7C_3.*

This hypothesis was investigated in chapter 5 by comparing the microstructure of the 2C-4Cr UHCS (previously studied in chapter 4) with a 2C-1Cr UHCS. Both UHCS were subjected to the same series of heat treatments in the same box furnace. The purpose of the study was to determine what effects, if any, the lower Cr content would have on coarsening behavior in the UHCS.

Lowering the Cr content had an unexpected effect on the particle distribution. Unlike the 4Cr UHCS, which exhibited particle denuded zones near network branches, cementite particle densities in the 1Cr UHCS were highest in clusters near network branches. The particle clustering and denuded zones might have been phenomena related to the steepness and depth of the solute gradient established by the cementite network branches. A steep gradient with little depth (penetration into the matrix) could theoretically result in denuded zones. A shallow

`

gradient with high depth could result in increased particle stability and clustering near the cementite network branches. Further investigation is needed to determine whether such a gradient existed, and why it might have had different steepness and depth in the 1Cr and 4Cr UHCS.

Quantitative analysis indicated that GB particles in the clusters were consistently larger than the homogenously distributed GB particles previously measured in the 4Cr UHCS. IG particle sizes were not determined. The coarsening exponent, n, of the 1Cr UHCS GB particles could fit with any of $n=3,4$, or 5, so it was not possible to determine whether or not the change in Cr caused a change in the dominant diffusion mechanism controlling coarsening. However, the increase in particle size in the 1Cr UHCS did indicate that higher Cr contents slowed down cementite coarsening, which supports the first statement in hypothesis 4. Hypothesis 3 was adjusted to reflect the observations of chapters 4 and 5:

Adjusted Hypothesis 3: *Idiomorphic cementite forms in the UHCS matrix during austenitizing heat treatments due to spheroidization and coarsening of pearlite. Since coarsening is a curvature driven process, the cementite network has a perturbing effect on coarsening near the network. The perturbation is reflected in a change in the spatial distribution of particles, with denuded zones or clustering occurring dependent on the UHCS composition.*

The hypothesis was further tested by observing the coarsening process in real-time. Chapter 6 describes four *in situ* CLSM heat treatments on 2C-4Cr UHCS. Three of the heat treatments were complicated by oxidation of the matrix, and were thus unsuitable for quantitative analysis since oxide particles were indistinguishable from cementite particles. One heat treatment did not oxidize during the isothermal hold, and oxidized in the network only during cooling. The non-oxidized sample showed regions with high and low particle densities. These regions were

also confirmed in a cross-section of the sample. The high particle density region appeared to contain smaller sub-grains than the low density regions. The coarsening exponent of particles in the high density regions was about 5, consistent with the IG particles in chapter 4. Low density regions were analogous to the denuded zones noted in chapter 4, but were not located adjacent to the network. This observation poses a challenge to the adjusted hypothesis 3, since coarsening behavior was perturbed such as to produce denuded zones without apparent localization near the cementite network in the CLSM samples.

Chapters 4, 5 and 6 addressed the mechanism and kinetics of the idiomorphic particles, which should have a minor influence on toughness. For significant toughness enhancement, hypothesis 2 suggests that network break-up is necessary. Nb had been employed successfully for network break-up and toughness enhancement in UHCS in previous studies in the literature. The following objective and hypothesis was developed regarding study of Nb for this dissertation.

Objective 5: *Investigate the effects of Nb concentration on microstructure during heat treatments and/or solidification in UHCS.*

Hypothesis 5: *Niobium alloying produces NbC in the liquid prior to or during austenite formation (depending on the Nb content in the steel) which should have a refining effect on the cementite network by providing additional sites for austenite dendrites to nucleate. Nb pulls carbon out of solution to form the NbC, which decreases the overall amount of cementite leading to a reduction in the network volume faction and connectivity.*

Chapter 7 was intended to investigate the effects of Nb on the 2C-4Cr network microstructure. Heat-treated 2C-4Cr UHCS base material was melted in a button melter with and without an addition of Nb powder. As the button melted samples experienced extremely rapid

`

cooling, portions of the Nb-free and Nb-modified button-melted samples were remelted in a tube furnace to allow solidification to progress at a slower rate.

The Nb modification affected the UHCS network microstructure in two ways: by forming NbC structures within the matrix, and by decreasing the effective amount of carbon available in for carbide formation. NbC structures had the potential to alter network spacing if given sufficient time to grow large enough, as was seen in the Nb-modified tube network spacing. However if the cooling rate was too fast, as it was in the Nb-modified button spacing, the NbC structures did have time to grow large enough to alter network spacing.

Nb alloying apparently caused a ternary eutectic rection L-> M_7C_3 + γ + NbC to occur in the Nb-modified tube sample, which was responsible for the reticulated network structure. The reaction did not take place in the Nb-modified button sample, either because of a higher C content or faster cooling rate suppressing the reaction.

In the Nb-free samples, solidification rate alone determined the network spacing by controlling the growth kinetics of austenite dendrites. The Nb button samples had the finest network spacing, followed by the base UHCS followed by the tube samples.

Adjusted Hypothesis 5: Niobium alloying produces NbC in the liquid prior to and/or during austenite formation (depending on the Nb content in the steel). Nb pulls carbon out of solution to form blocky NbC structures (if solidifying prior to ausenite) or Chinese script structures (if solidifying together with austenite). The NbC may increase or decrease the spacing of the cementite network, depending on length scale of the NbC structures. The reduction in C content of the liquid due to NbC formation can cause M_7C_3 formation by increasing the Cr/C ratio.

`

8.2 Future Work

Some questions remain regarding the hypotheses investigated in this dissertation. This section identifies specific areas that could be further explored while also suggesting experiments that could build upon the results of this dissertation.

Hypothesis 1, which predicted that hardness of UHCS depends primarily on the matrix phases, was resolved satisfactorily in chapter 2. The adjusted hypothesis 2 was more complicated, and suggests a significant amount of additional work for further clarification and validation/refutation of its claims. There are three main avenues for further investigation of the claims in adjusted hypothesis 2:

1. Critical connectivity. In chapter 3, connectivity indexes of only 3 different UHCS were plotted versus toughness, and of those only the data of Hamidzadeh *et al.* (*48*) spanned the critical connectivity. More data is needed to evaluate the claim that a critical connectivity is linked to a plateau in toughness.

2. Length Scale. Connectivity index is a dimensionless parameter, but carbide networks can have very different length scales (for instance, the network spacing in the button melted UHCS was much smaller the base UHCS or tube furnace melted UHCS in chapter 7.)

3. Contribution of matrix to toughness in the critical connectivity regime. A claim was made that, no matter its toughness, the matrix would not significantly influence toughness once the critical connectivity was exceeded. However, additional evidence for this claim is needed to validate this claim.

The points above should each be investigated individually. Point 1 is the most important argument, and should be prioritized over the others. Critical connectivity should be investigated by measuring toughness of UHCS samples with very similar matrix microstructures,

`

composition, and network volume fractions, but different network connectivities in the range of 0.5 to 0.9. The best way to modify the network connectivity while keeping the rest of the microstructure consistent is thermomechanical working. Ideally, a series of thermomechanical working experiments would be conducted using several different UHCS compositions to test the consistency of the critical connectivity index.

Serial sectioning over large length scales (hundreds of microns) to produce 3D microstructural data could yield 3D connectivity indices to compare with 2D analysis. This might be possible using new plasma focused ion beam instruments now commercially available (*138*). Analytically calculating the percolation threshold for a 3D UHCS microstructure and thereby predicting the critical 2D connectivity index needed to exit the plateau phase might also be possible. Critical metrics like average network branch length (length-scale) and probability of each node to be an endpoint/internal junction should be sufficient to perform this calculation. Both of these parameters are extracted from 2D micrographs using the AnalyzeSkeleton plugin.

If a consistent critical connectivity is supported by the series of experiments described above for a single length scale, then the experiments should be repeated for a very different length scale (different by an order of magnitude or more) to address point 2. If the critical connectivity index were to be the same for the different length-scales, no further work would need to be none. If the critical connectivity index were to differ for different length scales, than the metric for connectivity should be modified to include information about length scale, perhaps scaling the connectivity index by an empirical parameter determined by the series of experiments.

`

According to the adjusted hypothesis 2, the toughness of the microstructure should only affect toughness significantly in a UHCS with a network below the critical connectivity. To address point 3, toughness should be measured for four different cases:

(1) Low toughness matrix, network above critical connectivity.

(2) High toughness matrix, network above critical connectivity.

(3) Low toughness matrix, network below critical connectivity.

(4) High toughness matrix, network below critical connectivity.

The following arbitrary toughness values are assigned to the matrix and network: Network = 1 J, low toughness matrix = 4 J units, high toughness matrix = 10 J. Hypothesis 2 predicts that the UHCS of case (1) should have toughness close to 1 J. Case (2) should also have toughness close to 1 J, but slightly higher than case (1). Case (3) should have toughness between 1 J and 4 J based on the connectivity index of the UHCS. The smaller the index value, the closer the toughness will be to 4 J. Case (4) should have a toughness value between 1 J and 10 J based on the connectivity index. Testing the hypothesis in this manner will determine how much utility there is to toughening the matrix in a UHCS with a network above the critical connectivity.

Hypotheses 3 and 4 relate to particle coarsening kinetics. The main point of hypothesis 3 was confirmed in chapter 4; idiomorphic particles were formed from spheroidization and coarsening of cementite. However, as indicated in chapter 5, the role of Cr and the perturbing effects of the network carbides on the coarsening process still require considerable clarification. The main question raised in chapter 5 was why the change in Cr concentration from 4wt% to 1 wt% reversed the perturbing effect of the network from causing denuded zones to causing clustering.

`

The proposed answer to this question was that the Cr content in the UHCS changed the behavior of concentration gradients during the coarsening process. If this is the case, then for a given base UHCS composition there should be a critical Cr concentration at which clustering switches to denuded zones. For the UHCS studied in chapters 4 and 5, this concentration was somewhere between 1 and 4 wt%. The critical Cr concentration might be determined by casting and then heat treating multiple UHCS alloys with Cr contents varying from 1-4 wt%. At a minimum, 1.5, 2, 2.5, 3, and 3.5 wt% Cr UHCS should be examined. Only one heat treatment should be necessary for each different UHCS, since time and temperature did not appear to have an effect on whether clustering or denuded zones appeared. Thus, 8 hours at 970°C is suggested. The critical Cr composition should contain neither clustering nor denuded zones.

Chapter 7 demonstrated some interesting effects of cooling rate and Nb on the microstructure of UHCS. As noted in section 1.2.2 of the introduction to this dissertation, Won and Thomas (7) proposed an empirical expression for secondary dendrite arm spacing of solidifying austenite as a function of cooling rate in steels with carbon contents up to about 1wt%. The austenite secondary dendrite arm spacing should determine the network spacing in Nb-free UHCS, so it would be useful to extend the expression for secondary arm spacing to include UHCS carbon concentrations. This could be determined experimentally in the CLSM or the button melter by solidifying UHCS with different carbon contents at different rates and determining the dependence of secondary arm spacing on cooling rate and carbon content. The solidification experiments could alternatively be conducted in a tube furnace if the free surface in the CLSM was perturbing the spacing results.

The adjusted hypothesis 5 stated several claims regarding NbC structures that could be tested in CLSM. First, the claim that block NbC structures form before austenite solidification

`

and that the Chinese structure formed by cooperative solidification with austenite should be evaluated by observing solidification of an UHCS containing Nb in the CLSM at a slow solidification rate. In chapter 7 the solidification rate also appeared to have an effect on the length scales of both block and Chinese script NbC structures. Observing the growth of NbC structures at different solidification rates should be possible in the CLSM. Alternately, sizes of NbC structures could be evaluated in samples solidified at different rates in a tube furnace. The discussion relating to **Figure 7.18** in chapter 7 speculates that perhaps the Chinese Script NbC microstructure grew only within the small temperature window corresponding to the regime where the ratio of the volume fractions of NbC to austenite was greater than about 0.08. This speculation could also be tested in the CLSM by observing the morphology of NbC formed below that temperature regime.

`

References

1. R. C. Sharma, *Principles of the Heat Treatment of Steels* (New Age International Ltd., 1996).
2. C. W. Bale *et al.*, FactSage thermochemical software and databases - recent developments. *Calphad Comput. Coupling Phase Diagrams Thermochem.* **33**, 295–311 (2009).
3. T. Nishizawa, Effect of magnetic transition on phase equilibria in iron alloys. *J. Phase Equilibria.* **16**, 379–389 (1995).
4. A. Kagawa, T. Okamoto, Hot hardness of cementite. *J. Mater. Sci.* **18**, 225–230 (1983).
5. M. Umemoto, Y. Todaka, K. Tsuchiya, Mechanical Properties of Cementite and Fabrication of Artificial Pearlite. *Mater. Sci. Forum.* **426–432**, 859–864 (2003).
6. T. Okamoto, H. Matsumoto, Precipitation of Ferrite from Cementite. *Met. Sci.* **9**, 8–12 (1975).
7. Y. M. Won, B. G. Thomas, Simple model of microsegregation during solidification of steels. *Metall. Mater. Trans. A Phys. Metall. Mater. Sci.* **32**, 1755–1767 (2001).
8. J. S. Park, J. D. Verhoeven, Directional solidification of white cast iron. *Metall. Mater. Trans. A.* **27**, 2328–2337 (1996).
9. J. Rickard, I. C. H. Hughes, Eutectic structure in white cast iron. *BCIRA J.* **9** (1961), pp. 11–25.
10. G. Spanos, M. V. Kral, The proeutectoid cementite transformation in steels. *Int. Mater. Rev.* **54**, 19–47 (2009).
11. C. R. Brooks, *Principles of the Heat Treatment of Plain Carbon and Low Alloy Steels* (ASM International, 2000).
12. G. Meyrick, G. W. Powell, Phase Transformations in Metals and Alloys. *Annu. Rev. Mater. Sci.* **3**, 327–362 (1973).
13. A. R. Marder, B. L. Bramfitt, Effect of continuous cooling on the morphology and kinetics of pearlite. *Metall. Trans. A.* **6**, 2009–2014 (1975).
14. N. Ridley, A Review of the Data on the Interlamellar Spacing of Pearlite. **15**, 1019–1036 (1984).
15. E. O. Hall, The Deformation and Ageing of Mild Steel: III Discussion of Results. *Proc. Phys. Soc. Sect. B.* **64**, 747–753 (1951).
16. N. J. Petch, The Cleavage Strength of Polycrystals. *J. Iron Steel Inst.* **174**, 25 (1953).
17. J. T. Busby, M. C. Hash, G. S. Was, The relationship between hardness and yield stress in irradiated austenitic and ferritic steels. *J. Nucl. Mater.* **336**, 267–278 (2005).
18. J. Maity, A. Saha, D. K. Mondal, K. Biswas, Mechanism of accelerated spheroidization of steel during cyclic heat treatment around the upper critical temperature. *Philos. Mag. Lett.* **93**, 231–237 (2013).
19. J. D. Verhoeven, E. D. Gibson, The divorced eutectoid transformation in steel. *Metall. Mater. Trans. A.* **29**, 1181–1189 (1998).
20. J. Krawczyk, The effect of cast steel chemical composition on its microstructure and tribological properties in mill rolls. **47**, 137–148 (2011).
21. A. Brodziak, Z. Stradomski, A. Pirek, The influence of microstructure on the mechanical properties of metallurgical rolls made of G200CrMoNi4-3-3 cast steel. *Arch. Foundry Eng.* **9**, 21–24 (2009).
22. J. Krawczyk, R. Dziurka, E. Rożniata, the High-Temperature Tribology of Iron Matrix

`

Hypoeutectic Alloy After Under-Annealing Normalizing. *Metall. Foundry Eng.* **34**, 125 (2008).

23. J. Krawczyk, S. Parzych, Microstructure formation and properties of abrasion resistant cast steel. *Arch. Foundry Eng.* **10**, 295–300 (2010).

24. P. Kolmskog, *Does Bainite form with or without diffusion ? The experimental and theoretical evidence (Doctoral Thesis)* (KTH Royal Institute of Technology, Stockholm, 2013).

25. H. K. D. H. Bhadeshia, *Bainite in Steels* (University Press, Cambridge, MA, ed. 2, 2001).

26. S. a. Sajjadi, S. M. Zebarjad, Isothermal transformation of austenite to bainite in high carbon steels. *J. Mater. Process. Technol.* **189**, 107–113 (2007).

27. M. Umemoto, E. Yoshitake, I. Tamura, The morphology of martensite in Fe-C, Fe-Ni-C and Fe-Cr-C alloys. *J. Mater. Sci.* **18**, 2893–2904 (1983).

28. R. a. Grange, C. R. Hribal, L. F. Porter, Hardness of tempered martensite in carbon and low-alloy steels. *Metall. Trans. A.* **8**, 1775–1785 (1977).

29. O. D. Sherby, Ultrahigh Carbon Steels, Damascus Steels and Ancient Blacksmith. *ISIJ Int.* **39** (1999), pp. 637–648.

30. S. A. Fedosov, Investigation of modern fabricated pattern welded Damascus steel. *Metallurgist.* **51**, 681–695 (2007).

31. O. D. Sherby, J. Wadsworth, in *Journal of Materials Processing Technology* (2001), vol. 117, pp. 347–353.

32. J. R. Speer, W. L. Forster, Alloy of Iron. *US Pat. 1,346,343* (1913).

33. D. R. Lesuer, C. K. Syn, O. D. Sherby, "Ultrahigh Carbon Steel for Automotive Applications" (SAE Technical Paper 960314, 1996), , doi:10.4271/960314.

34. D. R. Lesuer, C. K. Syn, A. Goldberg, J. Wadsworth, O. D. Sherby, The case for ultrahigh-carbon steels as structural materials. *JOM.* **45**, 40–46 (1993).

35. H. Howe, *The Metallurgy of Steel vol. 1* (1890).

36. B. Walser, O. D. Sherby, Mechanical behavior of superplastic ultrahigh carbon steels at elevated temperature. *Metall. Trans. A.* **10**, 1461–1471 (1979).

37. O. D. Sherby, M. Young, D. Mar, B. Walser, E. M. Cady, Superplastic Ultra High Carbon Steel (1976).

38. J. Wadsworth, O. D. Sherby, The History of Ultrahigh Carbon Steels (1997).

39. R. . Heckel, H. W. Paxton, On the Morphology of Proeutectoid Cementite. *Trans. Am. Soc. Met.* **53**, 539–554 (1961).

40. G. Byun, S. Oh, C. Gil, S. Lee, Correlation of Microstructure and Microfracture Mechanism of Five Work Rolls. *Metall. Mater. Trans. A* (1999).

41. S. Lee, D. H. Kim, J. H. Ryu, K. Shin, Correlation of microstructure and thermal fatigue property of three work rolls. *Metall. Mater. Trans. A.* **28**, 2595–2608 (1997).

42. T. Oyama, O. D. Sherby, J. Wadsworth, B. Walser, Application of the divorced eutectoid transformation to the development of fine-grained, spheroidized structures in ultrahigh carbon steels. *Scr. Metall.* **18**, 799–804 (1984).

43. O. D. Sherby, J. Wadsworth, Ultrahigh Carbon Steels , Damascus Steel, and Superplasticity (1997).

44. T. Furuhara, E. Sato, T. Mizoguchi, S. Furimoto, T. Maki, Grain Boundary Character and Superplasticity of Fine-Grained Ultra-High Carbon Steel. *Mater. Trans.* **43**, 2455–2462 (2002).

45. *Steel Industry Annual Report: On competitive Conditions in the Steel Industry and*

Industry Efforts to Adjust and Modernize (USITC Publication 2316, 1990).

46. K. P. Liu, X. L. Dun, J. P. Lai, H. S. Liu, Effects of modification on microstructure and properties of ultrahigh carbon (1.9wt.% C) steel. *Mater. Sci. Eng. A*. **528**, 8263–8268 (2011).

47. M. Wang, S. Mu, F. Sun, Y. Wang, Influence of Rare Earth Elements on Microstructure and Mechanical Properties of Cast High-Speed Steel Rolls. *J. Rare Earths*. **25**, 490–494 (2007).

48. M. A. Hamidzadeh, M. Meratian, M. Mohammadi Zahrani, A study on the microstructure and mechanical properties of AISI D2 tool steel modified by niobium. *Mater. Sci. Eng. A*. **556**, 758–766 (2012).

49. M. A. Hamidzadeh, M. Meratian, A. Saatchi, Effect of cerium and lanthanum on the microstructure and mechanical properties of AISI D2 tool steel. *Mater. Sci. Eng. A*. **571**, 193–198 (2013).

50. M. Qian, L. Baicheng, W. Zhaochang, Breakup of eutectic carbide network of white cast irons at high temperatures. *J. Mater. Sci.* **30**, 3383–3386 (1995).

51. J. Pacyna, I. C. Science, Effect of annealing on structure and properties of ledeburitic cast steel. *J. Achiev. Mater. Manuf. Eng.* **24**, 84–90 (2007).

52. L. Richard, G. Krauss, Iron-chromium-carbon system at 870°C. *Metall. Trans. A*. **7**, 983–989 (1976).

53. J. M. Beswick, The effect of chromium in high carbon bearing steels. *Metall. Trans. A*. **18**, 1897–1906 (1987).

54. J. O. Andersson, T. Helander, L. Höglund, P. Shi, B. Sundman, Thermo-Calc & DICTRA, computational tools for materials science. *Calphad Comput. Coupling Phase Diagrams Thermochem.* **26**, 273–312 (2002).

55. G. D. de Almeida Soares, L. H. de Almeida, T. L. da Silveira, I. Le May, Niobium additions in HP heat-resistant cast stainless steels. *Mater. Charact.* **29**, 387–396 (1992).

56. K. G. Buchanan, M. V. Kral, Crystallography and morphology of niobium carbide in as-cast HP-niobium reformer tubes. *Metall. Mater. Trans. A Phys. Metall. Mater. Sci.* **43**, 1760–1769 (2012).

57. A. Noorian, S. Kheirandish, H. Saghafian, Evaluation of the Mechanical Properties of Niobium Modified Cast Aisi H 13 Hot Work Tool Steel. *Iran. J. Mater. Sci. Eng.* **7**, 22–29 (2010).

58. L. H. De Almeida, A. F. Ribeiro, I. Le May, Microstructural characterization of modified 25Cr-35Ni centrifugally cast steel furnace tubes. *Mater. Charact.* **49**, 219–229 (2002).

59. S. Karagoz, H. E. Fischmeister, Niobium-Alloyed High Speed Steel by Powder Metallurgy. **19**, 1395–1401 (1988).

60. S. Kheirandish, S. Mirdamadi, Y. H. K. Karrazi, Effect of niobium on cast structure of high speed steel. *Steel Res.* **68**, 457–461 (1997).

61. B. A. Migachev, Effect of niobium on the mechanical properties of steel 9Kh2MF, used for fabricating forming rolls. *Met. Sci. Heat Treat.* **43**, 103–106 (2001).

62. C. He-Xing, C. Zhe-Chuan, L. Jin-Cai, L. Huai-Tao, Effect of niobium on wear resistance of 15%Cr white cast iron. *Wear*. **166**, 197–201 (1993).

63. M. Fiset, K. Peev, M. Radulovic, The influence of niobium on fracture toughness and abrasion resistance in high-chromium white cast irons. *J. Mater. Sci. Lett.* **12**, 615–617 (1993).

64. P. Novák, D. Vojtěch, J. Šerák, Pulsed-plasma nitriding of a niobium-alloyed PM tool

`

steel. *Mater. Sci. Eng. A*. **393**, 286–293 (2005).

65.   Y. Ma, X. Li, Y. Liu, S. Zhou, X. Dang, Microstructure and properties of Ti-Nb-V-Mo-alloyed high chromium cast iron. *Bull. Mater. Sci.* **36**, 839–844 (2013).

66.   X. Zhi, J. Xing, H. Fu, B. Xiao, Effect of niobium on the as-cast microstructure of hypereutectic high chromium cast iron. *Mater. Lett.* **62**, 857–860 (2008).

67.   H. Mohrbacher, in *Materials Science & Technology* (2011), pp. 434–445.

68.   S. Kheirandish, H. Saghafian, J. Hedjazi, M. Momeni, Effect of heat treatment on microstructure of modified cast AISI D3 cold work tool steel. *J. Iron Steel Res. Int.* **17**, 40–45,52 (2010).

69.   M. E. Maja, M. G. Maruma, L. A. Mampuru, S. J. Moema, Effect of niobium on the solidification structure and properties of hypoeutectic high-chromium white cast irons. *J. South. African Inst. Min. Metall.* **116**, 981–986 (2016).

70.   F. Haddad, S. E. Amara, R. Kesri, S. Hamar-Thibault, Contribution to the study of the Fe-Nb-C ternary system. *J. Phys. IV Fr.* **122**, 35–39 (2004).

71.   R. Powell, T. Holland, B. Worley, Calculating phase diagrams involving solid solutions via non-linear equations, with examples using THERMOCALC. *J. Metamorph. Geol.* **16**, 577–588 (1998).

72.   "ASTM Standard E23, 2012, 'Standard Test Methods for Notched Bar Impact testing of Metallic Materials'" (ASTM International, West Conshohocken, PA, 2012), , doi:10.1520/E0023-12C.

73.   ASTM Standard E2298 - 15, 2009, "Standard Test Method for Instrumented Impact Testing of Metallic Materials" (2009), pp. 1–9.

74.   M. . Kral, G. Spanos, Three-dimensional analysis of proeutectoid cementite precipitates. *Acta Mater.* **47**, 711–724 (1999).

75.   E. M. Taleff, C. K. Syn, D. R. Lesuer, O. D. Sherby, Pearlite in Ultrahigh Carbon Steels: Heat Treatments and Mechanical Properties. **27**, 111–118 (1996).

76.   C. J. V. T. E.J. Pavlina, Correlation of Yield Strength and Tensile Strength with Hardness for Steels. *J. Mater. Eng. Perform.* **17**, 888–893 (2008).

77.   M. D. Hecht, B. A. Webler, Y. N. Picard, Digital image analysis to quantify carbide networks in ultrahigh carbon steels. *Mater. Charact.* **117**, 134–143 (2016).

78.   I. M. Bernstein, W. Patterson, The Role of Microstructure on the Strength and Toughness of Fully Pearlitic Steels. **7** (1976).

79.   A. Fernández-Vicente, M. Carsí, F. Penalba, E. Taleff, O. A. Ruano, Toughness dependence on the microstructural parameters for an ultrahigh carbon steel (1.3 wt.% C). *Mater. Sci. Eng. A*. **335**, 175–185 (2002).

80.   E. Rózniata, J. Pacyna, Effect of structure on mechanical properties of Cr-Ni-Mo cast steel. *J. Achiev. Mater. Manuf. Eng.* **28**, 224–230 (2007).

81.   Dietrich Stauffer, *Introduction To Percolation Theory: Revised Second Edition* (Taylor & Francis, ed. 2nd, 1994).

82.   M. Sahimi, J. D. Goddard, Elastic percolation models for cohesive mechanical failure in heterogeneous systems. *Phys. Rev. B*. **33**, 7848–7851 (1986).

83.   W. a. Curtin, H. Scher, Brittle fracture in disordered materials: A spring network model. *J. Mater. Res.* **5**, 535–553 (1990).

84.   D. Berrigan, L. W. Pickle, J. Dill, Associations between street connectivity and active transportation. *Int. J. Health Geogr.* **9**, 1–18 (2010).

85.   J. Dill, Measuring network connectivity for bicycling and walking. *83rd Annu. Meet.*

Transp. Res. Board, 20 (2004).

86. Y. S. Wu, L. J. van Vliet, H. W. Frijlink, K. van der Voort Maarschalk, The determination of relative path length as a measure for tortuosity in compacts using image analysis. *Eur. J. Pharm. Sci.* **28**, 433–440 (2006).

87. A. Odgaard, Three-dimensional methods for quantification of cancellous bone architecture. *Bone*. **20**, 315–328 (1997).

88. J. Kabel, a. Odgaard, B. Van Rietbergen, R. Huiskes, Connectivity and the elastic properties of cancellous bone. *Bone*. **24**, 115–120 (1999).

89. M. D. Abràmoff, P. J. Magalhães, S. J. Ram, Image Processing with ImageJ. *Biophotonics Int*. **11**, 36–42 (2004).

90. G. Polder *et al.*, Measuring shoot length of submerged aquatic plants using graph analysis Measuring shoot length of submerged aquatic plants using graph analysis (2010).

91. I. Arganda-Carreras, R. Fernández-González, A. Muñoz-Barrutia, C. Ortiz-De-Solorzano, 3D reconstruction of histological sections: Application to mammary gland tissue. *Microsc. Res. Tech.* **73**, 1019–29 (2010).

92. Z.-L. Zhang, Y.-N. Liu, J.-W. Zhu, G. Yu, Processing and properties of ultrahigh-carbon (1.6%C) steel. *Mater. Sci. Eng. A*. **483–484**, 64–66 (2008).

93. H. Berns, C. Broeckmann, Fracture Of Hot Formed Ledeburitic Chromium Steels. *Eng. Fract. Mech.* **58**, 311–325 (1997).

94. J. Hemanth, Effect of cooling rate on dendrite arm spacing (DAS), eutectic cell count (ECC) and ultimate tensile strength (UTS) of austempered chilled ductile iron. *Mater. Des.* **21**, 1–8 (1999).

95. M. D. Hecht, Y. N. Picard, B. A. Webler, Coarsening of Inter- and Intra-granular Proeutectoid Cementite in an Initially Pearlitic 2C-4Cr Ultrahigh Carbon Steel. *Metall. Mater. Trans. A Phys. Metall. Mater. Sci.* **48**, 2320–2335 (2017).

96. S. P. Rawal, J. Gurland, Observations on the effect of cementite particles on the fracture toughness of spheroidized carbon steels. *Metall. Trans. A*. **8**, 691–698 (1977).

97. C. K. Syn, D. R. Lesuer, O. D. Sherby, Influence of microstructure on tensile properties of spheroidized ultrahigh-carbon (1.8 Pct C) steel. *Metall. Mater. Trans. A*. **25**, 1481–1493 (1994).

98. J. Gurland, Observations on the fracture of cementite particles in a spheroidized 1.05% C steel deformed at room temperature. *Acta Metall.* **20**, 735–741 (1972).

99. Gene E. Lee, Ed., *Rolls for the Metalworking Industries* (Iron and Steel Society, Warrendale, PA, 2002).

100. G. Molinder, A quantitative study of the formation of austenite and the solution of cementite at different austenitizing temperatures for a 1.27% carbon steel. *Acta Metall.* **4**, 565–571 (1956).

101. D. Shtansky, K. Nakai, Y. Ohmori, Pearlite to austenite transformation in an Fe–2.6 Cr– 1C alloy. *Acta Mater.* **47**, 2619–2632 (1999).

102. G. R. Speich, a Szirmae, M. J. Richards, Formation of Austenite From Ferrite and Ferrite-Carbide Aggregates. *Scientist*. **245**, 1063–1074 (1968).

103. I. M. Lifshitz, V. V. Slyozov, The kinetics of precipitation from supersaturated solid solutions. *J. Phys. Chem. Solids*. **19**, 35–50 (1961).

104. C. Wagner, "Theorie der Alterung von Niederschlägen durch Umlösen (Ostwald-Reifung)" [Theory of the aging of precipitates by dissolution-reprecipitation (Ostwald ripening)]. *Zeitschrift für Elektrochemie*. **65**, 581–591 (1961).

105. M. Kahlweit, Ostwald ripening of precipitates. *Adv. Colloid Interface Sci.* **5**, 1–35 (1975).

106. M. V. Speight, Growth kinetics of grain-boundary precipitates. *Acta Metall.* **16**, 133–135 (1968).

107. A. J. Ardell, On the coarsening of grain boundary precipitates. *Acta Metall.* **20**, 601–609 (1972).

108. B. A. Lindsley, A. R. Marder, The morphology and coarsening kinetics of spheroidized Fe – C binary alloys. *Acta Mater.* **46**, 341–351 (1998).

109. P. Deb, M. C. Chaturvedi, Coarsening behavior of cementite particles in a ferrite matrix in 10B30 steel. *Metallography.* **354**, 341–354 (1982).

110. W. J. Nam, C. M. Bae, Coarsening behavior of cementite particles at a subcritical temperature in a medium carbon steel. *Scr. Mater.* **41**, 313–318 (1999).

111. A. M. Cree, R. G. Faulkner, A. T. Lyne, Cementite particle coarsening during spheroidisation of bearing steel SAE 52100. *Mater. Sci. Technol.* **11**, 566–571 (1995).

112. Z. Q. Lv *et al.*, Effect of alloying elements addition on coarsening behavior of pearlitic cementite particles after severe cold rolling and annealing. *Mater. Sci. Eng. A.* **489**, 107–112 (2008).

113. R. V. Day, J. Barford, Particle coarsening in the solid state. *Nature.* **217**, 1145–1146 (1968).

114. C.-Y. Li, J. . Blakely, A. . Feingold, Mass transport analysis for ostwald ripening and related phenomena. *Acta Metall.* **14**, 1397–1402 (1966).

115. A. A. Vasilyev, S. F. Sokolov, N. G. Kolbasnikov, D. F. Sokolov, Effect of alloying on the self-diffusion activation energy in γ-iron. *Phys. Solid State.* **53**, 2194–2200 (2011).

116. G. H. Zhang, J. Y. Chae, K. H. Kim, D. W. Suh, Effects of Mn, Si and Cr addition on the dissolution and coarsening of pearlitic cementite during intercritical austenitization in Fe-1mass%C alloy. *Mater. Charact.* **81**, 56–67 (2013).

117. E. L. Brown, G. Krauss, Retained carbide distribution in intercritically austenitized 52100 steel. *Metall. Trans. A.* **17**, 31–36 (1986).

118. N. V. Luzginova, L. Zhao, J. Sietsma, The Cementite Spheroidization Process in High-Carbon Steels with Different Chromium Contents. *Metall. Mater. Trans. A.* **39**, 513–521 (2008).

119. F. S. Birks, N., Meier, G.H. and Pettit, *Introduction to the High Temperature Oxidation of Metals* (Cambridge University Press, ed. 2nd, 2006).

120. C. A. Schneider, W. S. Rasband, K. W. Eliceiri, NIH Image to ImageJ: 25 years of image analysis. *Nat. Methods.* **9**, 671–675 (2012).

121. S. A. Saltikov, in *Proceedings of the Second International Congress for Stereology*, H. Elias, Ed. (Springer-Verlag New York Inc., Chicago, 1967), pp. 163–173.

122. D. L. Sahagian, A. A. Proussevitch, 3D particle size distributions from 2D observations: Stereology for natural applications. *J. Volcanol. Geotherm. Res.* **84**, 173–196 (1998).

123. E. Limpert, W. a. Stahel, M. Abbt, Log-normal distributions across the sciences: keys and clues. *Bioscience.* **51**, 341 (2001).

124. J. Heintzenberg, Properties of the log-normal particle size distribution. *Aerosol Sci. Technol.* **21**, 46–48 (1994).

125. D. P. Yao, Y. Z. Zhang, Z. Q. Hu, Y. Y. Li, C. X. Shi, The formation and growth of PFZ at grain boundary in Al-11.9 at.-%Li Alloy. *Scr. Metall.* **23**, 537–541 (1989).

126. T. Krol, D. Baither, E. Nembach, The formation of precipitate free zones along grain boundaries in a superalloy and the ensuing effects on its plastic deformation. *Acta Mater.*

52, 2095–2108 (2004).

127. R. W. Heckel, The growth and shrinkage rates of various size distributions. *Trans. Am. Soc. AIME*. **233**, 1994–2000 (1965).

128. K. M. Vedula, R. W. Heckel, Spheroidization of binary Fe-C alloys over a range of temperatures. *Metall. Trans.* **1**, 9–18 (1970).

129. J. Wang, P. van der Wolk, S. van der Zwaag, Determination of Martensite Start Temperature in Engineering Steels Part I. Empirical Relations Describing the Effects of Steel Chemistry. *Mater. Trans. JIM*. **41**, 761–768 (2000).

130. M. Umemoto, Z. G. Liu, K. Masuyama, K. Tsuchiya, Influence of alloy additions on production and properties of bulk cementite. *Scr. Mater.* **45**, 391–397 (2001).

131. M. J. Aziz, Pressure and Stress Effects on Diffusion in Si. *Defect Diffus. Forum*. **153–155**, 1–10 (1998).

132. F. S. Buffington, M. Cohen, Self-diffusion in alpha-iron under uniaxial compressive stress. *J. Met.* **4**, 859–860 (1952).

133. T. L. Christiansen, M. a. J. Somers, The Influence of Stress on Interstitial Diffusion - Carbon Diffusion Data in Austenite Revisited. *Defect Diffus. Forum*. **297–301**, 1408–1413 (2010).

134. S. W. Paddock, Confocal laser scanning microscopy. *Biotechniques*. **27**, 992–1004 (1999).

135. W. W. Mullins, Theory of Thermal Grooving. *J. Appl. Phys.* **28**, 333–339 (1957).

136. E. E. Underwood, Stereology, or the quantitative evaluation of microstructures. *J. Microsc.* **89**, 161–180 (1969).

137. M. N. Croker, R. S. Fidler, R. W. Smith, The Characterization of Eutectic Structures. *Proc. R. Soc. A Math. Phys. Eng. Sci.* **335**, 15–37 (1973).

138. T. L. Burnett *et al.*, Large volume serial section tomography by Xe Plasma FIB dual beam microscopy. *Ultramicroscopy*. **161**, 119–129 (2016).

`

Appendix A. Supplement to Chapter 4

A.1 Box Furnace

The particular box furnace used in Chapters 4 and 5 is located in room 3310 of Wean Hall at Carnegie Mellon University. **Figure A.1** shows the box furnace in operation, with the door open and closed. Temperature is maintained by resistive heating through coils inside the furnace. A small hole in the top of the furnace (not visible in the image) allows insertion of an external thermocouple to calibrate the temperature readout on the furnace. **Figure A.2** shows the results of such a calibration. The furnace readout was about 20°C too high according to the calibration; this difference was accounted for in the temperatures reported in Chapters 4 and 5.

Although all the samples reported in Chapter 4 were water-quenched, a few samples of as-cast 2C-4Cr UHCS were cooled through different methods. One sample was air cooled, and another sample was furnace cooled. I recorded the temperature readout during the furnace cooling, which is shown in **Figure A.3**. The exact rate of air cooling is not known, but is certainly slower than water-quenching.

Figure A.1 Box furnace – open and closed.

`
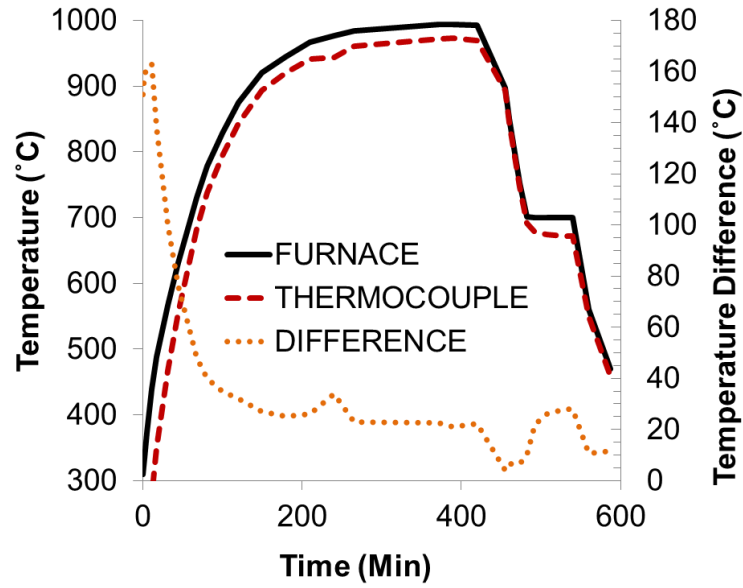
**Figure A.2** Calibration of temperature readout in box furnace using an inserted thermocouple.
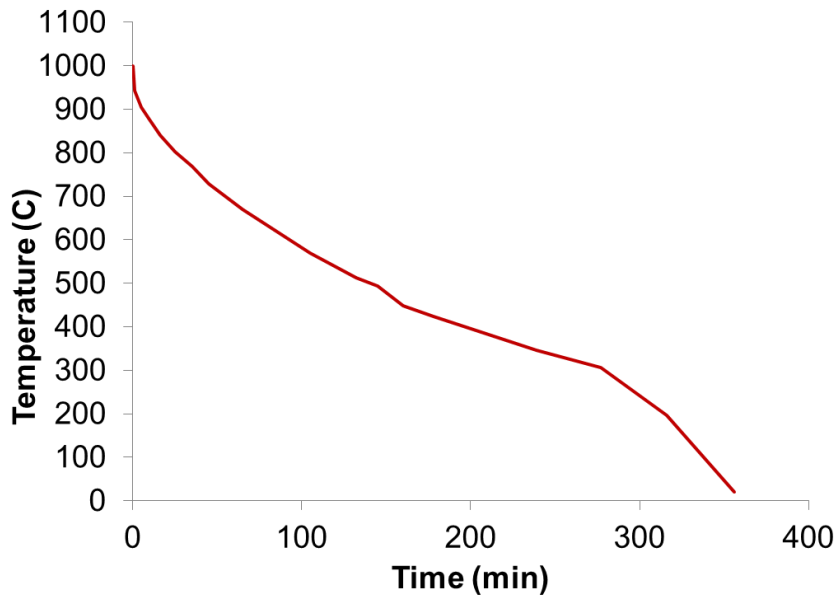
Figure A.3 Furnace cooling curve.

A.2 Cooling Rate and Temperature Effects on Hardness

Figure A.4 shows the matrix microstructures of 2C-4Cr UHCS samples which were isothermally held for 90 minutes at 970˚C and then water-quenched, air-cooled, or furnace-

cooled. It is apparent from the micrographs that the furnace cooled sample contained some pearlite in its matrix, while water-quenched and air cooled matrices did not. **Table A.1** shows measured Rockwell hardness of the three box furnace samples cooled by different methods, as well as MCC's as-cast (starting material for the box furnace studies) and heat-treated roll (MCC's industrial heat treatment) for comparison with the experimental cooling methods. The air- and water-quenched samples were significantly harder than the furnace cooled sample or MCC's samples, probably because of martensite or very fine bainite formation. The sample cooled in the box furnace furnace was even softer than the as-cast UHCS, indicating that the cooling rate in the box furnace was even slower than that cooling rate during centrifugal casting (and thus pearlite interlammelar spacing was higher).
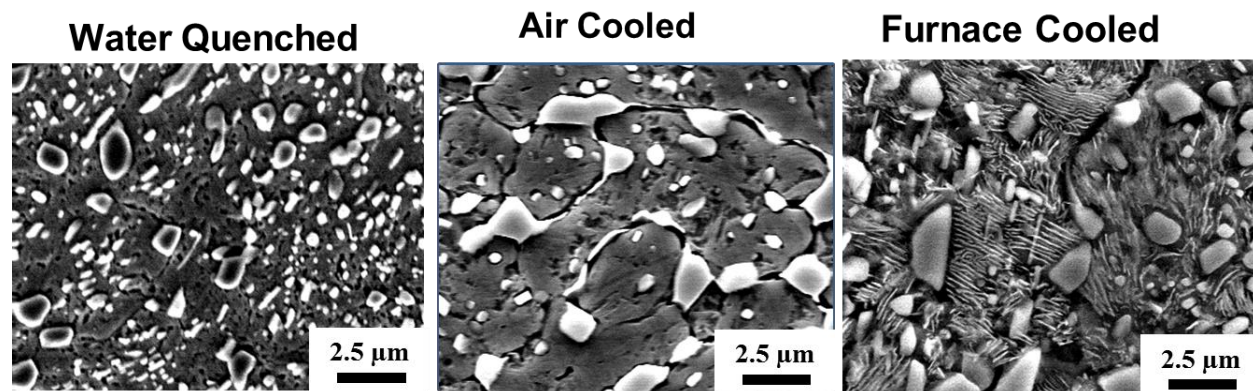
Figure A.4 Microstructures of 2C-4Cr UHCS samples cooled at three different rates.

Table A.1 Hardness of heat treated 2C-4Cr UHCS samples cooled at different rates.

Temp	Hold Time	Cooling	Hardness
970 ˚C	90 min	Water Quench	55.9 ± 0.6
970 ˚C	90 min	Air Cool	57.9 ± 0.2
970 ˚C	90 min	Furnace Cool	41.8 ± 0.2
No HT	No HT	As-Cast	44.2 ± 0.6
MCC HT	MCC HT	MCC	51.9 ± 0.3

`

Hardness was also measured as a function of the isothermal heat treatment temperature. **Table A.2** shows that the water-quenched hardness was much higher for samples quenched after 90 minute holds at 800°C and 900°C rather than 970°C. This increase in hardness could either be caused by an increased C content in the martensitic matrices of samples quenched at lower temperatures, or indicate that more martensite was forming when quenching the UHCS from 800°C or 900°C than from 970°C. For instance, **Figure 1.12** shows that the hardness of as-quenched martensite increases with C content. According to the phase diagram for the 2C-4Cr UHCS shown in **Figure 2.1**, the C content of the austenite should decrease with temperature, meaning that high C content martensite was unlikely. Thus, the most likely explanation for the hardness enhancement of isothermal quenches at lower temperature is that more martensite formed during quenching precisely because there was less C in solution in the austenite, since C lowers the martensite start temperature in steels (*129*)

Table A.2 Hardness of 2C-4Cr UHCS samples quenched after 90 minute isothermal holds at different temperatures.

Temp	Time	Cool	Hardness (RC)
970 °C	90 Min	Water Quenched	55.9 ± 0.6
900 °C	90 Min	Water Quenched	64.3 ± 0.2
800 °C	90 Min	Water Quenched	66.3 ± 0.2

A.3 Cr Content in Denuded Zones

Cr content within the denuded zones adjacent to the network branches was compared to the Cr content of the cementite network and particles and the normal (non-denuded) matrix. **Figure A.5** shows the locations of EDS point scans performed on 2C-4Cr UHCS which had undergone 3 heat treatment and quenching cycles (90 minutes at each of 970°C, 900°C, and 800°C, starting at 970°C). **Table A.3** shows the average Cr, Fe, C, and Si content measured at those locations (only

those four elements were selected for the scans). Cr content within the denuded zones and

normal matrix was identical in this UHCS sample.
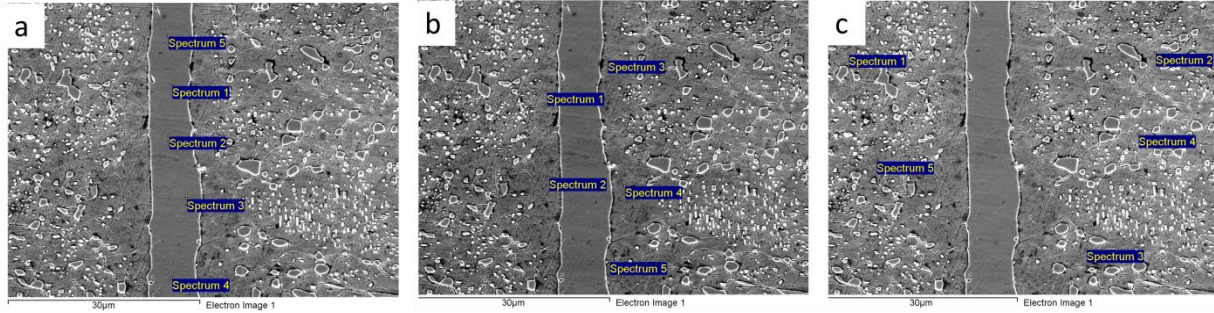
Figure A.5 EDS measurements at (a) the cementite network, (b) denuded zones adjacent to the network and (c) the matrix further away from the network.

Table A.3 EDS measurements of Fe, C, and Cr at indicated locations in 2C-4Cr UHCS heat treated at 970°C, 900°C, and 800°C for 90 minutes at each temperature (quenching after each).

EDS Measurement At:	Meas.	Fe	C	Cr	Si
Cementite Network [**Figure A.5 (a)**]	10	77 ± 1	5	18 ± 1	0
Denuded Zones [**Figure A.5 (b)**]	10	89 ± 1	1	9.3 ± 0.5	0.8 ± 0.1
Normal Matrix [**Figure A.5 (c)**]	10	89 ± 1	1	9.2 ± 0.9	0.7 ± 0.1
Cementite Particles [Not shown]	5	77 ± 1	5	18.1 ± 0.4	0

A.4 EBSD

Figure A.6 shows the microstructure of a 2C-4Cr UHCS heat treated in the box furnace for 90

minutes at 970°C. Particles were indexed by EBSD. The EBSD patterns always indicated that the

particles were cementite, although only the largest particles were indexed in this manner.
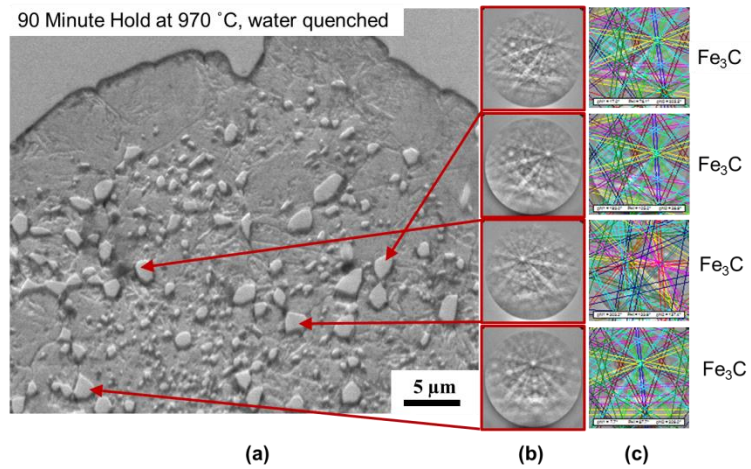
Figure A.6 EBSD on a box furnace sample heat treated at 970˚C indicates that particles were cementite.

`

Appendix B. Induction heated-treated 2C-4Cr UHCS

An experimental induction heat-treated 2C-4Cr UHCS roll was also provided by MCC. The heat treatment was the same as the conventionally heat-treated UHCS, and thus the resulting microstructure (shown in **Figure B.1** and **Figure B.2**) was very similar to that described in chapter 2, so that analysis is included as this appendix to the dissertation rather than a section of chapter 2. The main difference between the conventionally and induction heat-treated rolls was that the matrix of the induction heat-treated roll was entirely pearlitic, as shown in **Figure B.2**, rather than a combination of pearlite and bainite.
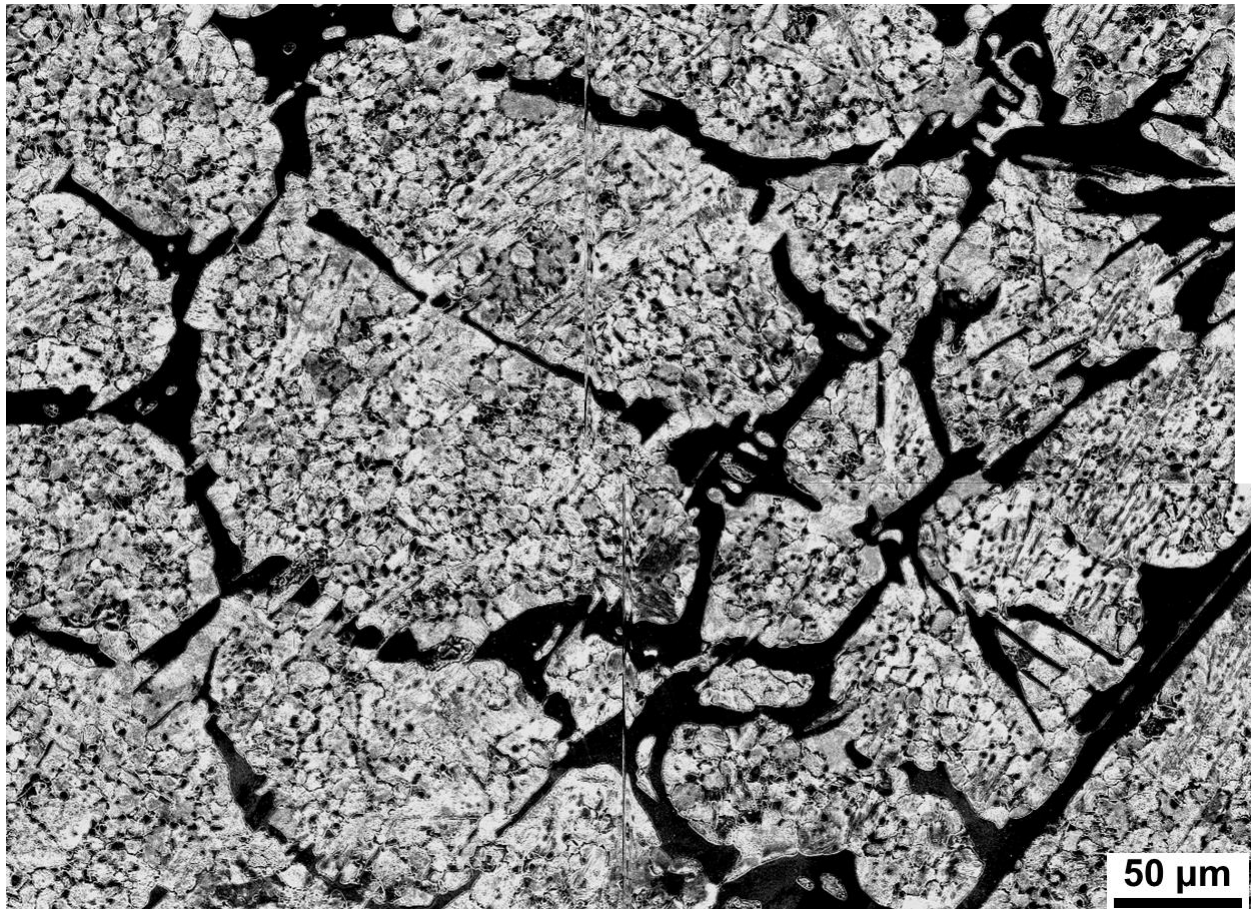
Figure B.1 Network and matrix microstructure of an induction heat-treated 2C-4Cr UHCS. This image is a composite of 4 higher magnification SEM micrographs which were matched at their edges to create a single image.

`
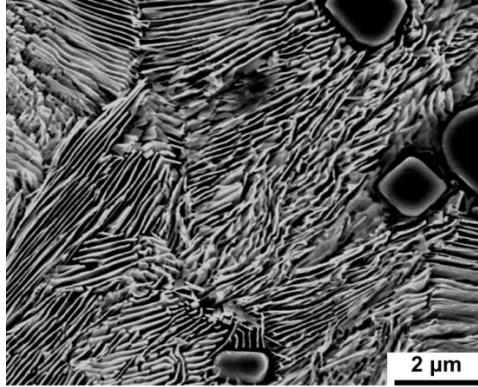
Figure B.2 Pearlite matrix in an induction heat-treated 2C-4Cr UHCS.
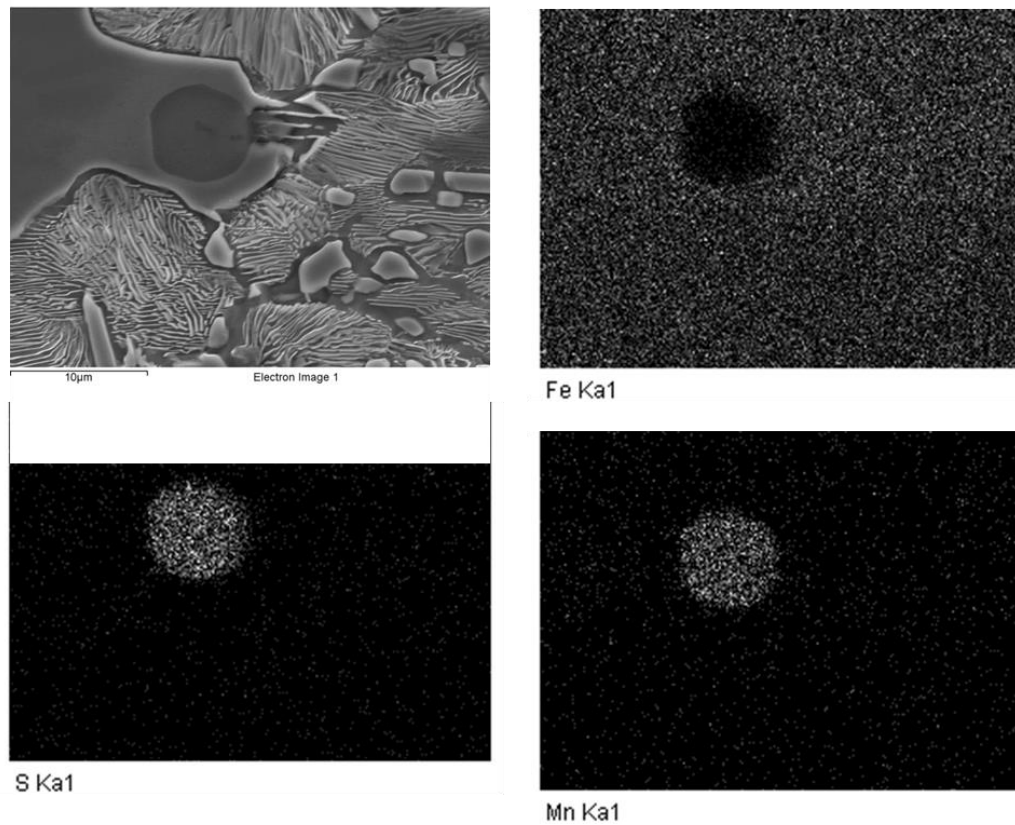
B.1 MnS Inclusions

Small volume fractions of MnS inclusions were present in all the UHCS rolls. Inclusions tended to be encased within cementite or NbC (all UHCS samples contained a small amount of NbC). **Figure B.3** shows an example of a MnS particle encased in cementite. **Figure B.4** shows an inclusion with Mn and S signals identified by EDS element mapping. **Figure B.5** shows a MnS particle encased within a NbC particle. The NbC was identified by EDS element mapping, which indicated a strong Nb signal around the particle, and the particle itself was identified by EDS point analysis shown in **Table B.1**. Shapes of the MnS inclusions were typically hexagonal.
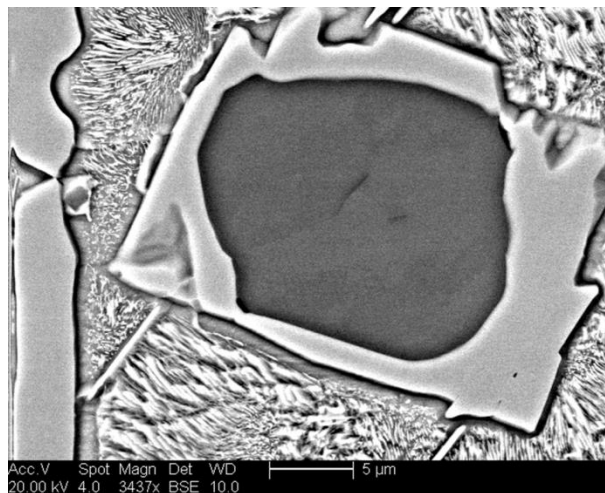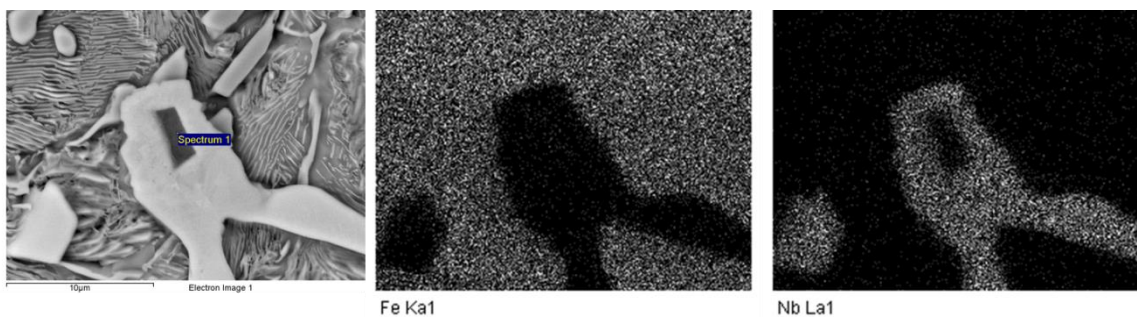

Figure B.3 MnS inclusion encased in cementite.

**Figure B.4** EDS element maps identify MnS inclusion in induction heat-treated 2C-4Cr UHCS.

Figure B.5 EDS element maps and point analysis identify MnS inclusion encased in NbC particle.

**Table B.1** Hardness of heat treated 2C-4Cr UHCS samples cooled at different rates.

Elements	C	O	Al	S	Ti	Cr	Mn	Fe	Total
Spectrum 1	4.32	6.18	1.54	30.64	2.22	0.47	51.02	3.60	100.00

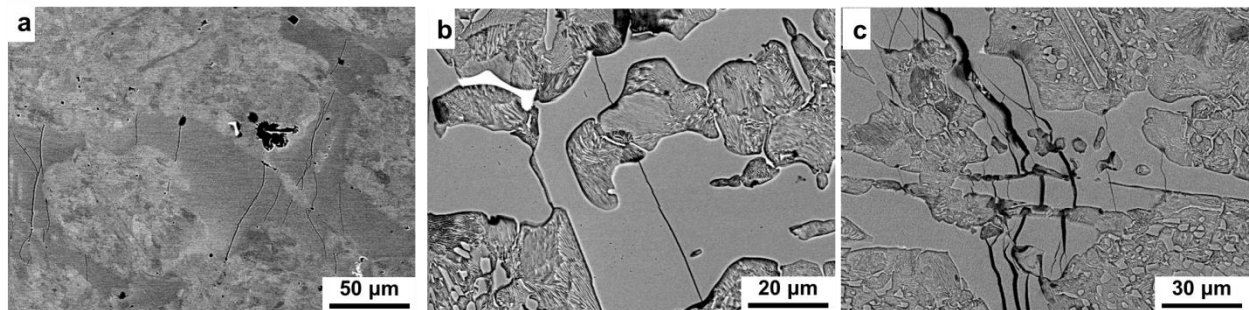## B.2 Cracking in Induction Heat-Treated 2C-4Cr UHCS

Some cracking was found in the induction heat-treated 2C-4Cr UHCS samples that were sectioned and polished for metallographic analysis. Since the UHCS was sent to us after the experimental heat treatment without undergoing any service, the cracks probably developed due to thermal stresses developed during the casting or heat-treatment processing. All observed cracks propagated along network cementite; several examples are shown in **Figure B.6**. **Figure B.7** shows a crack propagating through a cementite/MnS inclusion interface. **Figure B.8** shows examples from several different locations where cracks traveled perpendicular to the long axis of the network branches, yet did not penetrate into the matrix.
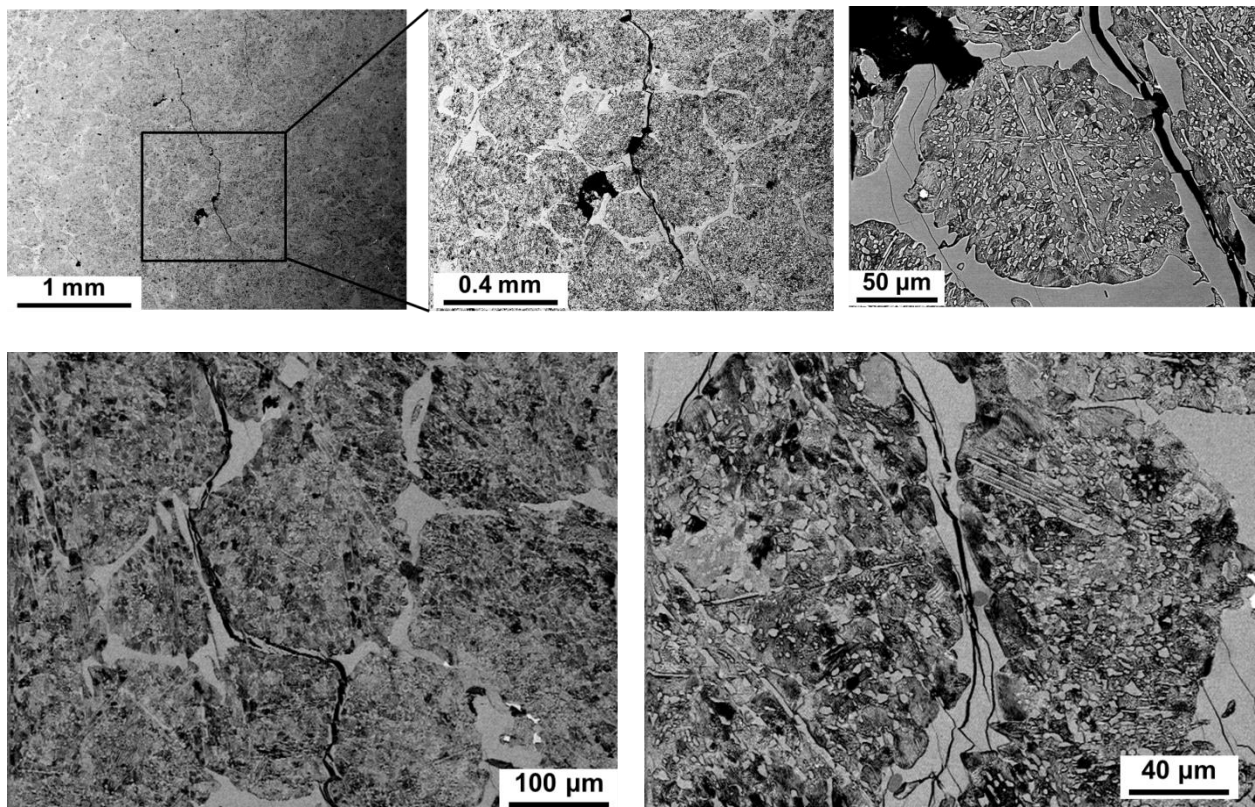
Figure B.6 BSE SEM micrographs showing cracks propagating along network branches in the induction heat-treated UHCS.
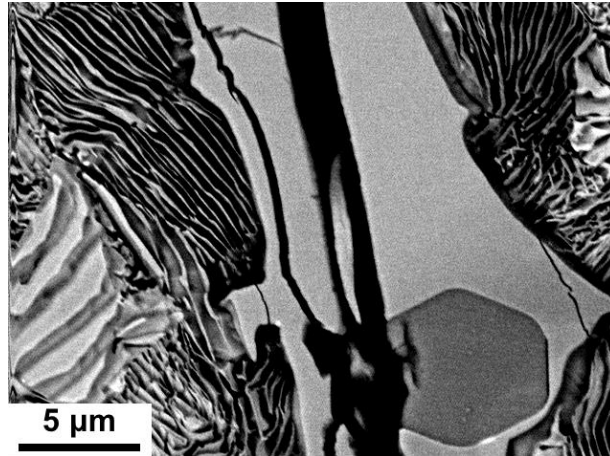
Figure B.7 BSE SEM micrograph of crack passing along MnS inclusion/cementite interface.

Figure B.8 BSE SEM micrographs showing cracks skipping over the matrix to propagate along network branches in induction heat-treated UHCS.

Appendix C. Supplement to chapter 7

C.1 Nb-V-Mo UHCS produced by MCC

The microstructure of a 2C-4Cr UHCS with the composition shown in **Table C.1** was also analyzed. The C content was much higher, and the Nb content was much lower than the samples investigated in Chapter 7. This UHCS was not included in chapter 7 because there was no control to compare it to, so any network refining or break-up effects are unknown. **Figure C.1** shows an OM micrograph of a polished and unetched sample. NbC structures with the Chinese Script morphology are visible in the sample.

Table C.1 Composition of Nb-V-Mo UHCS

Description	Fe	Nb	Cr	C	Mn	Mo	Si	Ni	V
Nb-V mod (MCC)	Bal.	0.99	3.48	2.30	0.71	0.92	0.60	0.72	0.94
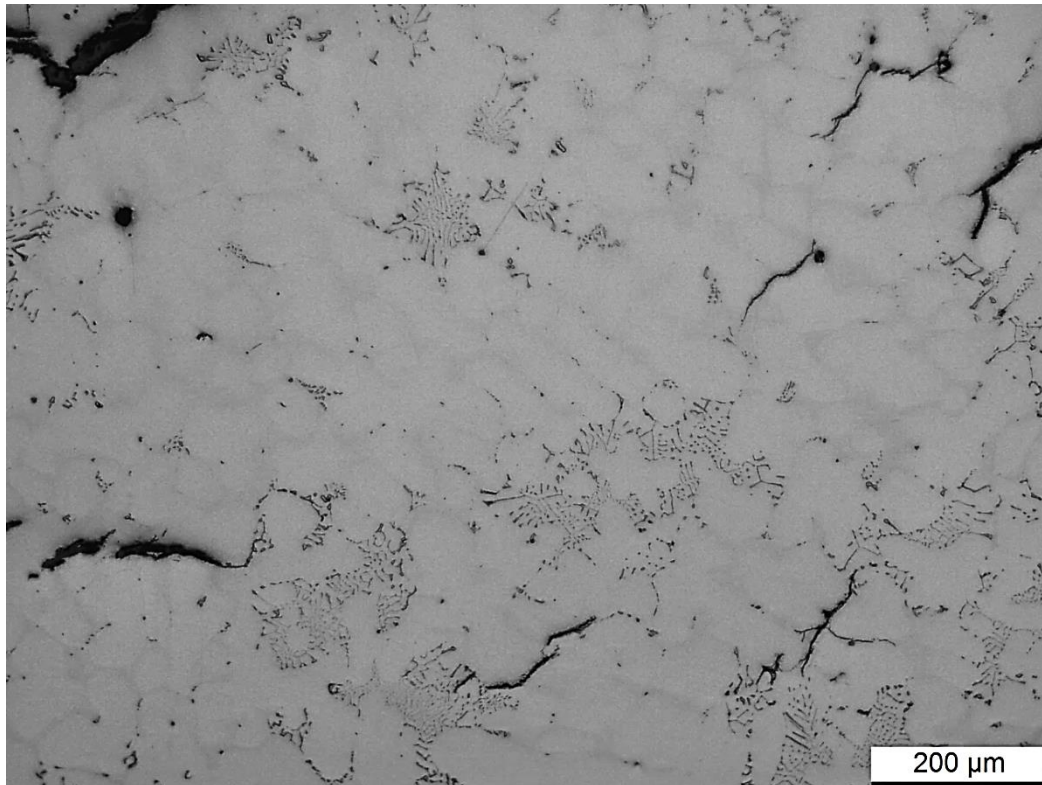
**Figure C.1** OM micrograph of Nb-V-Mo UHCS. NbC structures are visible.

Figure C.2 shows NbC structures in the Nb-V-Mo UHCS at three different magnifications. The sizes of the NbC structures were on the order of 100-200 μm; this is larger than the NbC structures in the Nb-modified button UHCS described in chapter 7, but smaller than the Nb-modified tube UHCS. This indicates that the solidification rate of the Nb-Mo-V UHCS was intermediate between the button and tube solidification rate. No blocky NbC structures were found in the Nb-Mo-V UHCS; this may be because the Nb content was not high enough to allow any Nb to solidify in the liquid prior to austenite nucleation, so all the NbC was formed cooperatively with the austenite. According to the pseudo-binary phase diagram shown in **Figure 1.27**, 1 wt% Nb is about the maximum amount of Nb that would avoid NbC solidification prior to austenite for the 2C-4Cr UHCS composition.
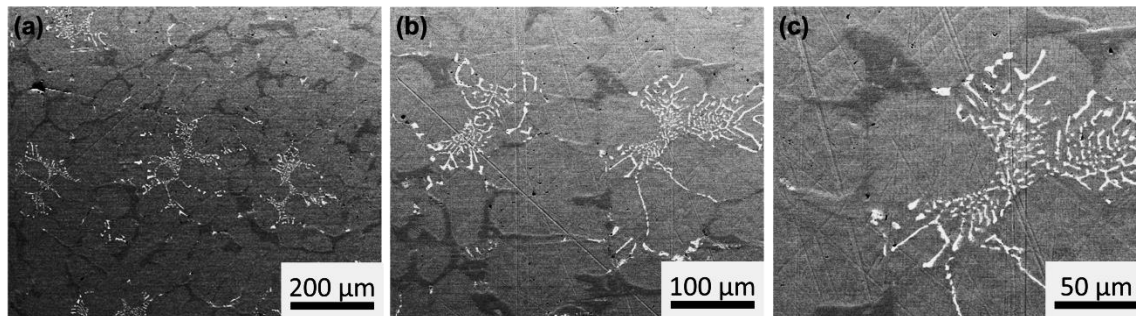

Figure C.2 BSE SEM micrographs showing NbC structures in the Nb-V-Mo UHCS at three different magnifications.

Figure C.3 shows the network in the Nb-MO-V UHCS. Network volume fraction and connectivity were high despite the Nb addition. **Figure C.4** shows the pearlitic matrix in the Nb-Mo-V UHCS.
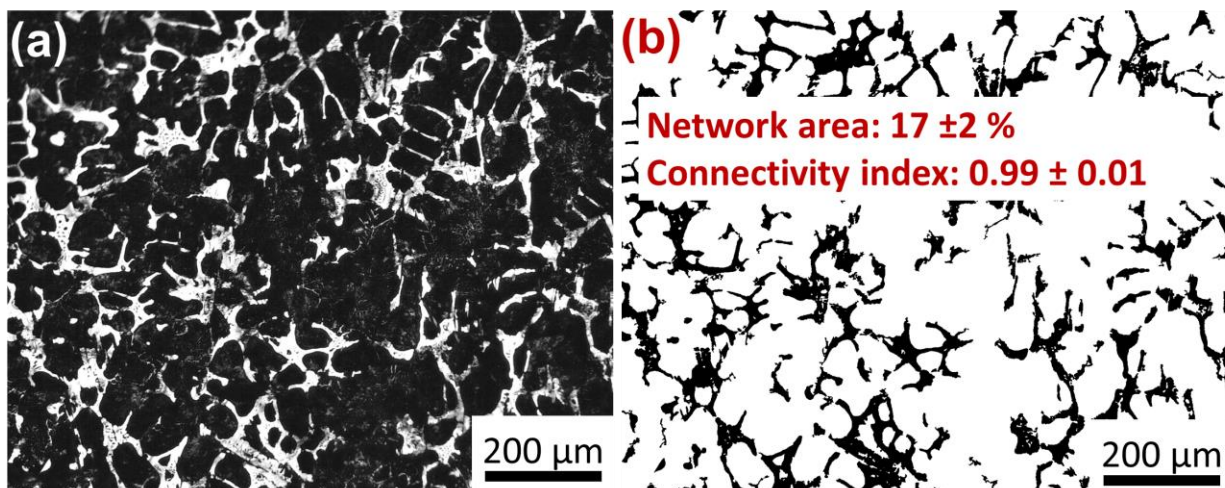
Figure C.3 (a) OM micrograph of etched Nb-V-MO UHCS (b) segmented to find network area and connectivity index.
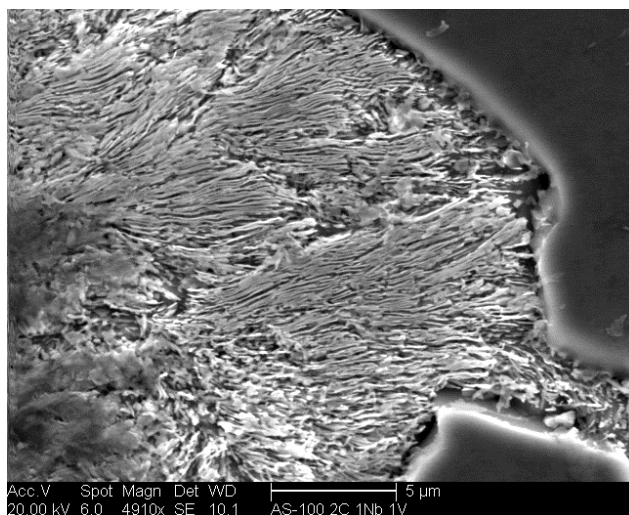
**Figure C.4** Pearlite Matrix in Nb-V-Mo UHCS.

C.2 Additional OM Micrographs of the Nb-Modified Tube UHCS

Figure C.5, **Figure C.6**, and **Figure C.7** show OM micrographs of the Nb-modified tube sample described in chapter 7. These OM micrographs help depict the sizes and morphologies of the NbC structures over large portions of the sample surface.
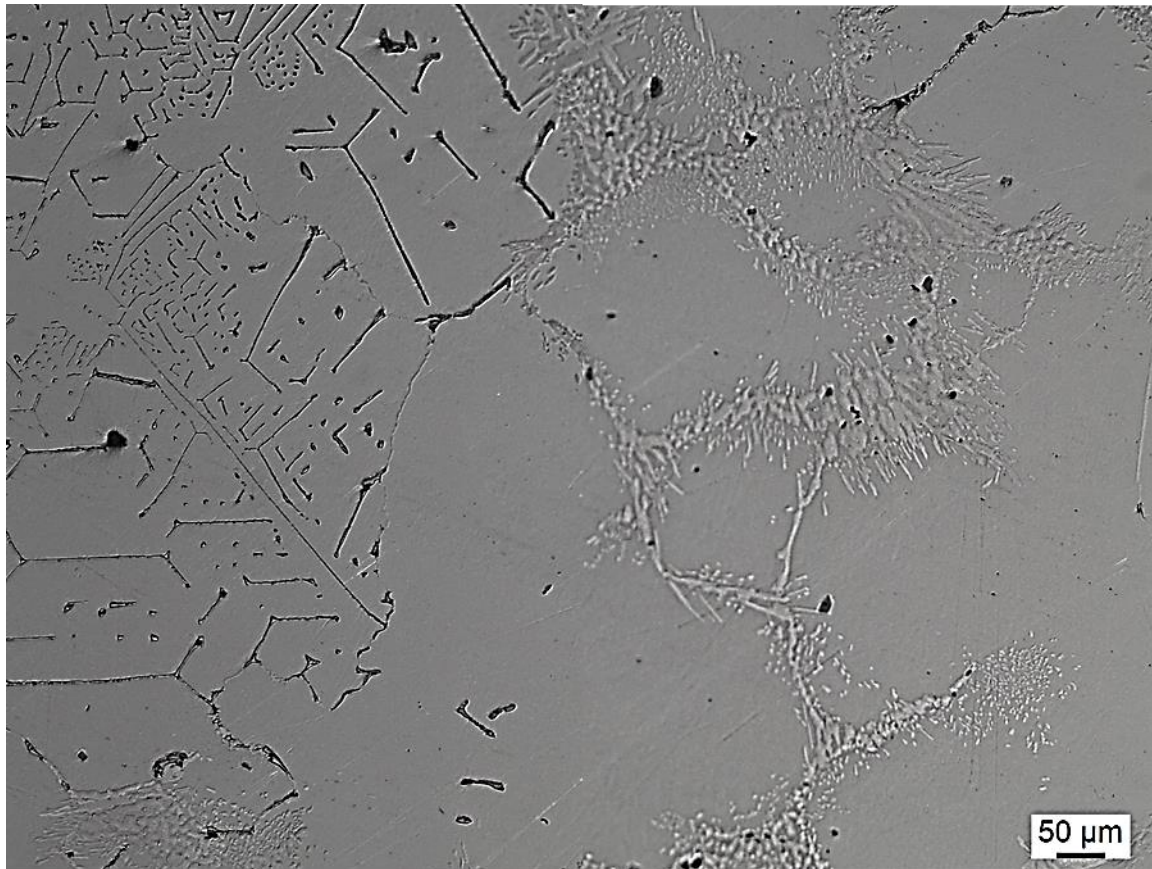
`

Figure C.5 OM micrograph of unetched Nb-modified tube UHCS microstructure. NbC structures and cementite/M_7C_3 network are visible.
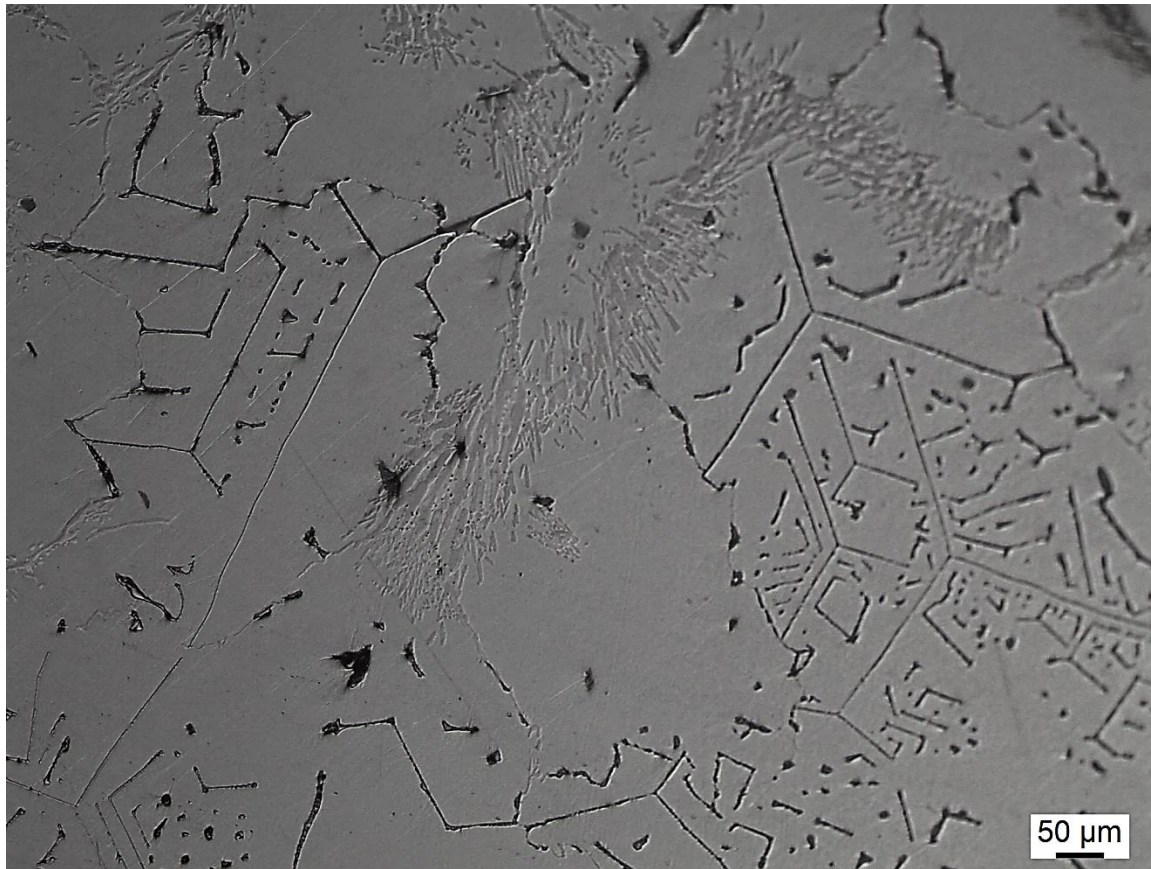
Figure C.6 OM micrograph of unetched Nb-modified tube UHCS microstructure. NbC structures and cementite/M_7C_3 network are visible.

Figure C.7 OM micrograph of unetched Nb-modified tube UHCS microstructure. NbC structures and cementite/M_7C_3 network are visible.